# Investigation Into Fuel Pre-treatments For Combustion Improvement On A Compression Ignition Engine

**Thesis by**

**Zhichao Zhang**

**In Partial Fulfilment of the Requirements**

**for the Degree of**

**Doctor of Philosophy (PhD)**

**SWAN Centre for Energy Research**

**School of Engineering**

**Date of Submission:**

**April 2019**

# Abstract

This project aims to improve the combustion performance of a compression ignition engine using three novel fuel pre-treatments, the employment of renewable fuels, nano additive modified fuels and supercritical (SC) fuel combustion, from the perspective of spray characteristics and engine performance. In this project, HVO and GTL are selected as the renewable fuels, whilst $CeO_2$ nanopowder and CNT are the nano additives. A CVV system is fabricated to investigate macroscopic spray characteristics of test fuels at various conditions. A 2D CFD model coupled with the DoE method is developed to correlate experimental conditions to macroscopic spray characteristics. A Cummins ISB4.5 diesel engine test rig is employed to obtain the in-cylinder behaviour and pollutant emissions. A 3D CFD model is built to study the advantages of SC fuel combustion.

GTL shows the smallest spray tip penetration during both the injection and post-injection periods, whilst DF has the largest penetration, but the average cone angles are almost the same. Nano additives have no impact on the average cone angle and spray tip penetration, except that CNT can increase the spray tip penetration slightly in the post-injection period. Empirical models are formulated and indicates different impacts of each experimental condition during injection and post-injection.

HVO and GTL have lower fuel consumption and $NO_x$, HC and PN emissions than DF. $CeO_2$ nanopowder can significantly reduce $NO_x$, HC and PN emissions, whilst CO can only be reduced in a certain engine load and speed range. CNT lowers down all emissions when blending with most test fuels except GTL.

Compared with conventional spray combustion, SC fuel combustion illustrates significantly higher in-cylinder peak pressure and thus improved engine output power. Moreover, the fuel concentration and temperature field during the SC combustion are more evenly distributed, which enables more sufficient combustion and reduction of $NO_x$ and soot generation.

# Acknowledgement

First, I should thank to my supervisory team in the Swan Centre for Energy Research, Newcastle University, Professor Tony Roskilly, Dr Yiji Lu, Dr Yaodong Wang and Dr Andrew Smallbone. Every time I met important problems, Professor Roskilly gave me guidance to find a way out and proceeded the project. Dr Lu is the one help me most in the experimental work, including fixing problems of the experimental system, providing data and software to configure the test rig and pushing the technician. Dr Wang's help enabled my CFD model to work and generate good results. Dr Smallbone always gave valuable ideas which contributed to the project.

Second, I should thank to my friends Dr Haoliang Ren and Dr Zeyuan Cheng from Beihang University, China. Their suggestions helped me fix problems of the CFD spray model and improve the CFD SC model, which saved much time for this project.

Third, Mrs Chenxuan Dong from Cummins Ltd provided valuable data for the configuration of experimental system and the validation of the CFD models. Thanks a lot to her.

I am also grateful to my friend Dr Long Jiang and Shi Chen, who helped me measure the properties of test fuels in this project.

The SAgE Faculty Doctoral Training Award (DTA) and the China Scholarship Council (CSC) provided me with financial support for this project. Great thanks to them.

I am grateful to my Master supervisor Professor Longfei Chen too. He gave me a lot of experience in doing PhD and helped me when I met difficulties in the project.

I should give the greatest thanks to my parents. Every time I feel upset or frustrated, their love makes me easy and confident to march to the success. I love them very much.

Finally, special thanks to my love Miss Lok Wun Chao. Her companion and encouragement enabled me to overcome many difficulties in my PhD project with less pressure.

# Table of content

# List of figures

# List of tables

# List of publications

## Publications based on this project:

1. Z Zhang, et al. Performance of carbon nanotubes and Cerium Oxide nanopowder of different sizes as single component fuel additives [J]. Fuel. (In review)
2. Z Zhang, et al. Investigation of the macroscopic characteristics of Hydrotreated Vegetable Oil (HVO) spray using CFD method [J]. Fuel, 2019, 237: 28-39.
3. Z Zhang, et al. Experimental and Numerical Investigation on the Macroscopic Characteristics of Hydrotreated Vegetable Oil (HVO) Spray. 9th International Conference on Applied Energy, ICAE2017.

## Other publications:

1. Z Zhang, L Chen, Y Lu*, et al. Lean ignition and blow-off behaviour of butyl butyrate and ethanol blends in a gas turbine combustor [J]. Fuel, 2019, 239: 1351-1362.
2. Chen L, Zhang Z*, Lu Y, et al. Experimental study of the gaseous and particulate matter emissions from a gas turbine combustor burning butyl butyrate and ethanol blends [J]. Applied Energy, 2017, 195: 693-701.
3. Chen L, Zhang Z, et al. Quantifying the effects of fuel compositions on GDI-derived particle emissions using the optimal mixture design of experiments [J]. Fuel, 2015, 154: 252-260.

# Chapter 1 . Introduction

## 1.1. Background

Currently, around 91% fuel for transportation is derived from fossil fuel and shares about 30% of total energy consumption [1]. With the development of transportation, the consumption of fossil fuel will keep increasing and thus results in a significant growth of oil price [2, 3], because fossil fuel cannot be renewed once consumed. Meanwhile, vehicle engines, especially compression ignition engines, produce a large amount of pollutant emissions including carbon monoxide (CO), nitrogen oxides ($NO_x$), unburnt hydrocarbons (HC) and particulate matter (PM) by burning fossil fuels, which leads to continuous deterioration of environment [4]. Therefore, stringent regulations have been made to limit vehicle engine emissions. In the latest standard for commercial compression ignition engines (mainly diesel vehicles), Euro VI, the emissions of CO, $NO_x$, HC and PM are limited to no more than 1.5, 0.13, 0.4 and 0.01 (g/kWh) respectively [5]. Moreover, the particulate number (PN) is also implemented in the Euro VI. Under these considerations, researchers and vehicle manufactures are motived to develop clean combustion engine techniques and renewable fuels.

$NO_x$ and PM from compression ignition engines are the two main targets for most techniques of reducing emissions due to their large amount and high toxicity, and they are usually reduced by employing the aftertreatment system. For $NO_x$ emissions, the most widely used types of aftertreatment are the selective catalytic reduction (SCR), lean $NO_x$ trap (LNT) and SCR filter (SCRF) and their combinations. However, they are sensitive to engine conditions (e.g., wall temperature, exhaust temperature, and exhaust velocity) and are complex to control at some conditions due to adding mixers and hydrocarbons and removing produced $NH_3$ and sulphate compounds [6]. In terms of PM or PN, manufactures are using the diesel particulate filters (DPF) in the aftertreatment system [7]. By this means, PM can be significantly reduced, nevertheless, the engine output power is also impacted because the filter will have negative impacts on the exhaust pressure after a period of running.

The treatment to the fuel prior to combustion, which is named as the fuel pre-treatment, may have the potential to overcome these drawbacks of after-treatments. The fuel pre-treatment is the approach before combustion, via which the fuel properties associated with combustion behaviours would be changed to improve the engine performance. In other words, the replacement of the standard diesel fuel with renewable fuels, blending fuels with various additives and any other solutions to change fuel properties for sufficient and clean combustion can be regarded as the fuel pre-treatment.

As a fuel pre-treatment, the renewable fuel has drawn the eyes of the public in recent decades. Renewable fuels, usually including biofuels and synthetic fuels, can be obtained from renewable sources or by renewable methods and have the potential of reducing pollutant emissions from compression ignition engines. For diesel engines, most biodiesels are fatty acid methyl esters (FAME) produced by transesterification process [8-10], such as rapeseed methyl ester (RME), soy methyl ester (SME) and palm oil methyl ester (PME) etc. FAMEs are capable of producing less $NO_x$ and PM in diesel engines compared with the standard diesel fuel. However, the high oxygen content and low energy density of FAMEs reduce the engine output power at some conditions. Moreover, the unsaturated compositions of FAME have adverse influence on the oxidation stability and thus their percentage blending with standard diesel fuel are limited to 7% [11, 12].

Compared with FAMEs, the hydrogen-treated biofuels and the synthetic fuels have more advantages for diesel engines. The hydrogen-treated fuel (non-FAME biofuel) is manufactured by hydrogenation of traditional biofuels, whilst the synthetic fuel is liquid fuel produced by synthetic technology, usually known as the Fischer-Tropsch (FT) process, from coals, gas or biomass [13, 14]. As a result, the hydrogen-treated fuel and the synthetic fuel are mixtures of n- and i-paraffin, which enable higher energy density than FAMEs. Therefore, new renewable fuels such as hydrogen-treated fuels or synthetic fuels should be developed and studied.

The employment of fuel additives is another fuel pre-treatment to change fuel properties. Alcohols such as methanol, ethanol and butanol are initially used as the fuel additive to reduce emissions. However, their high oxygen content has a negative impact on the thermal efficiency and engine power [15]. Consequently, nano additives, mainly nanopowder of metal or metal oxides, are becoming new fuel additive candidates which can improve the engine power and reduce most pollutant emissions.

In addition to renewable fuels and nano additives, another way to change fuel properties prior to combustion is pre-heating the fuel, which is commonly used in ship engines burning heavy fuels. The advantage of pre-heating heavy fuels is mainly reducing the viscosity of the fuel to improve spray quality for more sufficient combustion. Similarly, in diesel engines, pre-heating would be also helpful for combustion, especially heating the diesel fuel to the supercritical state (SC). The SC fuel is usually used in rocket engines to obtain sufficient fuel-oxidant mixture by heating high pressure fuels to over its critical point, because fuels at SC state have as low viscosity and high diffusivity as gas but similar density to liquid, which enables more sufficient fuel-air mixing process for combustion. Accordingly, it is also promising to employ SC fuel for the combustion in compression ignition engines to obtain more complete and cleaner combustion.

## 1.2. Aims and objectives

According to aforementioned context, this project is aimed at studying the performance of three fuel pre-treatments, the employment of renewable fuels, nano additive modified fuels and supercritical (SC) fuel combustion, from the perspective of spray characteristics and engine performance. The research will be a fundamental exploration of renewable energy, higher combustion efficiency and cleaner combustion for compression ignition engines. Therefore, the objectives of this project are:

- Review previous research works regarding renewable fuels and nano additives, and their characteristics in spray and diesel engine combustion. Meanwhile, study the behaviour of SC fuels and relevant literature associated with its diesel engine application.
- Construct a constant volume vessel (CVV) system to conduct comparative experiments on the macroscopic spray characteristics of selected renewable fuels and nano additive modified fuels. Moreover, analyse the influence of experimental conditions on the macroscopic spray characteristics during both injection and post-injection periods. The results of these experiments would be the fundamental knowledge for analysing engine performance.
- Build a computational fluid dynamics (CFD) spray model to study the macroscopic spray characteristics at more extreme conditions than the spray experiment, where the influence of fuel injection pressure, fuel temperature, ambient pressure and ambient temperature on macroscopic spray characteristics can be focused. And then quantitively correlate the macroscopic spray characteristics with these fuel conditions and ambient conditions.
- Investigate the in-cylinder behaviour and pollutant emissions of the renewable fuels and nano additive modified fuels on a commercial diesel engine test rig under various speed and load conditions.
- Build a CFD cylinder model to conduct the SC fuel combustion and compare its in-cylinder behaviour and pollutant emissions with conventional spray combustion in diesel engines.

By these objectives, a comprehensive understanding would be obtained on the advantages and potential of renewable fuels, nano additive modified fuels and SC fuel combustion for the application in compression ignition engines.

## 1.3. Thesis outline

Based on the aims and objectives of this project, the thesis is organised as the following chapters:

### Chapter 1 . Introduction

Introduce the background of the research topics and highlight the aims and objectives of the project.

### Chapter 2 . Literature review

Introduce the fundamental knowledge of liquid fuel spray and the in-cylinder behaviour and pollutant emissions of compression ignition engines.

Summarise previous work on renewable fuels, nano additives and SC fuel combustion from the perspective of spray and engine performance, and analyse the gap between their studies and this work.

Introduce important methodologies or tools, e.g., the CFD code and design of experiments (DoE) etc., which can be used to research the fuel spray and SC fuel combustion.

### Chapter 3 . Macroscopic characteristics of fuel spray

Describe key properties of hydrotreated vegetable oil (HVO) and gas to liquid synthetic fuel (GTL), and then blend the standard diesel fuel (DF) and GTL with the multi-wall carbon nanotube (CNT) and $CeO_2$ nanopowder of two different sizes.

Describe the features of the CVV system and test its performance.

Conduct spray experiments of DF at various conditions and analyse the influence of experimental conditions on the average cone angle and spray tip penetration during both injection and post-injection periods.

Conduct spray experiments of HVO, GTL and DF at high ambient pressure and temperature, and compare their differences in the average cone angle and spray tip penetration.

Conduct spray experiments of nano additives modified DF and GTL at high ambient pressure and temperature, and compare their differences in the average cone angle and spray tip penetration.

### Chapter 4 . CFD model of fuel spray

Build a 2D CFD model according to the CVV and validate it by experimental average cone angle and spray tip penetration.

Investigate the macroscopic spray characteristics under extended fuel conditions and ambient conditions to obtain the impact of fuel injection pressure, fuel temperature, ambient pressure and ambient temperature on the average cone angle and spray tip penetration.

Formulate a quantitive correlation between the conditions and the spray tip penetration.

### Chapter 5 . Engine performance

Describe the Cummins ISB4.5 diesel engine test rig.

Conduct experiments to analyse the in-cylinder behaviour and pollutant emissions of nano additives modified DF at various engine speeds and loads.

Investigate the in-cylinder behaviour and pollutant emissions of HVO and GTL, as well as nano additives modified GTL at fixed engine speed and load.

### Chapter 6 . CFD model of supercritical fuel combustion

Build a CFD model according to the features of cylinder in the diesel engine in a period of time, and describe the theoretical principles of spray combustion and SC fuel combustion.

Validate the model by conventional spray combustion data of the diesel engine during the period.

Analyse the in-cylinder pressure, fuel distribution, temperature field and the soot and $NO_x$ generation of the SC fuel combustion to evaluate its advantages in diesel engines, compared with the spray combustion.

### Chapter 7 . Conclusions and future work

Conclude the main results or discoveries in this research work, and propose recommendations for future work.

# Chapter 2 . Literature review

In this chapter, the knowledge of the liquid fuel spray and the in-cylinder behaviour and pollutant emissions of compression ignition engines is firstly summarised. With the fundamental knowledge, a review of previous studies is then conducted on renewable fuels, nano additives and SC fuel combustion from the perspective of spray and engine performance. After the review, the gap of previous work can be found and thus bring in the research topic of this thesis.

## 2.1. Diesel fuel spray

Spray, also known as atomization, is a process that liquid fuel is injected into the air, breaks out into droplets and then evaporates, which has a significant impact on combustion characteristics, especially in terms of $NO_x$, CO, unburnt hydrocarbon (HC) as well as particle emissions [16, 17].

During the spray in compression ignition engines, the initial fuel velocity is over $10^2$ ms/s, and the outer surface of the injected fuel breaks up into droplets of closed size to the orifice of the injector. The liquid column from the injector to a finite length is named the breakup length (shown in Figure 2.1), beyond which the liquid column disintegrates and the air content in the spray increases. In the following process, the spray diverges, the penetration increases and the velocity decreases. Meanwhile, the droplets evaporates during this process [18]. Previous studies [19-25] have developed several theories to understand the spray and most of them consider it to consist of two process: the primary breakup and secondary breakup. The primary breakup refers to the process that liquid fuel is injected and breaks up into various discrete large-scale structures, which is relevant to factors such as aerodynamic stability and turbulent flow. The secondary breakup means the following breakup from large-scale structures to small droplets, which is mainly impacted by aerodynamic stability.

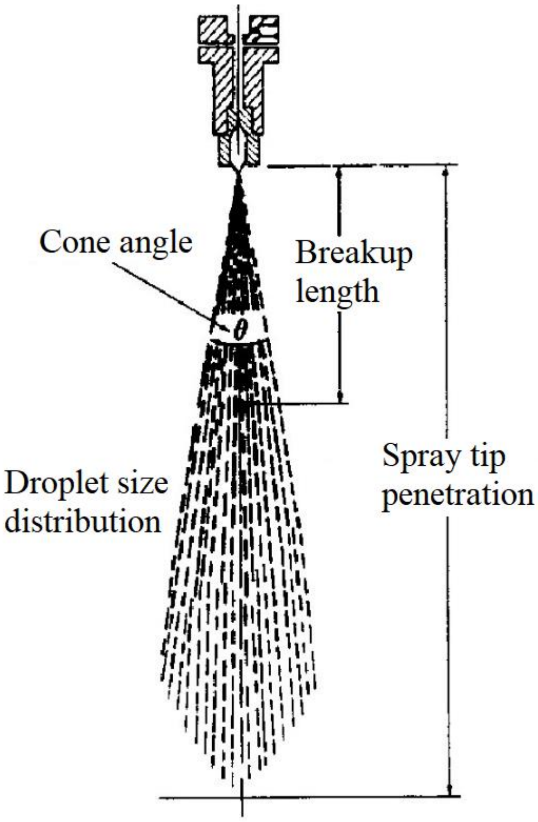

Figure 2.1. Schematic of fuel spray and its major parameters [26]

To a single droplet, the interaction of four forces, surface tension, viscous force, aerodynamic force and inertial force, determine its behaviour during the process. Obviously, the aerodynamic force and inertial force are factors causing instability and breakup of droplets, but surface tension and viscous force are those inhibiting the instability. In order to analyse the balance between aerodynamic force and surface tension, the Weber number is defined below [19]:

$$We = \frac{\rho_a v_a^2 d_0}{\sigma} \tag{2.1}$$

Where $\rho_a$ and $v_a$ is the density and relative velocity of air, and $d_0$ and $\sigma$ refers to surface tension, respectively. Considering the balance of force and energy conservation, $We$ larger than 12 always means the droplet is likely to break up.

Several parameters are introduced to indicate the spray quality. Among them, the spray tip penetration, cone angle and spray area are the commonly used macroscopic characteristics (shown in Figure 2.1). The spray tip penetration is usually used to stand for the fuel liquid penetration or fuel vapour penetration [27], depending on the method of measurement. The liquid penetration is defined as the length from the head of spray to the tail [28, 29], which is obtained by high speed camera or Schlieren photography [12, 30-33]. However, the vapour penetration can only be measured when Schlieren photography is employed because it takes the distribution of fuel vapour into account [32], which cannot be directly observed by camera. The difference between the liquid penetration and vapour penetration is illustrated in Figure 2.2.

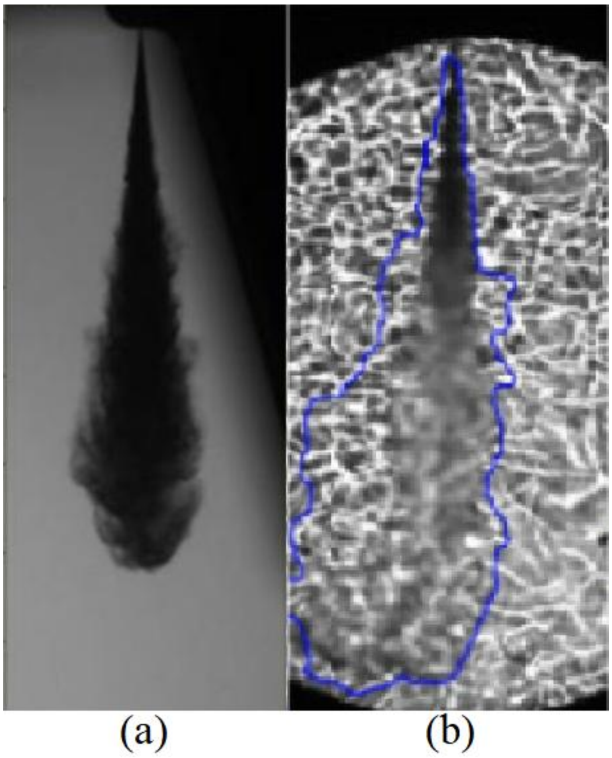

Figure 2.2. Illustration of the liquid penetration (a) and vapour penetration (b) [29, 32]

The cone angle can also be observed by optical measuring technologies. Its definition varies in different literature. Lefebvre [20] defines it as the angle formed by two straight lines drawn from the orifice to the outer periphery of the spray at a distance of 60 multiplying the orifice downstream of the nozzle. Chen et al. [34] use the angle formed by two lines from the tail of the spray to the outer periphery of the spray at the first 1/3 length of the spray tip penetration. Some others [35] define it as the angle formed by two tangential lines touching the outer boundaries of the spray on both sides and joining together at the nozzle exit. Different definitions of cone angle are shown in Figure 2.3.

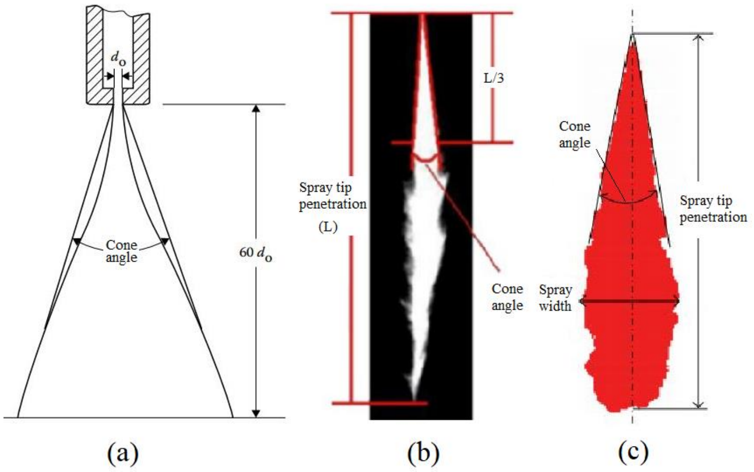

Figure 2.3. Various definitions of cone angle in literature [20, 34, 35]

Compared with the macroscopic characteristics, the microscopic characteristics mainly refer to the droplet size distribution, which is usually indicated by the Sauter Mean Diameter (SMD). The SMD is defined by the equation below [36]:

$$SMD = \frac{\int D_d^3 dn}{\int D_d^2 dn} \tag{2.2}$$

Where $dn$ is the number of droplets with the diameter $D_d$. According to the equation, SMD is total volume over the total surface spray, which indicates the characteristics of evaporation-combustion process [16]. The SMD can be measured by Malvern particle size analyser and Phase Doppler Particle Analyser (PDPA). These instruments mainly use the Fraunhofer or Mie scatter of laser through particles to calculate the particle size distribution. The difference between Malvern and PDPA is that Malvern use one laser beam to measure the mean size of particles in a line, whilst PDPA has two laser beams to measure the mean size of particles at one point. The principle of Malvern is illustrated in Figure 2.4.

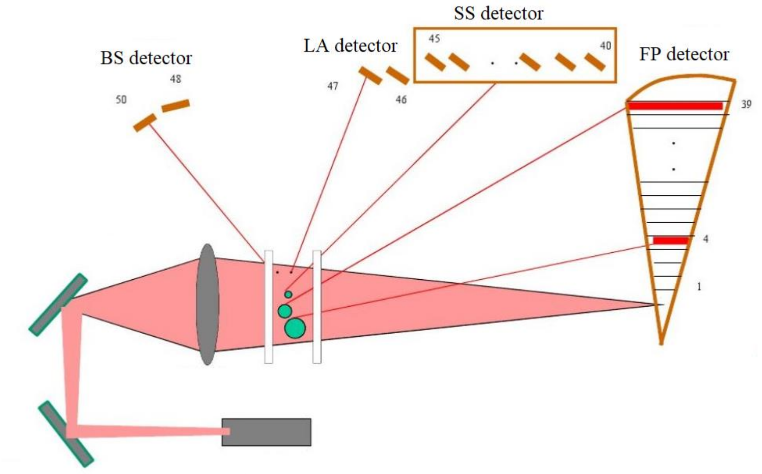

Figure 2.4. Principle of Malvern particle size analyser [37]

Therefore, a typical experimental system for measuring all the spray characteristics is shown in Figure 2.5, where the constant volume vessel is used to conduct the spray at certain conditions, the high speed camera is for the observation of macroscopic spray characteristics, and the laser measurement is for the microscopic spray characteristics.

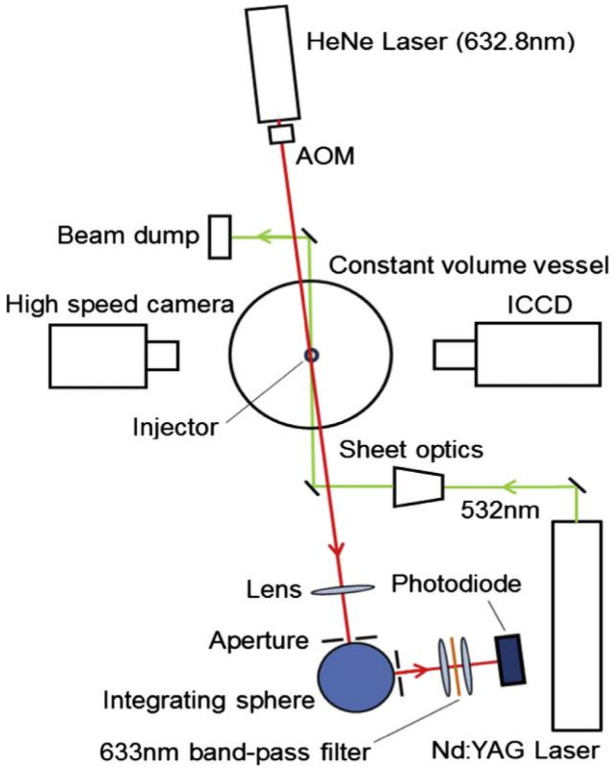

Figure 2.5. A typical CVV system with optical setup [38]

Summary

The knowledge of fuel spray is helpful to understand the detailed process of spray, and parameters to provide criteria of evaluating the spray quality. Moreover, the methods of measuring spray characteristics can be employed as potential tools for this research work.

## 2.2. Diesel engine performance

### *2.2.1. Combustion behaviour*

The diesel engine is one type of compression ignition engines, where the fuel is injected into the cylinder and mixed with the hot compressed air. The fuel is then auto-ignited and combust to release energy, which converts to mechanical energy by driving the piston. The combustion of the diesel engine is complex and dependent on many parameters, such as injection strategy, injection pressure, spray quality and timing. The in-cylinder pressure and heat release rate during a typical in-cylinder combustion are illustrated in Figure 2.6 and Figure 2.7.

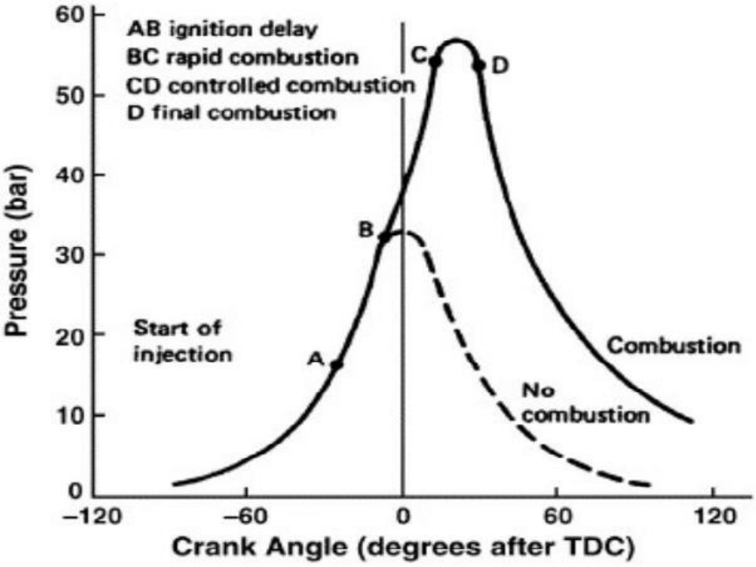

Figure 2.6. Hypothetical pressure diagram for a compression ignition engine [39]

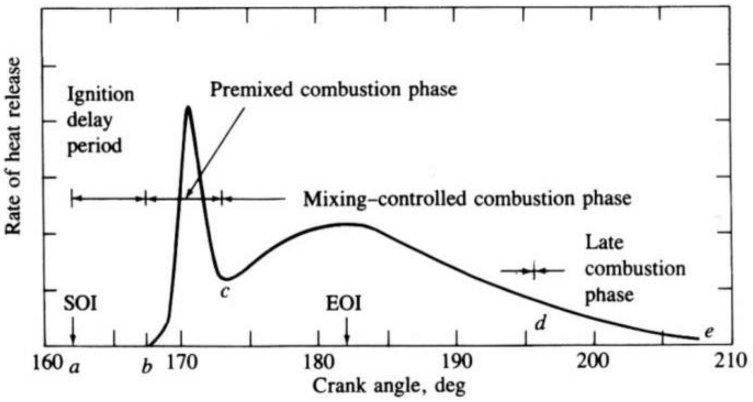

Figure 2.7. Heat release rate diagram for a compression ignition engine [18]

In Figure 2.6, the fuel is injected at the point A, and then mixes with air until B. This period is called the ignition delay. It is important to engine combustion performance and dependent on air temperature, fuel droplet size and fuel-air mixing properties [40]. The rapid combustion happens during B to C, and its length can be enlarged by shorter ignition delay. C to D is the controlled combustion, the major type of combustion, which is slower and mainly determined by the speed of fuel-air mixing [18]. After D, the combustion continues but becomes further slower with the expansion of the cylinder.

### *2.2.2. Pollutant emissions*

During the combustion process, many side reactions occur and thus produce pollutants. In diesel engines, nitrogen oxides ($NO_x$), particulate matter (PM) are the emissions of the highest level, whereas and unburned hydrocarbons (HC) and carbon monoxide (CO) are usually slightly lower.

**$NO_x$ formation**

$NO_x$, mainly the nitric oxide (NO), is produced directly in the combustion. Three mechanisms are developed to describe the NO formation. The thermal mechanism is put forth by Zeldovich [41], which takes place in high oxygen zones of high temperature (no less than 1800 K) due to the high activation energy [42]. The mechanism dominates the NO formation and can be summarised by Equation (2.3) and (2.4).

$$O + N_2 \rightleftharpoons N + NO \qquad (2.3)$$

$$N + O_2 \rightleftharpoons O + NO \qquad (2.4)$$

The extended thermal mechanism for near-stoichiometric fuel-air mixture is then developed by adding another reaction [43]:

$$N + OH \rightleftharpoons \mathrm{N}O + H \qquad (2.5)$$

These reactions can be enhanced by increasing temperature, and the reaction rate constants have been obtained by experiments [44].

The prompt mechanism is prevalent in low-temperature, fuel-rich and short residence time conditions, which results in small amount of NO formation [45]. In the mechanism, hydrocarbon radicals react with nitrogen and forms cyano molecules (CN) and amines ($NH_x$), and finally become NO via intermediate reactions [46]. The main reactions can be shown in the following equations:

$$CH + N_2 \rightleftharpoons \mathrm{HC}N + N \tag{2.6}$$

$$N + O_2 \rightleftharpoons NO + O \tag{2.7}$$

$$HCN + \mathrm{OH} \rightleftharpoons H_2O + CN \tag{2.8}$$

$$CH + O_2 \rightleftharpoons NO + CO \tag{2.9}$$

The $N_2O$-intermediate mechanism is proposed by Melte and Pratt [47], which is for $NO_x$ formation from $N_2$ via nitrous oxide ($N_2O$). This mechanism can contribute as much as 90% of $NO_x$ formation when under elevated pressure, low temperature and oxygen-rich conditions, which are common in gas turbines and CI engines. Therefore, about 30% of the NOx formation in these engines can be attributed to the $N_2O$-intermediate mechanism [41, 48]. The mechanism can be described by the following equations:

$$O + N_2 + \mathrm{M} \rightleftharpoons \mathrm{M} + N_2O \tag{2.10}$$

$$N + N_2O \rightleftharpoons NO + NH \tag{2.11}$$

$$O + N_2O \rightleftharpoons \mathrm{NO} + NO \tag{2.12}$$

**PM formation**

PM, generally called soot or smoke, is usually generated in fuel-rich regions of the flame [19]. As shown in Figure 2.8, PM can be formed through a fast route via addition reactions and condensation of the aromatic rings into a carbonaceous structure, or through slower fragmentation-polymerization reactions. Aromatic compounds thus act as seed molecules for molecular growth and polymerization to form larger polycyclic aromatic hydrocarbons (PAHs) that produce mature soot [49].

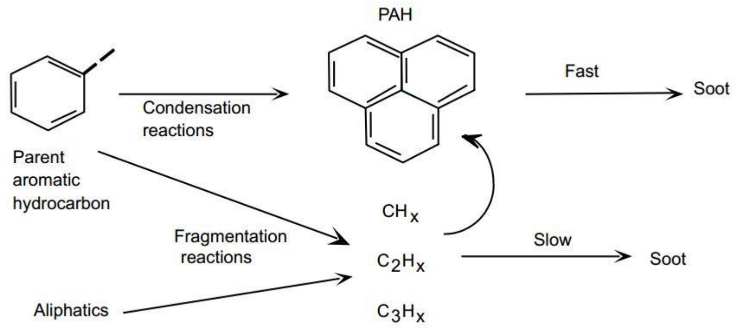

Figure 2.8. Simplified PM formation mechanism [49]

PM can be categorised by three types according to their size. As illustrated in Figure 2.9, the smallest particles are the nuclei mode, which is usually smaller than 50 nm. PMs between 50 nm and 1000 nm are called the accumulation mode, and those larger than 1000 nm is the coarse mode [50]. The solid line and the dotted line in Figure 2.9 are the number concentration and the mass concentration respectively. Obviously, PM of the accumulation mode contributes to the most PM mass emissions, although that of the nuclei mode has the highest number concentration.

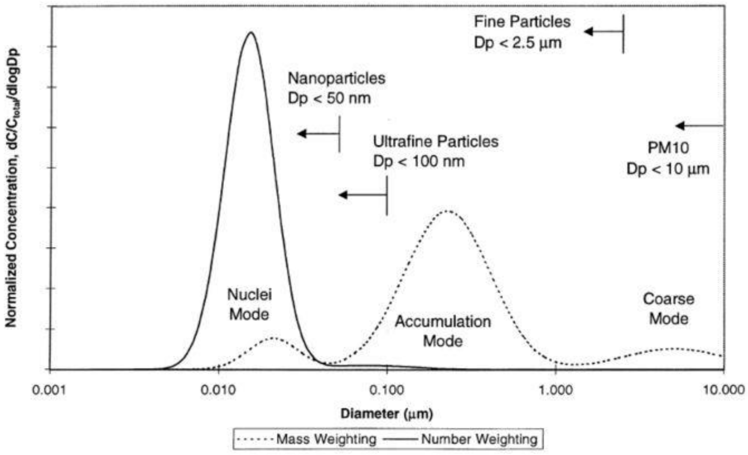

Figure 2.9. PM size distribution from the engine [50]

The nucleation mode PM is volatile state and has a spherical shape. It can grow to the accumulation mode or even to the coarse mode by agglomeration with other particles and absorption of fresh particles, as shown in Figure 2.10 [51]. In fuel rich zones, the oxidation of fuel compositions tends to be hindered at high temperature, and thus pyrolytic reactions occurs instead, where fuel molecules break up and form the PAH. The PAH is usually called the soot precursor because it is easy to form nucleation PM due to its ring structure [52].

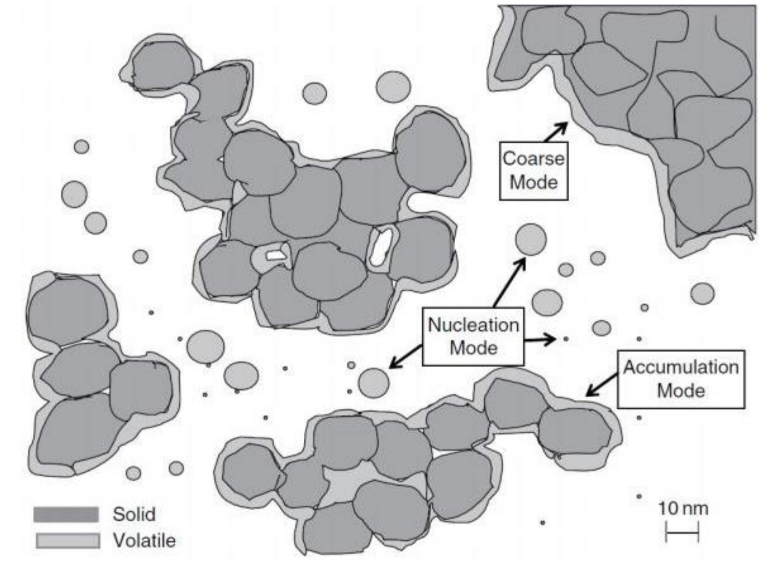

Figure 2.10. Structure of PM of the three modes [51]

As illustrated in Figure 2.10, PM of the three modes consists of the volatile and non-volatile compositions, and can be further divided into five subgroups: carbonaceous, ash, sulphates, organics and nitrates. PM from diesel engines is usually made of 1 ~ 2% ash, 10 ~ 90% organics, 10 ~ 90% carbonaceous, <5% sulphates and <1% nitrates. The fractions of them varies with engine modes and loads [51]. The main sources of these PM compositions are shown in Figure 2.11, which demonstrates that the fuel and lubrication oil contribute most to the PM emissions.

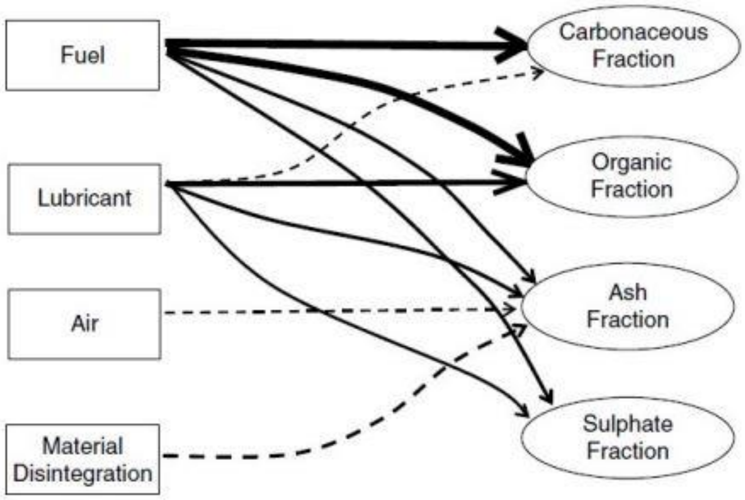

Figure 2.11. Sources of PM compositions [51]

**HC formation**

HC is a mixture of unburnt fuel vapour and the lighter products of the thermal degradation of the fuel, which are associated with incomplete combustion [18, 53]. Three mechanisms have been developed to describe the HC formation during combustion.

The first mechanism is for the areas where the fuel is too lean to ignite just after the start of injection. In these areas, the flame cannot propagate further and thus side reactions such as the fuel pyrolysis and partial oxidation occur. Therefore, some fuel compositions or the products of side reactions escape the cylinder. In this mechanism, the amount of HC is highly dependent on the ignition delay and engine conditions [54]. The second mechanism is for the zones where the fuel-air ratio is over the combustion limit during combustion. At the end of the injection, no time remains for further fuel-air mixing and combustion. Therefore, some fuel exhaust without burning. It usually happens at high load conditions where the injection duration is very long [54]. The third mechanism is flame quenching or fuel impingement on the cylinder wall. As HC emission is sensitive to temperature, the fuel impingement can reduce the wall temperature and thus cause an increase of HC emission [54]. The first and second mechanisms are illustrated in Figure 2.12.

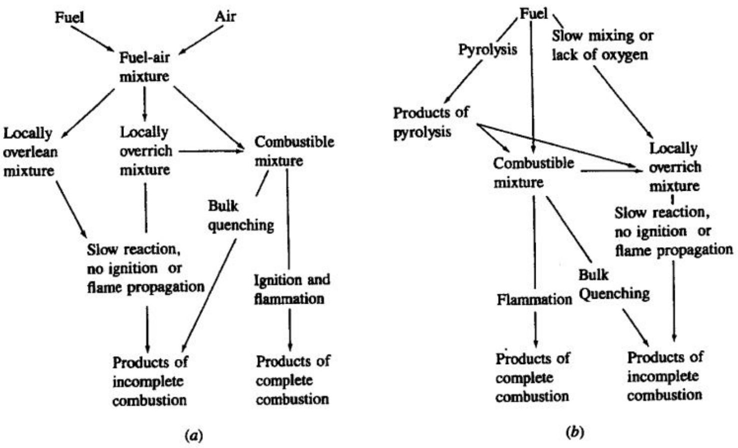

Figure 2.12. The first (a) and second (b) mechanism of HC formation [18]

## CO formation

CO emission is mainly controlled by the fuel-air equivalence ratio [18]. CO can be formed via three routes: incomplete combustion in low oxygen zones, dissociation of $CO_2$ at very high temperature, and intermediate product formation[55]. In the fuel rich mixture, CO concentration increases with increasing equivalence ratio, whilst it does not change with equivalence ratio in the fuel lean mixture. CO emission from diesel engines is usually very low and thus is less important compared with other pollutants [18].

Summary

The combustion behaviour in compression ignition engines is summarised to characterise the features of each combustion period. Moreover, the pollutant emissions from compression ignition engines, including $NO_x$, PM, HC and CO, are analysed by many studies on their characteristics and mechanisms of formation. They are the fundamental knowledge to understand the combustion behaviour and pollutant emissions of compression ignition engines with various fuel pre-treatments.

## 2.3. Renewable fuels for diesel engines

### *2.3.1. Production and properties of renewable fuels*

Due to the unsustainability of fossil fuels and the environmental problems, renewable fuels such as biofuels and synthetic fuels are developed by researchers and fuel producers. The employment of various renewable fuels thus becomes the most popular fuel pre-treatment in different type of engines for more environmentally friendly performance.

For diesel engines, the biodiesel is becoming a widely used renewable fuel because it has renewable sources and does not require retrofitting of diesel engines. In Europe, the biodiesel production has arrived at 8.6 million tonnes by 2011 and the capability of annual biodiesel production is over 23 million tonnes [56].

Biodiesels used to be extracted from rapeseed oil, soybean oil, coconut oil and palm oil, which are called the first generation biofuels [57]. Nowadays, more biodiesels are produced from non-edible sources such as jatropha curcas, croton, waste vegetable oil and lignocellulose [55]. The method of the production of biodiesels is usually the transesterification due to its high conversion efficiency and low cost [58]. The transesterification process is illustrated in Figure 2.12, where the crude oil reacts with alcohols to produce biodiesels, and catalysts are employed to enhance the solubility of alcohol and thus accelerate the reaction [59, 60].

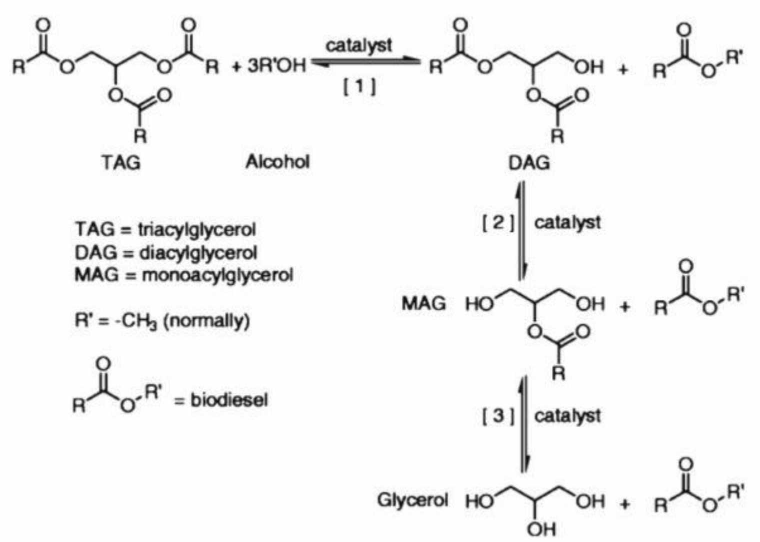

Figure 2.13. Biodiesel production process [60]

As a result of the transesterification process, most biodiesels are fatty acid methyl esters (FAME), such as rapeseed methyl ester (RME), soy methyl ester (SME) and palm oil methyl ester (PME) etc. [8-10]. Therefore, the properties of biodiesels varies and depend on the type of feedstock [61]. In Europe, properties of biodiesels should comply with the European Union Standards for biodiesels (EN14214) for commercial application [62]. For biodiesels, properties including cetane number (CN), density, viscosity, cloud point, flash point, lower heating value (LHV) and impurity content etc. are important to engine performance.

CN is an important factor indicating the ability of auto-ignition for diesel fuels. It is a value based on cetane and 1-methylnapthalene, whose CN are defined as 100 and 0 respectively [63]. Higher CN means shorter ignition delay and lower noise level, and probably also influences pollutant emissions [63-65]. Biodiesels usually have the CN from 48 to 61, and the CN of standard diesel fuel is limited to no less than 51 [66]. The density and viscosity of most biodiesels are higher than standard diesel fuel [67, 68], and the viscosity of biodiesels is strongly dependent on temperature. Usually, high viscosity has negative impact on fuel spray but low viscosity also has poor lubrication. Therefore, it is limited within the range of 1.9 ~ 6.0 $mm^2/s$ [69]. The LHV is the amount of energy per unit of fuel contains, which is important to fuel economy and thermal efficiency [70]. The LHV of biodiesels are lower than standard diesel fuel, main because biodiesels have high oxygen content and thus lower hydrogen and carbon content [63]. As a result, most biodiesels have lower output power compared with standard diesel fuel.

Hydrotreated Vegetable Oil (HVO) is the second generation biodiesel produced by the hydrogenation process. Compared with traditional biodiesels, HVO is a mixture of n- and i-paraffin, which has high cetane number and high energy density, and excludes aromatics, naphthene, sulphur and oxygenates, which enables high oxidation stability and high percentage of blending with standard diesel fuel [11, 12]. As a result, it is beneficial in improving engine output and reducing emissions. Furthermore, unlike biodiesels, HVO has good storage stability and excellent cold starting without suffering from deposition and low engine output, and thus makes it a promising biodiesel [71, 72].

Apart from HVO, the synthetic fuel is another renewable fuel to replace fossil fuels as it can be produced from coals, gas or biomass by Fischer-Tropsch (FT) process [13, 14]. The gas to liquid fuel (GTL) is one type of synthetic fuel from natural gas. The key steps of converting natural gas to GTL is illustrated in Figure 2.14. In the process, oxygen separated from air is blown into a reactor with methane at the beginning. Then, the syngas, mainly hydrogen and carbon monoxide, is formed using either partial oxidation or steam reformation. In the next step, the gas goes through a Fischer-Tropsch reactor to form long-chain hydrocarbon molecules, which in the last step are cracked and fractioned into diesel and other fuels [73].

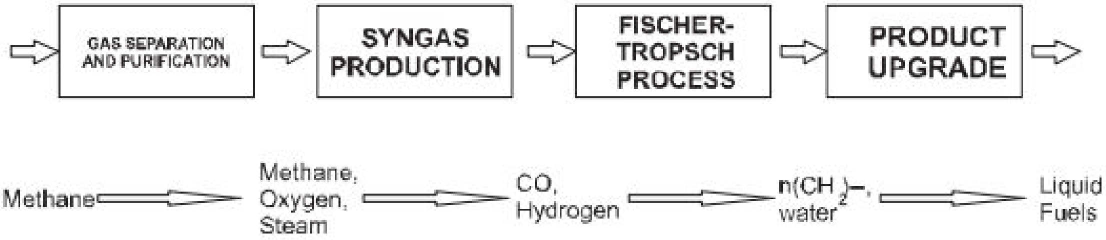

Figure 2.14. Key steps of GTL production [73]

As a result, GTL has high CN, ultralow aromatics content and no sulphur [74]. Moreover, previous study also indicates GTL has smaller density, higher LHV, higher flash point and closed viscosity compared with standard diesel fuel [75, 76]. A comparison among the standard diesel fuel, traditional biodiesels (FAMEs), HVO and GTL is illustrated in Table 2.1.

| Property | Standard diesel fuel | FAMEs | HVO | GTL |
|---|---|---|---|---|
| Density at 15 °C (kg/m$^3$) | 835 ~ 840 | 877 ~ 885 | 780 | 778 |
| Viscosity at 40 °C (mm$^2$/s) | 2.65 ~ 2.82 | 4.18 ~ 4.55 | 3.02 | 2.56 ~ 2.74 |
| LHV (MJ/kg) | 42.9 ~ 43.05 | 37.2 ~ 37.9 | 43.9 | 43.6 |
| Cloud point (°C) | ≈−5 | ≈−5 | −25 ~ −5 | −25 ~ 0 |
| Sulphur content (mg/kg) | <10 | 0 | 0 | 0 |
| CN | >51 | 52 ~ 65 | >75 | 79 |
| Aromatics content (%) | 27.5 | 0 | 0 | 1.4 |
| Oxygen content (%) | 0 | 10.6 | 0 | 0 |
| 100% distillation temperature (°C) | 360 | 370 | 320 | 330 |

Table 2.1. Summary of properties of renewable fuels [55, 75-77]

Table 2.1 demonstrates that HVO and GTL have lower density, higher LHV and CN than standard diesel fuel, and their viscosity are closed. These characteristics enable HVO and GTL to have similar spray quality and release more energy during combustion than the standard diesel fuel. Moreover, due to the absence of sulphur and low aromatics content, HVO and GTL are capable of producing less pollutant emissions. In contrast, FAMEs also have less pollutant emissions than standard diesel fuel. However, their high viscosity has negative influence on spray and the oxygen content will also reduce the engine efficiency at some conditions. Therefore, HVO and GTL are superior renewable fuels for diesel engines in terms of engine efficiency and pollutant emissions.

### *2.3.2. Spray characteristics of renewable fuels*

A series of studies were conducted on the spray characteristics of various renewable fuels. Chen et al. [34] compared the spray properties of biodiesel (FAME) derived from waste cooking oil and its blend with standard diesel and found biodiesel experienced longer penetration and larger size of droplets due to its larger viscosity and surface tension. Nevertheless, this study was done at room temperature and room pressure, which is far from the condition in the diesel engine. Mohan et al. [78] selected the same fuel to study its spray characteristics in a constant volume vessel. Their results demonstrated that the biodiesel had longer spray penetration and smaller cone angle than diesel fuel. Moreover, the spray penetration reduced with increasing ambient pressure, whilst the cone angle shows no change at different injection pressure. Gao et al. [79] studied the spray structure at the near-nozzle region, and found the spray penetration increased almost linearly with increasing injection pressure at the initial breakup stage. However, these researches did not consider the effect of ambient temperature. In contrast, several researchers [80-82] investigated spray characteristics of various fuels (e.g., waste cooking oil, gasoline-ethanol blends and soybean biodiesel etc.) at a different ambient temperature and all reported reduced penetration at high ambient temperature. Nevertheless, the ambient pressures in these studies were all not set to constant when increasing the ambient temperature, so the reduced penetration cannot be certainly attributed to increasing ambient temperature.

The previously reported works were all about FAMEs but not HVO or GTL. Hulkkonen et al. [29] and Sugiyama et al. [83] compared the spray properties of HVO and standard diesel fuel at the same conditions but found no significant difference between them in terms of spray tip penetration and cone angle. In contrast, Thomas et al. [84] investigated the spray characteristics of some biofuels containing HVO at constant ambient temperature and pressure and reported HVO produced the shortest spray tip penetration and the largest overall cone angle. However, the influences of injection pressure, fuel temperature, ambient pressure and ambient temperature were not considered in the work. Kannaiyan et al. [85] investigated the spray characteristics of GTL in a spray chamber at various injection pressure. They noticed that the lower viscosity and surface tension of GTL lead to faster disintegration and dispersion of droplets than conventional jet fuel. Nevertheless, this work was conducted under atmospheric conditions.

### *2.3.3. Engine performance of renewable fuels*

Many research works have been done on the engine performance of renewable fuels. Jeon et al. [86] studied the flame temperature and soot emissions of biodiesel derived from soybean in a single cylinder experimental diesel engine at fixed load and speed. Results showed that soot was formed to a higher concentration in the middle of combustion process, but it was oxidised by the oxygen content and high temperature throughout combustion, and thus emitted at lower level than diesel fuel. However, other pollutants were not mentioned in this work. Özener et al. [87] selected biodiesel from soybean oil and blended it with diesel fuel. Their experiments were done in a single-cylinder direct injection diesel engine at varying speed. Results demonstrated a decrease in torque, CO emissions and HC emissions. Meanwhile, $NO_x$ emissions were found increased. This work considered the impact of various speed but did not take different torque and PM emissions into account. Shen et al. [88] investigated the performance of waste cooking oil biodiesel blends on both light-duty and heavy-duty diesel trucks on road. They found the total fuel consumption when burning biodiesel blends did not clearly decrease, and the CO, HC, $NO_x$ and PM2.5 emissions all decreased with increasing biodiesel content. The results in this research is more closed to actual conditions but the influence of engine speed and load cannot be identified. Nabi et al. [89] did engine experiments at both varying speed and load on waste cooking oil, and demonstrated that the biodiesel had slightly less power, higher brake specific fuel consumption (BSFC), and it produced lower CO, HC and PM (both mass and number) and higher $NO_x$. Lapuerta et al. [90] reviewed many studies on the engine performance of different biodiesels (FAMEs), and concluded that the reduction in output power between biodiesels and diesel fuel can only be seen at full load, and PM emissions can be reduced sharply by biodiesels which slightly increased $NO_x$ emissions and BSFC. However, Kumar et al. [91] found less $NO_x$ emissions can only be produced by long chain and saturated biodiesels and the fuel consumption increased after reviewing previous works.

Compared with various researches on FAME based biodiesels, engine performance of HVO and GTL started to be investigated in recent years. Millo et al. [11] studied the emissions of HVO and some other biofuels in a diesel engine and found reduced CO and HC but comparable $NO_x$ emissions with standard diesel fuel. Sugiyama et al. [83] did similar research on HVO in an inline 4 cylinder diesel engine at fixed speed and varying torque and found soot can also been reduced apart from CO and HC, but $NO_x$ emissions sometimes were higher than standard diesel fuel. Lehto et al. [92] studied HVO in a single-cylinder engine with 30% exhaust gas recirculation (EGR) and demonstrated HVO generated less smoke and can adapt to higher EGR conditions than standard diesel fuel. Singh et al. [93] employed a heavy-duty diesel engine to study the emissions and fuel consumption of HVO. It was reported that the PM, CO, HC and BSFC were all lower than those of diesel fuel. Researchers also reviewed studies on HVO performance in engines or vehicles and summarised that HVO can reduce $NO_x$, PM, HC and CO emissions without any change to the engine and its control [94]. Wu et al. [75] studied the performance of GTL and its blends with diesel fuel in a six cylinder turbocharged direct injection diesel engine at various load-speed conditions and pump timings, and found the peak in-cylinder pressure of GTL is slightly lower than that of diesel fuel although the LHV of GTL is higher. Meanwhile, the CO, HC, PM and $NO_x$ emissions of GTL are reduced simultaneously at different conditions. Abu-Jrai et al. [95] employed GTL in a single cylinder direct injection diesel fuel at 25% and 50% load and varying speed with EGR. They noticed that GTL has higher brake thermal efficiency and lower $NO_x$ and smoke emissions. However, other emissions such as HC and CO were not considered. Hassaneen et al. [96]compared the performance of GTL and rapeseed methyl ester (RME) in a six cylinder diesel engine at varying speed and load, and found GTL has lower BSFC and $NO_x$ emissions than RME, but its CO and HC emissions are higher than RME. Besides, the majority of PM emissions of GTL have larger size than those of RME. Similarly, Ushakov et al. [97] studied the emissions of GTL in a turbocharged heavy duty diesel engine at propulsion and generator modes, and demonstrated reductions in $NO_x$, CO and smoke and slight increase in HC emissions. Furthermore, Hao et al. [98] tested the on-road performance of GTL and proved the bus using GTL has slightly lower fuel economy and greenhouse gas (GHG) emissions than diesel buses.

Summary

Compared with most biodiesels (FAME), HVO and GTL are two renewable fuels which can both improve the engine power and reduce most emissions according to previous researches on their engine performance. In contrast, studies on their spray characteristics are limited and the influence of fuel conditions and ambient conditions on the spray characteristics are not thoroughly analysed.

## 2.4. Nano additives for diesel engines

### *2.4.1. Properties of nano additives*

Nano fluid is a mixture consisting of nano-sized materials dispersed in a base fluid, which is widely used in different fields [99]. Recently, nano materials are employed as additives to enhance the properties of fuels, which becomes an effective fuel pre-treatment to improve engine output and reduce pollutant emissions [100, 101]. Among various nano additives, the metallic or metallic oxide nano materials such as $Al_2O_3$, CuO, ZnO, MnO, $Fe_2O_3$ are the most popular type of nano additives. They are capable of providing higher power output, higher thermal efficiency, lower $NO_x$ and HC emissions, because these metallic oxides release extra oxygen at high temperature to oxidize fuel compositions and pollutants, and thus result in higher combustion rate and less emissions [100-105]. Researchers [106] believe the advantages of nano additive modified fuels are mainly because the nano additives improve the chemical-physical properties such as thermal conductivity, mass diffusivity, viscosity and flash point etc. Among the metallic oxide nano additives, Cerium oxide ($CeO_2$) is a newly developed one involved in some researches. $CeO_2$ nanopowder can take and release the free oxygen without any further decomposition via the reaction below at high temperature [107].

$$4CeO_2 \rightleftharpoons 2Ce_2O_3 + O_2 \tag{2.13}$$

Consequently, $CeO_2$ nanopowder can provide enough oxygen for the fuel at the fuel-rich zones as an oxygen buffer during the combustion process in the cylinder, and thus promote combustion for diesel engines [107]. Moreover, $CeO_2$ nanopowder is capable of oxidizing CO and carbon deposits on the cylinder wall, which results in reduction of CO and HC of diesel engines when blending with fuels. Meanwhile, the $Ce_2O_3$ can deoxidize $NO_x$ at high temperature environments in the engine cylinder. As a result, $CeO_2$ nanopowder acts as a catalyst for diesel fuels to reduce pollutant emissions of diesel engines via the following reactions [108].

$$2CeO_2 + CO \rightarrow Ce_2O_3 + CO_2 \tag{2.14}$$

$$(2x + y)CeO_2 + C_xH_y \rightarrow \left[\frac{2x+y}{2}\right] Ce_2O_3 + \frac{x}{2}CO_2 + \frac{y}{2}H_2O \tag{2.15}$$

$$Ce_2O_3 + 2NO \rightarrow 2CeO_2 + 1/2\, N_2 \tag{2.16}$$

However, the influence of $CeO_2$ nanopowder on PM is rarely found in literature, and the impact of its size on fuel properties and engine performance have not been studied yet.

Carbon nanotubes (CNT) is another nanomaterial widely used in many fields and sometimes blended with other additives in diesel fuel as an additive enhancer. Some researchers claim that CNT can accelerate the combustion rate and efficiency to reduce emissions such as CO and HC for diesel engines when blending with metallic oxide nanopowder [109]. Furthermore, some other researchers believe CNT can not only promote fast combustion reactions, but also improve the fuel-air mixing for more complete combustion [101]. However, CNT in most studies was blend with other nano additives in fuels. Therefore, the performance of CNT alone in diesel engines and its impact on fuel properties are still unclear.

### *2.4.2. Spray of nano additive modified fuels*

The spray characteristics of nano additive modified fuels is rarely mentioned in previous studies. Therefore, it is necessary to do relevant research to understand the spray characteristics of nano additive modified fuels. By this means, the impact of nano additives on fuel physical properties (spray characteristics) would be clear, which helps understand whether it is the physical properties or the chemical mechanism of nano additives that influences the engine performance.

### *2.4.3. Engine performance of nano additive modified fuels*

Many researches have been done on various nano additives to investigate their improvement to diesel engines. Most nano additives were found capable of improving the ignition and combustion behaviour due to their high surface area to volume ratio and more reactive surfaces [101]. Moreover, HC and PM emissions can be reduced but CO and $NO_x$ emissions experienced an increase when using these nano additives [101, 106], because these nano additives have highly oxygenated structure (e.g., metallic oxides), which promotes the oxidization of HC and PM at high temperature.

Compared with most nano additives, Cerium oxide nanopowder has the potential to reduce $NO_x$ emissions and thus draws researchers' attention. Vairamuthu et al. [107] added Cerium oxide nanopowder to the biodiesel-diesel blend and burn them in a diesel engine at constant speed and load. Results indicated that the unburnt hydrocarbon (HC) and $NO_x$ were reduced with improved brake thermal efficiency. According to aforementioned context, $CeO_2$ nanopowder converts to $Ce_2O_3$ ,which can deoxidize $NO_x$ via Equation (2.16). Nevertheless, their work did not study the performance of $CeO_2$ at different speeds and loads. Accordingly, Saraee et al. [108] tested the performance of diesel fuel with Cerium Oxide nano additive of three different concentrations at varying engine speed, and found significant reduction of $NO_x$ and HC but increased CO emissions. However, the impact of load on the performance of $CeO_2$ nano additive was not considered. In contrast, Aghbashlo et al. [110, 111] emulsified biodiesel-diesel-nano $CeO_2$ blends with water for engine test at 1000 rpm speed and varying load. It was found that the emulsions with $CeO_2$ had lower CO, HC and $NO_x$ emissions but increased brake thermal efficiency and normalized exergy destruction. The reduction of HC and CO in these studied is mainly caused by the oxidization by $CeO_2$ via Equation (2.14) and (2.15). However, these researches did not mention particulate matters (PM) emissions with the existence of $CeO_2$ nano additive. Therefore, Gross et al. [112] studied the kinetic and reaction mechanism of $CeO_2$ with emitted PM in a cell. They reported that $CeO_2$ is capable of oxidizing PM and its catalysis would be improved with rising temperature. However, this investigation was done in a cell with constant heating rate, where its condition was far from that in an engine cylinder. Furthermore, the influence of different sizes of nano $CeO_2$ has been rarely studied in previous research works. In addition, most researches on $CeO_2$ nano additive introduced in surfactants or emulsified fuels which disturbed results and thus made it difficult to identify the actual influence of $CeO_2$ on engine performance and emissions.

In terms of the CNT, some researchers [109, 113, 114] attempted to mix it with other additives such as Cerium oxide nanopowder, silver nanoparticles and ethanol in engine experiments. Different levels of improvement of engine performance were reported in these studies. However, most of them employed CNT as an enhancer to accelerate the dispersion of other additives instead of a single component additive directly contributing to the combustion of fuels. As a result, the effect of CNT on engine performance cannot be recognised. Accordingly, Ghanbari et al. [115] used multi wall CNT as a single component additive in diesel-biodiesel blended fuels and found the blended fuel with CNT has lower brake specific fuel consumption and CO emissions but increased HC emissions than neat diesel fuel. However, this research compared the performance of diesel-biodiesel-CNT blends with neat diesel fuel, so the influence of CNT alone was still unclear. Moreover, the impact of varying engine load was not taken into account in this work.

Summary

Spray characteristics of nano additive modified fuels have not been studied yet. Most nano additives cannot reduce the $NO_x$ and CO emissions, whilst Cerium oxide nanopowder can reduce $NO_x$, PM, HC and CO simultaneously because its catalytic effect can oxidize PM, HC and CO, and deoxidize $NO_x$ during combustion. However, limited research studies have investigated the influence of the size of $CeO_2$ nanopowder on the engine performance under various engine operational conditions. Moreover, CNT is also an extraordinary nanomaterial which was rarely researched as a single component nano additive. Therefore, the $CeO_2$ nanopowder with different sizes and CNT should be investigated as the diesel additives under various engine speed and load conditions.

## 2.5. Supercritical (SC) fuel combustion

### *2.5.1. Definition of SC fuels*

Supercritical (SC) state is the state that the temperature and pressure of a fluid exceed its critical point, where the fluid cannot be compressed to liquid state no matter how high the pressure is. Figure 2.15 is the P-T phase diagram of a single component fluid and illustrates the location of SC region in the diagram. The black curves are the boundaries among solid, liquid, vapour and SC, and the colourful lines present three ways of phase transition from a liquid state (S1) to a SC state (S2).

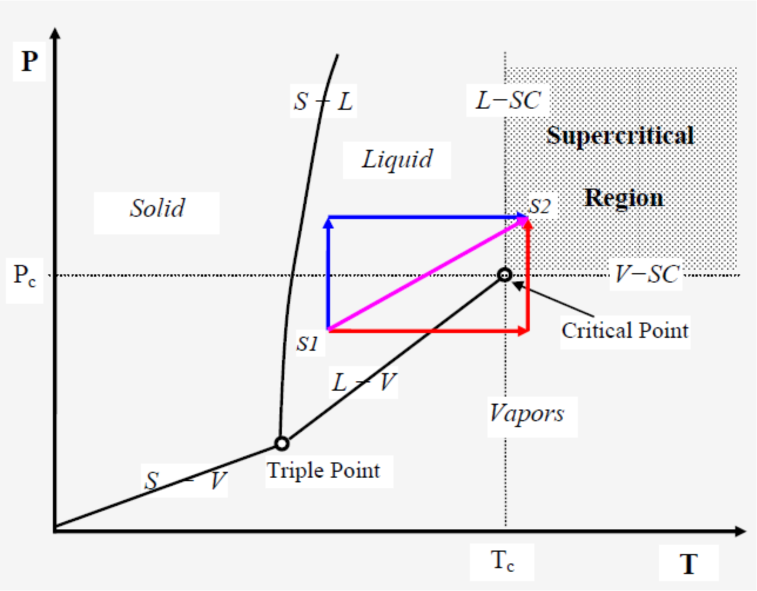

Figure 2.15. P-T phase diagram for a single fluid [116]

The fluid at the SC state is known as a SC fluid, which has both the liquid and vapour characteristics. The SC fluid has high density like liquid, and its ultra-low surface tension results in no phase boundaries with other fluid [117]. Together with the high diffusion coefficient, fast heat and mass transport, the SC fluid is also similar to gas phase. As shown in Figure 2.16, during the transition of the hexadecane-$CO_2$ mixture from liquid to SC state, the phase boundary between $CO_2$ and hexadecane disappears [116]. Moreover, the SC fluid has no enthalpy of vaporization. These characteristics enable the SC fluid to sufficiently mix or faster interact with other fluids [117].

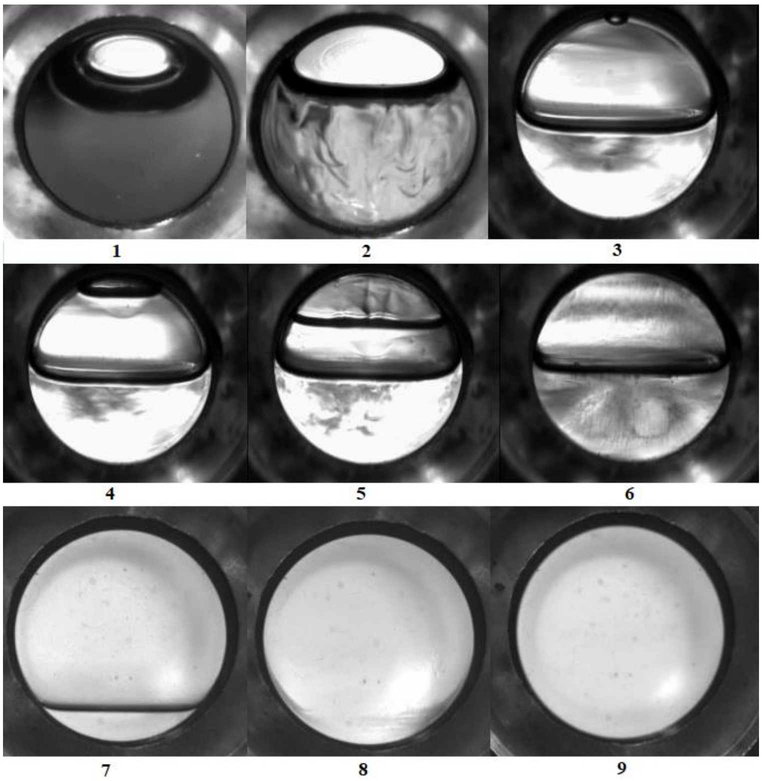

Figure 2.16. Phase transition of hexadecane-$CO_2$ mixture from liquid to SC state [116, 118]

Due to the advantages above, the SC fluid is usually employed in biodiesel production [116, 119-132] and rocket engine combustion [133], but the application of SC fuel in compression ignition engines is limited. In terms of SC fuel for compression ignition engines, it can mix with air more sufficiently and does not cost time or absorb heat to break up and evaporate. Therefore, SC fuel combustion is another fuel pre-treatment with the potential of achieving clean and high efficiency engines [116, 134, 135].

### *2.5.2. Properties of SC fuels*

Properties of SC fluid are still not well understood and traditional theories cannot describe the behaviour of SC fluid [136]. Therefore, it is important to study the properties of SC fuels before application in diesel engine combustion. The equation of state (EOS) is one of the most important tools of predicting SC fluid behaviour. To SC fuels, the well-known ideal EOS is invalidated due to its obviously different properties from the ideal gas. Accordingly, some researchers demonstrated that the Soave-Redlich-Kwong (SRK) EOS is capable of predicting the behaviour of SC fluids [118, 137, 138]. Meanwhile, some studies proved the Peng-Robinson (PR) EOS can also describe the SC fuel injection and combustion [139-141]. The SRK and PR EOS are shown in Equation (2.13) and (2.14).

$$p = \frac{RT}{V-b} - \frac{a}{V^2+bV} \tag{2.13}$$

$$p = \frac{RT}{V-b} - \frac{a}{V^2+2bV-b^2} \quad (2.14)$$

Where $p$, $T$, $V$ and $R$ are the pressure (Pa), temperature (K), specific molar volume ($m^3$/kmol) and the universal gas constant (J·/(K·mol)), whilst $a$ and $b$ are constants. The details of the two equations will be explained in Chapter 6.

Due to complex composition of diesel, many thermal properties of the diesel fuel around the SC state are difficult to obtain [142-146]. Therefore, researchers always employed surrogates to simplify the modelling work on specific fuel properties [147]. The critical points of some popular surrogates are listed in Table 2.2.

| Fuel | $T_c$ (K) | $P_c$ (bar) |
|---|---|---|
| n-pentane | 469.8 | 33.7 |
| n-hexane | 507.4 | 30.3 |
| n-heptane | 540.3 | 27.4 |
| n-octane | 569.2 | 25.1 |
| n-decane | 617.6 | 21.1 |
| n-dodecane | 659.2 | 18.1 |
| n-hexadecane | 722.4 | 14.0 |

Table 2.2. Critical points of some fuels [148, 149]

Kumar et al. [150] selected the n-hexadecane as the diesel surrogate to predict the specific heat and thermal conductivity over the critical pressure (about 1.576 MPa) and critical temperature (about 722 K). As illustrated in Figure 2.17, pressure and temperature have no impact on the specific heat of the diesel surrogate at high temperature and high pressure, whilst the thermal conductivity keeps increasing with growing temperature and pressure.

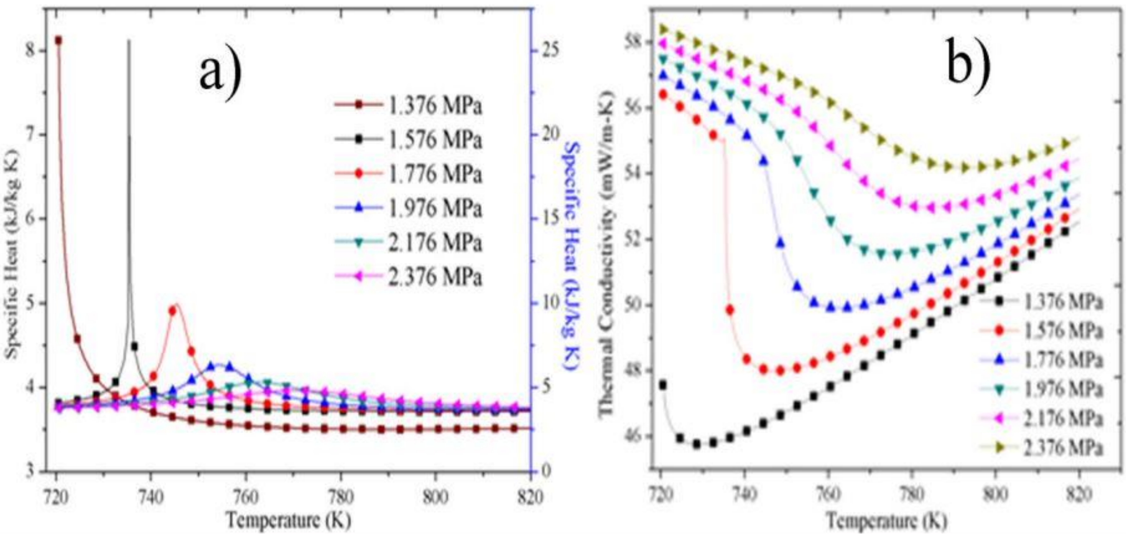

Figure 2.17. Specific heat and thermal conductivity of n-hexadecane at various pressure and temperature [150]

Furthermore, Lin et al. [141] employed various multi components diesel fuel surrogates to estimate the density, heat capacity, viscosity and thermal conductivity of real diesel fuel. The results of highest accuracy are shown in Figure 2.18. It demonstrates that density of the diesel fuel surrogate decreases significantly with increasing temperature, whilst pressure can only produce significant impact on density at SC state (> 700 K and > 20 bar), which means the SC diesel fuel surrogate becomes a gas-like compressible fluid. The heat capacity increases with increasing temperature and has no comparable change with pressure at SC state. In contrast, the viscosity of diesel fuel surrogate is not sensitive to either pressure or temperature at SC state. The thermal conductivity at SC state stays stable with increasing temperature but is increased by growing pressure.

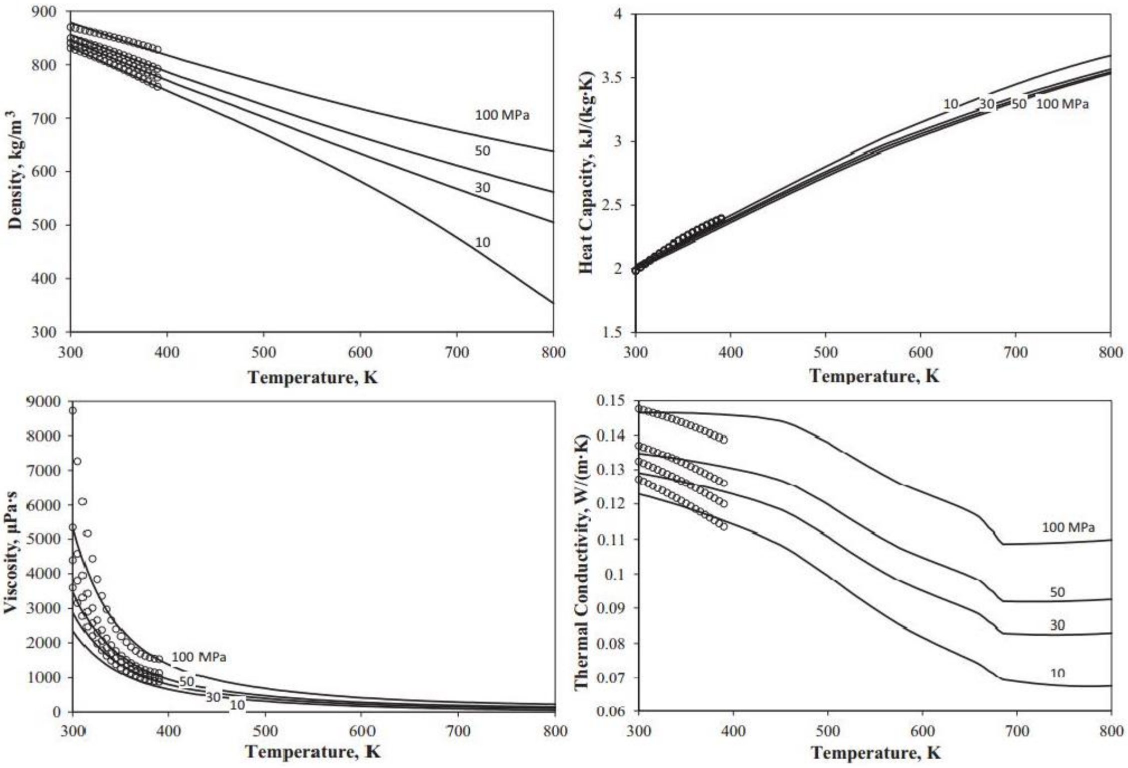

Figure 2.18. Estimated key properties of the diesel fuel from liquid to SC state [141]

### *2.5.3. SC fuel combustion for diesel engines*

The first challenge of employing the SC fuel combustion in diesel engines is that diesel fuels tend to coke before reaching the SC state during heating process [116, 151-153]. G. Anitescu, S. Rahmani and G. Karakas [151, 154, 155] proved that coking can be prohibited by adding anti-coking agents such as carbon dioxide, water, ethanol and gasoline, which are also called diluents in these researches. Moreover, G. Anitescu et al. [154] investigated the volatility and compositions of gasoline-diesel blends during heating process, the phase transition from liquid-vapour to SC state, as well as the thermal stability in the heating-cooling cycles. They emphasized that the decomposition of heavier compounds was prevented by the solvating effect of the lighter hydrocarbons from the gasoline.

The second challenge is that heating fuels to the SC state by exhaust gas is demanding to most diesel engines [156]. Fortunately, the critical temperature of diesel fuel (around 450 °C) was found to be significantly lowered down to about 390 °C by the addition of gasoline [157]. However, the method of mixing diesel and gasoline is impacted by the issue of miscibility in liquid state [158-163] and combustion instability [164]. As a result, the volume fraction of gasoline in the diesel-gasoline blends has to be restricted to a narrow range of 10−20%, even with some additives [154].

As most researches on the SC fuel combustion were focused on the properties of fuels at the SC state and during the transition to the SC state, the actual performance of SC fuel combustion has not been studied in diesel engines so far. In the past, only a combustion experiment was done in a flow reactor, where the SC diesel fuel with some $CO_2$ was flowing and mixing with high pressure and high temperature air to keep the diesel fuel burning at the SC state. As a result, the organic products in the SC fuel combustion were found significantly lower than conventional combustion, and $NO_x$ was not found in the products of SC fuel combustion [165]. Nevertheless, the condition in the flow reactor was still far from that in the cylinder of diesel engine.

Summary

The SC fuel has unique characteristics compared with liquid fuel, which enable it to mix and burn with air faster and more sufficiently in the SC environment. However, most studies of SC fuel combustion are investigated on its properties at the SC state and during the transition, where the SC fuel combustion in the compression ignition engine is rarely found. Consequently, it is worth researching the performance of SC fuel combustion in the cylinder of the compression ignition engine and evaluating its influence on the engine output and emissions.

## 2.6. Computational fluid dynamics (CFD) method

Computational fluid dynamics (CFD) is a branch of fluid mechanics that uses numerical analysis and data structures to solve and analyse problems associated with fluid flows [166]. CFD simulations provide insight into the details of how products and processes work, and allow new products to be evaluated in the computer, even before prototypes have been built [167]. The procedure of CFD analysis usually consists of the geometric model construction, meshes or cells generation, model configurations, set solver, run calculation and post-processing, which is illustrated in Figure 2.19.

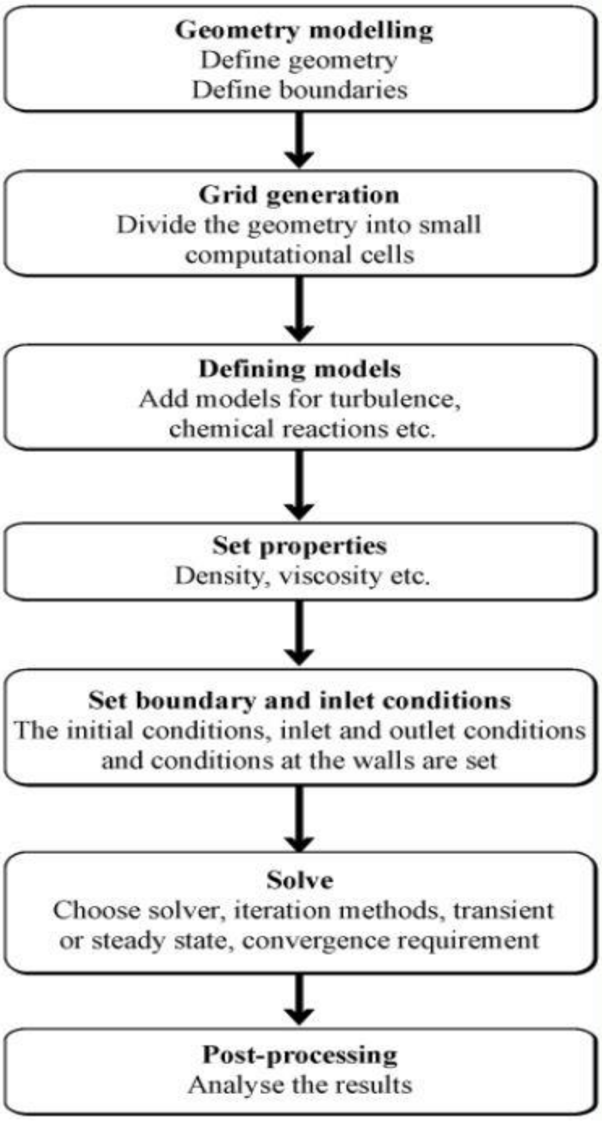

Figure 2.19. Steps of CFD simulations [167]

CFD codes, such as the ANSYS Fluent, KIVA and AVL FIRE, are popular in the analysis on turbulence, heat transfer and reactions of single-phase flow, discrete phase materials and multi-phase flow etc. [41, 168]. Moreover, they allows users to configure various sub models such as turbulent viscosity, droplets breakup, combustion models and products formation etc., and provides interfaces of user defined functions to improve its performance in some specific cases. Consequently, many researchers employed CFD codes to study spray and combustion of various fuels, as the details of spray (e.g., spray shape and droplet parameters) and combustion (e.g., pressure, temperature, distribution of reactants and products) can be directly observed.

To the studies of liquid fuel spray, the Wave model [169] and KHRT model [170] are the two widely used breakup models in various CFD codes, and they showed a good agreement with experimental data when predicting spray characteristics of various fuels [171-176]. In terms of engine combustion, the combustion model together with the breakup model dominates the performance of the CFD simulation [169], and the mechanism of reactions also matters if combustion products are taken into account [177]. Zhou et al. [178] employed the KIVA-3V to study the spray combustion of diesel fuel surrogates in a diesel engine-like environment. Their CFD model was found capable of accurately predicting the ignition delay and flame lift-off length at different ambient conditions. Ismail et al. [169] selected the ANSYS Fluent to simulate the spray combustion in a diesel engine cylinder, and demonstrated that the employment of RNG k-ε turbulence model, Wave breakup model, non-premixed combustion model, thermal and prompt $NO_x$ mechanisms and one-step soot mechanism was capable of predicting spray droplets and combustion behaviour (pressure and HRR) as well as $NO_x$ and soot emissions with overall high precision when appropriate values were set to important parameters in these sub models. Maghbouli et al. [177] employed KIVA-4 coupled with CHEMIKIN II mechanism and FORTRAN programming to simulate the whole cycle of a direct injection turbo-charged diesel engine at full and mid loads. Results indicated that the predicted in-cylinder pressure, HRR and emissions (CO, $CO_2$ and HC) agreed with experimental data well. A typical configuration of the CFD model for spray combustion is illustrated in Figure 2.20.

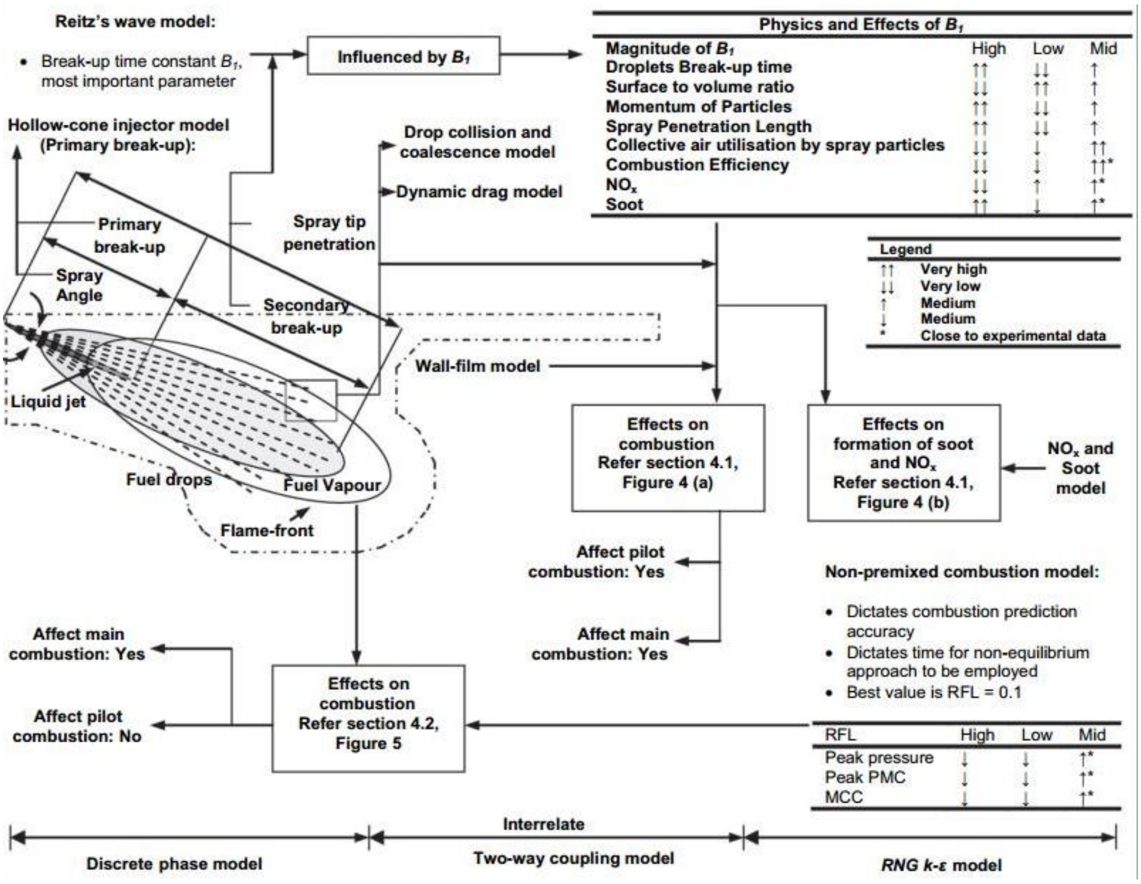

Figure 2.20. Configurations of sub models for the diesel engine combustion [169]

### Summary

The CFD method has been proved an efficient and accurate approach to predict fuel spray and combustion in compression ignition engines. In this project, the breakup models in the CFD code ANSYS Fluent would help build the spray model to investigate spray characteristics at more various conditions than experiments. Moreover, the exploration of the SC fuel combustion in compression ignition engines can be conducted by the CFD method of non-premixed combustion model coupled with $NO_x$ and soot formation mechanisms.

## 2.7. Design of experiments (DoE)

DoE is an mathematical method based on statistics to design variables of experiments for a minimal amount of experiments and correlate these variables with experimental results according to a statistical certainty [179]. The primary goals of a design experiment are to determine the variables and their magnitude which influence the response, the levels for these variables and how to manipulate these variables to control the response.

Most designs of experiments can be divided into two steps: screening and optimization. The screening design is usually used to prepare operating conditions of experiments, especially for those with many factors. DoE approach has various types for different objectives, among which the mixture design and response surface are the most widely used ones. Normally, mixture design is adaptive to the study on the effect between several factors whose sum is one and their responses, whilst the response surface method is for the independent variables and their responses. As DoE is capable of identifying several significant factors from a large set for further optimization with a minimum number of experiments, it is superior to the traditional one-factor-at-a-time approach due to its high efficiency which can highly reduce the costs of experiments and easily indicate the significance of each factor to results [180]. Therefore, the significance of DoE is increasing and it has been induced to the field of engineering such as fuel cell and fuel production [181-184].

Recently, some researchers have introduced the DoE method to the research work on fuel spray and engine emissions as a powerful tool. Chen et al. [185] formulated nine groups of fuels by four representative fuel substances with different mass fractions, which was done via the Mixture Design Method (MDM) of DoE and thus significantly reduced the times of experiments. Moreover, the measured number concentration of PM is quantitively correlated with the mass fraction of each component of the fuels by DoE. Finally, the best percentages of fuel substances in regard of PM emissions was obtained according to the correlation. However, the MDM is particularly for the design of compositions of mixtures but cannot be used in other fields involving independent variables.

| Fuels | N-octane (A) | Isooctane (B) | Xylene (C) | Ethanol (D) |
|---|---|---|---|---|

| | | | | |
|---|---|---|---|---|
| 1 | 0.05 | 0.55 | 0.25 | 0.15 |
| 2 | 0.10 | 0.40 | 0.35 | 0.15 |
| 3 | 0.10 | 0.45 | 0.35 | 0.10 |
| 4 | 0.10 | 0.50 | 0.25 | 0.15 |
| 5 | 0.10 | 0.55 | 0.25 | 0.10 |
| 6 | 0.05 | 0.50 | 0.35 | 0.10 |
| 7 | 0.075 | 0.50 | 0.30 | 0.125 |
| 8 | 0.05 | 0.60 | 0.25 | 0.10 |
| 9 | 0.05 | 0.45 | 0.35 | 0.15 |

Table 2.3. Designed mixture fractions by DoE [185]

Unlike mixture design method in DoE, response surface method (RSM) is capable of controlling each variable independently. Longfei Chen et al. [186] employed the RSM of DoE to investigate the droplet size distribution of kerosene-ethanol blends spray. The Sauter Mean Diameter (SMD) at different fuel pressure and inlet air flow rate were measured by a Malvern particle size analyser. With DoE, an equation of SMD was constructed based on the empirical equation in Lefebvre's book [19] to correlate it with experimental variables such as viscosity and surface tension of fuels, fuel pressure and inlet air pressure. Moreover, the significance of these parameters to SMD can be obtained. This research provided useful experience of using the RSM of DoE method in the investigation of spray characteristics.

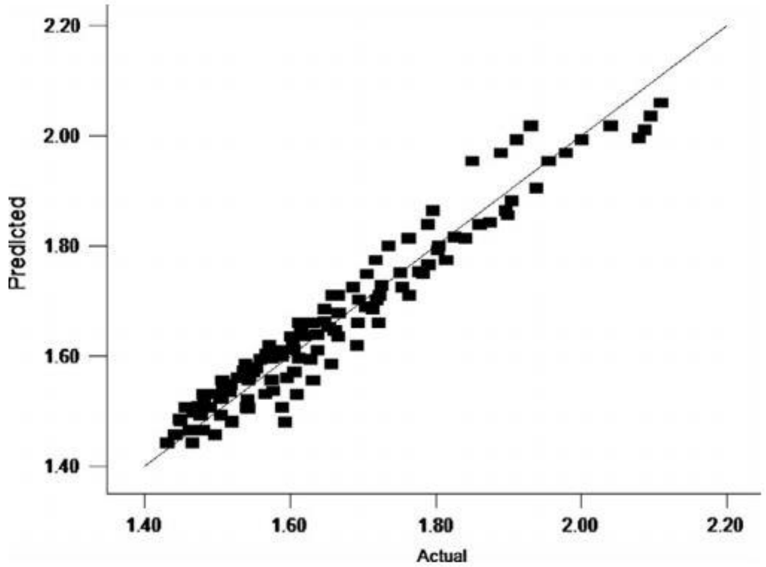

Figure 2.21. Prediction of the DoE equation on the SMD [186]

Apart from the application in experiments, the DoE method is also validated to simulation work. A study [187] on spray models introduced DoE to calibrate the Reitz and Diwakar model (R&D)

model and KHRT model for diesel fuel spray and compared them with the experimental data in a CVV. In order to validate the two models, DoE method were applied to confirm three different values of constants corresponding to flow conditions in respectively with only a few runs. Moreover, the DoE analysis found the significance of these constants in the two models to the SMD and spray tip penetration.

Summary

DoE is an experimental method including various approaches for designing experiments and analysing results based on mathematical statistics. It can not only effectively reduce the number of experiments but also correlate experimental variables to the results with the analysis on the significance of each independent variable. Therefore, DoE would be employed in this project to design conditions of spray experiments and spray simulation, and analyse the influence of fuel condition and ambient conditions on spray characteristics.

## 2.8. Summary of Chapter 2

A literature review is done in this chapter to introduce the knowledge of the liquid fuel spray and the in-cylinder behaviour and pollutant emissions of compression ignition engines. Meanwhile, previous studies on renewable fuels, nano additives and SC fuel combustion as fuel pre-treatments are analysed from the perspective of spray and engine performance. The main results can be summarised as follows:

- The spray tip penetration and the cone angle are the most representative macroscopic spray characteristics, which can be measured by a CVV system with optical observation instruments to indicate the spray quality.
- The in-cylinder pressure and HRR are usually measured to indicate the combustion performance of fuels in compression ignition engines. $NO_x$, PM, HC and CO are the most important pollutant emissions from compression ignition engines, which are determined by fuel compositions and engine conditions.
- HVO and GTL are two renewable fuels which can both improve the engine power and reduce most pollutant emissions, compared with traditional biodiesels (FAME). However, studies on their spray characteristics are limited and the influence of fuel conditions and ambient conditions on the spray characteristics are not thoroughly analysed.
- Most nano additives cannot reduce the $NO_x$ and CO emissions, whilst Cerium oxide nanopowder can reduce $NO_x$, PM, HC and CO simultaneously. However, research studies never investigated the influence of the size of $CeO_2$ nanopowder on the engine performance under various engine operational conditions. Moreover, CNT is also an extraordinary nanomaterial which was rarely researched as a single component nano additive.

Furthermore, spray characteristics of nano additive modified fuels have not been studied yet.

- The SC fuel has unique properties such as liquid-like density and gas-like viscosity and diffusivity etc., which enable it to mix and burn with air faster and more sufficiently in the SC environment. As a result, the engine output power would be improved and most pollutant emissions can be reduced by employing SC fuel combustion. However, most studies of SC fuel are about its behaviour at the SC state and during the transition, and the SC fuel combustion in the compression ignition engine is rarely investigated.
- The CFD method is demonstrated an efficient and accurate method to predict fuel spray and combustion in compression ignition engines. And the DoE can not only reduce the number of experiments but also correlate experimental variables to the results with the analysis on the significance of each independent variable. The two methods will be helpful for the investigation of spray characteristics and SC fuel combustion.

According to literature review, the spray characteristics of HVO and GTL were not investigated at varying fuel condition and ambient condition, and the influence of HVO on $NO_x$ emissions was disputable among previous studies. For nano additive modified fuels, their spray characteristics were not mentioned in literature, and previous researches on $CeO_2$ nanopowder engine performance did not consider the impact of its size, whilst CNT was rarely used as fuel additive before. Furthermore, SC fuel combustion was not investigated in an engine cylinder-like environment yet.

Therefore, the major novelty of this project is to investigate the SC fuel combustion in the CI engine cylinder. Another novelty is to investigate the influence of $CeO_2$ nanopowder size on CI engine and the performance of CNT as a fuel additive. It is also innovative to quantitively study the spray characteristics during both injection and post-injection periods of HVO and GTL at varying fuel condition and ambient condition, and confirm the influence of HVO on $NO_x$ emissions.

# Chapter 3 . Macroscopic characteristics of fuel spray

This chapter is to conduct spray experiments on the standard diesel fuel (DF), renewable fuels - Gas to Liquid fuel (GTL) and Hydrotreated Vegetable Oil (HVO), and nano additive modified fuels, where their macroscopic characteristics of spray are investigated. The common rail pressure (fuel injection pressure), ambient pressure and ambient temperature are experimental variables and their influences on the spray tip penetration and the cone angle are analysed. The carbon nanotubes (CNT) and Cerium Oxide ($CeO_2$) nanopowder of 25 nm and 50 nm are employed as the nano additives to modify the DF and the renewable fuel (GTL). The chapter helps understand whether the renewable fuels and nano additives will influence fuel physical properties e.g., spray characteristics.

## 3.1. Fuel formulation

The renewable fuels in this experiment are the HVO and GTL. The additives to modified fuels are the multi-wall carbon nanotube with 40 ~ 60 nm diameter size and 2μm length (CNT), Cerium Oxide ($CeO_2$) nanopowder with the maximum size of 25nm (Ce25) and 50nm (Ce50) respectively. The parameters of the three types of nano additives are listed in Table 3.1. The CNT is provided by the Shenzhen Nanotech Port LTD, and the Ce25 and Ce50 are bought on the Sigma-Aldrich.com.

| Type | Bulk density (g/cm$^3$) | Size (nm) | Specific surface area (m$^2$/g) |
|---|---|---|---|
| CNT | 0.22 | 40 ~ 60 (diameter)<br>2000 (length) | Min 110 |
| Ce25 | 0.53 | Max 25 | 30 ~ 50 |
| Ce50 | 0.53 | Max 50 | 30 ~ 50 |

Table 3.1. Key parameters of nano additives*

*Provided by the sellers

Figure 3.1. CNT and Cerium Oxide nanopowder of Max 25 nm and 50 nm

The CNT, Ce25 and Ce50 are blended with standard diesel fuel (DF) and GTL respectively with 40 ppm concentration and then vibrated by a Fisherbrand 15060 ultrasonic vibrator for two hours to obtain stable and homogeneous mixtures (suspension). Unlike many studies, no surfactant is used for the fuel blending, because this project intends to directly compare the difference of engine performance between nano additive modified fuels and pure fuels, where the existence of surfactant would influence the result of the comparison. After 24 hours' standing, the mixtures are moved to the fuel tank of the CVV system as the modified fuels. The mixtures can stay stable with no deposition for at least one week. After one week, some nano additives will deposit at the bottom of fuel bottle. The standard diesel fuel, provided by the Coryton Advanced Fuels Ltd, is used as a reference. These nano additive modified fuels are named as DF-Ce25, DF-Ce50 and DF-CNT respectively. The main physical properties are listed in Table 3.2.

Figure 3.2. Fisherbrand ultrasonic vibrator

| Fuel | Density at 15 °C (kg/m$^3$) | Viscosity at 40 °C (mPa·s) |
|---|---|---|
| DF | 840.4 | 2.82 |
| DF-Ce50 | 840.4 | 2.82 |
| DF-Ce25 | 840.4 | 2.81 |
| DF-CNT | 840.4 | 2.77 |
| GTL | 780 | 2.72 |
| GTL-Ce50 | 780 | 2.71 |
| GTL-Ce25 | 780 | 2.71 |
| GTL-CNT | 780 | 2.65 |
| HVO | 780.1 | 3.02 |

Table 3.2. Physical properties of nano additive modified standard diesel fuel*

*The density of DF, HVO and GTL are provided by Coryton and Shell respectively, and the viscosity of all test fuels are measured by an NDJ-9S.

Considering different sizes of Cerium Oxide nanopowder have no comparable impact on physical properties of fuels, only the fuels with Ce25 (DF-Ce25 and GTL-Ce25) are selected to conduct the spray experiments. Some samples of these test fuels are shown in Figure 3.3.

Figure 3.3. Samples of test fuels for the spray experiments

## 3.2. Constant volume vessel (CVV) system

### *3.2.1. The CVV*

As shown in Figure 3.4, the experimental rig contains a common rail fuel delivery system, an optical diagnostic device, a cooling system and a constant volume vessel (CVV). The fuel is delivered by a SPRAGUE PRODUCTS PowerStar P4 high pressure pump to a common rail, which enables as high as 1800 bar fuel pressure. Then, it reaches a single-hole injector, where an amount of fuel is injected and the other goes back to the fuel tank via the bypass pipe. A high-speed PHANTOM V710 CCD camera is employed to observe the spray during experiments with the background light from a 100W Xenon lamp. The cooling system is used to keep important parts of the CVV from overheating, whilst the computers control the heater, thermostat, injector and camera and record experimental data.

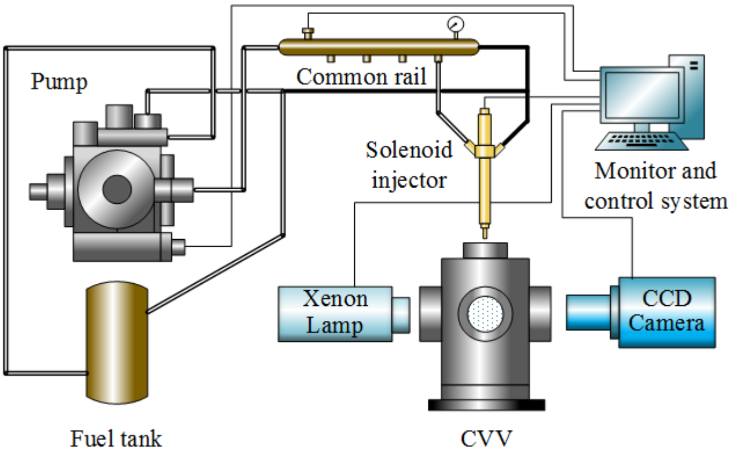

Figure 3.4. Schematic experimental system

The CVV is fabricated for fuel atomization and combustion by the company REACTORS & AUTOCLAVES LTD. It is designed to be resistant to corrosion and oxidation and withstand internal air pressure and temperature at up to 100 bar and 1000 K respectively. A 4.5 kW ceramic band heater is around the wall of the vessel and heats the internal air temperature to about 700K. A three-blade impellor is installed at the bottom for agitation inside and driven by a Micro Mag Drive motor outside. A high-pressure nitrogen bottle provides up to 70 bar internal air pressure for the CVV. Four fused silica glass windows with 90 mm viewing size and 70 mm thickness are equally located on the wall for optical diagnostics. The windows and the seal are cooled by the cooling system to stay within 150 ℃ and 260 ℃ respectively. The internal pressure of the CVV is monitored by a Grems 3100b pressure transducer, and the internal temperature as well as the temperature of the windows and the heater are measured by 1mm K-type thermocouples. The accuracy of the pressure transducer and thermocouples are 1.5% and 0.75% respectively. The main parameters of the CVV are shown in Table 3.3.

| | |
|---|---|
| Total internal volume | 5.65 litres (Ø200mm bore x 400mm) |
| Maximum working pressure | 100 bar |
| Maximum working temperature | 700 K |
| Heater | 4.5KW, Insulated, clamp on, ceramic band heater fitted with stainless steel cladding |
| Closure type | Flanged and bolted or to suit |
| Mounting style | Fixed vessel – removable cover |
| Materials | Inconel 625 gr 2 (vessel and cover)<br>SA 479-316 Stainless steel (all other pressurised parts) |

Table 3.3. List of key parameters of the CVV

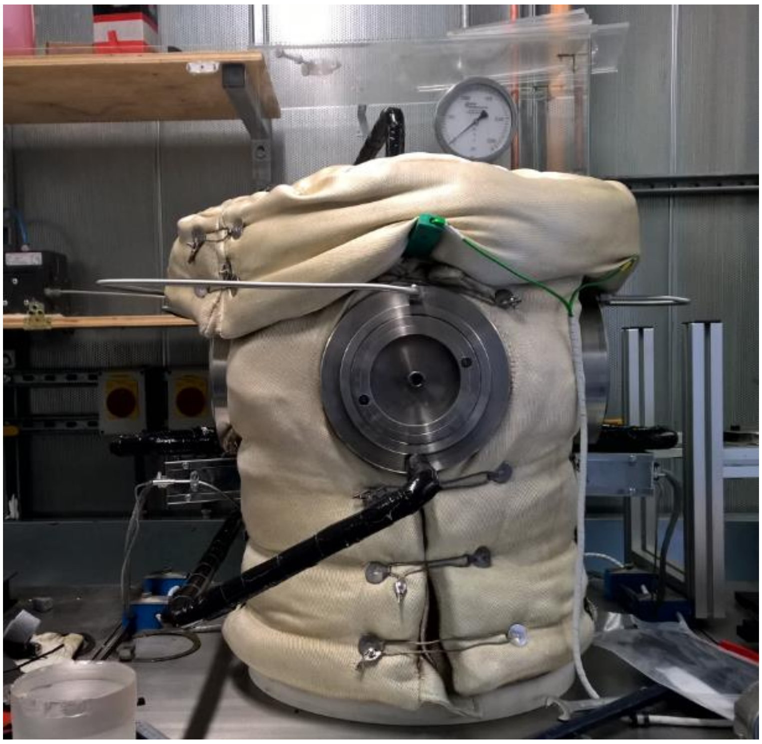

Figure 3.5. The constant volume vessel (CVV)

### ***3.2.2. Cooling system***

The cooling system is a serial system connecting the four windows, the seal and the motor and finally with a LAUDA Ultracool UC4 process circulation chiller, as shown in Figure 3.6. The chiller offers reliable temperature control and ensures secure processing. Meanwhile, it is already equipped with an antifreeze protection thermostat to prevent freezing of the heat exchanger. During experiments, the chiller provides water of high flow rate driven by the internal pump at setpoint temperature (15℃). The water flows through jackets around the windows, the seal and the motor to absorb heat and then return to the water tank in the chiller. The main technical features of the LAUDA Ultracool UC4 process circulation chiller are listed in Table 3.4.

Figure 3.6. LAUDA Ultracool UC4 thermostat

| | |
|---|---|
| Cooling capacity (kW) | 4.9 |
| Coolant | Water |
| Water pressure (bar) | 4.2 |
| Tank Volume (L) | 20 |
| Pump pressure (bar) | Max 2.8 |
| Pump flow (L/min) | Max 13.8 |
| Power (kW) | 1.81 |
| Working temperature (℃) | -5 ~ 25 |
| Ambient temperature (℃) | -15 ~ 50 |
| Overall Dimensions (mm) | 600x 600 x 700 |

Table 3.4. Main technical features of the LAUDA Ultracool UC4 process circulation chiller

### *3.2.3. Optical diagnostic devices*

The spray in the vessel is observed through a window by a high-speed PHANTOM V710 CCD camera with a Nikon AF Zoom-Nikkor 24-85 mm f/2.8-4D lens, which has a maximum resolution of 1280 × 800 pixels and maximum sample rate of 75,000 fps. Due to the high frame rate of the camera, the exposure time is quite short (several microseconds) and the view of the camera is too dark to observe anything. Accordingly, a 100W Xenon lamp is installed on the opposite side to provide homogeneous background light via a diffuser film for observation during spray process. The camera is triggered by a TTL signal to record images at the capture mode. The camera and lens are controlled by the software from PHANTOM, where the mode, resolution, exposure time, sample rate et al. can be configured and the recorded images can be saved in the hard drive, as shown in Figure 3.7.

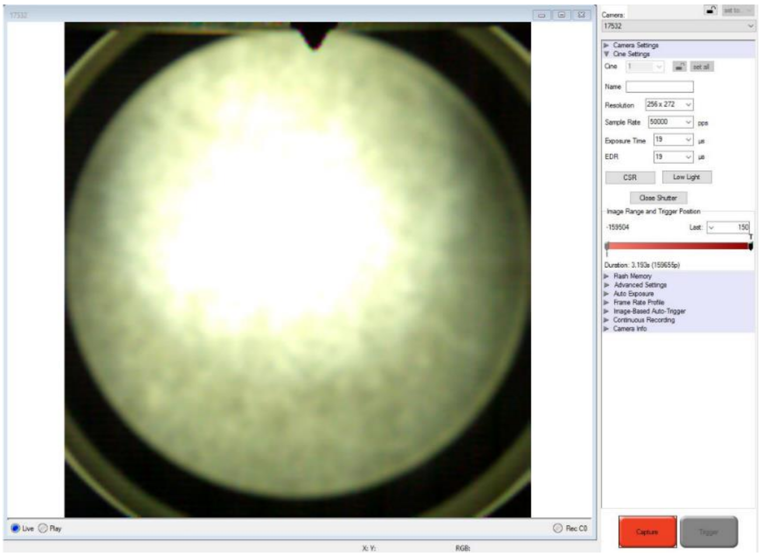
Camera: 17532

Cine 1

Name

Resolution 256 x 272

Sample Rate 50000 pps

Exposure Time 19 µs

EDR 19 µs

Image Range and Trigger Position

-159504 Last: 150

Duration: 3.193s (159655p)

Figure 3.7. Panel of the camera and lens configuration software

### *3.2.4. System monitor and control software*

A LabVIEW program named ‘Monitor and control’ receives signals of the internal air pressure and temperature, temperature of the windows, the motor and the seal via serial interface RS232 protocol, as shown in Figure 3.8 and Figure 3.9. Meanwhile, the switches of the heater and the thermostat and the set point of ambient air temperature are controlled by the program automatically to ensure the internal condition of the vessel to satisfy the requirement of experiments and protect windows and the seal from overheating.

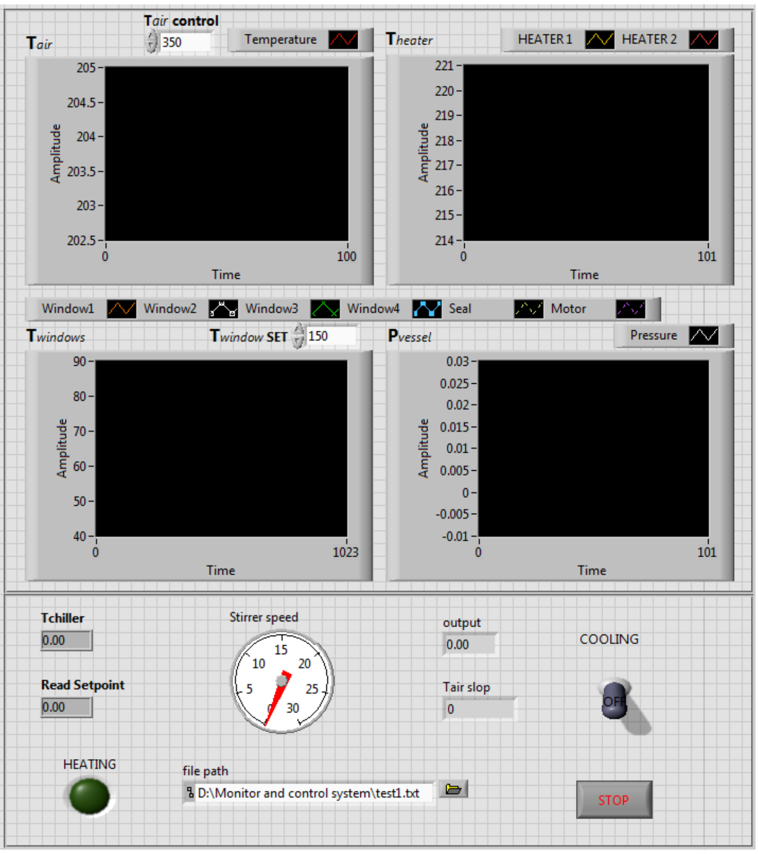

Tair control 350

Twindow SET 150

Tchiller 0.00

Read Setpoint 0.00

output 0.00

Tair slop 0

file path D:\Monitor and control system\test1.txt

Figure 3.8. Front panel of the Monitor and control program

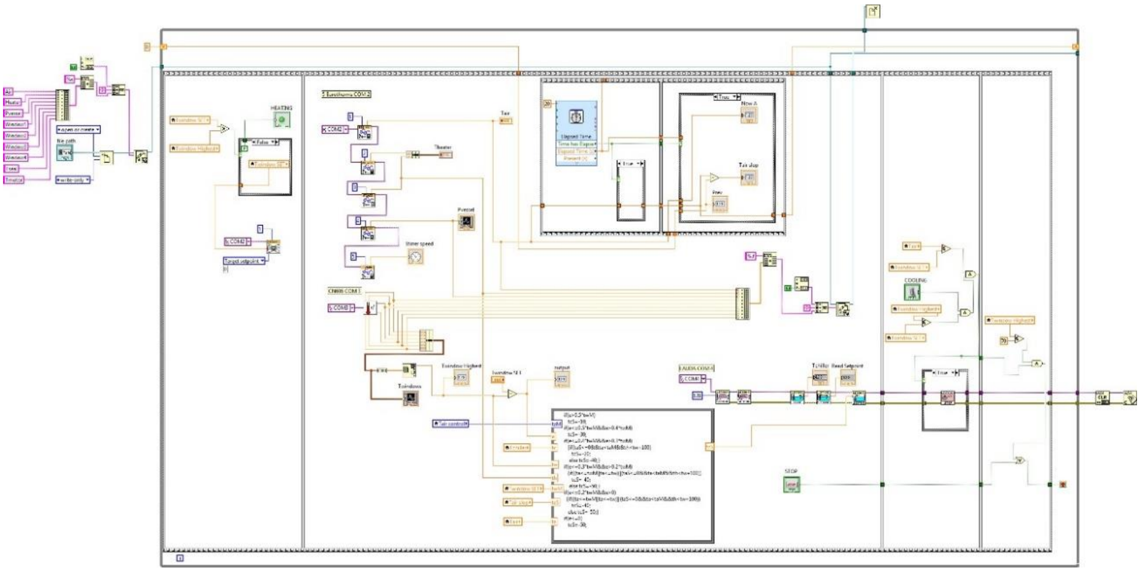

Figure 3.9. Block diagram of the Monitor and control program

Another LabVIEW program named ‘Injector and camera control’ is made to set the injection duration, dwell time and injection times. Meanwhile, it is capable of generating one positive TTL signal and a negative TTL signal simultaneously via a National Instrument data acquisition card PCI-6071E. As a result, the injector is triggered by the rising edge of the positive TTL signal, whilst the high speed CCD camera is triggered by the falling edge of the negative one at the same time. The program consists of three modes, ‘Test’, ‘Injection and Recording’ and ‘Calibration’, which are used to test the fuel delivery system, conduct spray experiments and calibrate the injector, respectively. The front panel and block diagram of the LabVIEW program are shown in Figure 3.10 and Figure 3.11.

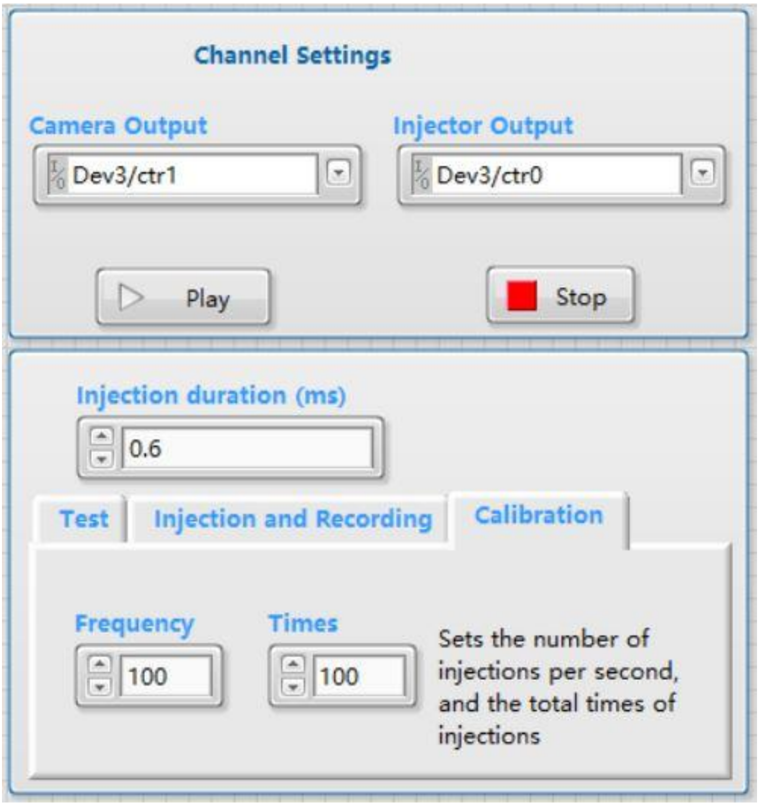
Channel Settings

Camera Output: Dev3/ctr1

Injector Output: Dev3/ctr0

Injection duration (ms): 0.6

Frequency: 100

Times: 100

Sets the number of injections per second, and the total times of injections

Figure 3.10. Front panel of the Injector and camera control program

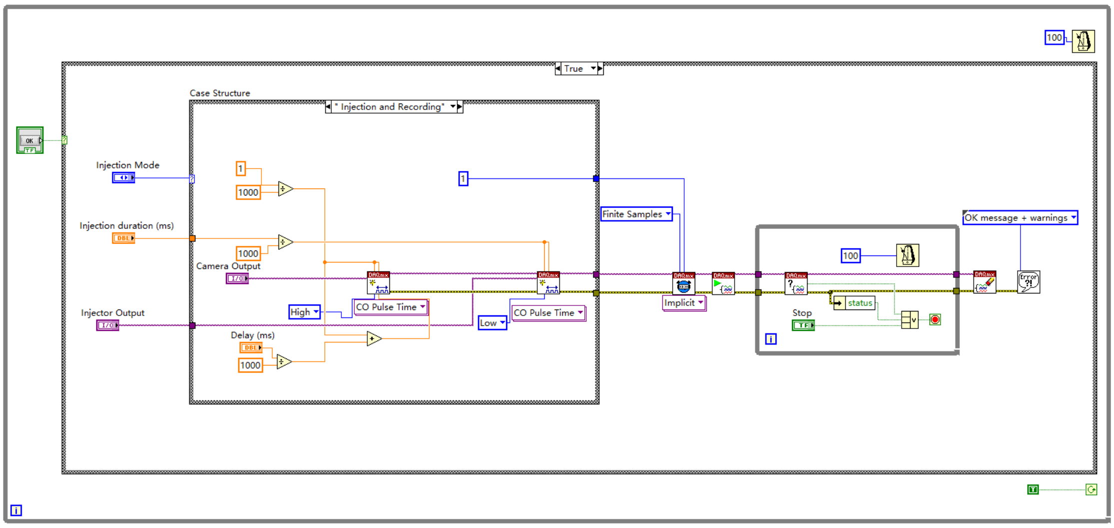

Figure 3.11. Block diagram of the Injector and camera control program

## 3.3. System performance

### *3.3.1. Injector calibration*

A single-hole solenoid injector with 0.16 mm orifice diameter is selected according to the specification of a Cummins ISB 4.5 diesel engine and installed at the top of the CVV. The injected mass of standard diesel fuel at different rail pressure should be measured for the injector, which is important to evaluate the performance of the injector and calculate the injection rate in the future. Accordingly, the standard diesel fuel is injected with the duration of 0.6 ms at rail pressure from 600 bar to 1800 bar for the calibration.

The calibration rig is made of an aluminium modular profile system as shown in Figure 3.12.

Figure 3.12. Injector calibration

The injector is hold vertically by a steel disc on a plastic cylinder to collect the injected fuel. The injector is connected to the common rail via a high-pressure flexi-pipe. In the Calibration model of the Injector and camera control program, 500 times of injection and 10 Hz frequency are selected and the injection duration is set to 0.6 ms. The calibration is done at various rail pressure and each calibration is repeated three time. The results of the calibration are illustrated in Table 3.5.

| Rail pressure (bar) | Injection duration (ms) | Number of injections | Average mass per injection (mg) |
|---|---|---|---|
| 900 | 0.6 | 500 | 3.18 |
| 1200 | 0.6 | 500 | 4.26 |
| 1500 | 0.6 | 500 | 5.52 |
| 1800 | 0.6 | 500 | 6.74 |

Table 3.5. Injected mass of standard diesel fuel at each rail pressure

### *3.3.2. Thermal properties of the CVV*

The highest internal temperature is tested and the duration of the highest temperature is recorded for many times. Among these tests, the CVV performs best at the highest ambient temperature of 327 °C (600K) and the highest ambient pressure of 40 bar.

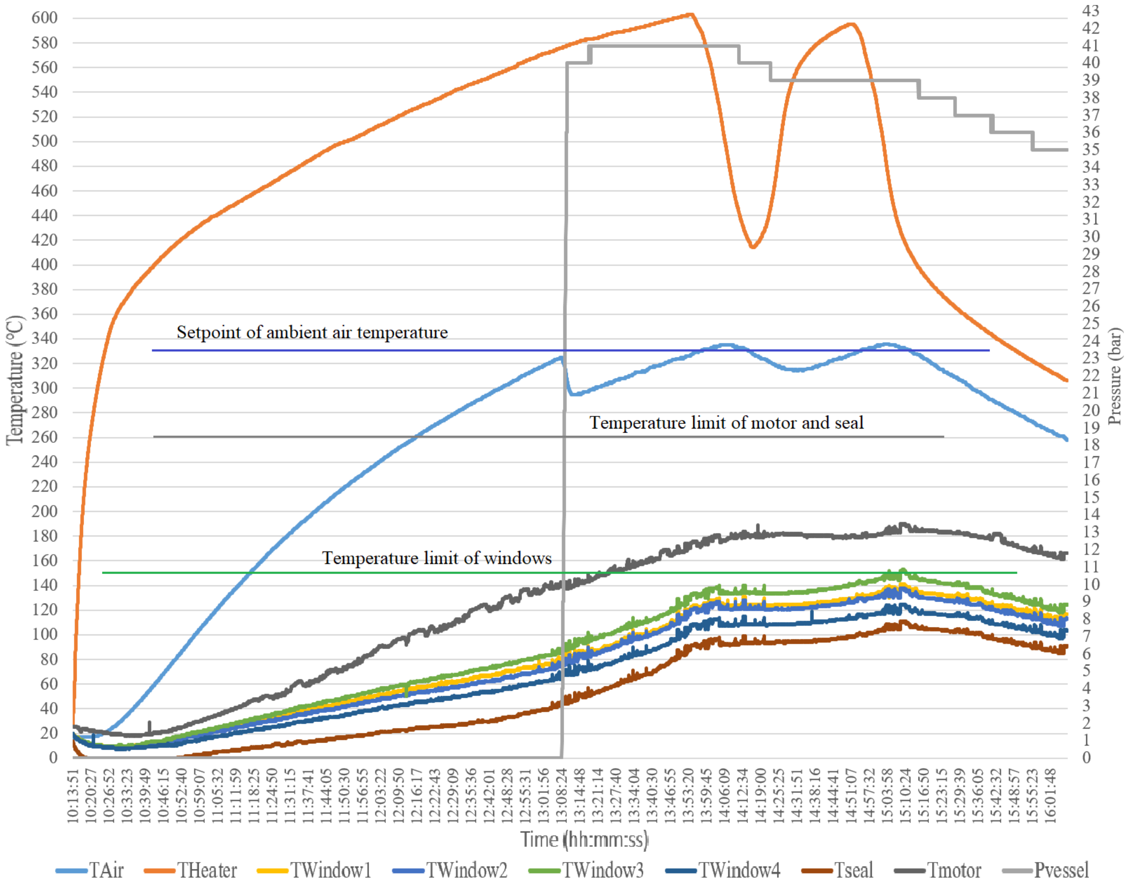

Figure 3.13. The temperature and pressure in the CVV during a test

As shown in Figure 3.13, the ambient air temperature can reach around 327 °C (600K) with the variance no more than 10 °C. Moreover, it stays within this range for over 30 minutes, which is much more than the duration of each spray injection (in milliseconds). The ambient pressure experiences a gradual drop from over 40 bar to about 35 bar during 3 hours, which is attributed to the air leakage around the motor driving the stirrer and a broken bolt at the bottom of the

CVV. However, the leakage is not serious, because the spray injection is quite fast compared with the duration that the ambient pressure stays within the variance of 1 bar (about 10 minutes). Furthermore, the temperature of each window, the seal of the vessel and the motor can be limited to no more than 160 ℃ and 180 ℃ respectively.

### 3.4. Experimental conditions

According to the performance of the CVV, the ranges of experimental variables are listed in Table 3.6.

| $P_r$ (bar) | $T_f$ (K) | $P_a$ (bar) | $T_a$ (K) | $d_0$ (mm) |
|---|---|---|---|---|
| 900 ~ 1800 | Room temperature | 10 ~ 40 | 303 ~ 600 | 0.16 |

Table 3.6. The range of experimental variables

In order to reduce the times of experiments, Design of Experiments (DoE) is adopted to design the experimental conditions, which are listed in Table 3.7.

| Conditions | $P_r$ (bar) | $P_a$ (bar) | $T_a$ (K) | Conditions | $P_r$ (bar) | $P_a$ (bar) | $T_a$ (K) |
|---|---|---|---|---|---|---|---|
| 1 | 900 | 10 | 303 | 33 | 1500 | 10 | 303 |
| 2 | 900 | 10 | 426 | 34 | 1500 | 10 | 426 |
| 3 | 900 | 10 | 506 | 35 | 1500 | 10 | 506 |
| 4 | 900 | 10 | 600 | 36 | 1500 | 10 | 600 |
| 5 | 900 | 20 | 303 | 37 | 1500 | 20 | 303 |
| 6 | 900 | 20 | 426 | 38 | 1500 | 20 | 426 |
| 7 | 900 | 20 | 506 | 39 | 1500 | 20 | 506 |
| 8 | 900 | 20 | 600 | 40 | 1500 | 20 | 600 |
| 9 | 900 | 30 | 303 | 41 | 1500 | 30 | 303 |
| 10 | 900 | 30 | 426 | 42 | 1500 | 30 | 426 |
| 11 | 900 | 30 | 506 | 43 | 1500 | 30 | 506 |
| 12 | 900 | 30 | 600 | 44 | 1500 | 30 | 600 |
| 13 | 900 | 40 | 303 | 45 | 1500 | 40 | 303 |
| 14 | 900 | 40 | 426 | 46 | 1500 | 40 | 426 |
| 15 | 900 | 40 | 506 | 47 | 1500 | 40 | 506 |
| 16 | 900 | 40 | 600 | 48 | 1500 | 40 | 600 |
| 17 | 1200 | 10 | 303 | 49 | 1800 | 10 | 303 |
| 18 | 1200 | 10 | 426 | 50 | 1800 | 10 | 426 |
| 19 | 1200 | 10 | 506 | 51 | 1800 | 10 | 506 |
| 20 | 1200 | 10 | 600 | 52 | 1800 | 10 | 600 |
| 21 | 1200 | 20 | 303 | 53 | 1800 | 20 | 303 |
| 22 | 1200 | 20 | 426 | 54 | 1800 | 20 | 426 |
| 23 | 1200 | 20 | 506 | 55 | 1800 | 20 | 506 |
| 24 | 1200 | 20 | 600 | 56 | 1800 | 20 | 600 |
| 25 | 1200 | 30 | 303 | 57 | 1800 | 30 | 303 |
| 26 | 1200 | 30 | 426 | 58 | 1800 | 30 | 426 |
| 27 | 1200 | 30 | 506 | 59 | 1800 | 30 | 506 |

| | | | | | | | |
|---|---|---|---|---|---|---|---|
| 28 | 1200 | 30 | 600 | 60 | 1800 | 30 | 600 |
| 29 | 1200 | 40 | 303 | 61 | 1800 | 40 | 303 |
| 30 | 1200 | 40 | 426 | 62 | 1800 | 40 | 426 |
| 31 | 1200 | 40 | 506 | 63 | 1800 | 40 | 506 |
| 32 | 1200 | 40 | 600 | 64 | 1800 | 40 | 600 |

Table 3.7. Experimental conditions

### 3.5. Experimental procedures

In the experiment, the injection duration is set to 0.6ms, which is defined from start of injection (SOI) to the end of injection (EOI). The start of injection (SOI) is the time when the injected fuel is just visible, and the end of injection (EOI) is the time when the tail of the spray leaves the injector. The time before and after the EOI can be respectively called the injection and post-injection periods. The spray tip penetration is the length from the head to the tail of the liquid spray. The cone angle is defined according to literature [34], which is the angle formed by two lines from the tail of the spray to the outer periphery of the spray at 1/3 length of the spray tip penetration, as shown in Figure 3.14.

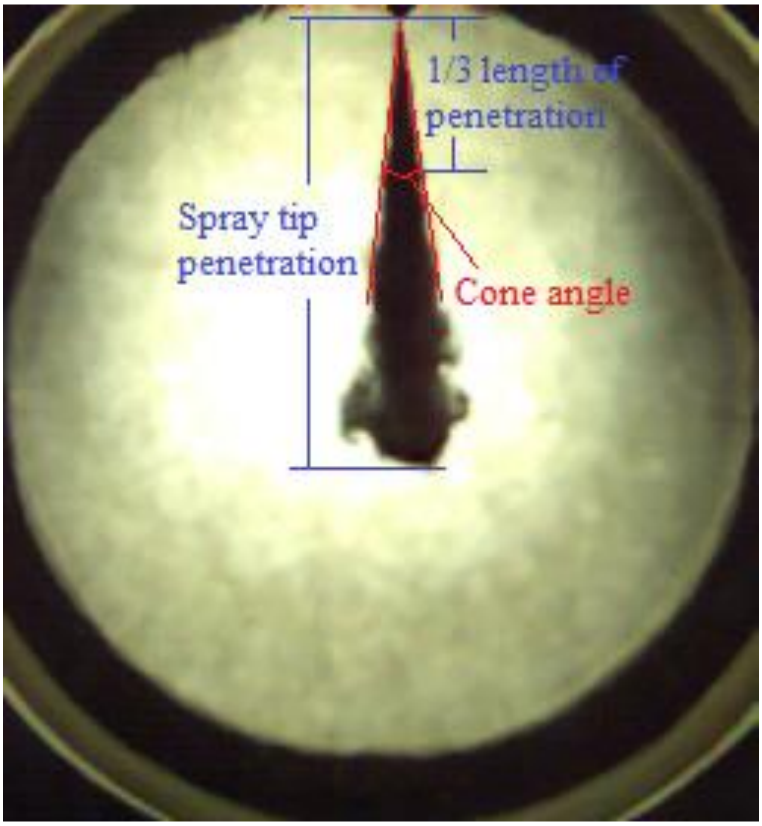

Figure 3.14. Illustration of spray tip penetration and cone angle

The camera is set to 256 × 272 pixels resolution at a sampling rate of 50,000 fps and exposure time of 19 μs to capture the image of spray with the interval of 0.02ms. The sample time is 1ms for the experiment. Before experiment, a ruler is put in the centre of the view as a reference, as shown in Figure 3.15. When the internal pressure and temperature reach the designed values, the injector and the camera are triggered simultaneously. Then, the fuel is injected into the CVV and the camera starts to capture images every 0.02 ms. Therefore, 30 images of spray can be obtained for the injection (0 ~ 0.6 ms), and 20 images are obtained for the post-injection (0.6 ~ 1 ms). These images are displayed on a computer and the spray tip penetration and cone angle are measured manually.

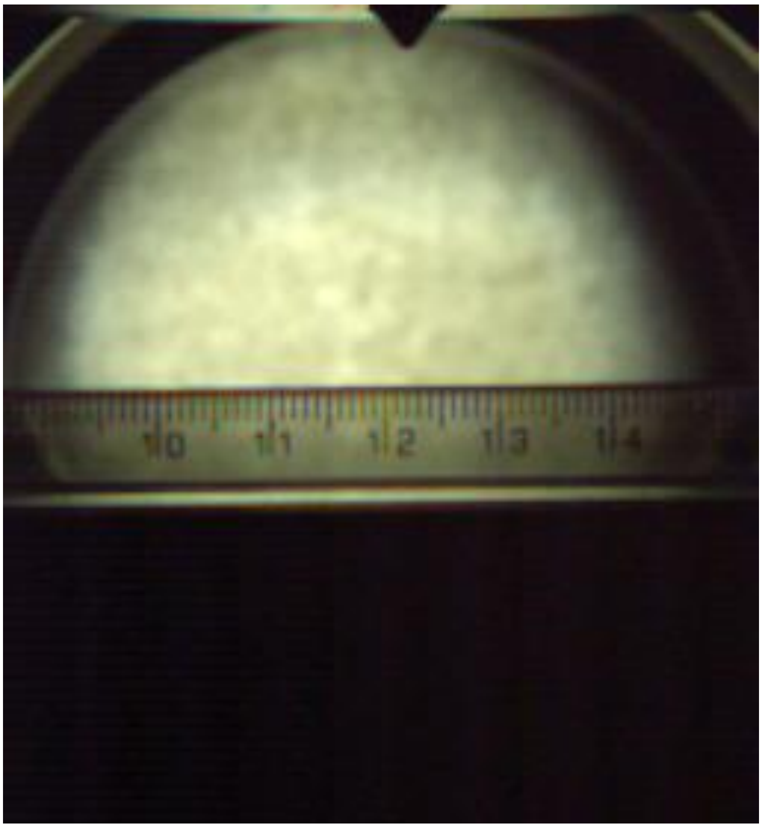

Figure 3.15. Reference for measurement

## 3.6. Results: Influence of experimental conditions on spray characteristics

### *3.6.1. Cone angle and spray tip penetration under various conditions*

The standard diesel fuel is employed to study the influence of rail pressure, ambient pressure and ambient temperature on spray characteristics. As known, the spray tip penetration and cone angle are the most important macroscopic characteristics indicating the quality of spray, which is mainly determined by the breakup and evaporation of droplets. The breakup is a process breaking the balance between the dynamic force and the viscosity and surface tension of the droplet. The dynamic force is determined by the momentum of droplets and the interaction with ambient gas. Therefore, penetration can be likely promoted by higher droplets velocity and higher fuel properties such as density, viscosity and surface tension, and reduced by higher ambient gas density and higher evaporation rate. In contrast, larger cone angle always occurs when a stronger breakup happens, but the evaporation may result in smaller cone angle. Usually, the shorter penetration and larger cone angle are expected for spray combustion in a diesel engine.

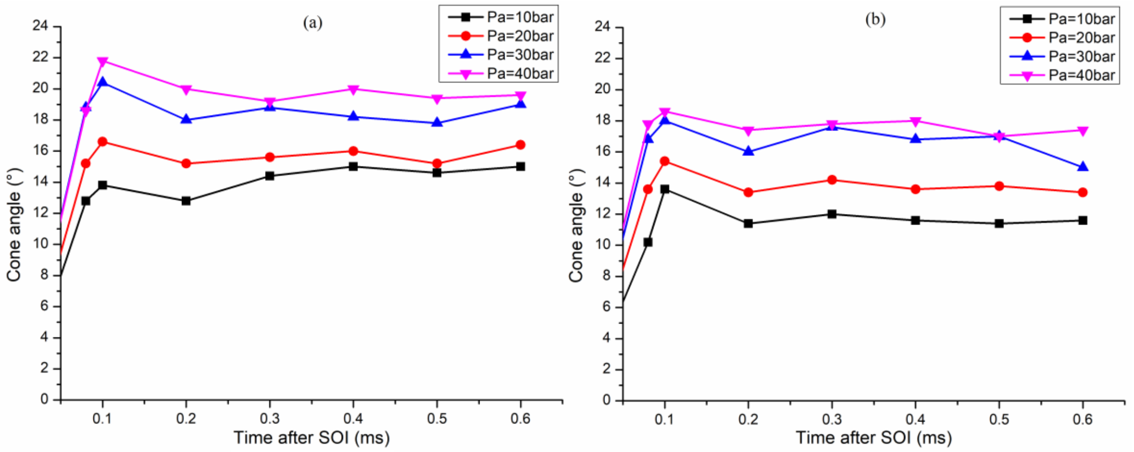

Figure 3.16. Cone angle of standard diesel fuel at 1800 bar rail pressure and various ambient pressure with the ambient temperature of 303K (a) and 600 K (b)

Figure 3.16 is an example of the cone angle against sample time at 1800 bar rail pressure and various ambient conditions, where the cone angle at all conditions experiences a dramatic jump to the peak at about 0.1ms after the SOI, and then fluctuates slightly but keeps relatively stable until the EOI. Literature [81] explains that the time of the peak cone angle is the breakup time, before which the spray is yet fully developed and has a blob-like shape resulting in larger cone angle. After the breakup time, the spray becomes relative stable in a period during the injection (about 0.3 ~ 0.6ms). Accordingly, we employ the average cone angle as one of the factors indicating spray quality in this experiment, which is the mean value of the cone angle between 0.3ms and 0.6ms.

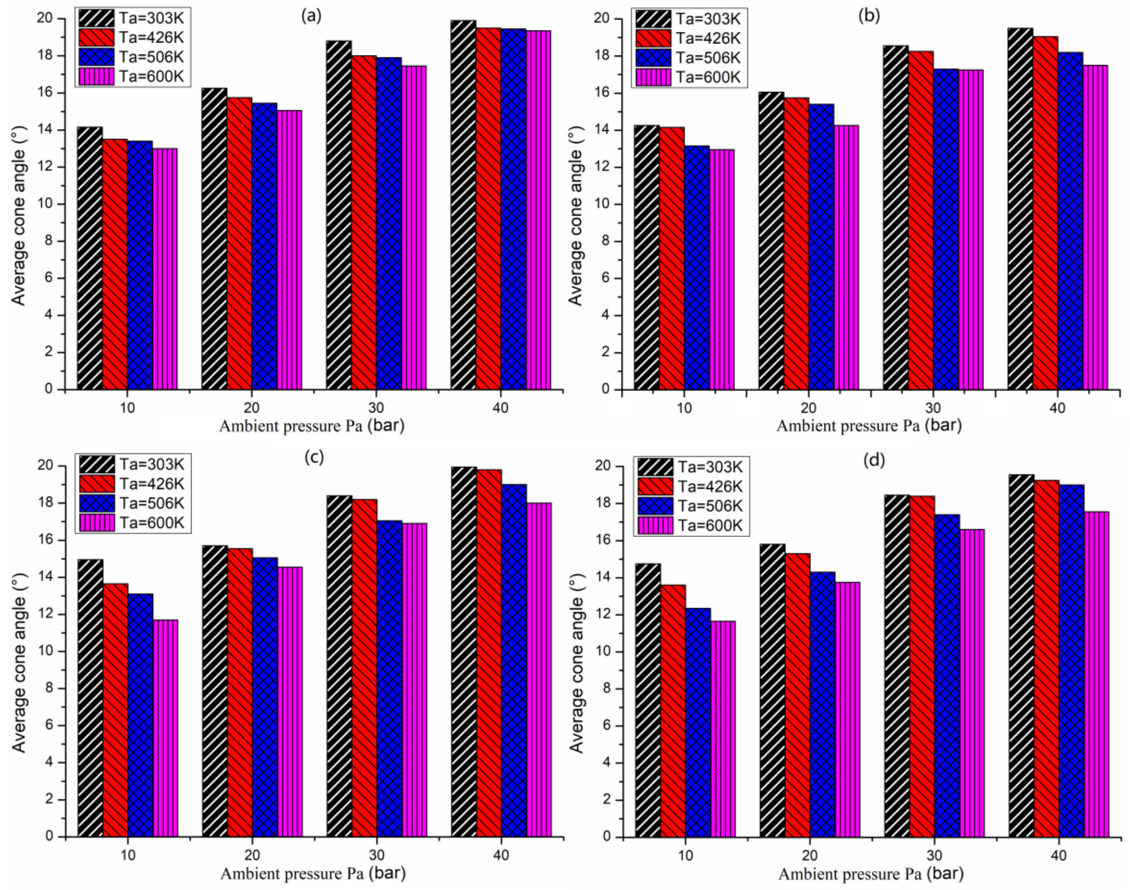

Figure 3.17. Average cone angle of standard diesel fuel at various ambient conditions and rail pressure of 900 bar (a), 1200 bar (b), 1500 bar (c) and 1800 bar (d)

First, the average cone angle at the same ambient conditions are very closed to each other regardless of varying rail pressure. It agrees with the conclusion in literature [78], where the cone angle is demonstrated not sensitive to injection pressure. Second, the average cone angle increases significantly with increasing ambient pressure, and the level of increase seems not to change at most ambient temperature and rail pressure. It is because ambient pressure dominates the breakup of liquid fuel, and thus higher ambient pressure promotes fuel to break up to smaller droplets due to stronger impinging and friction between the fuel and ambient gas (nitrogen).

In terms of ambient temperature, the average cone angle reduces slightly when the ambient temperature grows, which is mainly caused by the enhanced evaporation around the boundary of the spray at high temperature. However, the extent of reduction of average cone angle is impacted by rail pressure and ambient pressure. At 10 bar ambient pressure, the average cone angle experiences larger reduction at higher rail pressure. When it comes to 40 bar ambient pressure, the reduction of average cone angle is also promoted by increasing rail pressure, but its dropping rate is slower than that at 10 bar ambient pressure. It means the influence of rail pressure on the evaporation of droplets is more significant at low ambient pressure due to the larger surface of spray boundary, which enables more fuel droplets to absorb heat from hot ambient gas.

Figure 3.18 ~ Figure 3.21 show the spray tip penetration against sample time under all ambient conditions at the rail pressure of 900 bar, 1200 bar, 1500 bar and 1800 bar, respectively.

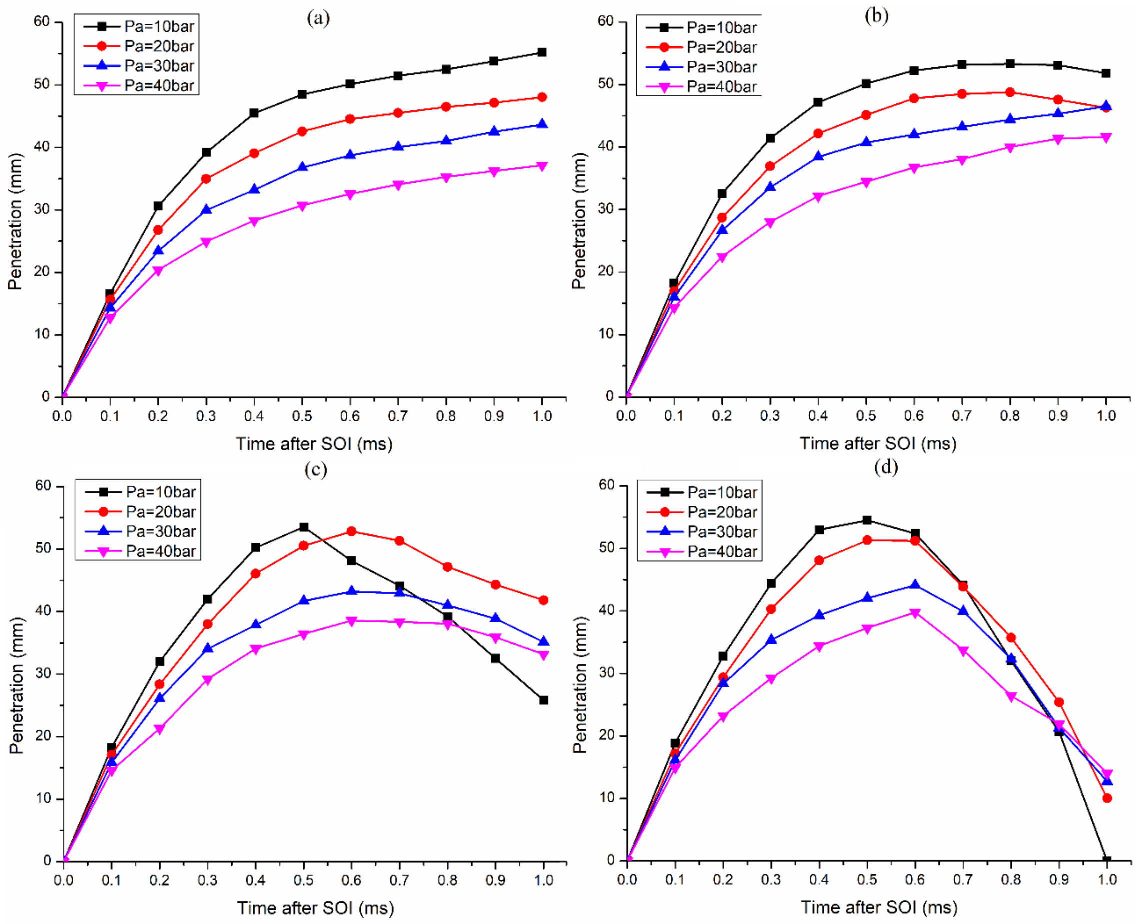

Figure 3.18. Effect of ambient pressure on spray tip penetration of standard diesel fuel at 900 bar rail pressure with the ambient temperature of 303K (a), 426K (b), 506K (c) and 600K (d)

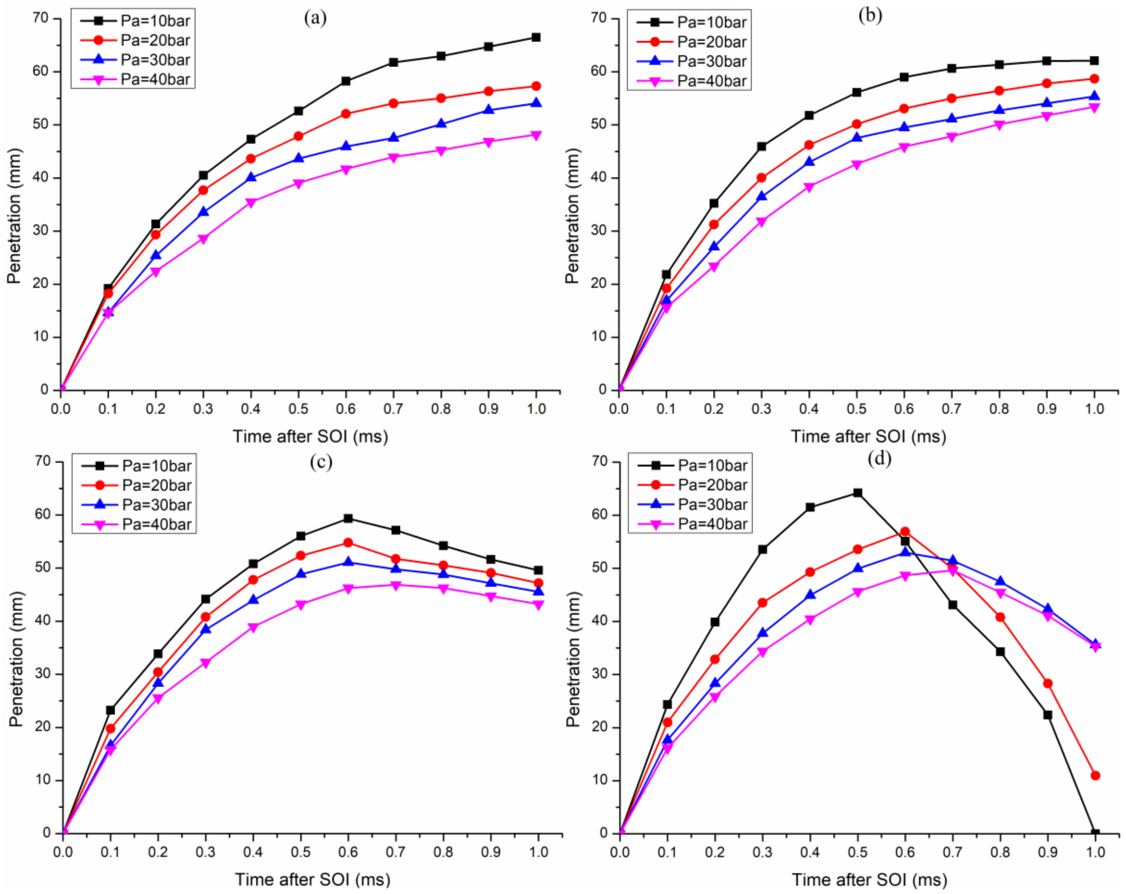

Figure 3.19. Effect of ambient pressure on spray tip penetration of standard diesel fuel at 1200 bar rail pressure with the ambient temperature of 303K (a), 426K (b), 506K (c) and 600K (d)

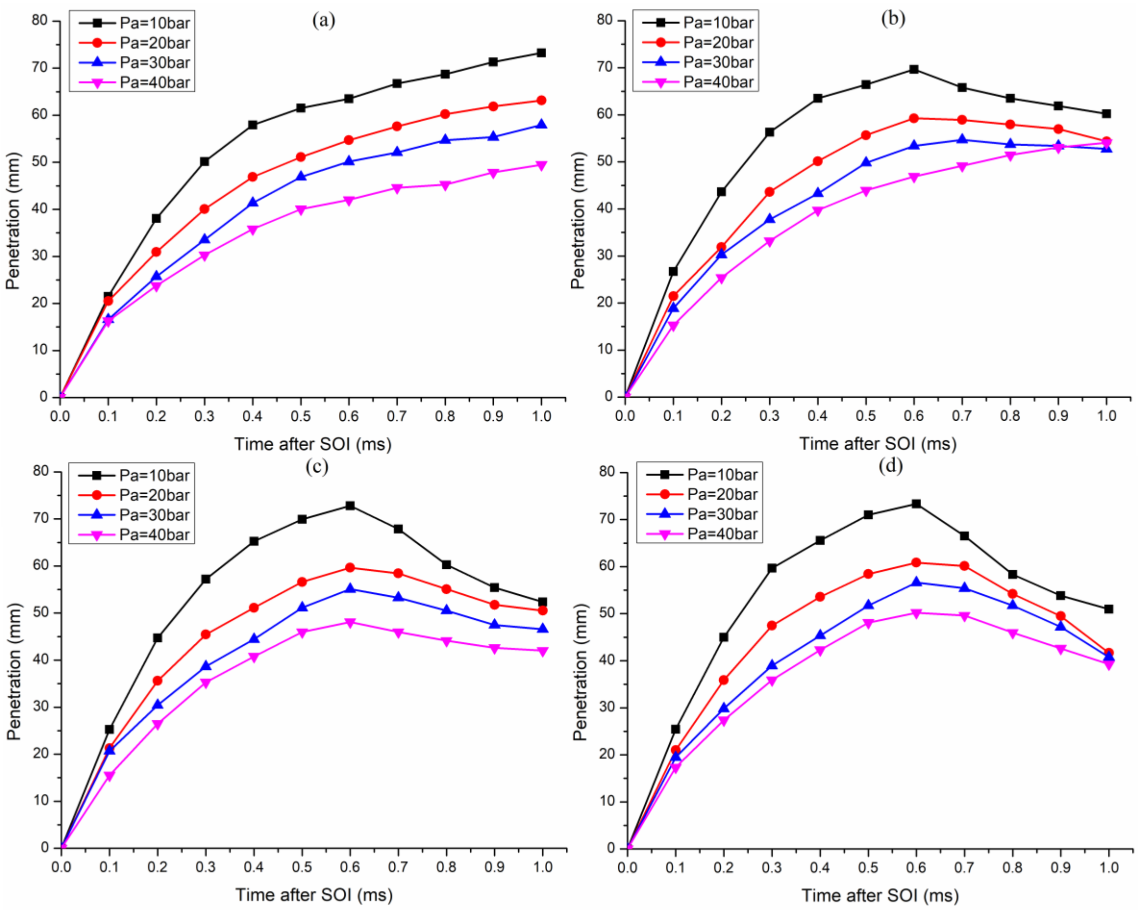

Figure 3.20. Effect of ambient pressure on spray tip penetration of standard diesel fuel at 1500 bar rail pressure with the ambient temperature of 303K (a), 426K (b), 506K (c) and 600K (d)

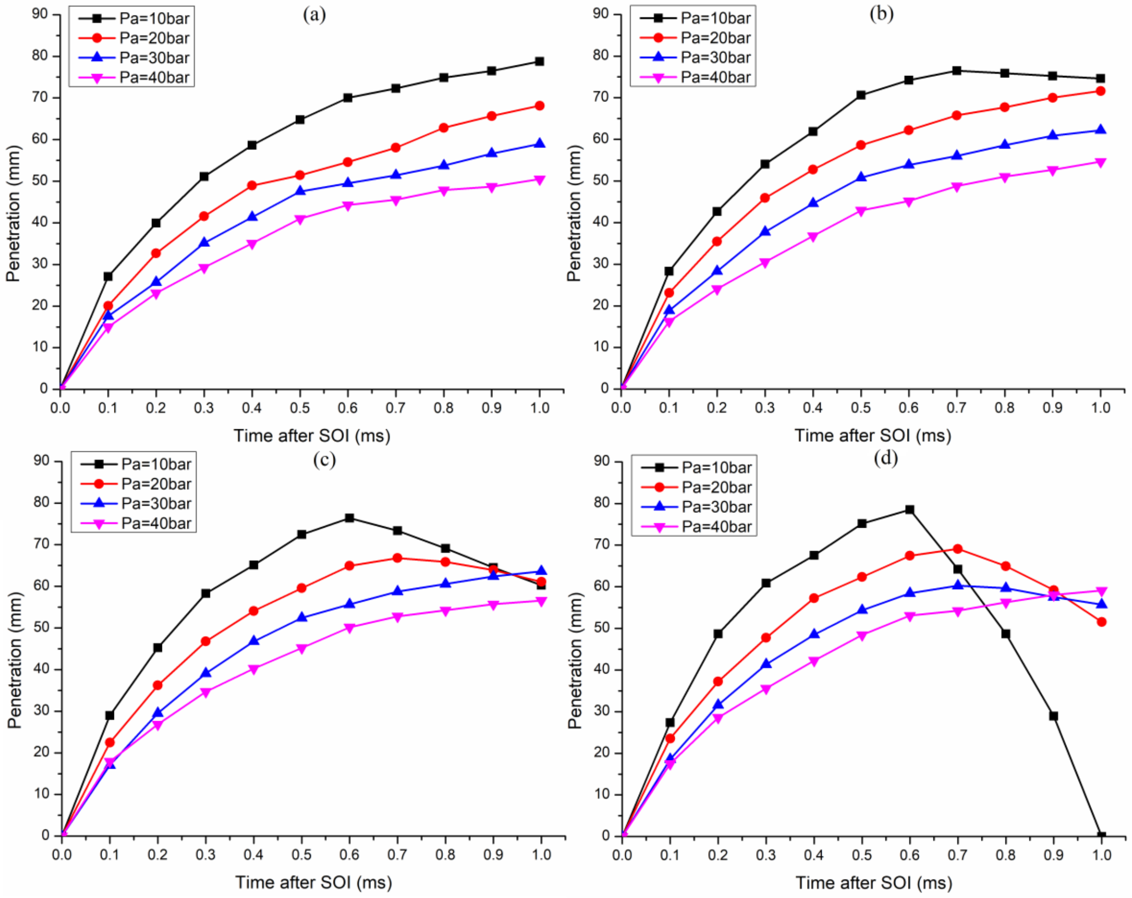

Figure 3.21. Effect of ambient pressure on spray tip penetration of standard diesel fuel at 1800 bar rail pressure with the ambient temperature of 303K (a), 426K (b), 506K (c) and 600K (d)

As shown in Figure 3.18 to Figure 3.21, the spray tip penetration in the injection and post-injection periods has different tendencies.

During the injection (0 ~ 0.6ms), the spray tip penetration is increasing with sampling time under all ambient pressure at cold conditions. However, the penetration of low ambient pressure (10 ~ 20 bar) tends to drop around the end of injection (about 0.5 ~ 0.6ms) when the ambient temperature is high (506 ~ 600K), especially at low rail pressure. The reasons are twofold: fist, the sharp and long penetration at low ambient pressure has larger surface of spray boundary, and thus absorb heat faster to evaporate in the hot ambient gas; second, lower ambient pressure means the ambient gas has smaller density and hence easier for evaporation. Overall, the spray tip penetration at higher ambient pressure is always much smaller than that at lower ambient pressure at all ambient temperatures, because the stronger interaction with fuel significantly enhances the breakup of droplets. It also agrees with the results in previous work [31], where the impinging effect was found dominant in breakup process.

In the post-injection period (after 0.6ms), the tendencies of penetration are more complicated because the impact of ambient temperatures becomes more significant. At 300K, penetrations at all ambient pressures keep increasing regardless of different rail pressures, and the penetration at lower ambient pressure are all shorter than that at the higher one. As the evaporation effect is not significant at cold condition and the fuel droplets can only penetrate forward by inertia, the ambient pressure still dominates in the post-injection period at cold condition. When the ambient temperature rises, penetrations at all ambient pressures and rail pressures start to reduce with time, and those at lower ambient pressure and lower rail pressure start earlier. Consequently, penetrations at 10 and 20 bar ambient pressure sometimes even drop to shorter than those at 30 and 40 bar, such as those in Figure 3.18 (c) and Figure 3.18 (d). These phenomena reveal that evaporation plays the most important role in the post-injection period at hot condition, because the droplets have a rather low velocity in this period due to lack of the rail pressure, and thus the influence of ambient pressure is weakened.

In order to further study the impact of ambient temperature, Figure 3.22 to Figure 3.25 are shown here to illustrate the spray tip penetration at varying ambient temperature during the whole sample time.

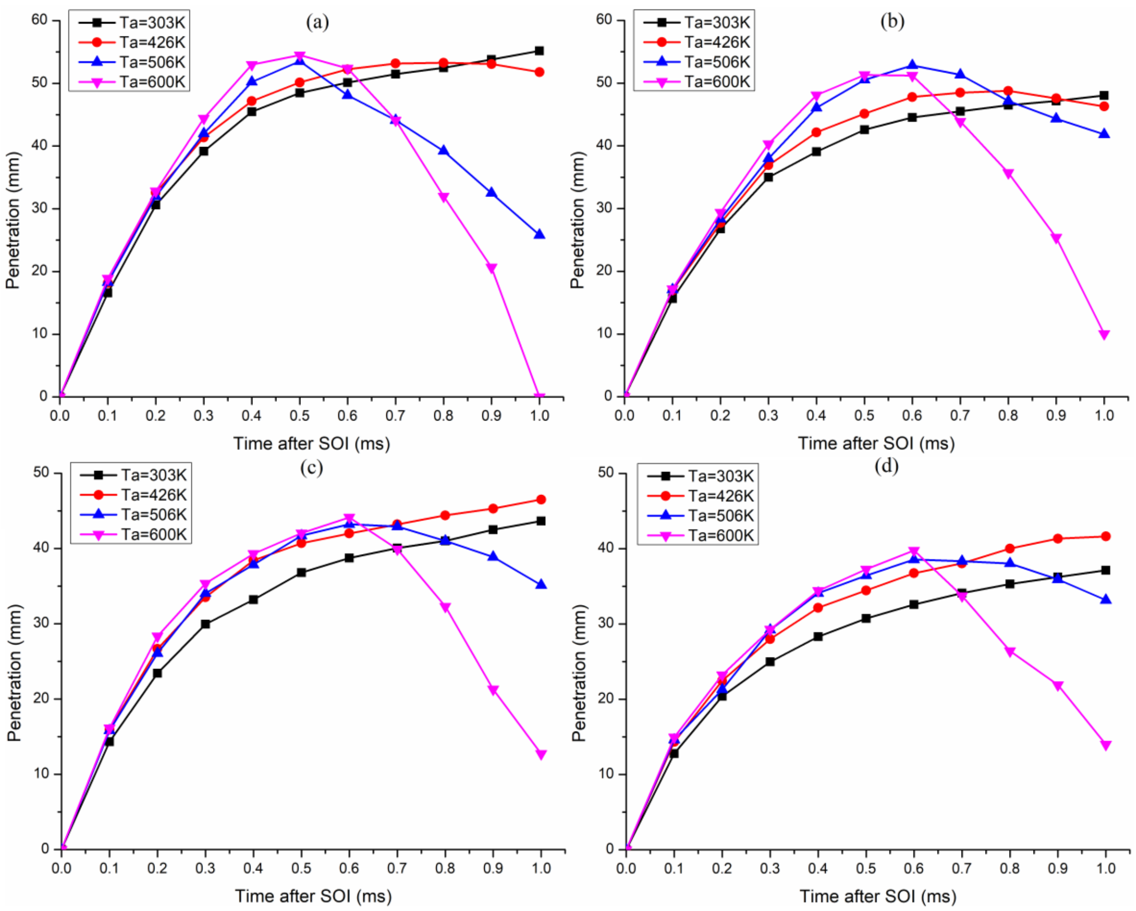

Figure 3.22. Effect of ambient temperature on spray tip penetration of standard diesel fuel at 900 bar rail pressure with the ambient pressure of 10 bar (a), 20 bar (b), 30 bar (c) and 40 bar (d)

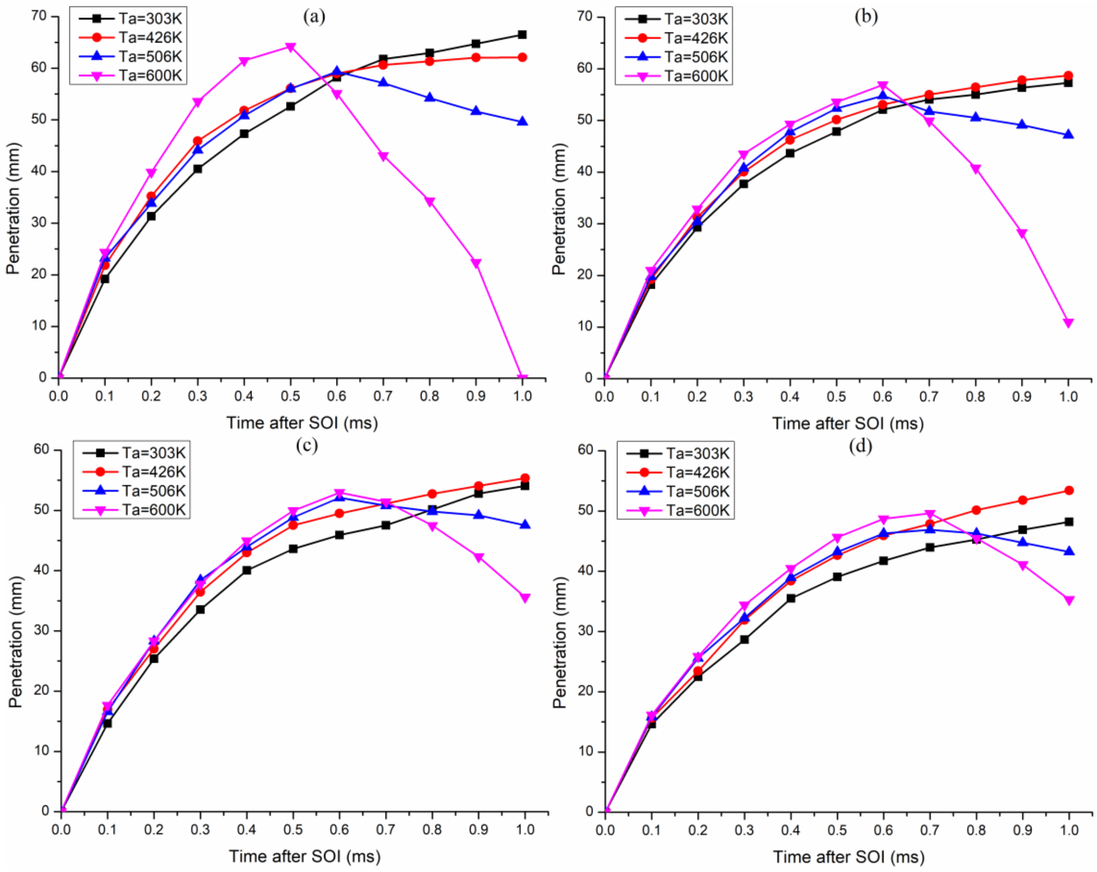

Figure 3.23. Effect of ambient temperature on spray tip penetration of standard diesel fuel at 1200 bar rail pressure with the ambient pressure of 10 bar (a), 20 bar (b), 30 bar (c) and 40 bar (d)

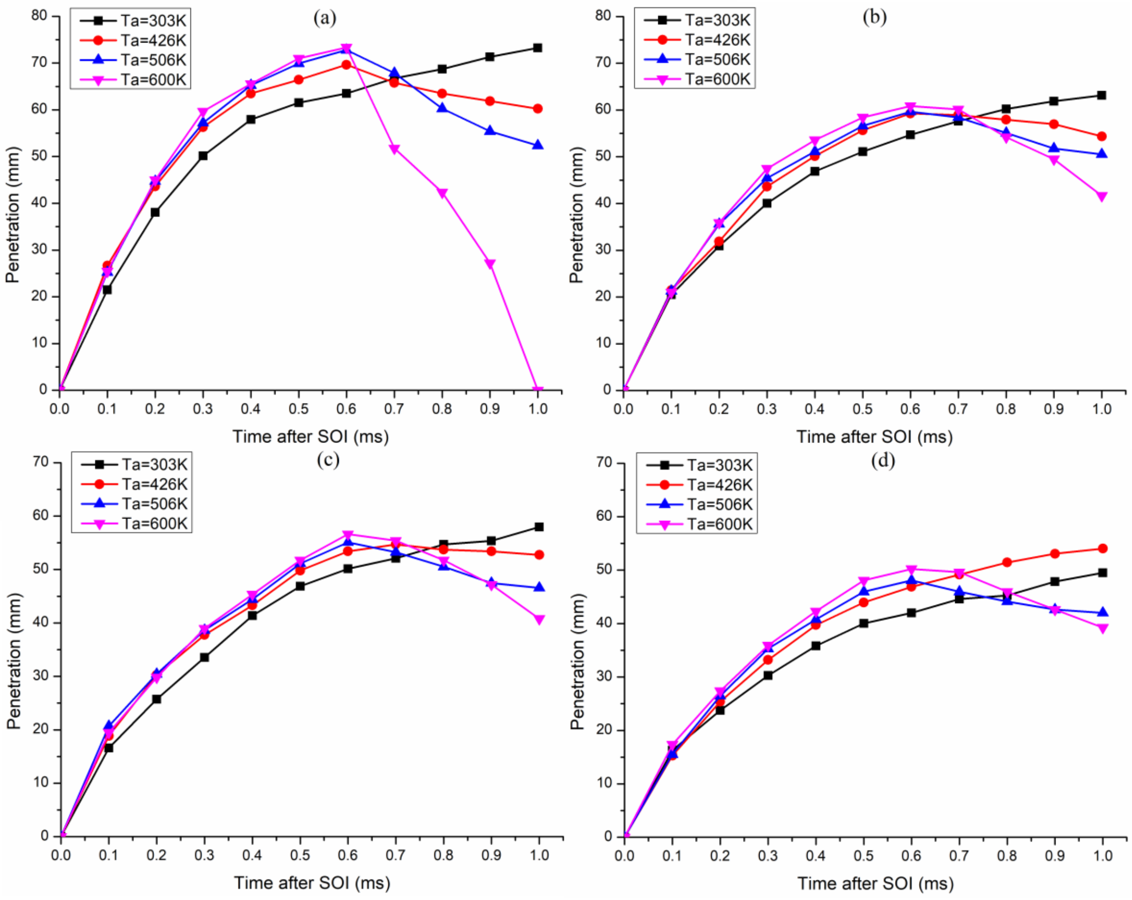

Figure 3.24. Effect of ambient temperature on spray tip penetration of standard diesel fuel at 1500 bar rail pressure with the ambient pressure of 10 bar (a), 20 bar (b), 30 bar (c) and 40 bar (d)

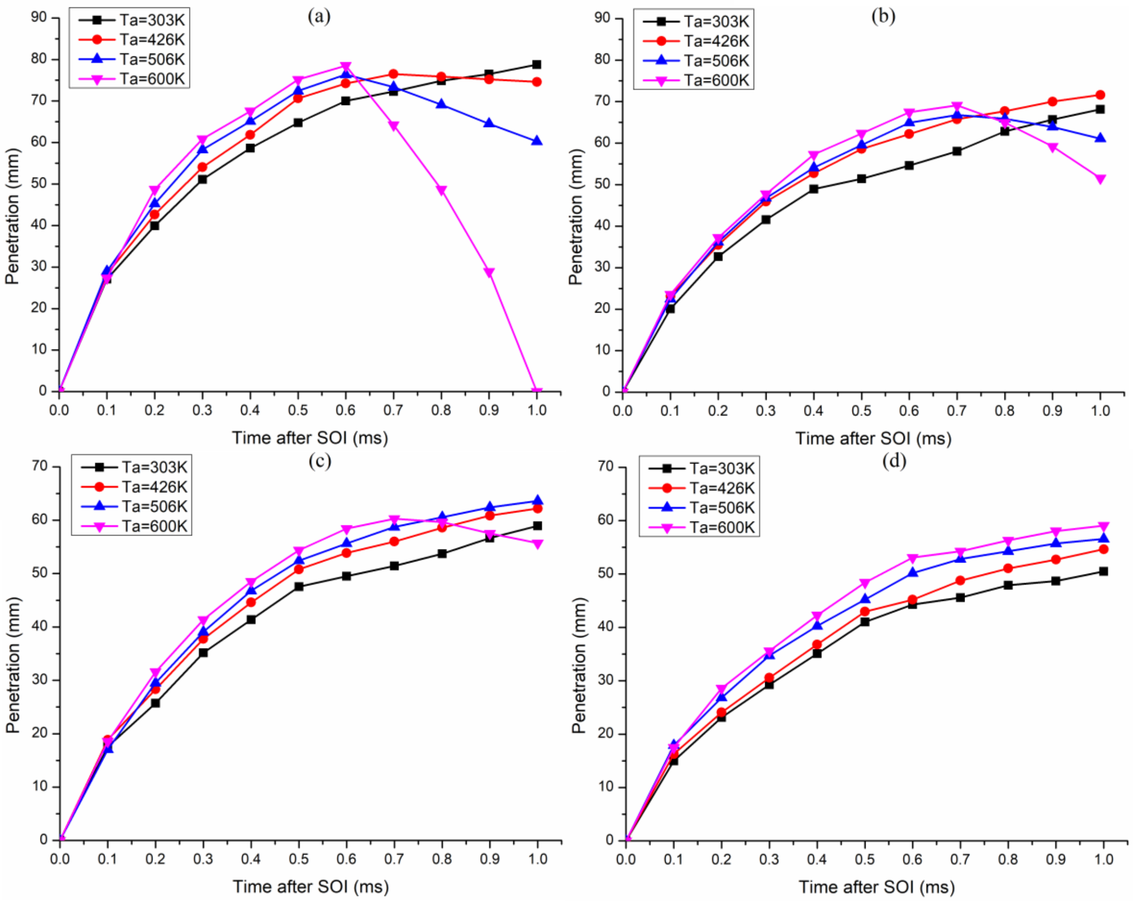

Figure 3.25. Effect of ambient temperature on spray tip penetration of standard diesel fuel at 1800 bar rail pressure with the ambient pressure of 10 bar (a), 20 bar (b), 30 bar (c) and 40 bar (d)

During injection, penetrations at most ambient pressure increase with increasing ambient temperature regardless of different rail pressure. It indicates that the fuel can penetrate longer distance at higher ambient temperature because the density of ambient gas decreases at the higher temperature and constant pressure. As a result, the dynamic drag force on injected fuel droplets is becoming weaker and produces longer penetration. However, the penetration under 900 bar rail pressure starts to drop with sample time at high ambient temperature around the end of injection (0.5 ~0.6ms) in Figure 3.22, because the small amount of injected fuel and lower velocity of droplets enables faster evaporation. Therefore, penetrations under rail pressure higher than 900 bar can still maintain growing until after the end of injection.

In the post-injection period, the penetration keeps growing when the ambient pressure is 40 bar at 1800 bar rail pressure. In contrast, the penetration starts to drop with increasing ambient temperature when the ambient pressure is no more than 30 bar, and the dropping rate of penetration at higher ambient temperature is larger than that at lower ambient temperature. Furthermore, when the rail pressure drops to lower than 1800 bar, the penetration is reduced by high ambient temperature even the ambient pressure is as high as 40 bar. It indicates that the ambient temperature becomes dominant in the post-injection period and its influence can be enhanced by reducing rail pressure and ambient pressure, because droplets has lower velocity at these conditions and thus are not capable of breaking up after the EOI. Therefore, they can only evaporate and diffuse to the ambient gas. Moreover, the spray at low ambient pressure is sharper and longer and thus has larger surface of boundary to evaporate, which makes its penetration to drop faster.

### *3.6.2. Summary*

These experiments aims to investigate the influence of experimental conditions on spray characteristics during both injection and post-injection periods, which is rarely studied yet. Meanwhile, the spray characteristics of standard diesel fuel will be a reference for the investigation of renewable fuels and nano additive modified fuels.

At various rail pressure, ambient pressure and ambient temperature, the average cone angle is found to increase significantly at higher ambient pressure but reduces with increasing ambient temperature, whilst the rail pressure has no comparable impact on it. In terms of the spray tip penetration, it can be significantly reduced by growing ambient pressure but increases with ambient temperature slightly during the injection period. In the post-injection period, high ambient temperature becomes dominant and is capable of reducing penetration when the ambient pressure is low due to the faster evaporation.

## 3.7. Results: Spray characteristics of renewable fuels

### *3.7.1. Average cone angle and spray tip penetration at hot ambient conditions*

In order to incorporate the influence of both breakup and evaporation on the macroscopic characteristics of spray, only the condition 52 and condition 64 in Table 3.7 are employed to conduct the spray experiment on the renewable fuels GTL and HVO. The DF is used as a reference. Therefore, the average cone angle and spray tip penetration at 1800 rail pressure and 600K ambient temperature are obtained at the ambient pressure of 10 bar and 40 bar respectively.

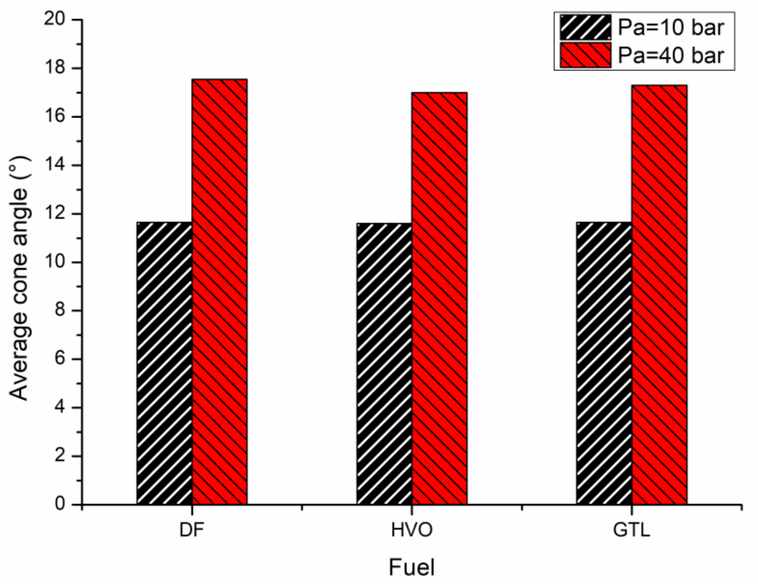

Figure 3.26. Average cone angle of renewable fuels

As shown in Figure 3.26, the average cone angle of the three test fuels at both 10 bar and 40 bar ambient pressure are very closed, although the difference at 40 bar ambient pressure are more obvious, where DF has the largest average cone angle and HVO has the smallest one. Usually, the cone angle can be significantly enlarged by stronger breakup and slightly reduced by faster evaporation. At 40 bar ambient pressure, HVO has the largest viscosity among the fuels and thus experiences the weakest breakup process. Meanwhile, HVO has lighter compositions than DF and thus easier to evaporate. These two factors enable the smallest average cone angle for HVO. In contrast, GTL has the lowest viscosity which tends to enlarge the cone angle. However, it has similar light compositions to HVO and thus make it faster to evaporate. Consequently, the average cone angle is larger than HVO but smaller than DF. At 10 bar ambient pressure, the breakup of all fuels is not relatively strong as that at 40 bar, which narrows the gap between DF and HVO and thus results in closed cone angle.

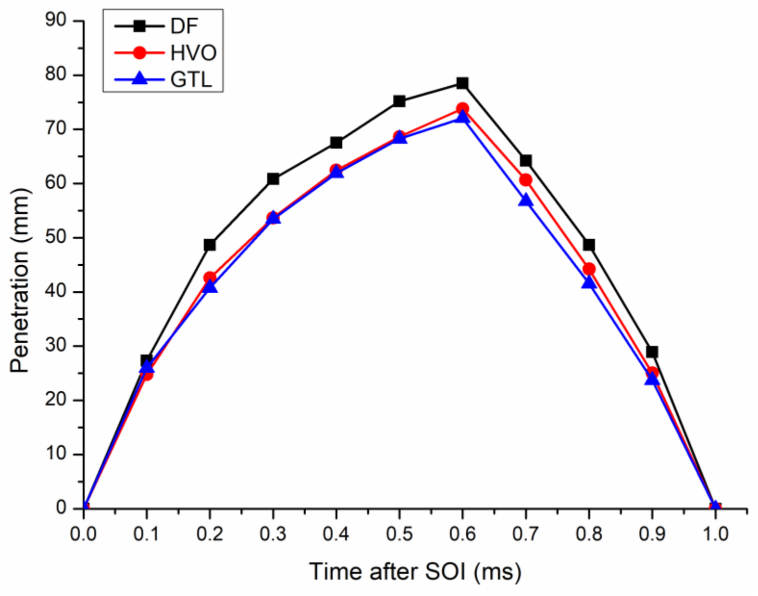

Figure 3.27. Spray tip penetration of renewable fuels at 10 bar ambient pressure

Figure 3.27 illustrates the spray tip penetration of all the test fuels at 10 bar ambient pressure and 600K ambient temperature. The fuel velocity and breakup play the most important roles in spray during injection, whilst the evaporation becomes dominant after the injection. As a result, the penetration of all fuels increases with time before the EOI and then drops to zero. During the injection period, the spray tip penetration of GTL and HVO are almost the same, because the difference of density and specific heat between them are not significant. In contrast, the penetration of DF is significantly larger than that of the two renewable fuels, which is mainly attributed to its higher density. During the post-injection period, the penetration of GTL stays at the lowest level, because GTL is a mixture of relatively lighter paraffin and lacks of polycyclic aromatic hydrocarbons (PAH) and thus easier to evaporate compared with DF. The penetration of HVO becomes larger than that of GTL during post-injection due to its larger viscosity. The difference between them at 10 bar ambient pressure is smaller than that at 40 bar, because the spray boundary area at 10 bar ambient is larger and thus results in faster evaporation.

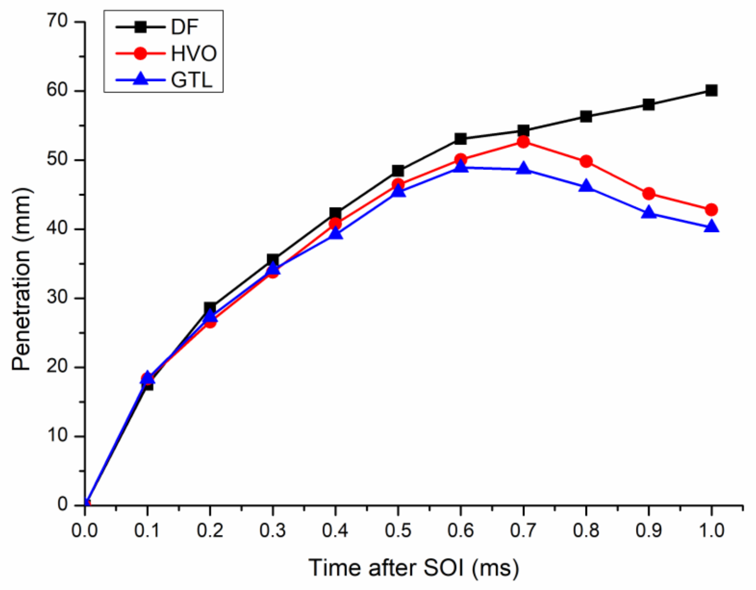

Figure 3.28. Spray tip penetration of renewable fuels at 40 bar ambient pressure

When the ambient pressure rises to 40 bar, the spray tip penetration of all fuels increases with sample time, and the penetration of HVO and GTL are almost at the same level during the injection. It is because the ambient pressure and density dominate the breakup process of spray at constant rail pressure, whilst the impacts of other properties and ambient temperature are not comparable. However, in the post-injection period, the penetration of DF keeps increasing with time, whilst that of HVO and GTL becomes to drop. The phenomena are mainly because the evaporation dominates in the post-injection period and thus enables shorter penetration for the renewable fuels due to their lighter compositions, as HVO and GTL have lower 100% distillation temperature than DF (EN590) [77]. The difference between HVO and GTL during post-injection at 40 bar ambient pressure is larger than that at 10 bar, because HVO has larger viscosity and then generates larger droplets evaporating slower, and the evaporation rate at 40 bar is not as high as that at 10 bar.

### *3.7.2. Summary*

The renewable fuels (HVO and GTL) has very closed average cone angle to DF. DF has the largest spray tip penetration during both the injection and post-injection periods due to its larger density, whilst GTL has the smallest penetration caused by its smallest density and viscosity.

## 3.8. Results: Spray characteristics of nano additive modified fuels

### *3.8.1. Average cone angle and spray tip penetration at hot ambient conditions*

The spray experiment of nano additive modified fuels is also conducted at 1800 rail pressure, 600K ambient temperature and the ambient pressure of 10 bar and 40 bar respectively. Considering the $CeO_2$ nanopowder of 25nm and 50nm sizes has almost the same impact on the physical properties of fuels, only the DF-Ce25 and GTL-Ce25 are selected as the $CeO_2$

nanopowder modified fuels. Therefore, the DF-Ce25, DF-CNT, GTL-Ce25 and GTL-CNT are employed in the spray experiment, and DF and GTL are the reference. The average cone angle and spray tip penetration of all nano additive modified fuels are obtained and shown in Figure 3.29 ~ Figure 3.32.

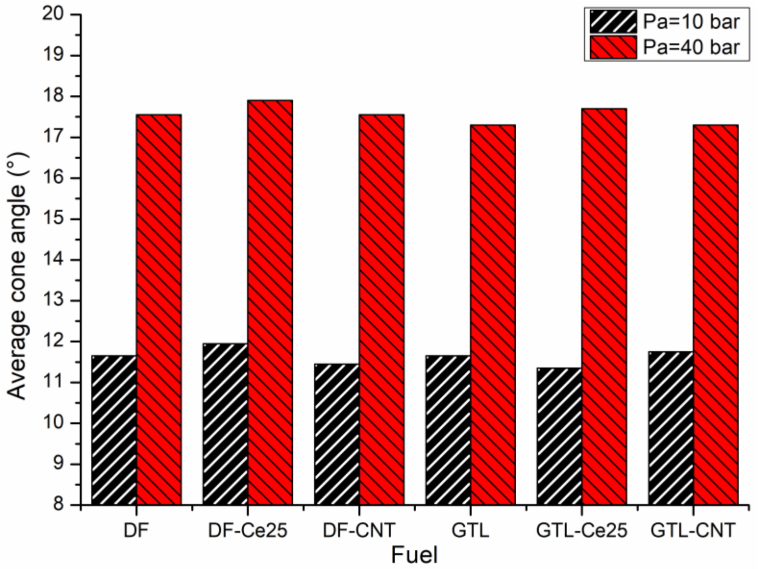

Figure 3.29. Average cone angle of nano additive modified fuels

As illustrated in Figure 3.29, the average cone angle of all the test fuels are very closed and the variance is within 1° at each ambient pressure. As mentioned above, the cone angle is mainly determined by the breakup and slightly influenced by the evaporation. The result indicates that the addition of $CeO_2$ nanopowder and CNT has no comparable impact on breakup and evaporation for either DF or GTL during injection period, and thus cannot change the average cone angle significantly.

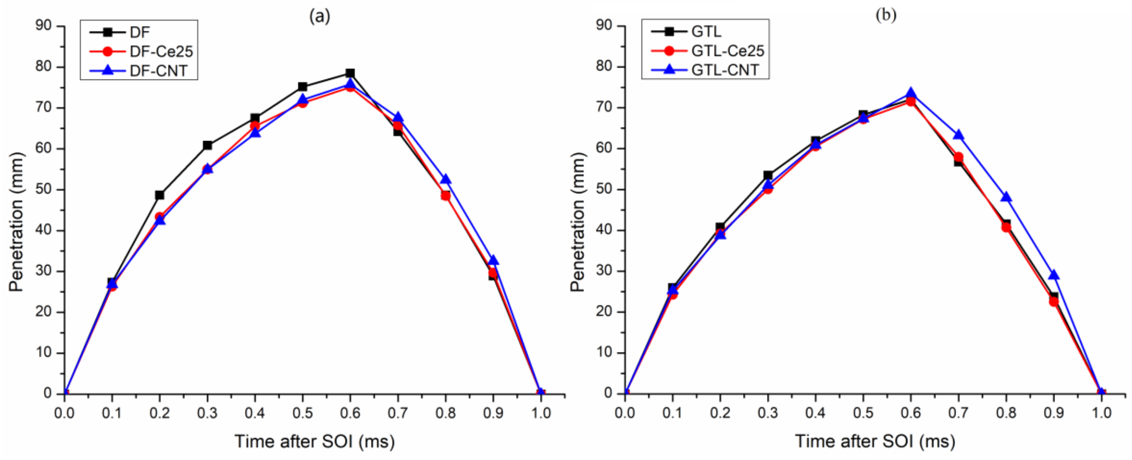

Figure 3.30. Spray tip penetration of nano additive modified fuels at 10 bar ambient pressure

In terms of the spray tip penetration, the nano additive modified fuels have the same tendency as DF and GTL at 10 bar ambient pressure, which is increasing with time during the injection and then dropping to zero in the post-injection period. Moreover, the overall level of penetration of DF and GTL is higher than that of them with nano additives during injection, which is mainly due to the reduced viscosity and increased thermal diffusivity of the modified fuels. Nevertheless, the penetration of DF-CNT and GTL-CNT becomes slightly larger than other fuels at the post-injection period, because a large amount of fuel is inside the CNT, and the fuel can only evaporate via the two ends of CNT instead of all directions due to the thick wall and hollow structure. As a result, the duration of evaporation of the liquid fuel is enlarged, as shown in Figure 3.31. The details will also be mentioned in the Chapter 5.

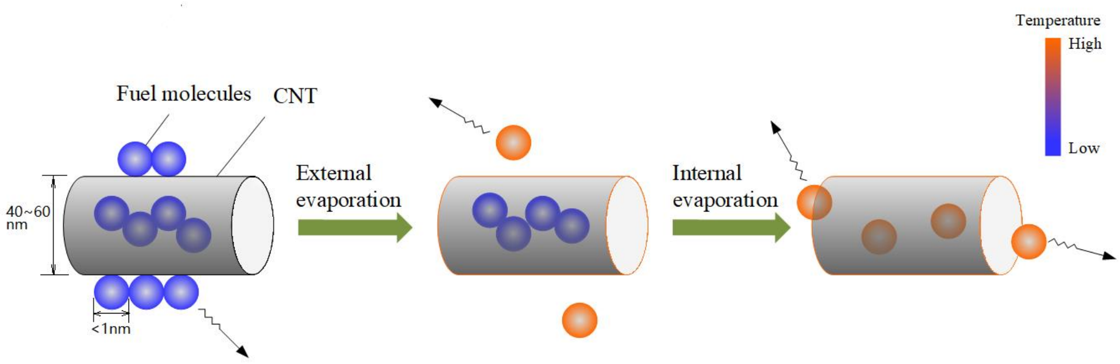

Figure 3.31. Illustration of the two-step evaporation of DF-CNT

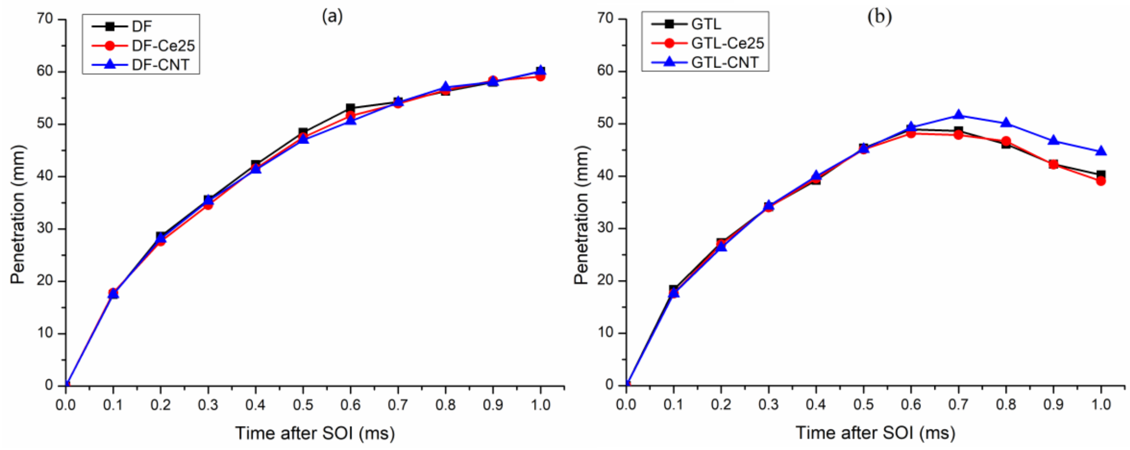

Figure 3.32. Spray tip penetration of nano additive modified fuels at 40 bar ambient pressure

When the ambient pressure rises to 40 bar, the difference between pure fuels and modified fuels is neglect during the injection, because the higher ambient pressure enhances the breakup of droplets which makes the impact of fuel properties not comparable. In the post-injection period, the penetration of DF and its modified fuels keeps increasing gradually with no difference, whilst that of GTL and its modified fuels starts to drop and GTL-CNT has overall larger penetration than others. This phenomenon is highly likely attributed to the lighter compositions of GTL which improves the influence of evaporation.

### *3.8.2. Summary*

The nano additive modified fuels have no significant difference in average cone angle and spray tip penetration compared with the pure fuels, as their low concentration has no comparable impact on most physical properties. CNT is capable of slowing down the evaporation process, because its thick wall and hollow structure reduce the evaporation rate of the fuel inside it, which cannot evaporate via all directions.

## 3.9. Summary of Chapter 3

In this chapter, the influences of rail pressure, ambient pressure and ambient temperature are investigated firstly on the macroscopic characteristics of spray by experiments on the DF in a CVV system. And then, spray experiments of renewable fuels (HVO and GTL) and nano additive modified fuels (DF-Ce25, DF-CNT, GTL-Ce25 and GTL-CNT) are conducted. The main results are summarised below:

- The rail pressure is capable of increasing the spray tip penetration significantly but has no impact on the average cone angle, which can only be reduced significantly by decreasing ambient pressure and increasing ambient temperature.
- During injection, the spray tip penetration can be significantly reduced by growing ambient pressure but increased by ambient temperature slightly.

- In the post-injection period, high ambient temperature enables faster evaporation and thus reduces penetration.
- The renewable fuels (HVO and GTL) has almost the same average cone angle as DF.
- DF has the largest spray tip penetration during both the injection and post-injection periods due to its larger density, whilst GTL shows the smallest penetration due to the smallest density and viscosity.
- Nano additives ($CeO_2$ nanopowder and CNT) have no significant impact on average cone angle.
- $CeO_2$ nanopowder cannot change the spray tip penetration at most conditions, whilst CNT is likely to increase it in the post-injection period because a large amount of fuel molecules are inside the CNT. Due to the thick wall and hollow structure, these fuel molecules can only evaporate via the two ends of CNT instead of all directions. As a result, the whole evaporation rate is reduced.

The influence of experimental conditions, renewable fuels and nano additive modified fuels on macroscopic spray characteristics is summarised in Table 3.8. However, the ambient pressure and ambient temperature are lower than those in an CI engine cylinder. In order to more precisely analyse the spray characteristics at cylinder-like environment, the CFD approaches would be employed to simulate the spray process. Meanwhile, the impact of more experimental conditions such as fuel temperature could also be studied by CFD method.

| Factor | $P_r$ | $P_a$ | $T_a$ | HVO | GTL | $CeO_2$ | CNT |
|---|---|---|---|---|---|---|---|
| Cone angle | N/A | + | - | N/A | N/A | N/A | N/A |
| Spray tip penetration (Injection) | + | - | + | - | - | N/A | N/A |
| Spray tip penetration (Post-injection) | N/A | - | - | - | - | N/A | + |

Table 3.8. Summary of the influence of all factors on macroscopic spray characteristics

*'+' means the growing value of the factor will increase the corresponding result, and '-' means the growing value of the factor will decrease the corresponding result, whilst 'N/A' indicates the factor has no comparable impact on the corresponding result.

# Chapter 4 . CFD model of fuel spray

Chapter 3 investigated spray characteristics at various experimental conditions, but the ambient temperature and ambient pressure are still lower than those in the CI engine cylinder. Moreover, as many spray-related fuel properties including density, viscosity and surface tension etc. are strongly dependent on fuel temperature, it is also necessary to research the influence of fuel temperature on spray. Consequently, this chapter is intended to investigate the macroscopic characteristics of liquid fuels at larger range of ambient conditions (temperature and pressure) and meanwhile, study the influence of more factors including fuel temperature. As detail properties of HVO at various temperature are found in literature and its spray characteristics at various conditions were rarely mentioned in previous studies, this chapter employs Hydrotreated Vegetable Oil (HVO) as the test fuel. Thus, its spray tip penetration and cone angle will be analysed at varying fuel condition (rail pressure and fuel temperature) and ambient condition (ambient pressure and temperature) via the CFD method. Furthermore, a DoE model is formulated to provide a quantitive correlation between the spray tip penetration and the fuel condition as well as ambient condition.

## 4.1. Geometric model and meshing work

As the inside of the CVV is cylindrical, it can be simplified to a 2D symmetrical geometric model shown in Figure 4.1. According to the volume of the CVV in Chapter 3, the length and the width of the model are 270 mm and 75 mm.

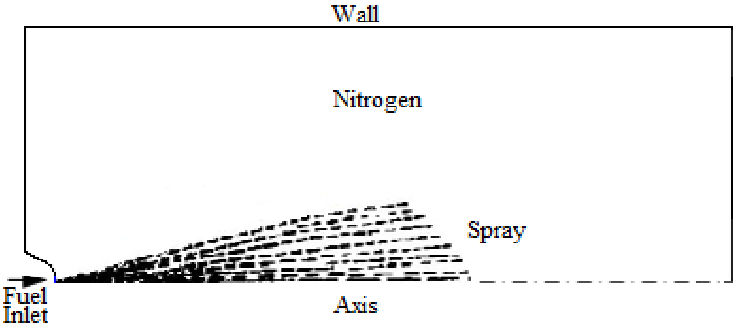

Figure 4.1. Illustration of the 2D CVV model

Considering the simply geometry, structural cells are employed to mesh the fluid domain, and the total amount of cells are 180628. The orifice diameter of the fuel inlet is 0.16 mm, and thus the zone around it is refined to obtain higher accuracy. The meshed geometric model of the CVV is illustrated in Figure 4.2. The model is then imported to ANSYS Fluent 18.1 to simulate spray.

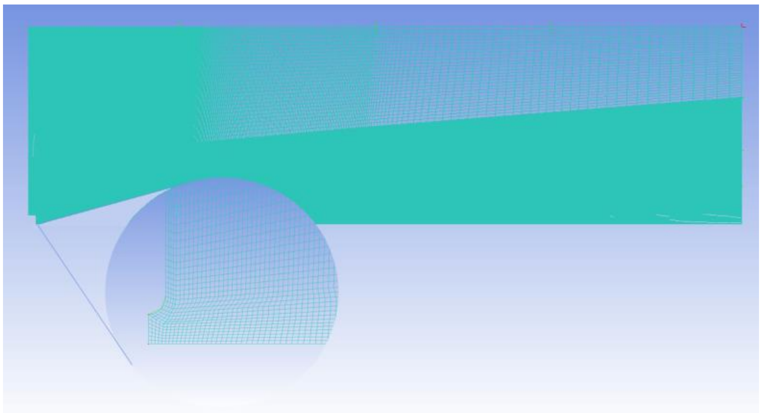

Figure 4.2. The meshed CVV model and its refinement around the injector

## 4.2. Numerical methodologies

### *4.2.1. Breakup models*

Two breakup models have been developed for liquid fuel spray and combustion in diesel engines. The Wave breakup model of Reitz is appropriate for high-speed fuel injections, which considers the droplets breakup is induced by the relative velocity between the gas phases and the liquid phases. During the breakup, the Kelvin-Helmholtz instability is assumed to be dominant, and the size of child droplets is proportional to the wavelength of the unstable surface wave on the parent droplet, as shown in Equation (4.1) [188].

$$r = B_0\Lambda \tag{4.1}$$

Where $r$ is the radius of the child droplet, $B_0$ is constant and usually set to 0.61 according to Reitz's work [189]. The changing rate of the radius of the droplet is given by

$$\frac{\mathrm{d}a}{\mathrm{d}t} = -\frac{(a-r)}{\tau},\ r \leq a \tag{4.2}$$

Where $a$ is the radius before breakup and $\tau$ is the breakup time determined by

$$\tau = \frac{3.726 B_1 a}{\Lambda\Omega} \tag{4.3}$$

$B_1$ is the breakup time constant and it determines how quickly the parcel will lose mass [188]. $\Omega$ is the maximum growth rate and $\Lambda$ is the corresponding wavelength of parent droplet, which can be calculated by:

$$\frac{\Lambda}{a} = 9.02\frac{(1+0.45Oh^{0.5})(1+0.4Ta^{0.7})}{(1+0.87We_2^{1.67})^{0.6}} \tag{4.4}$$

$$\Omega\sqrt{\frac{\rho a^3}{\sigma}} = \frac{0.34+0.38We_2^{1.5}}{(1+Oh)(1+1.4Ta^{0.6})} \tag{4.5}$$

Where $Oh = \sqrt{We}/Re$ is the Ohnesorge number, $Ta = Oh\sqrt{We}$ is the Taylor number and $Re = \rho U^2 \mathrm{a}/\sigma$ is the Reynolds number. The footnote 1 and 2 mean the liquid phase and the gas phase respectively.

The KHRT breakup model is usually for high Weber number sprays, and thus also commonly used for diesel spray and combustion. It considers both the impact of Kelvin-Helmholtz waves driven by aerodynamic forces and the effect of Rayleigh Taylor instabilities caused by the acceleration of shed drops. Both mechanisms describe droplet breakup by tracking wave growth on the surface of the droplet and believe breakup occurs due to the local fastest growing instability. The KHRT breakup model also assumes that a liquid core exists in the near-nozzle region and introduces the Levich core length to model the breakup due to Kelvin-Helmholtz wave growth [170].

In the KHRT breakup model, child droplets are shed from the liquid core in the near-nozzle region and experience sudden acceleration when ejected into the freestream. The length of the liquid core (Levich core length) is obtained by:

$$L = C_L d_L\sqrt{\frac{\rho_l}{\rho_g}} \tag{4.6}$$

Where $C_L$ is the Levich constant which is a reference nozzle diameter. The Rayleigh-Taylor (RT) model is based on wave instabilities on the droplet surface. And the number of the fastest growing wave is

$$K_{RT} = \sqrt{\frac{-g_t(\rho_p-\rho_g)}{3\sigma}} \tag{4.7}$$

$g_t$ here is the droplet acceleration along the droplet track. The radius of the child droplets can be obtained by:

$$r_c = \frac{\pi C_{RT}}{K_{RT}} \tag{4.8}$$

where $C_{RT}$ is the breakup radius constant and has a default value of 0.1.

### *4.2.2. Model setup*

The surface injection is selected for the injection type. Both the Wave model and the KHRT model are selected as the breakup models. The breakup constants $B_0$ and $B_1$ are 0.61 and 20 in the Wave model, as literature [169] demonstrated that these values enable the model to predict the spray tip penetration and the SMD well simultaneous for spray and combustion in the diesel engine. To the KHRT model, literature [190] recommended to set the $B_0$ and $B_1$ to 0.61 and 18 because the configuration was proved to predict the spray tip penetration, local droplet size and droplet velocity with high accuracy. The initial droplet diameter at the inlet is set to 0.16mm, and the dynamic-drag is employed as the drag law. The RNG k-ε model and the Standard Wall Functions are selected for the viscous model and the near-wall treatment. The main properties of HVO at various temperature come from literature [176].

## 4.3. CFD model validation

### *4.3.1. Boundary conditions*

The CVV system in Chapter 3 is employed to provide the experimental data to validate the CFD model. In the CVV system, the hydrotreated vegetable oil (HVO) at 80 °C fuel temperature is injected at 1800 bar rail pressure, 100°C ambient temperature and 70 bar ambient pressure. The injection duration is 0.6 ms. The key properties of HVO are listed in Table 4.1.

| Fuel type | Density (kg/m$^3$) at 15 °C | Viscosity (mm$^2$/s) 40 °C | Surface tension (N/m) at 40 °C | Aromatics content | Cetane number | LHV (kJ/kg) |
|---|---|---|---|---|---|---|
| HVO | 780.1 | 3.02 | 0.0280 | 0 | 78 | 43902 |

Table 4.1. The main properties of HVO

The injection rate of the injector at 1800 bar rail pressure is obtained by an approximate method. The detailed procedure is shown below:

1) The total mass of injected fuel (M) at 1800 bar rail pressure and 0.6 ms injection duration is obtained by the injector calibration, which is the area beneath curve in Figure 4.3. And then mark the mass flow rate at $t_i$ and $t_{i+1}$ on the curve.

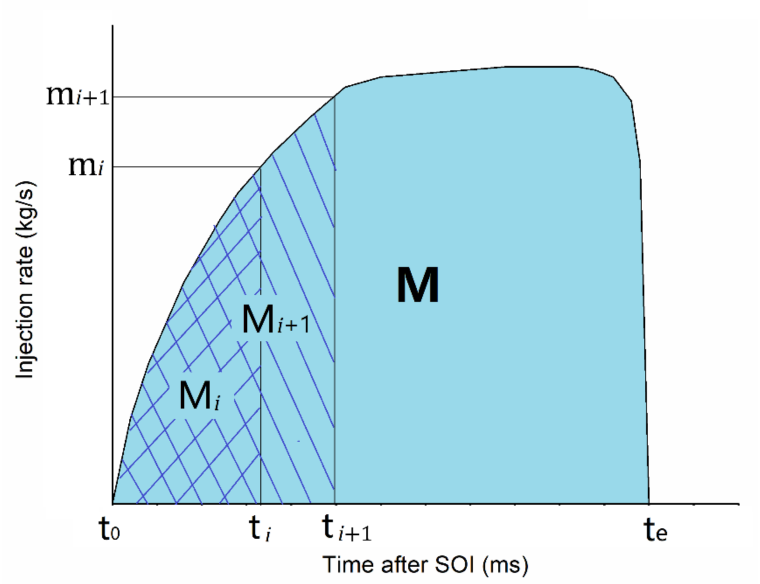

Figure 4.3. Calculation of injection rate

2) During experiment, we can obtain the spray tip penetration (L) and the width of the spray field (W) at $t_i$ and $t_{i+1}$, as shown in the figure below.

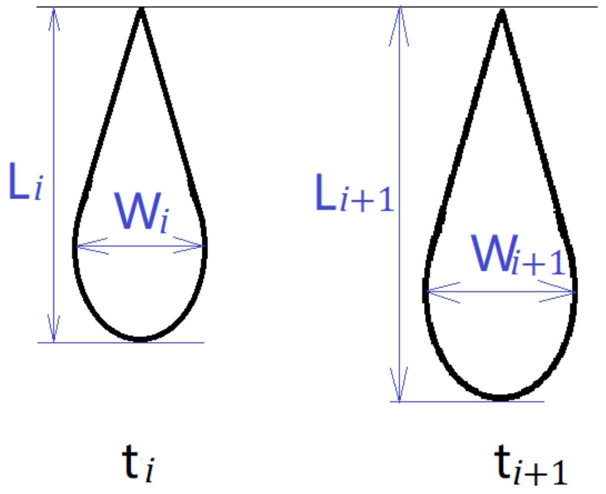

Figure 4.4. Illustration of penetration of width

3) Now we assume that the mass of injected fuel ($M_i$) by $t_i$ is proportional to the $L\cdot W^2$, which can be shown in the following function:

$$M_i = c \cdot L_i \cdot W_i^2 \tag{4.9}$$

Where *c* is constant, and the footnote *i* is the order of time.

4) If $t_i$ and $t_{i+1}$ are closed enough, we can obtain the following relationship:

$$M_{i+1} - M_i = (m_{i+1} + m_i) \cdot (t_{i+1} - t_i)/2 \quad (4.10)$$

5) Meanwhile, $M_i$ must also satisfy the equation below:

$$M = \sum_{i=0} (M_{i+1} - M_i) \qquad (4.11)$$

With the help of Microsoft Excel, we can obtain the $m_i$ which satisfies the Equation (4.9) to (4.11) at the same time. After smooth, we finally obtain the injection rate at 1800 bar rail pressure as shown in Figure 4.5.

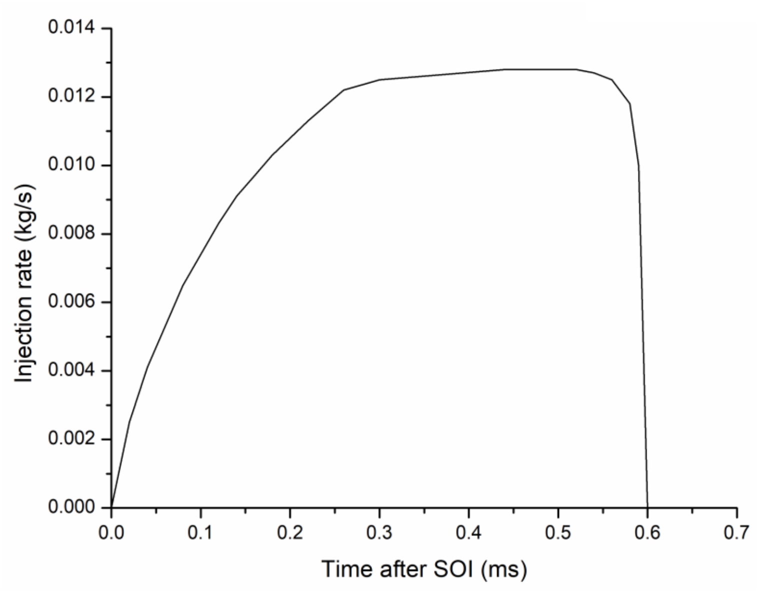

Figure 4.5. Injection rate at 1800 bar rail pressure

### *4.3.2. Validation of spray tip penetration and average cone angle*

The CFD model was run under the same condition as the experiments. Figure 4.6 illustrates the spray obtained by experimental and numerical method (Wave model) at 0.6ms after SOI, which also indicates the definition of the spray tip penetration and cone angle. Figure 4.7 and Figure 4.8 show the comparison of cone angle and spray tip penetration after SOI between experiments and the two breakup models at 1800 bar rail pressure, 100°C ambient temperature and 70 bar ambient pressure.

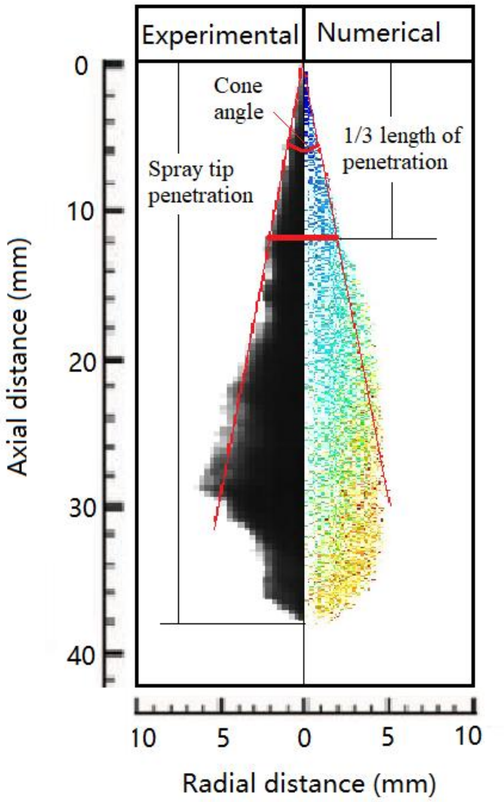

Figure 4.6. Comparison between the experimental and numerical (Wave model) spray at 1800 bar rail pressure, 100°C ambient temperature and 70 bar ambient pressure

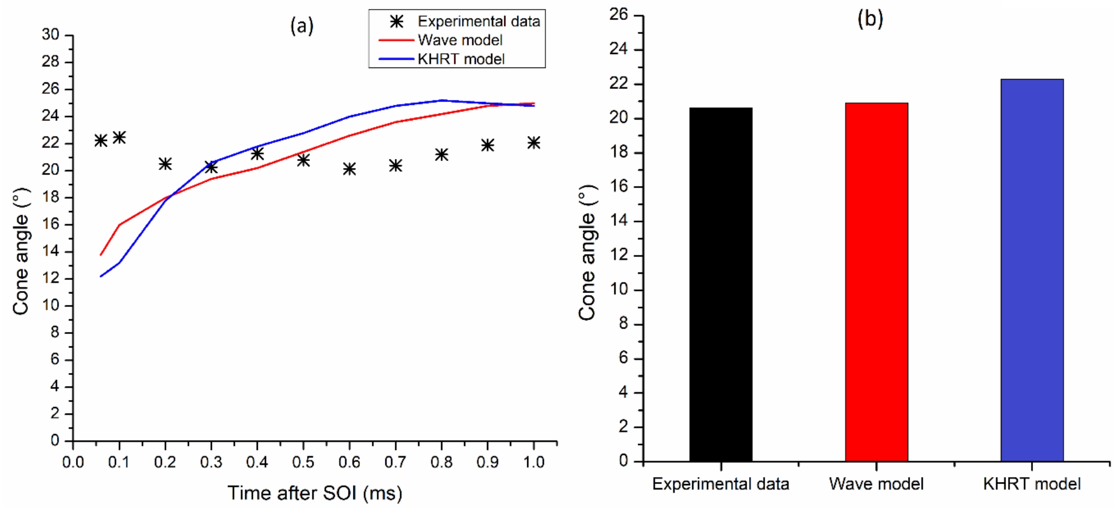

Figure 4.7. Comparison of cone angle (a) and average cone angle (b) between experimental and numerical results

As shown in Figure 4.7 (a), the experimental cone angle fluctuates and reaches its peak at about 0.1ms but stays within the range of 20.1° to 22° after 0.3ms. It indicates that the spray is not stable until about 0.3ms, as the flow rate of the injector is still increasing dramatically in this period. Literature [81] also explains that the time of the peak cone angle is the breakup time, before which the spray is yet fully developed and has a blob-like shape resulting in larger cone angle. In contrast, the predicted cone angles by the two breakup models both increase with sample time. The difference between the experimental cone angle and predicted cone angle can be attributed to the different impact of rail pressure on actual spray and the two breakup models for prediction. Previous research [78] demonstrated that the cone angle is not sensitive to injection pressure, which means increasing or decreasing injection pressure has no impact on cone angle. However, both the Wave model and the KHRT model consider the effects of Kelvin-Helmholtz (K-H) waves, which is influenced by the injection velocity and droplet surface tension. According to the injection rate, the injection velocity at the beginning of injection increase with time, and thus change the K-H waves to result in larger cone angle.

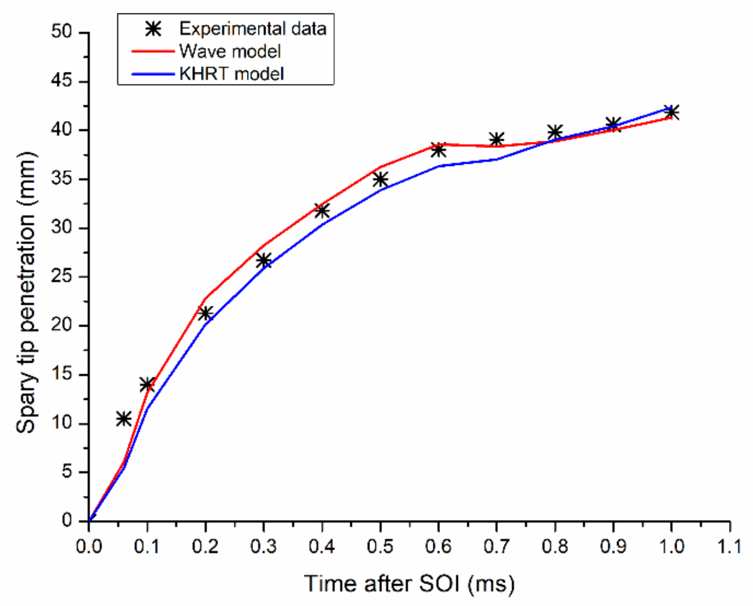

Figure 4.8. Comparison of spray tip penetration between experimental and numerical methods

As shown in Figure 4.8, the spray tip penetration obtained by experiments increases with sample time but the increasing rate is reducing. Spray tip penetrations predicted by both the Wave breakup model and the KHRT breakup model agree with the experimental data well. The bias of Wave model is within 10% in the whole duration except that before 0.1 ms, the breakup time, whilst the bias of KHRT model is slightly larger. Both models under-estimate penetration before breakup because the two models are both for secondary breakup whilst the actual breakup in this period still has not begun, which means less energy loss happens to droplets in actual spray than the predicted spray. During 0.6ms ~ 0.7ms, the penetration predicted by the Wave model experienced slight drop whilst that predicted by the KHRT model and the experimental data both grow slightly. It is possibly because the Wave model is mainly used for high-speed injections but the actual speed in this period reduced dramatically. Consequently, the actual droplet breakup significantly decays and results in shorter penetration than the predicted one by the Wave model. And the bias should only occur at relatively high ambient pressure and low ambient temperature, where the breakup is fiercer and changes more sharply once the injection stops.

Consequently, as recommended in previous study [81], the average cone angle between 0.3 ms and 0.6 ms is employed as a factor indicating spray quality in this study because the cone angle is relatively stable in this duration and the error of the predicted average cone angle for this period is also acceptable as shown in Figure 4.7 (b). Meanwhile, the predicted data of spray tip penetration from breakup time (no earlier than 0.1ms) is analysed by the Wave breakup model in the paper due to its higher precision.

## 4.4. Design of fuel and ambient conditions

Hiroyasu et al. [191] proposed the model of the spray tip penetration in the following equations:

$$S_1 = 0.39 \cdot (\frac{2 \cdot \Delta P}{\rho_f})^{\frac{1}{2}} \cdot t \qquad \text{when } t < t_b \tag{4.12}$$

$$S_2 = 2.95 \cdot (\frac{\Delta P}{\rho_a})^{\frac{1}{4}} \cdot \sqrt{d_0 \cdot t} \qquad \text{when } t \geq t_b \tag{4.13}$$

Where $\Delta P$ is the pressure drop across the outlet of the injector, $\rho_f$ is the density of the fuel, $\rho_a$ is the density of the air, and $d_0$ is the inner diameter of the injector. $t$ refers to the time after the SOI and $t_b$ is the breakup time. $S_1$ and $S_2$ are the length of spray tip penetration before and after the breakup, respectively.

Since the model of $S_1$ is of high accuracy, only the model of $S_2$ is being discussed here. Previous study [84] found the $S_2$ of Hiroyasu model is only validated at relatively low fuel pressure and low ambient pressure. Therefore, a more precise model for $S_2$ is in need.

As known, $\rho_a$ can be obtained by the ambient temperature $T_a$ and ambient pressure $P_a$, and the pressure drop $\Delta P$ is determined by the common rail pressure $P_r$ and ambient pressure $P_a$. Therefore, the spray tip penetration can be formulated by the rail pressure $P_r$, the ambient pressure $P_a$, the ambient temperature $T_a$, the inner diameter of the injector $d_0$ and time after SOI t. In this research, $d_0$ is constant, and thus Equation (4.13) can be re-written as:

$$S_2 = a \cdot {P_r}^b \cdot {P_a}^c \cdot {T_a}^d \cdot t^e \tag{4.14}$$

Where $a, b, c, d$ and $e$ are constant and will be obtained by calculations.

Table 4.2 lists all the fuel and ambient conditions for the CFD calculations, where the rail pressure, fuel temperature, ambient pressure and ambient temperature are all variables.

| Conditions | $P_r$ (bar) | $T_f$ (K) | $P_a$ (bar) | $T_a$ (K) |
|---|---|---|---|---|
| 1 | 600 | 300 | 70 | 700 |
| 2 | 600 | 300 | 10 | 300 |
| 3 | 600 | 300 | 70 | 300 |
| 4 | 600 | 300 | 10 | 700 |
| 5 | 600 | 300 | 26 | 458 |
| 6 | 600 | 387 | 10 | 458 |
| 7 | 600 | 387 | 26 | 458 |
| 8 | 600 | 387 | 26 | 300 |
| 9 | 600 | 387 | 26 | 700 |
| 10 | 600 | 387 | 70 | 458 |
| 11 | 600 | 500 | 26 | 458 |
| 12 | 600 | 500 | 70 | 300 |
| 13 | 600 | 500 | 10 | 700 |
| 14 | 600 | 500 | 10 | 300 |
| 15 | 600 | 500 | 70 | 700 |
| 16 | 1800 | 300 | 10 | 700 |
| 17 | 1800 | 300 | 70 | 300 |
| 18 | 1800 | 300 | 70 | 700 |
| 19 | 1800 | 300 | 26 | 458 |
| 20 | 1800 | 300 | 10 | 300 |
| 21 | 1800 | 387 | 26 | 458 |
| 22 | 1800 | 387 | 26 | 700 |
| 23 | 1800 | 387 | 70 | 458 |
| 24 | 1800 | 387 | 10 | 458 |
| 25 | 1800 | 387 | 26 | 300 |
| 26 | 1800 | 500 | 10 | 700 |
| 27 | 1800 | 500 | 10 | 300 |
| 28 | 1800 | 500 | 70 | 300 |
| 29 | 1800 | 500 | 70 | 700 |
| 30 | 1800 | 500 | 26 | 458 |

Table 4.2. Operating conditions

## 4.5. Results of CFD spray calculations

### *4.5.1. Macroscopic spray characteristics of HVO*

As the Wave breakup model is demonstrated more accurate than the KHRT model in the aforementioned context, only the Wave breakup model is used here to predict the spray tip penetration and the average cone angle at various conditions. As known, the spray tip penetration and cone angle are the most important macroscopic characteristics indicating the quality of spray, which is mainly determined by the breakup and evaporation of droplets. The breakup is a process breaking the balance between the dynamic force of the droplet and the viscosity and surface tension of the droplet. The dynamic force is determined by the momentum of droplets and the interaction with ambient gas. Therefore, penetration can be likely promoted by higher droplets velocity and higher fuel properties such as density, viscosity and surface tension, and reduced by higher ambient gas density and higher evaporation rate. In contrast, larger cone angle always occurs when a stronger breakup happens, but the evaporation may result in smaller cone angle. Usually, the shorter penetration and larger cone angle are expected for spray combustion in a diesel engine.

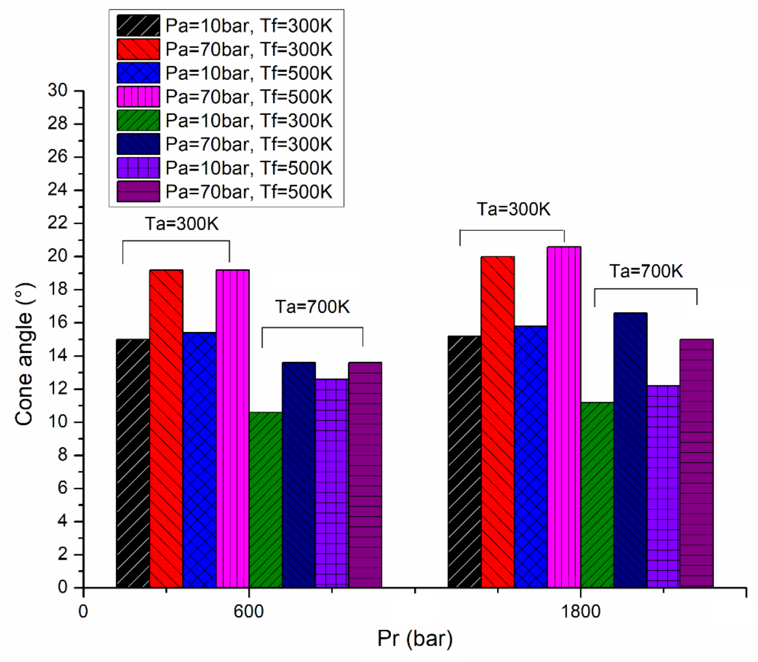

Figure 4.9. Average cone angle at various conditions

As cone angle is a relatively stable value against sample time during the injection, only the average cone angle between 0.3ms and 0.6ms after the SOI is considered to stand for the quality of spray, as shown in Figure 4.9. At cold ambient condition ($T_a$=300K), the cone angles at 1800 bar rail pressure are only slightly higher than those at 600 bar rail pressure and those at high ambient pressure are always smaller than those at low ambient pressure, which means ambient pressure is dominant and the impact of rail pressure on cone angle is not significant at cold ambient condition. However, at hot ambient condition ($T_a$=700K), the cone angle at 1800 bar rail pressure is closed to that at 600 bar when the ambient pressure is 10 bar, whilst it becomes higher when the ambient pressure is 70 bar. It indicates that at the hot ambient condition, the effect of evaporation is dominant at low ambient pressure, but is exceeded by that of breakup when ambient pressure rises. The fuel temperature can only increase the average cone angle at 10 bar ambient pressure and 700K ambient temperature due to more sufficient breakup.

However, when ambient pressure and rail pressure are 70 bar and 1800 bar respectively, smaller cone angle occurs at higher fuel temperature probably because the smaller droplets evaporate soon after breakup.

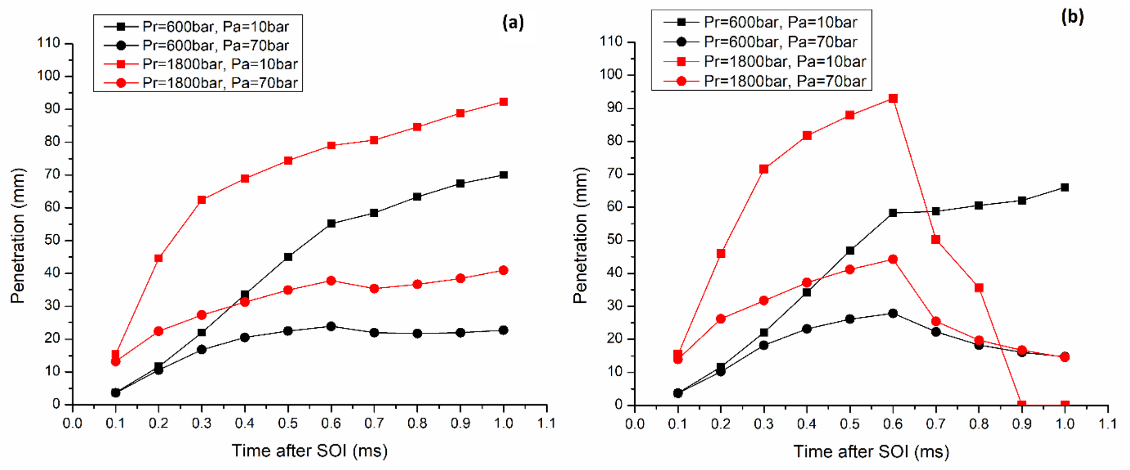

Figure 4.10. Effect of ambient pressure on spray tip penetration (a) $T_f$ =300K, $T_a$=300K (b) $T_f$=300K, $T_a$=700K

Figure 4.10 (a) and (b) indicates the spray tip penetration increase with sample time during the injection (0.1ms ~ 0.6ms) under all conditions, and the ambient pressure has an obviously negative impact on spray tip penetration. During the injection, the penetration at 10 bar ambient pressure is always much higher than that at 70 bar, due to its higher velocity of droplets. Moreover, the increasing rates of penetration at 1800 bar rail pressure are all higher than those at 600 bar at the beginning of injection (before 0.3ms) when the ambient pressures are 10 bar, whilst both rail pressures are almost the same during injection when the ambient pressure is 70 bar. The phenomena reveal that higher ambient pressure is beneficial to atomization. According to the force analysis of droplet, the higher density of the ambient gas (nitrogen) at high ambient pressure brings much larger dynamic drag force to droplets and thus promote droplets breakup to smaller droplets, whilst the impact of ambient pressure on droplet viscosity and surface tension is neglectable. It also agrees with the results in previous work [31], where the impinging effect was found dominant in breakup process. When the ambient pressure is 10 bar, the more injected fuel mass and higher initial velocity of droplets have the more significant impact on penetration than the ambient gas. However, when droplets eject to downstream, the impact of rail pressure decays and that of ambient pressure becomes dominant, which reduces the increasing rate of penetration after the EOI at the cold ambient condition, as shown in Figure 4.10 (a). In contrast, the impact of ambient gas at 70 bar is much stronger determines the droplet breakup at the cold condition. Therefore, the increase rate of penetration at two different rail pressures is similar to each other in Figure 4.10 (a). In general, when the ambient temperature is not high, the rail pressure dominates the fuel spray at the beginning of injection at low ambient pressure because it determines the initial velocity of droplets, whilst the high ambient pressure is more significant at both rail pressures during the whole injection due to its impact on droplets breakup.

In the post-injection period (after 0.6ms), the tendencies of penetration are more complicated because the impact of temperatures (fuel and ambient gas) also arises. At low temperatures, penetrations at low ambient pressure (10 bar) keep increasing with similar rates regardless of rail pressure. However, at high ambient pressure (70 bar) penetrations only increase slightly, as shown in Figure 4.10 (a). It indicates that the evaporation effect is not significant, so the fuel droplets can still penetrate forward driven by inertia and impacted by the ambient pressure. The penetrations at high ambient pressure both experience slight drop during 0.6ms ~0.7ms, similar to that in Fig. 6, which is caused by the bias on the breakup of Wave model. With the temperature increasing, the penetrations at the two rail pressure show different tendencies. As shown in Figure 4.10 (b), penetrations at 1800 bar rail pressure view dramatic drop at all ambient pressures after the EOI, whilst those at 600 bar rail pressure convert from a slight increase to gradually decrease. These phenomena reveal that evaporation plays the most important role in the post-injection period because the droplets have a rather low velocity and thus the impact of the rail pressure and ambient pressure weakens. As droplets at higher rail pressure and ambient pressure have smaller size due to more drastic breakup before EOI and thus become vapour sooner after the EOI than those at lower rail pressure and ambient pressure. Different increasing and decreasing rates at ambient pressure are mainly caused by the different droplet velocities at the EOI.

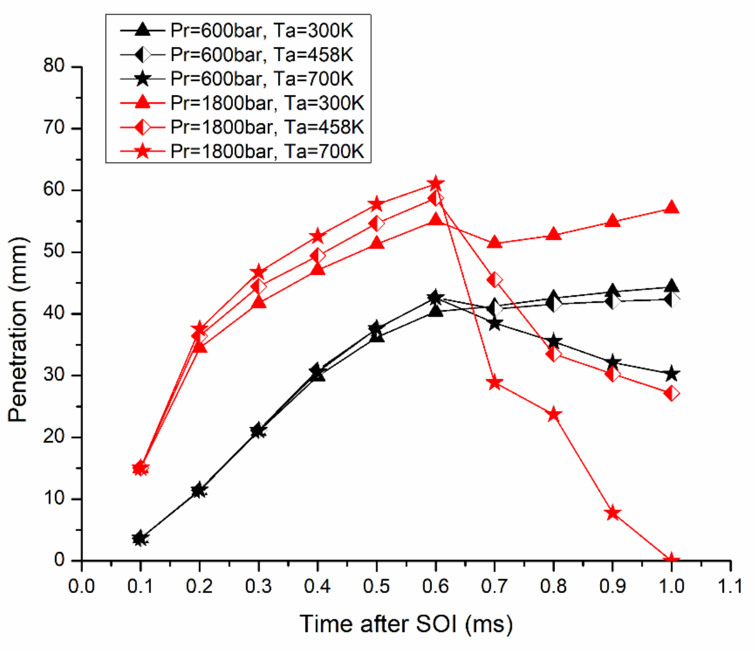

Figure 4.11. Effect of ambient temperature on spray tip penetration when $T_f$=387K and $P_a$=26 bar

The effect of ambient temperature on spray tip penetration at 387 K fuel temperature and 26 bar ambient pressure is shown in Figure 4.11. Results indicated the penetrations all increased with sample time during injection but shown different tendencies after the EOI. During injection, penetrations at 1800 bar rail pressure increase with increasing ambient temperature during the injection, whilst those at 600 bar rail pressure have no obvious difference in this period. It indicates that the fuel injected at 1800 bar can penetrate longer distance at higher ambient temperature because the density of ambient gas decreases at the higher temperature and constant pressure. Nevertheless, the effect of ambient temperature is not significant when the rail pressure is low because the initial droplet velocity is not high enough so that the impact of ambient gas density on droplets is not significant. It is also shown in Figure 4.11 that penetrations at both rail pressures change from a slight increase to sharp drop with increasing ambient temperature after the EOI and the decreasing rate is larger at higher rail pressure. It means ambient temperature becomes the dominant factor in the post-injection period, which is probably because droplets can no longer break up after the EOI and only evaporate and diffuse to the ambient gas. The larger decreasing rate of penetration at 1800 rail pressure is due to the smaller droplet size produced by more severe breakup during injection.

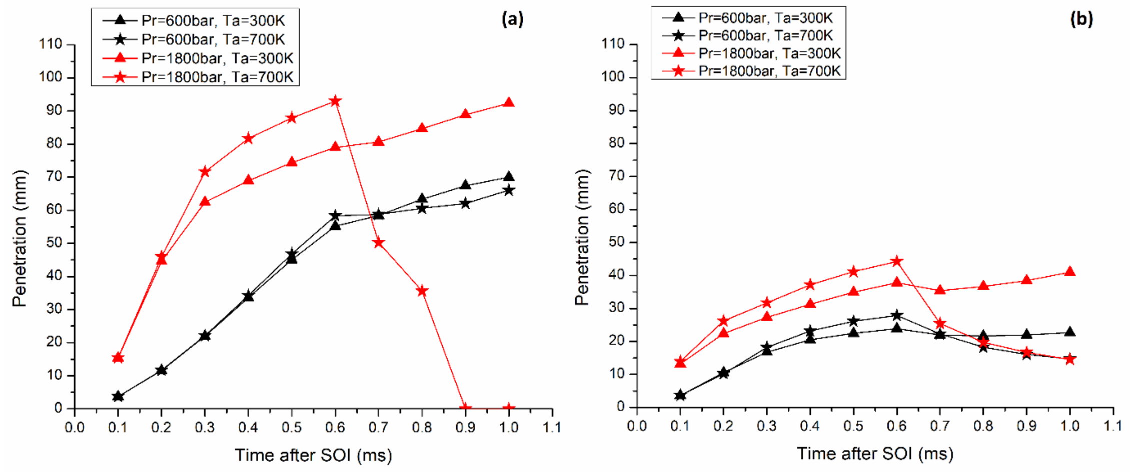

Figure 4.12. Effect of ambient temperature on spray tip penetration (a) $T_f$=300K, $P_a$=10 bar (b) $T_f$=300K, $P_a$ =70 bar

When the ambient pressure reduces to 10 bar (a) or increases to 70 bar (b), the impact of ambient temperature on penetrations of fuel injected at 1800 bar is quite similar as shown in Figure 4.12. Spray tip penetration at higher ambient temperature is longer than that at lower ambient temperature during the injection, and then the penetration at lower ambient temperature keeps increasing gradually but that at high temperature decreases dramatically. As the density of ambient gas reduces with increasing temperature at constant pressure, the dynamic drag force on injected fuel droplets becomes weaker and thus results in longer penetration. Meanwhile, as the velocity of the droplet during injection is quite high, the amount of evaporated fuel is not comparable in such short duration. After the injection, the velocity of droplets slows down soon at high ambient pressure and then evaporation starts to play a more important role in penetration proceeding, whilst the impact of evaporation is comparable with that of ambient pressure at 10 bar because the velocity of droplets is higher and decreases slower under this condition.

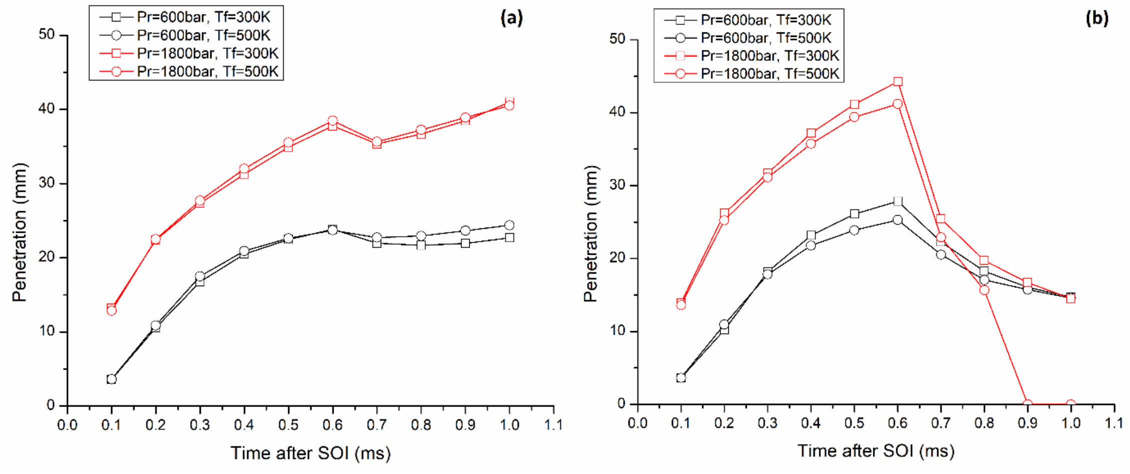

Figure 4.13. Effect of fuel temperature on spray tip penetration (a) $P_a$=70 bar, $T_a$=300K (b) $P_a$=70 bar, $T_a$=700K

From Figure 4.13 (a), the penetrations at the two different fuel temperatures are almost the same at either rail pressure during injection, because the velocity of the droplet is fast, and the ambient temperature is low (300K). As a result, the dynamic force on droplets is dominant compared to the small evaporation rate under this condition. After the EOI, the penetrations at 1800 bar rail pressure do not show the difference with varying fuel temperature, because the initial droplets velocity during post-injection is still very high at 1800 bar rail pressure. However, fuel injected at 600 bar has different penetrations, which increase slightly at high fuel temperature instead of decreasing. It is inferred that the hot droplets warm up the local ambient gas and thus the density of ambient gas around the droplets reduces slightly and results in a bit longer penetration.

In contrast, when the ambient temperature is 700 K in Figure 4.13 (b), the effect of evaporation is significantly enhanced and becomes dominant after the EOI. Consequently, the penetrations in the injection period experience a slight decrease with increasing fuel temperature and the decrease becomes more significant in the post-injection period reduce at both rail pressures.

### *4.5.2. DoE models of spray tip penetration*

As previously discussed, the penetration model after the breakup time is formulated by DoE method to correlate independent variables (rail pressure, fuel temperature, ambient pressure and ambient temperature) to response (spray tip penetration). Given the results above, spray tip penetrations before and after the end of injection (EOI), which can also be called injection and post-injection respectively, are quite different. Therefore, two models were formulated for penetrations in the two periods (except those before breakup). As shown in Table 4.3, an analysis of variance (ANOVA) is thus performed to investigate the fitness and significance of the formulated models and each variable.

| Factor | R1 | | R2 | |
|---|---|---|---|---|
| | F-value | P-value | F-value | P-value |
| Model | 525.17 | 0.0001 | 82.31 | 0.0001 |
| A | 522.59 | 0.0001 | not significant | not significant |
| B | not significant | not significant | 3.24 | not 0.0738 |
| C | 158.89 | 0.0001 | 220.86 | 0.0001 |
| D | 3.43 | 0.0657 | 65.20 | 0.0001 |
| E | 1416.64 | 0.0001 | 39.71 | 0.0.0001 |
| $R^2$ | 0.9231 | | 0.6942 | |
| Adj $R^2$ | 0.9213 | | 0.6858 | |
| Pred $R^2$ | 0.9180 | | 0.6686 | |
| Adeq Precision | 86.142 | | 35.071 | |

Table 4.3. ANOVA of experimental factors and the models

The factor A, B, C, D and E are the rail pressure ($P_r$), fuel temperature ($T_f$), ambient pressure ($P_a$), ambient temperature ($T_a$) and the sample time ($t$), whilst the R1 and R2 stand for the spray tip penetration during injection and post-injection respectively. The F-value represents the comparison between the model variance (Regression) and its residual (error) variance. A high F-value (>1) is acceptable because it means the regression is much larger than the residual. The P-value is the probability that a factor has no effect on the response even though the F-value is high. A P-value of less than 0.05 means the factor is significant to the response, but a P-value larger than 0.1 implies the factor is insignificant. Usually, it is overall significant when the P-value of a model is less than 0.05 and that of each factor is less than 0.1. In this study, the models have the F-value of 525.17 and the P-value of 0.0001 to R1, whilst those of R2 are 82.31 and 0.0001 respectively. It means the model is significant to predict the spray tip penetration during injection and post-injection periods, and only 0.01% chance that the F-values of 525.17 and 82.31 occur due to noise. Moreover, factors A, C and E all have large F-values and small P-values to R1, which indicates the spray tip penetration during injection is significantly impacted by the rail pressure ($P_r$), ambient pressure ($P_a$) and sample time ($t$). Similarly, the rail pressure ($P_r$), ambient pressure ($P_a$), ambient temperature ($T_a$) and sample time ($t$) have a significant impact on the spray tip penetration in the post-injection period because the F-values are all larger than 1 and P-values are all smaller than 0.1.

The $R^2$ is a measure of the amount of variation around the mean explained by the model, and the Adj $R^2$ is that adjusted to compensate for the addition of variables to the model. High $R^2$ (close to unity) and Adj $R^2$ are acceptable for the model. The Pred $R^2$ is used to measure how good the model can predict new response values. The model is statistically sound if the difference between the Pred $R^2$ and Adj $R^2$ is within 0.2. The Adeq Precision is a signal-noise ratio and is usually desirable when it is larger than 4 [192]. In this research, the models of R1 and R2 have high $R^2$, Adj $R^2$ and Adeq Precision, and the differences between the Pred $R^2$ and Adj $R^2$ are small, which indicates the two models are accurate in predicting the spray tip penetrations at both injection and post-injection periods.

The ANOVA provides an overall evaluation of the influence of each factor on spray characteristics, and gives suggestions of improving spray quality by controlling these factors. During injection, the rail pressure and ambient pressure are the most significant factors influencing spray tip penetration, and the influence of ambient temperature is weaker, whilst the fuel temperature has no impact on the spray tip penetration. During post-injection, rail pressure no longer affects spray tip penetration. The ambient temperature and ambient pressure become the most significant factor, and fuel temperature can also influence spray tip penetration.

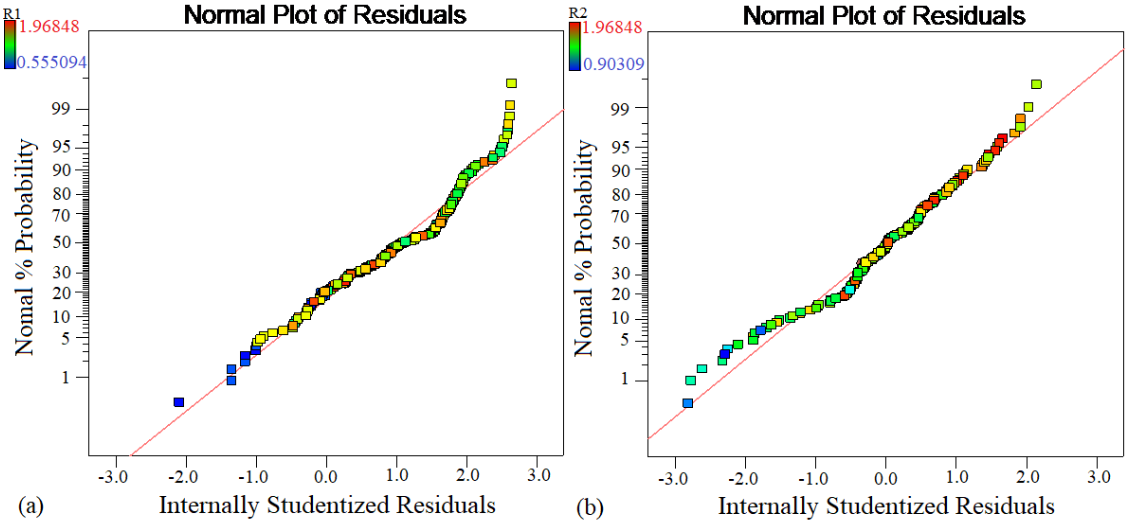

Figure 4.14. Normal probability plots of residuals for R1 (a) and R2 (b)

The normal probability plot in Figure 4.14 indicates whether the residuals follow a normal distribution, where the points follow a straight line. Figure 4.14 shows that the points of R1 and R2 narrowly scatter around the straight lines. It reveals that the residuals for R1 and R2 follow normal distributions well and the derived models will not be improved by any transformation to R1 and R2, which in other words means the models are valid.

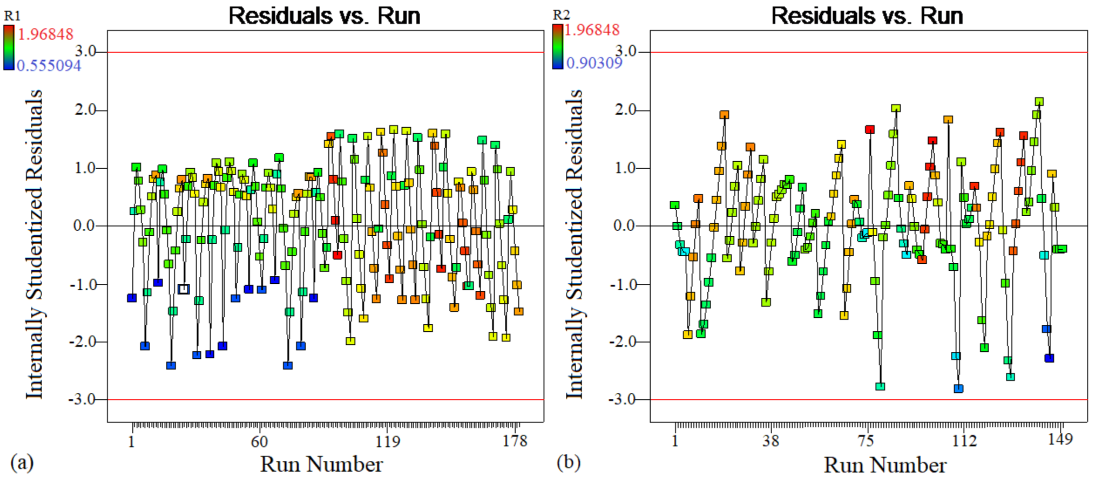

Figure 4.15. Residuals of R1 (a) and R2 (b) versus the run order

The residuals versus run plots are employed to find lurking time-related variables that may influence the response. A random scatter means no systematic effect on the response is caused by the run order and is thus desirable. As shown in Figure 4.15, the residuals of R1 and R2 have no evident trends associated with the run order, which reveals the possibility can be excluded that R1 and R2 are impacted by any time-dependent factors.

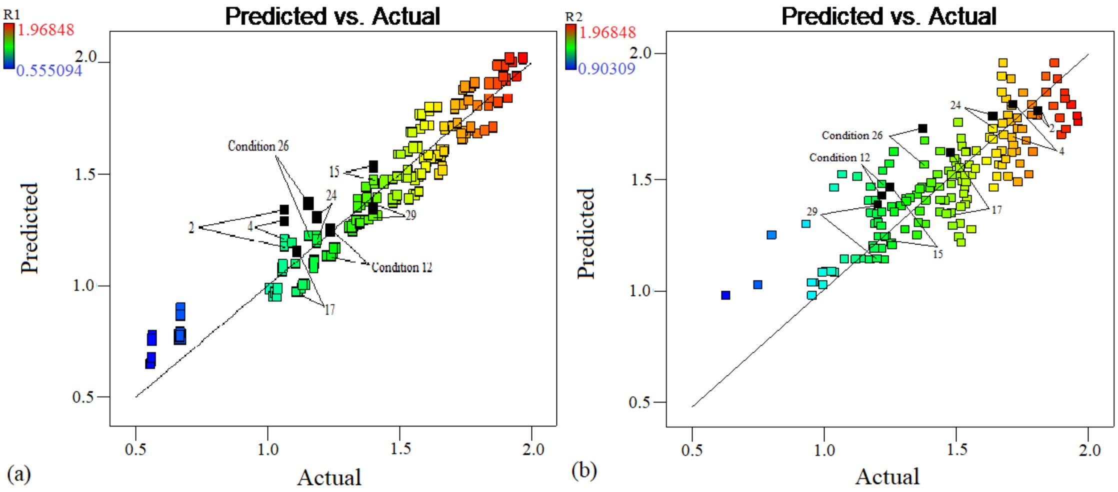

Figure 4.16. The predicted values of R1 (a) and R2 (b) versus actual values

Figure 4.16 is the comparison between the actual values and predicted values by the DoE models of R1 and R2. It means the models are precise if most scatter points are located closed to the central line in the graphs. According to the distribution of the coloured point in Figure 4.16, the derived DoE models are precise to predict R1 and the precision for R2 is lower.

After the analysis of variance (ANOVA) and the diagnostics, the coded Equation (4.15) and (4.16) are obtained to quantitively analyse the effect of each factor on responses regardless of its unit. In the coded equations, factors A, B, C, D and E are coded to the interval of [-1, 1] as shown in Table 4.4.

| Variable | Factor | R1 | | R2 | |
|---|---|---|---|---|---|
| | | -1 | 1 | -1 | 1 |
| $\log_{10} P_r$ | A | 2.778 | 3.255 | 2.778 | 3.255 |
| $\log_{10} T_f$ | B | 2.477 | 2.699 | 2.477 | 2.699 |
| $\log_{10} P_a$ | C | 1 | 1.845 | 1 | 1.845 |
| $\log_{10} T_a$ | D | 2.477 | 2.845 | 2.477 | 2.845 |
| $\log_{10} t$ | E | -1 | -0.223 | -0.223 | 0 |

Table 4.4. The coded factors and the levels in the analysis on R1 and R2

$$R_1 = 1.33 + 0.16 \cdot A - 0.11 \cdot C + 0.016 \cdot D + 0.4 \cdot E \tag{4.15}$$

$$R_2 = R_2 = 1.57 - 0.022 \cdot B - 0.18 \cdot C - 0.1 \cdot D - 0.09 \cdot E \tag{4.16}$$

The coefficients of the coded equations stand for the importance of corresponding factors: A positive value indicates a synergistic effect, whilst a negative value means an antagonistic effect, and the absolute value indicates the significance to the R1 and R2. As illustrated in the coded equations, factor A has a synergistic effect on R1 and R2, whilst C has an antagonistic effect. D is the most significant factor in reducing R2 but has no significant effect on R1. These phenomena also agree with the results in Figure 4.10 ~ Figure 4.13.

The uncoded models reveal the actual correlation between the spray tip penetration and independent variables:

$$\log_{10} \mathrm{S} = 0.034177 + 0.6813 \cdot \log_{10} P_r - 0.25976 \cdot \log_{10} P_a + +0.087668 \cdot D + 1.01863 \cdot \log_{10} t, \qquad t_b < t < t_{EOI} \tag{4.17}$$

$$\log_{10} S = 4.05892 - 0.20026 \cdot \log_{10} T_f - 0.43379 \cdot \log_{10} P_a - 0.54129 \cdot \log_{10} T_a - 0.80936 \cdot \log_{10} t\,, \qquad t > t_{EOI} \tag{4.18}$$

Where $P_r$, $T_f$, $P_a$, $T_a$ and $t$ refer to the rail pressure (bar), ambient pressure (bar), ambient temperature and sample time. $S$ refers to the spray tip penetration. The $t_b$ and $t_{EOI}$ are the time of breakup and the end of injection (EOI) respectively. Therefore, the final form of the spray tip penetration models can be described below:

$$S = 1.0819 P_r^{0.6813} P_a^{-0.25976} T_a^{0.087668} t^{1.01863}, \qquad t_b < \mathrm{t} < t_{EOI} \tag{4.19}$$

$$S = 11453.0195 T_f^{-0.20026} P_a^{-0.43379} T_a^{-0.54129} t^{-0.80936}, \quad t > t_{EOI} \qquad (4.20)$$

The main differences between the DoE models and other empirical models are twofold: first, the DoE models can describe the spray tip penetration during the post-injection period; second, the effect of evaporation is taken into account in the DoE model, as it includes the factor of ambient temperature and fuel temperature. Figure 4.16 also compares the precision of the DoE model and the Hiroyasu model, where the black scatter points are the results of the Hiroyasu model and the coloured ones are the DoE model. As Figure 4.16 is the comparison between the predicted values by models and the actual values, more closed location of the points to the central line usually indicates a more precise model. Accordingly, at cold ambient condition (e.g., Condition 12, 17 and 29), where the evaporation is not significant, the DoE model has lower precision than the Hiroyasu model. However, when the ambient temperature rises and evaporation becomes significant (e.g., Condition 2, 4, 15, 24 and 26), the precision of DoE model exceed that of Hiroyasu model during the whole injection process.

The perturbation plot is employed as a comparison among the effects of all factors at a certain point (usually the midpoint) under all conditions. In the perturbation plots, the responses are plotted by varying one factor and fix others. Therefore, a steep slope of a factor means the response is sensitive to it, whilst a flat line indicates insensitivity.

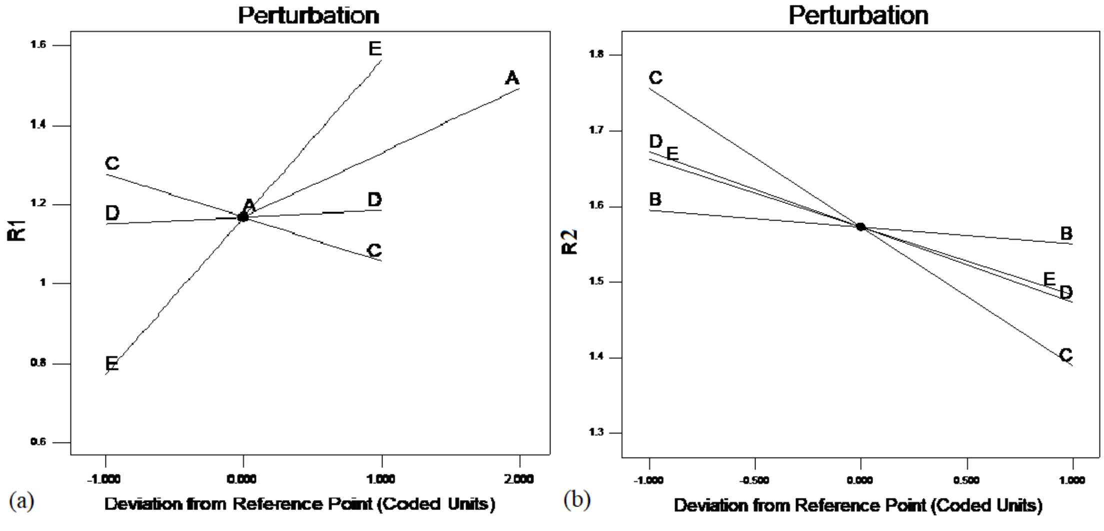

Figure 4.17. Perturbation plots of the R1 (a) and R2 (b) models

According to the slop of each line in Figure 4.17, the spray tip penetration during injection is easily increased by rail pressure and sample time and slightly increased by ambient temperature, but reduced by ambient pressure. During post-injection, ambient pressure, ambient temperature can significantly reduce spray tip penetration with sample time, and fuel temperature can only slightly reduce spray tip penetration. The results are also in consistency with the phenomena in Figure 4.10 ~ Figure 4.13.

## 4.6. Summary of Chapter 4

In this Chapter, a CFD model is established to investigate the macroscopic characteristics of HVO at various fuel and ambient conditions. Furthermore, the DoE models of spray tip penetrations during injection and post-injection periods are formulated to quantitively correlate the spray tip penetration with the fuel temperature, rail pressure, ambient temperature and ambient pressure. The main conclusions are drawn as follows:

- The Wave model is better than KHRT model and it can predict the spray tip penetration and average cone angle well compared with the experimental data.
- The average cone angle becomes larger at high ambient pressure, and the impact of ambient pressure can be weakened by increasing ambient temperature at 600 bar rail pressure but improved at a high ambient temperature and 1800 bar rail pressure.
- During the injection period, the spray tip penetration can be significantly promoted by higher rail pressure and lower ambient pressure at all conditions due to the promotion to droplets breakup. The ambient temperature and fuel temperature only have small influence.
- During the post-injection period (after the EOI), penetrations at most conditions significantly decrease when increasing ambient temperature and fuel temperature because evaporation dominates this period.

The spray characteristics of HVO at some conditions in this chapter are more closed to those in the CI engine cylinder. Furthermore, the influence of increasing temperature on spray invokes the idea that 'what if the fuel temperature is over its critical temperature?', which would be explored in Chapter 6. The influence of fuel condition and ambient condition on the macroscopic spray characteristics of HVO is summarised in Table 4.5.

| Factor | $P_r$ | $T_f$ | $P_a$ | $T_a$ |
|---|---|---|---|---|
| Cone angle | N/A | +<br>(at low $P_a$ and high $T_a$) | + | - |
| Spray tip penetration (Injection) | + | -<br>(at high $T_a$) | - | + |
| Spray tip penetration (Post-injection) | N/A | -<br>(at high $T_a$) | - | - |

Table 4.5. Summary of the influence of all factors on macroscopic spray characteristics

*'+' means the growing value of the factor will increase the corresponding result, and '-' means the growing value of the factor will decrease the corresponding result, whilst 'N/A' indicates the factor has no comparable impact on the corresponding result.

# Chapter 5 . Engine performance

As investigation on spray in Chapter 3 has demonstrated $CeO_2$ nanopowder cannot change fuel physical properties significantly, its potential influence on engine performance should be attributed to chemical mechanisms. In terms of renewable fuels and CNT, they are demonstrated to influence spray characteristics in Chapter 3 and 4w, and thus their impact on engine performance might be comprehensive. Therefore, in this chapter, the in-cylinder behaviour and pollutant emissions of renewable fuels and nano additive modified fuels are investigated to estimate their benefits to the engine and analyse the impact of the size of nano additives. The multi wall carbon nano tubes (CNT) and Cerium Oxide ($CeO_2$) nanopowder with the maximum size of 25nm (Ce25) and 50nm (Ce50) are employed as nano additives to modified the standard diesel engine and renewable fuels.

## 5.1. Engine test rig

The engine employed in this project is a Cummins ISB4.5 heavy-duty four-stroke diesel engine, which is equipped with a common rail system providing maximum 1800 bar pressure, four solenoid eight-hole injectors and a wastegate turbocharger. The specifications of the diesel engine are listed in Table 5.1.

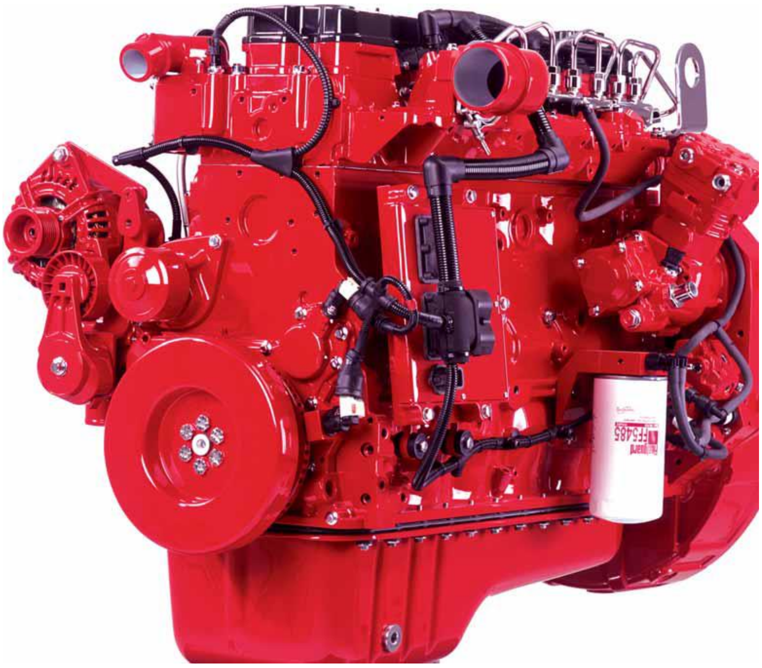

Figure 5.1. Experimental diesel engine

| Parameter | Value |
|---|---|
| Engine model | ISB4.5 |
| Displacement (L) | 4.5 |

| | |
|---|---|
| Number of cylinders | 4 |
| Stroke length (mm) | 124 |
| Bore size (mm) | 107 |
| Compression ratio | 17.3 |
| Injection method | Common rail direct injection |
| Injection pressure (bar) | 1800 bar |
| Injector type | Solenoid eight-hole injector |
| Aspiration | Wastegate turbocharger |
| Speed (rpm) | 800 ~ 2500 |
| Torque (Nm) | Max 760 at 1400 ~ 1800 rpm |
| Power (kW) | Max 152 at 2300 rpm |
| Emission standard | Euro V |

Table 5.1. Specifications of experimental diesel engine

As illustrated in Figure 5.2, the engine is connected with a DSG 230kW eddy current dynamometer to control the speed and torque. The mas flow rate of the fuel is measured by a Promass 80 Coriolis flow meter. An AVL 365C crank angle encoder is assembled at free end of the crank shaft to record the crank angle every 0.5 degree, as it detects 720 light pulses generated by a marker disk during one cycle. The in-cylinder pressure of the third cylinder is monitored by an AVL QC34C high-speed pressure transducer. The sensor is water-cooled to ensure long lifetimes and can measure up to 250 bar pressure with the frequency of maximum 69 kHz. The detected signals are amplified to -10 V to 10V by an AVL 2P2E channel amplifier and then acquired by a National Instrument (NI) DAQ card PCI-6251 connected to a computer. 16 analogue inputs of 16-bit resolution are designed on the card with 1.25 MS/s for 1 channel mode or 1 MS/s with multi-channel mode. Meanwhile, 24 digital input/output channels are available at 10 MHz. Due to two TDC signals in one cycle, the camshaft signal is to determine the TDC before the air intake stroke.

A wastegate turbocharger is mounted after the exhaust manifold to increase the engine efficiency and power by compressing more air into the cylinder. The wastegate is a bypass valve which is controlled by an actuator according to the configuration of ECU. Consequently, the turbine and compressor speeds can be adjusted by diverting exhaust gas away from the turbine. After the turbocharger, the temperature of exhaust gas reduces from about 700 °C to less than 350 °C. And then the pollutant emissions and particulate matters emissions are measured by a gas analyser and a particle counter.

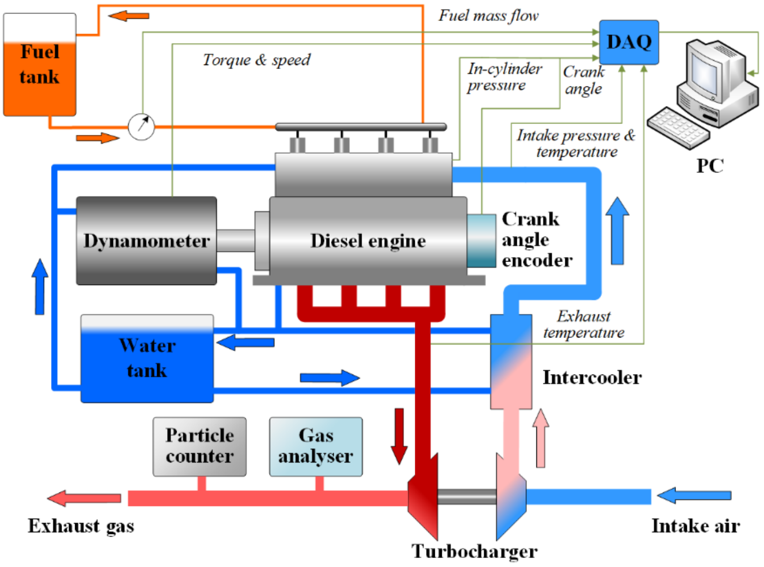

Figure 5.2. Layout of the engine test rig

A Horiba MEXA 1600D gas analyser is employed to measure gaseous pollutant emissions in this project, as shown in Figure 5.3. It directly samples gas from the main stream of exhaust and then heats it to 190 °C as emission standards require. The air-fuel ratio (AFR) is calculated at the same time. The instrument consists of three modules to measure different gas compositions. The AIA-260 analyser measures the CO and $CO_2$ concentrations via the non-dispersive infrared (NDIR) method, as different gas molecules absorb infrared energy of different wavelengths and the extent of absorption is proportional to gas concentration at constant pressure. Considering the high concentration of water vapour, the gas sample is dehumidified in the sample handling system (SHS) prior to the analyser to avoid interference during measurement. The FCA-266 measures HC and $NO_x$ concentration in the exhaust gas. The information of HC concentration is obtained via flame ionisation detection (FID), where the sample gas is mixed with the $H_2$ and then burns with oxygen in a burner. The hot $H_2$ flame produces ions which are proportional to the amount of carbon atoms in the sample, and the ions then migrate to the electrodes to generate electrical signals. $NO_x$ concentration is measured by chemiluminescence, which stimulates NO molecules to higher energy level and then release light during attenuation. Therefore, the NO concentration can be obtained as the intensity of light is proportional to it.

Figure 5.3. Horiba 1000SPCS (left) and Horiba MEXA 1600D (right)

A Horiba 1000SPCS particle counter is employed to measure particulate number (PN). It consists of a primary diluter (PND1), an evaporation tube (ET), a secondary diluter (PND2) and a condensation particle counter (CPC) as shown in Figure 5.4. The exhaust gas flows through the PND1 first to filter out coarse particles, and is heated to 150 °C to remove volatile particles. Then, it is further heated to 300 ~ 400 °C in the ET to remove all volatile compositions, after which the hot aerosol is diluted by cool air in the PND2 to prevent condensation. Finally, particles are surrounded by the condensed butanol vapour and thus grow larger to be detected by laser beam. As a result, particles between 23 nm and 10 µm can be measured. The range and accuracy of all instruments above are listed in Table 5.2.

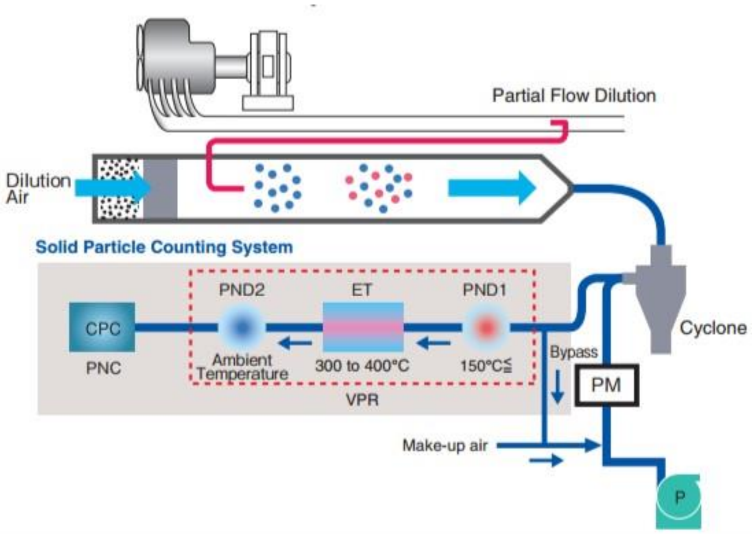

Figure 5.4. Schematic and principle of Horiba 1000SPCS [193]

| Instrument | Measuring range | Accuracy |
|---|---|---|
| DSG dynamometer | 0 ~ 750 Nm | ± 1 Nm & ±10 rpm |
| AVL 365C crank angle encoder | 0 ~ 20000 rpm | ±0.5° |
| AVL QC34C pressure transducer | 0 ~ 250 bar | ±0.2 bar |
| Horiba MEXA 1600D gas analyser | 3000 ppm (CO)<br>5000 ppm ($NO_x$)<br>1000 ppm (HC) | ±1% |
| Horiba SPCS 1000 CPC | 23〜10000nm | ±10% |
| Thermocouples | 0 ~ 1200 °C | ±0.75% |
| Promass 80 flow meter | 0 ~ 2000 kg/h | ±0.15% |

Table 5.2. Measuring range and accuracy of instruments

The water cooling system is used to cool down the engine, dynamometer, lubrication oil, and intake air. The water of maximum 40 °C is driven by a PENTAX CM90 pump to flow through the whole system and return to the water tank within 80 °C. As a result, the inlet air temperature of the engine and outlet water temperature of the dynamometer can be maintained within 50 °C and 65 °C respectively, beyond which the alarm will run. Moreover, the engine would be automatically shut down if the water temperature is over 70 °C. The water pressure remains no higher than 0.5 bar to provide flow rate of water and security of parts.

| Parameter | Value |
|---|---|
| Power (kW) | 0.75 |
| Size of inlet & outlet (mm) | 25 |
| Volume flow rate (L/min) | 20 ~ 90 |
| Delivery head (m) | 1 ~ 22 |

Table 5.3. Specification of water pump

Parameters such as oil temperature and air intake pressure etc. are detected by pressure sensors and thermocouples as shown in Table 5.4. These signals are collected via a National Instrument data acquisition card PCI-6251 and sent to a PC running a DSG DaTAQ Pro system.

| Sensor | Location | Code | Range | Accuracy |
|---|---|---|---|---|
| Block water pressure | At engine block | PTX 1 | 0 ~ 2.5 bar | ±0.1 bar |
| Air intake pressure | In air intake manifold | PTX 2 | 0 ~ 5 bar | |
| Oil pressure | After oil filter | PTX 3 | 0 ~ 10 bar | |
| Crankcase pressure | At blowby hose | PTX 4 | 0 ~ 2.5 bar | |
| Exhaust restriction pressure | In exhaust manifold | PTX 5 | 0 ~ 5 bar | |
| Water inlet temperature | At Water inlet pipe | T0001 | 0 ~ 1200 °C | ±0.75% |
| Water outlet temperature | Water outlet pipe | T0002 | | |
| Oil temperature | Below oil pan | T0003 | | |
| Air intake temperature | At air intake manifold | T0004 | | |
| Fuel temperature | At fuel outlet hose | T0005 | | |
| Intercooler water out temperature | After intercooler water side | T0006 | | |
| Exhaust gas temperature | At exhaust manifold | T0007 | | |
| Dyno cooling water temperature | At dyno cooling outlet hose | T0008 | | |
| Fuel return temperature | After fuel return cooler | T0009 | | |

Table 5.4. Pressure and temperature sensors in the engine test rig

## 5.2. System monitor and control software

DSG DaTAQ Pro system is a sophisticated software, which controls most parameters of the engine, dynamometer, fuel delivery system and water cooling system. It supports maximum 512 input channels including both low and high speed analogue inputs such as fuel flow rate, temperature, pressure, speed and torque with the sampling rate of maximum 40 kHz. The software enables several modes to control the throttle and dynamometer, as the throttle can be operated by the signal from the ECU. During experiments, the throttle is usually set to speed mode and the dynamometer stays at the torque mode. Then, the user can configure either the torque or the speed individually to obtain a steady engine state via the PID control. Accordingly, the user can write a program of a sequence of points containing speed, torque, duration etc. on the DSG DaTAQ Pro system. By this means, the engine test rig can automatically run the sequence of points (engine conditions) via the program. And the data of the engine condition and parameters detected by sensors are saved during running.

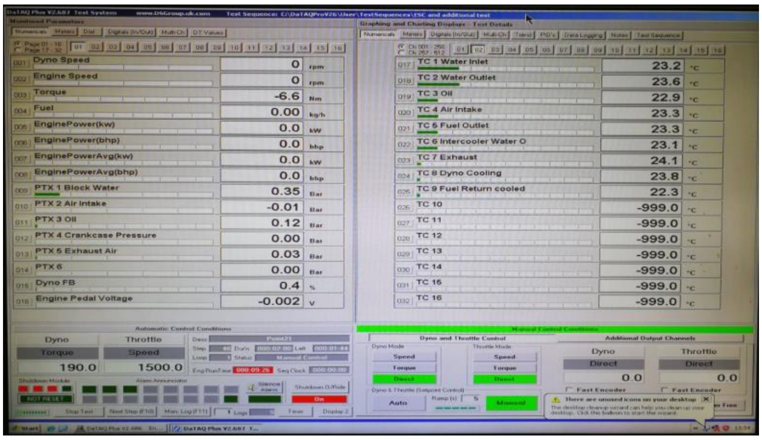

| | | | |
|---|---|---|---|
| 001 | Dyno Speed | 0 | rpm |
| 002 | Engine Speed | 0 | rpm |
| 003 | Torque | -6.6 | Nm |
| 004 | Fuel | 0.00 | kg/h |
| 005 | EnginePower(kw) | 0.0 | kW |
| 006 | EnginePower(bhp) | 0.0 | bhp |
| 007 | EnginePowerAvg(kw) | 0.0 | kW |
| 008 | EnginePowerAvg(bhp) | 0.0 | bhp |
| 009 | PTX 1 Block Water | 0.35 | Bar |
| 010 | PTX 2 Air Intake | -0.01 | Bar |
| 011 | PTX 3 Oil | 0.12 | Bar |
| 012 | PTX 4 Crankcase Pressure | 0.00 | Bar |
| 013 | PTX 5 Exhaust Air | 0.03 | Bar |
| 014 | PTX 6 | 0.00 | Bar |
| 015 | Dyno FB | 0.4 | % |
| 016 | Engine Pedal Voltage | -0.002 | V |

| | | | |
|---|---|---|---|
| 017 | TC 1 Water Inlet | 23.2 | °C |
| 018 | TC 2 Water Outlet | 23.6 | °C |
| 019 | TC 3 Oil | 22.9 | °C |
| 020 | TC 4 Air Intake | 23.3 | °C |
| 021 | TC 5 Fuel Outlet | 23.3 | °C |
| 022 | TC 6 Intercooler Water O | 23.1 | °C |
| 023 | TC 7 Exhaust | 24.1 | °C |
| 024 | TC 8 Dyno Cooling | 23.8 | °C |
| 025 | TC 9 Fuel Return cooled | 22.3 | °C |
| 026 | TC 10 | -999.0 | °C |
| 027 | TC 11 | -999.0 | °C |
| 028 | TC 12 | -999.0 | °C |
| 029 | TC 13 | -999.0 | °C |
| 030 | TC 14 | -999.0 | °C |
| 031 | TC 15 | -999.0 | °C |
| 032 | TC 16 | -999.0 | °C |

Automatic Control Conditions: Dyno Torque 190.0; Throttle Speed 1500.0

Manual Control Conditions – Additional Output Channels: Dyno Direct 0.0; Throttle Direct 0.0

There are unused icons on your desktop

The desktop cleanup wizard can help you clean up your desktop. Click this balloon to start the wizard.

Figure 5.5. Display of the DSG DaTAQ Pro system

A LabVIEW program named In-cylinder data acquisition is written to monitor the in-cylinder pressure continuously with crank angle. It acquires analogue signals from the amplifier and the digital signals in a clock counter. On the front panel, the number of cycles can be put in and then the in-cylinder pressure versus crank angle is displayed on the graph chart.

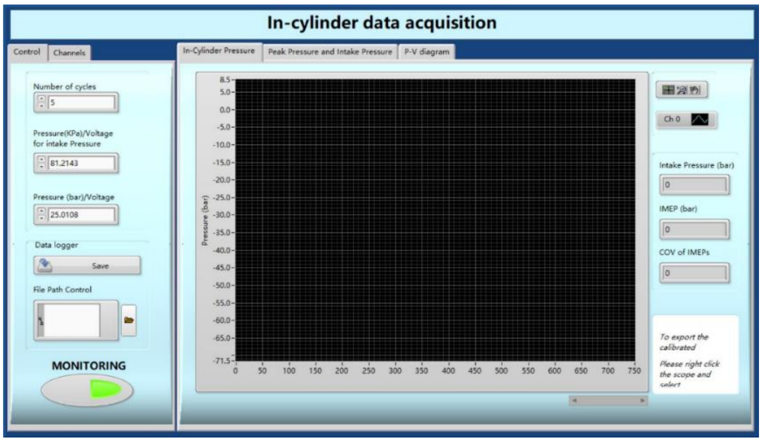

Number of cycles: 5

Pressure(KPa)/Voltage for intake Pressure: 81.2143

Pressure (bar)/Voltage: 25.0108

Intake Pressure (bar): 0

IMEP (bar): 0

COV of IMEPs: 0

*To export the calibrated*

*Please right click the scope and select*

Figure 5.6. Front panel of the In-cylinder data acquisition program

The program also acquires another analogue input signal from the intake manifold to compensate the sensor drift of the piezoelectric pressure transducer, as it can only measure the relative value instead of the absolute value of the in-cylinder pressure. Therefore, the intake manifold pressure is recorded and the difference between it and in-cylinder pressure at the BDC is used to compensate the drift.

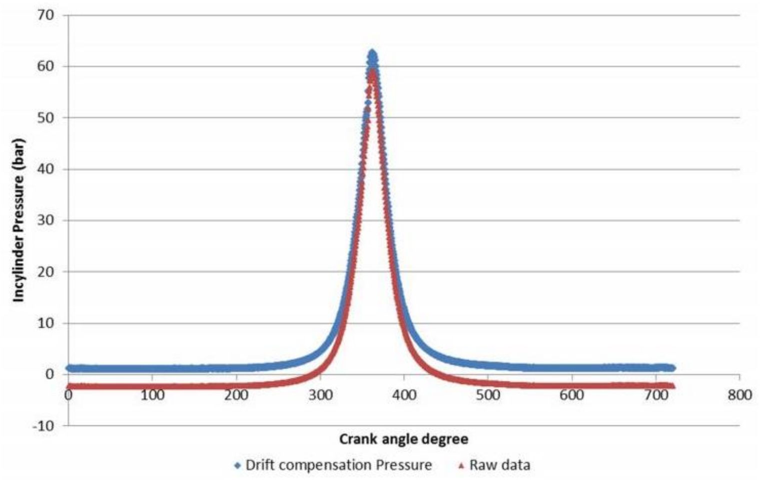

Figure 5.7. Example of pressure drift compensation

A Matlab program is then employed to calculate the heat release rate (HRR) from the obtained in-cylinder pressure as well as other engine parameters including speed, torque, BSFC etc. The code is illustrated in Appendix A.

## 5.3. Nano additives with standard diesel fuel

### *5.3.1. Fuel formulation*

The nano additive modified fuels in this experiment are the DF-Ce25, DF-Ce50 and DF-CNT, which are used for spray experiments in Chapter 3. The additives used here are the multi-wall carbon nanotubes (CNT) with 40 ~ 60 nm diameter size and 2μm length, Cerium Oxide ($CeO_2$) nanopowder with the maximum size of 25nm (Ce25) and 50nm (Ce50) respectively, which are also mentioned Chapter 3.

| Fuel | Density (kg/m$^3$) at 15 °C | Viscosity (mPa·s) at 40 °C | Thermal diffusivity (mm$^2$/s) at 40 °C | LHV (kJ/kg) |
|---|---|---|---|---|
| DF | 840.4 | 2.82 | 0.0879 | 42853 |
| DF-Ce50 | 840.4 | 2.82 | 0.0897 | 42853 |
| DF-Ce25 | 840.4 | 2.81 | 0.0940 | 42853 |
| DF-CNT | 840.4 | 2.77 | 0.1020 | 42853 |

Table 5.5. Properties of nano additive modified DF*

*The density and LHV of DF are provided by Coryton, and the viscosity and thermal diffusivity of all test fuels are measured by an NDJ-9S and an LFA 467 Hyper Flash, respectively.

### *5.3.2. Experimental conditions*

The European stationary cycle (ESC) is employed as shown in Figure 5.8, where the point 1 to 13 is the order of the engine condition in test sequence and the percentage is the weight factor of the results at each point. Besides, the idle speed here is 800 rpm, and the speeds at A, B and C are 1490 rpm, 1855 rpm and 2220 rpm respectively.

The points in the ESC have been programmed to the DSG DaTAQ Pro system. Each point has a transition of 10 ~ 20 seconds and a steady duration of 120 seconds. An interval of idle state is set between any two points and lasts for 30 ~ 120 seconds. A warming up process is conducted first for about 20 minutes until all the parameters of the engine test rig are in their ranges. When the warming up process finishes, there is 60 seconds before the ESC test starts, during which the In-cylinder data acquisition program is triggered, whilst the Horiba 1000SPCS particle counter and Horiba MEXA 1600D gas analyser begin to measure emissions. Therefore, the in-cylinder pressure and pollutant emissions of each modified fuel can be obtained.

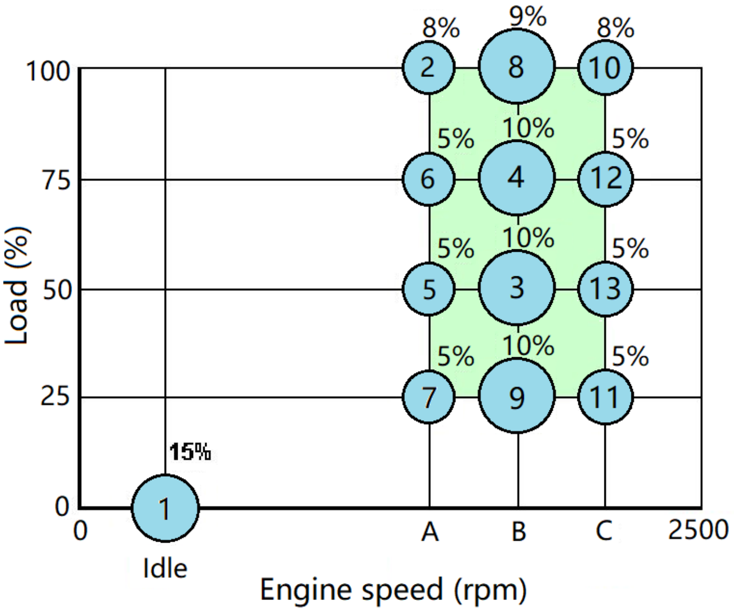

Figure 5.8. European stationary cycle (ESC) for the experimental engine

### 5.3.3. Fuel consumption

The brake specific fuel consumption (BSFC) is the ratio of fuel mass flow rate over the engine brake power. In this project, the average BSFC (kg/kWh) is employed (Equation (5.1)), as it indicates the overall level of fuel consumption during the whole experiments.

$$\overline{BSFC} = \frac{\sum m_f \cdot WF_i)}{\sum(Power_i \cdot WF_i)} \tag{5.1}$$

Where $m_f$ is the mass flow rate of fuel at a point in Figure 5.8, *Power* is the produced engine brake power (kW), WF is the corresponding weight factor and the footnote *i* is the order of the point.

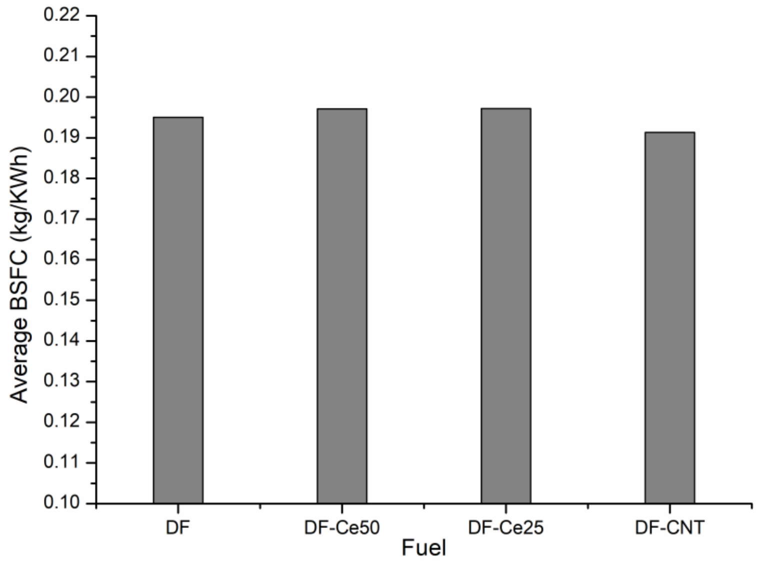

Figure 5.9. Average BSFC of nano additives modified DF

As shown in Figure 5.9, the average BSFC of all test fuels are almost the same. It means the additions of nano additives has no comparable influence on fuel consumption of the diesel engine, because the nano additives can only change physical-chemical properties associated with spray and reaction rate of fuel compositions and products. However, the lower heating value (LHV), which determines power output, cannot be changed by such small amount of additives and thus brings neglectable difference to fuel consumption at the same operating conditions.

### *5.3.4. In-cylinder behaviour*

In-cylinder pressure is a parameter which significantly influences the engine power output, engine noise and $NO_x$ emissions. Figure 5.10 to Figure 5.15 indicate that the in-cylinder pressure and corresponding HRR of all test fuels increase with the growth of load regardless of the engine speed, which is caused by more burnt fuel and more radical combustion. However, the differences of in-cylinder pressure and HRR between DF and DF with $CeO_2$ nanopowder are slight and vary with different speeds.

At 1490 rpm, the in-cylinder pressure of DF-Ce25 and DF-Ce50 are always higher than that of DF, especially at the peak. And lower heat release rate (HRR) is also observed for DF at most peaks as shown in Figure 5.11. On one hand, the addition of $CeO_2$ does not have comparable impact on DF properties, which cannot improve spray for more sufficient combustion. On the other hand, previous study [194] claims that $CeO_2$ acts as a catalyst which provides more oxygen to accelerate the combustion reaction via the conversion shown below.

$$4CeO_2 \rightleftharpoons 2Ce_2O_3 + O_2 \tag{5.2}$$

According to the catalysis of $CeO_2$, during combustion, $CeO_2$ nanopowder helps oxidize fuel molecules by converting to $Ce_2O_3$ and $O_2$, and the newly formed $O_2$ continues to oxidize more fuel molecules. By this means, the combustion process is enhanced. In return, $Ce_2O_3$ deoxidizes pollutants such as $NO_x$ and then converts to $CeO_2$ again. As a result, the overall in-cylinder combustion is improved and some pollutants can be reduced by the catalytic reactions of $CeO_2$ nanopowder.

Figure 5.10 also illustrates that the difference between fuels with $CeO_2$ nanopowder and those without it. From the figure, it can be seen that difference is becoming smaller with increasing load and finally negligible at 100% load. In addition, DF-Ce25 always has higher in-cylinder pressure than DF-Ce50 at most load conditions, because the $CeO_2$ in the DF-Ce25 has smaller size and larger surface area and thus invokes higher reaction rate.

When the speed rises to 1855 rpm, the in-cylinder pressure of DF-Ce25 and DF-Ce50 is still higher than that of DF the during the main combustion period at most loads, but the difference between them becomes smaller. It is because higher speed shortens the duration of each cycle, and thus the residence time of fuel is not enough for all the catalyst to participate in the reactions. At 2220 rpm engine speed, DF-Ce25 and DF-Ce50 have lower in-cylinder pressure than DF at most loads, because the residence time of fuel is further shortened and many nanoparticles of $CeO_2$ act as nucleus for the unburnt fuel and thus causes incomplete combustion. As $CeO_2$ nanopowder of 25 nm is smaller and contributes more to the formation of smaller particles, DF-Ce25 sometimes produce lower in-cylinder pressure than DF-Ce50 at high speed.

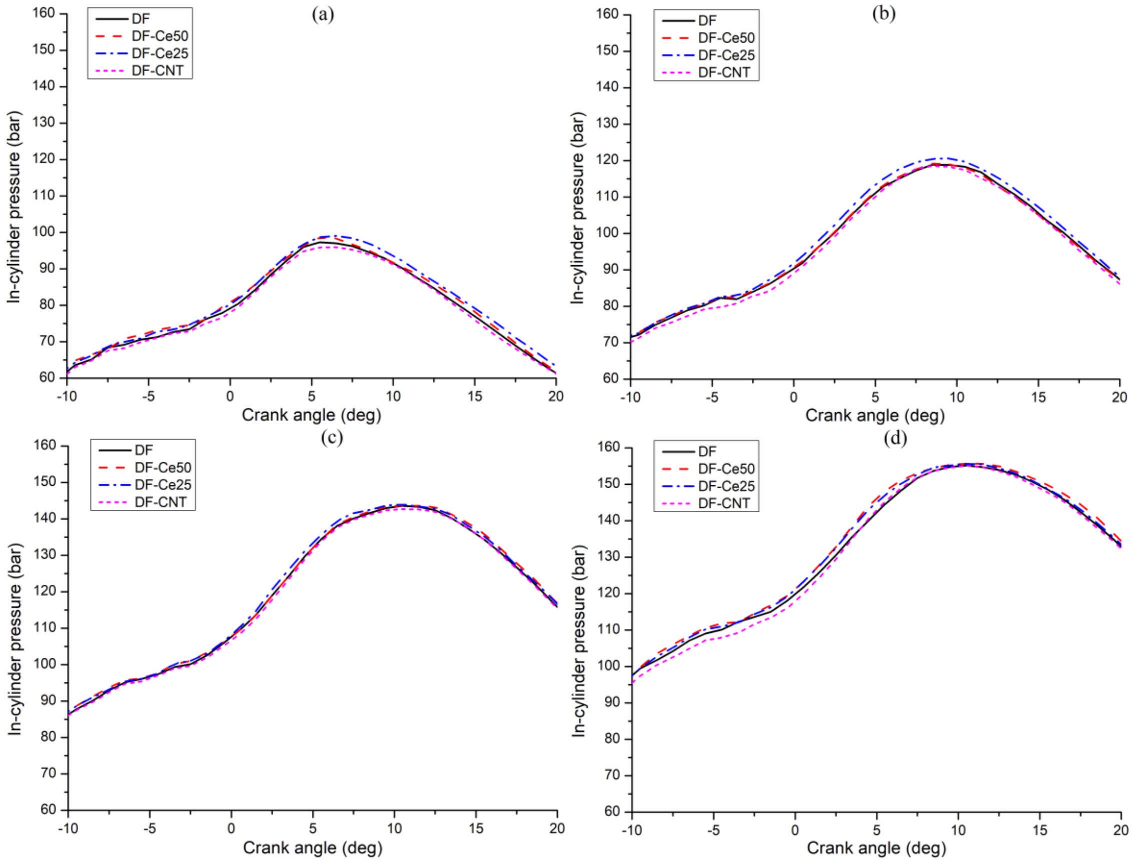

Figure 5.10. In-cylinder pressure of nano additives modified DF at 1490 rpm and 25% (a), 50% (b), 75% (c) and 100% (d) load

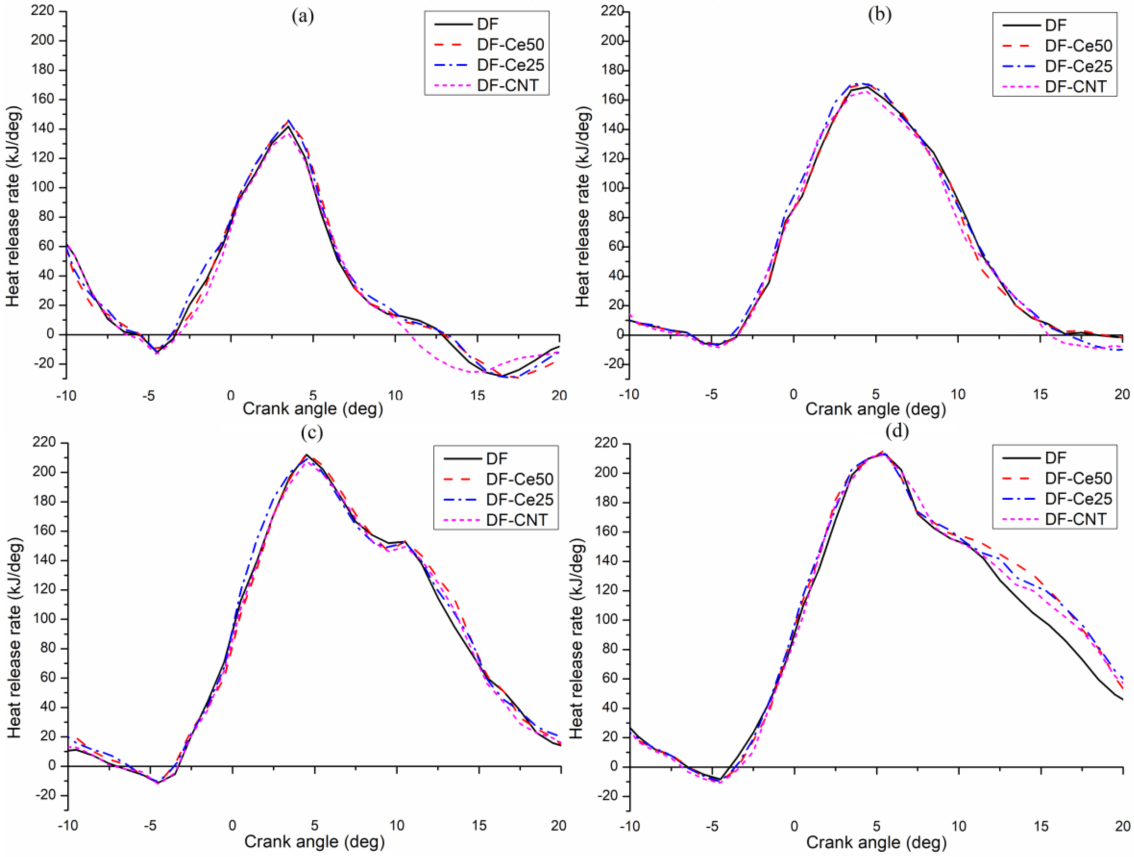

Figure 5.11. HRR of nano additives modified DF at 1490 rpm and 25% (a), 50% (b), 75% (c) and 100% (d) load

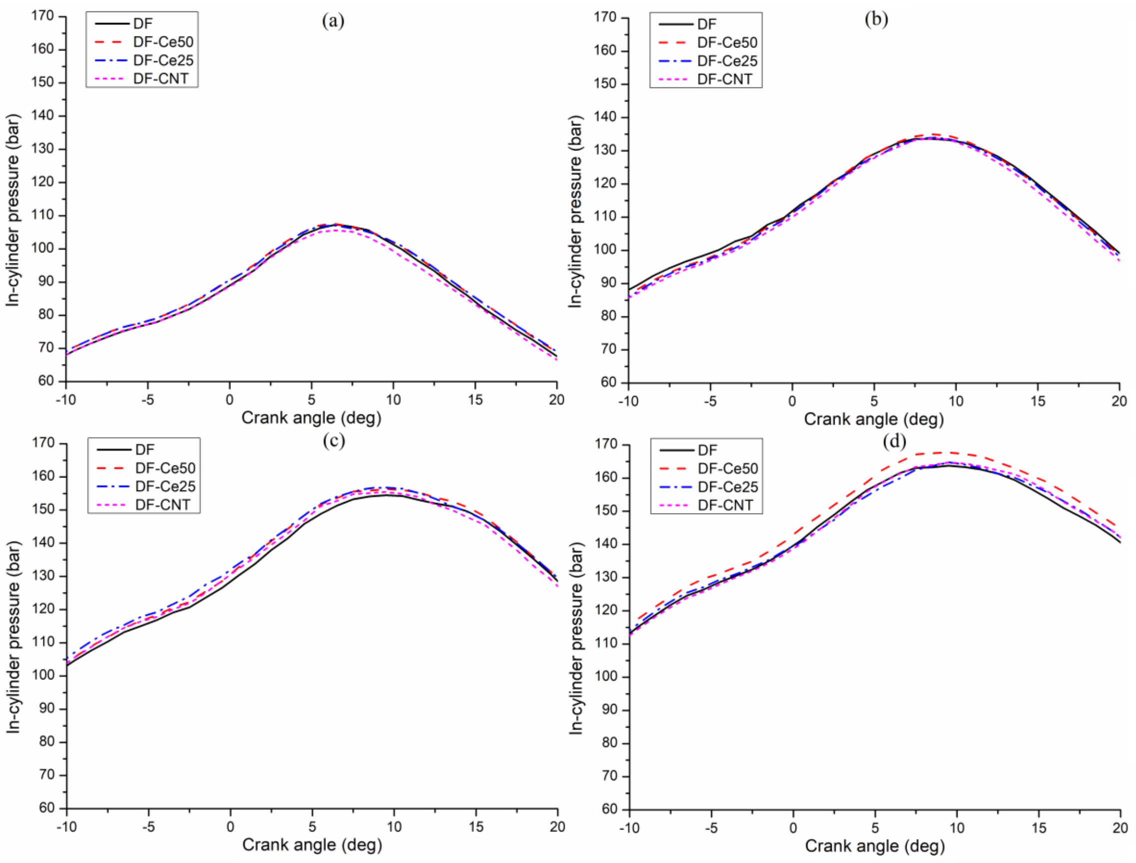

Figure 5.12. In-cylinder pressure of nano additives modified DF at 1855 rpm and 25% (a), 50% (b), 75% (c) and 100% (d) load

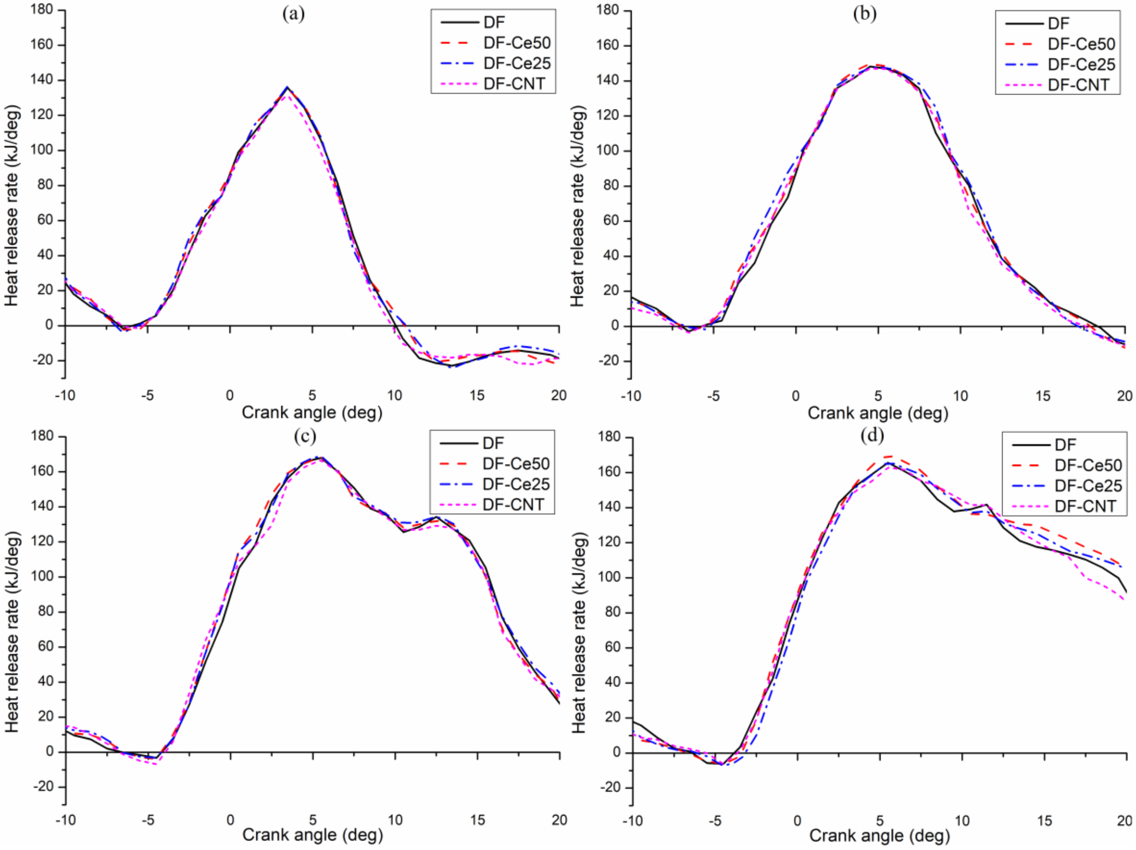

Figure 5.13. HRR of nano additives modified DF at 1855 rpm and 25% (a), 50% (b), 75% (c) and 100% (d) load

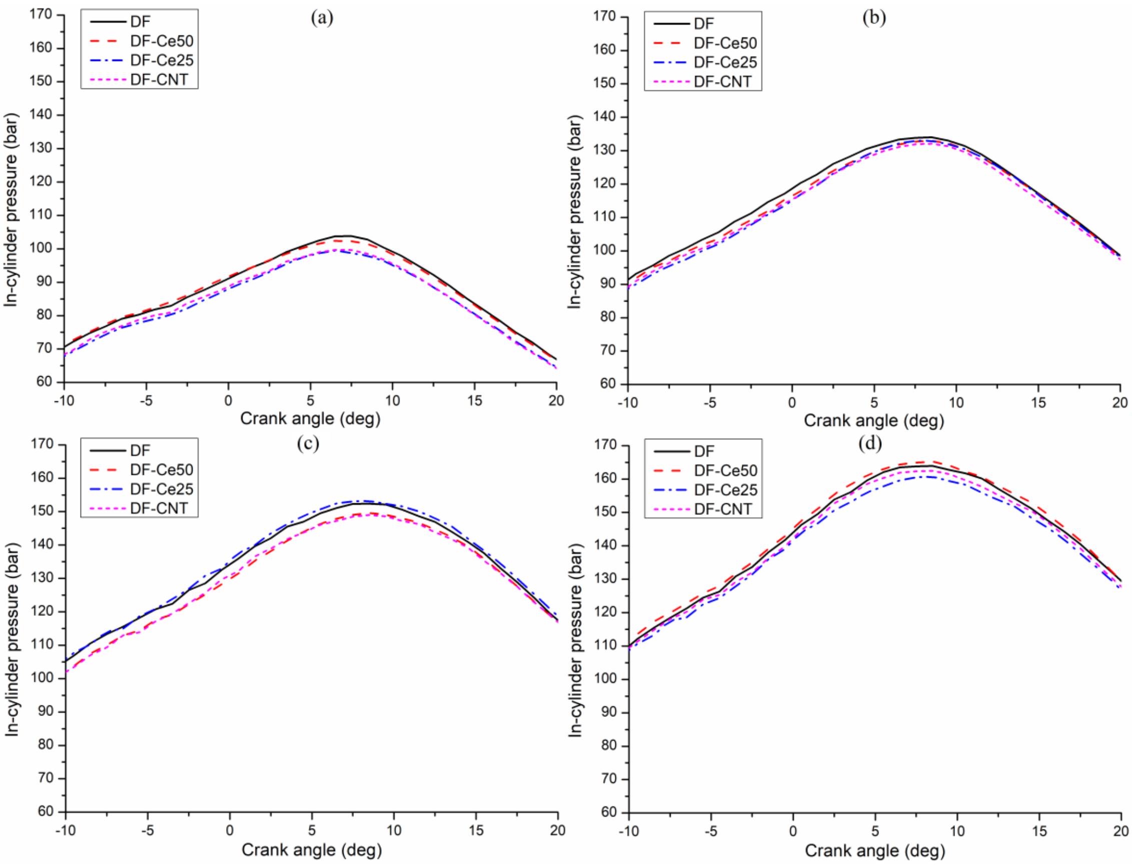

Figure 5.14. In-cylinder pressure of nano additives modified DF at 2220 rpm and 25% (a), 50% (b), 75% (c) and 100% (d) load

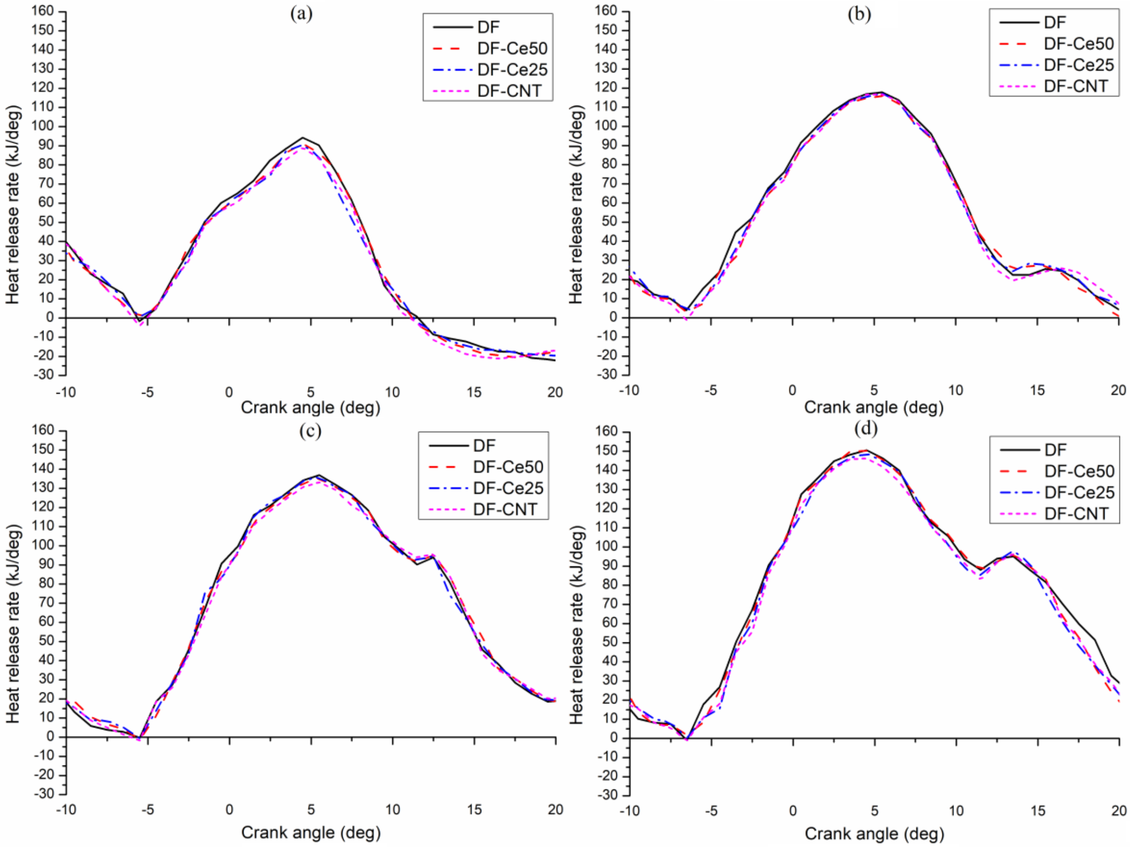

Figure 5.15. HRR of nano additives modified DF at 2220 rpm and 25% (a), 50% (b), 75% (c) and 100% (d) load

In contrast, DF-CNT produces slightly lower in-cylinder pressure than DF during the main combustion period, especially at the beginning of the combustion (about -5° crank angle) under most load and speed conditions. It is mainly determined by the unique evaporation process of DF-CNT. During injection, the liquid fuel outside the CNT firstly absorbs heat from the compressed air and evaporates, and then the CNT wall absorbs heat from the air. Due to the thick wall and hollow structure of the CNT, a large amount of liquid fuel is inside the CNT, which can only absorbs heat from the heated CNT wall and then evaporate. However, the fuel inside can only evaporate via the two ends of CNT instead of all directions, as shown in Figure 3.31, which limits the overall evaporation rate. As a result, duration of the evaporation process is enlarged and more heat is absorbed by the fuel-CNT mixture , which results in lower in-cylinder pressure and HRR.

### *5.3.5. CO emissions*

The emissions of gaseous pollutants are measured by concentration with the unit of ppm. The specific emission is employed with the unit of g/kWh to compare emissions of test fuels. The conversion between concentration and specific emission of CO is done via the following equations [55].

$$CO_S = \frac{0.000966 \cdot c_{CO} \cdot m_g}{Power} \tag{5.3}$$

Where the c is the concentration of each emission (ppm), *Power* is the output power rate of the engine (kW), $m_g$ is the mass flow rate of exhaust gas (kg/h). CO emissions of all test fuels are illustrated in Figure 5.16 to Figure 5.18, corresponding to different engine speeds. At 1490 rpm, the CO concentration of all test fuels increases with increasing load at all engine speeds, because the air-fuel ratio becomes lower at high load and thus causes incomplete combustion due to the lack of oxygen. When the engine speed increases to 1855 rpm and 2220 rpm, CO concentration of all test fuels experiences a dramatic drop first and then a growth respect to load. It is because at high speed, the duration of combustion is shorter and thus results in more incomplete combustion, which promotes the formation of CO. However, the overall reduction of combustion time reduced the amount of all the products including CO. Consequently, CO concentration is impacted by the two controversy effects of engine speed and load.

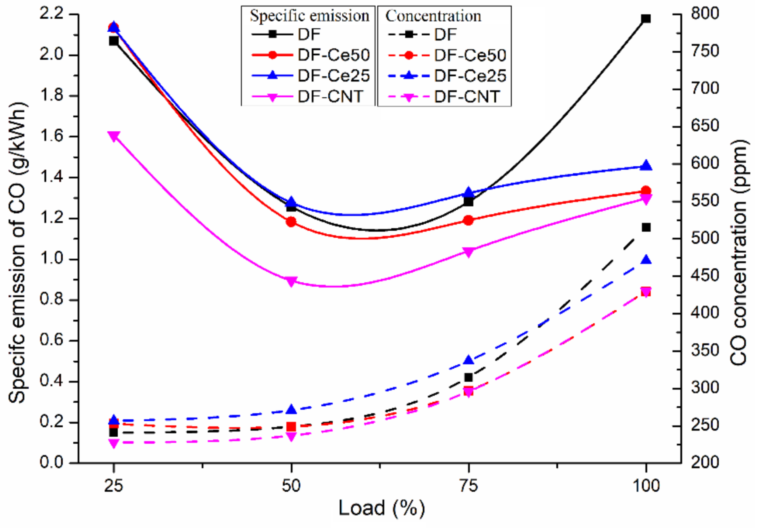

Figure 5.16. CO emissions of nano additives modified DF at 1490 rpm engine speed

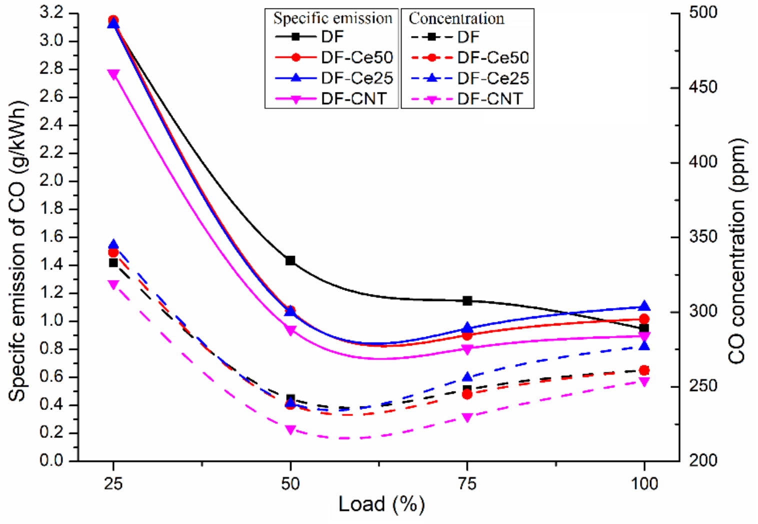

Figure 5.17. CO emissions of nano additives modified DF at 1855 rpm engine speed

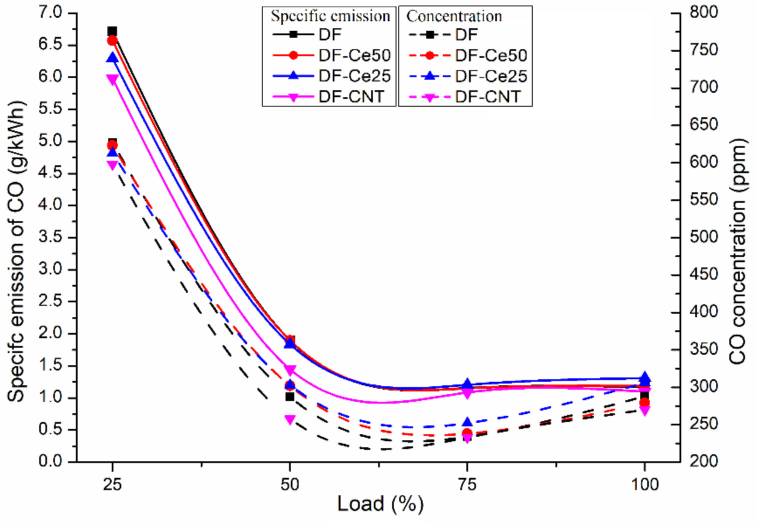

Figure 5.18. CO emissions of nano additives modified DF at 2220 rpm engine speed

The specific emission of CO is employed to compare each test fuel. DF-CNT shows advantages in reducing CO emission at almost all speed and load conditions, because its modified physical properties such as lower viscosity and higher thermal diffusivity etc. contribute to more uniform fuel-air mixture and more sufficient combustion.

In contrast, the impact of $CeO_2$ nanopowder on the specific emission of CO is varying with engine condition. At 1490 rpm, the specific CO emission of DF-Ce25 and DF-Ce50 is higher than DF at low load, and then that of DF-Ce50 reduces to lower than DF at about 35% load, whilst that of DF-Ce25 stays higher than DF until about 80% load. When the engine speed grows to 1855 rpm, both DF-Ce50 and DF-Ce25 produce slightly larger or similar amount of specific emission of CO than DF at 25% load, after which their CO emission stays lower than that of DF. The CO emission of DF-Ce25 eventually exceeds that of DF at about 90% load, whilst that of DF-Ce50 surpasses DF at about 95% load. At 2220 rpm, the CO emission of DF-Ce50 and DF-Ce25 can stay lower than that of DF when the load is less than 50%. According to literature [195, 196], the impact of $CeO_2$ on reducing CO emission of standard diesel or biodiesel has a maximum load limit, after which CO emission will increase to higher than that of DF. From this research we found there is also a minimum load limit for $CeO_2$, before which the specific emission of CO is also higher than that of the fuel without it. Moreover, both the minimum limit and the maximum limit varies with engine speed and load. Accordingly, we define the two limits as the MIN engine limit and the MAX engine limit to specific emission of CO and illustrate them in Figure 5.19. Diesel fuel with $CeO_2$ produce lower CO emissions than that without $CeO_2$ at engine conditions between the two limits. It is obvious that the DF-Ce50 has larger space between the two limits, which means DF-Ce50 is better for reducing CO emissions than DF-Ce25.

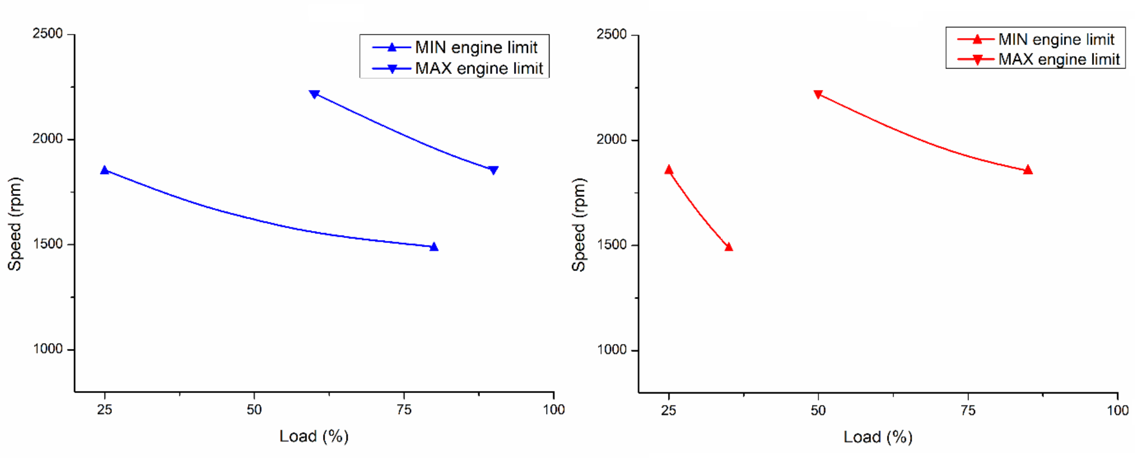

Figure 5.19. MIN engine limit and MAX engine limit to specific emission of CO for the DF-Ce25 (a) and DF-Ce50 (b)

### 5.3.6. NO$_x$ emissions

Similar to CO emissions, the concentration of NO$_x$ is also converted to specific emission by the equation below [55].

$$NO_{x_S} = \frac{0.001587 \cdot c_{NO_x} \cdot m_g}{Power} \tag{5.4}$$

At each speed, the NO$_x$ concentration of all test fuels rises with increasing load, because temperature dominates the formation of NO$_x$ via the thermal path. Therefore, more NO$_x$ is emitted at higher load condition due to the higher in-cylinder temperature.

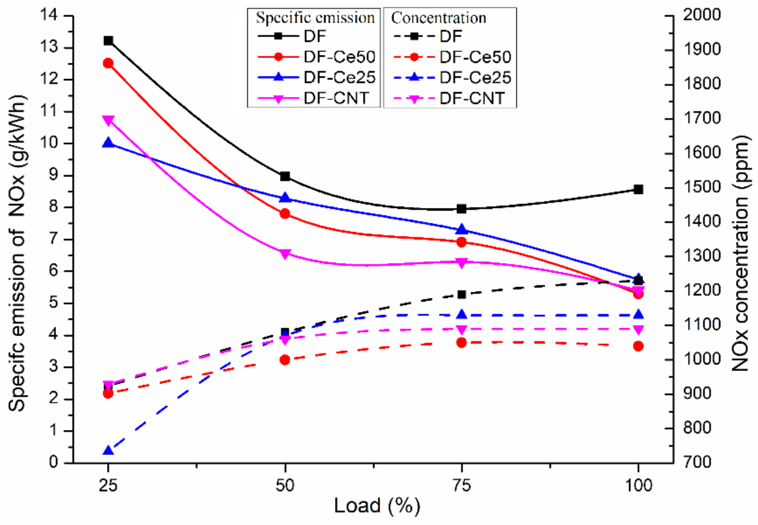

Figure 5.20. NO$_x$ emissions of nano additives modified DF at 1490 rpm engine speed

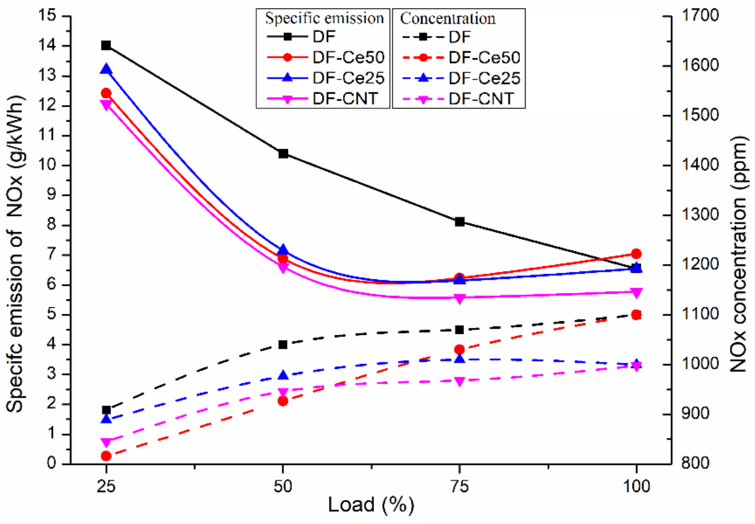

Figure 5.21. $NO_x$ emissions of nano additives modified DF at 1855 rpm engine speed

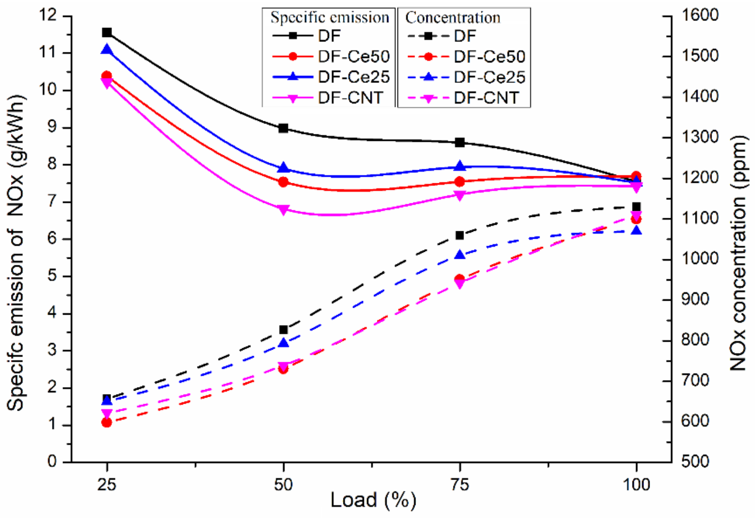

Figure 5.22. $NO_x$ emissions of nano additives modified DF at 2220 rpm engine speed

Among the test fuels, the DF-CNT has overall the lowest specific emission of $NO_x$, which can be attributed to three reasons. First, DF-CNT produces lower combustion temperature caused by the longer fuel evaporation in aforementioned context. Second, DF-CNT generates more uniform spray field due to its lower viscosity and thermal diffusivity. Third, CNT is in fact a form of elemental carbon, which can probably act as a deoxidizer during combustion via the equation below and thus prohibit the formation of $NO_x$.

$$C + 2NO \rightarrow N_2 + CO_2 \tag{5.5}$$

The fuels with $CeO_2$ nanopowder also reduce $NO_x$ emissions at most conditions, because $CeO_2$ is a catalyst which can convert between $CeO_2$ ($Ce^{+4}$) and $Ce_2O_3$ ($Ce^{+3}$). During combustion, the $CeO_2$ help oxidize unburnt fuel compositions, whilst the $Ce_2O_3$ is used to deoxidize products of strong oxidizability. Consequently, $NO_x$ emissions are mainly reduced via the following equation for DF-Ce25 and DF-Ce50.

$$Ce_2O_3 + 2NO \rightarrow 2CeO_2 + 1/2\, N_2 \qquad (5.6)$$

Moreover, DF-Ce25 appears to have higher specific emission of $NO_x$ than DF-Ce50 at most conditions, which is caused by the different size of $CeO_2$ nanopowder. Given that $CeO_2$ converts between $CeO_2$ and $Ce_2O_3$ via reversible reactions, a faster rate of the reaction from $CeO_2$ to $Ce_2O_3$ will hinder the reaction from $Ce_2O_3$ to $CeO_2$, vice versa. As $NO_x$ is deoxidized by $Ce_2O_3$, $CeO_2$ nanopowder of 25 nm experiences higher reaction rate from $CeO_2$ to $Ce_2O_3$ due to its larger surface area and in return lowers down the rate for $Ce_2O_3$ reacting with $NO_x$.

Figure 5.20 to Figure 5.22 also illustrate that all fuels with nano additives have lower specific emissions of $NO_x$ than standard diesel, and the difference between them varies with speed and load. According to literature [108], the oxygen concentration, residence time and temperature determine the amount of $NO_x$ emissions from the diesel engine. More oxygen and residence time provide more opportunities for $N_2$ to be oxidized, and higher temperature contributes to the formation of $NO_x$ via the thermal path. Meanwhile, catalysts such as $CeO_2$ are demonstrated to have better activity at higher temperature [112]. Therefore, the phenomenon of $NO_x$ emissions of all the test fuels should be attributed to the comprehensive effects of the two reasons above.

At 1490 rpm, the difference of specific emission of $NO_x$ between standard diesel and diesel with nano additives is small at 25% load and then increases to the largest at 100% load. It is because the residence time and amount of air are enough for both the oxidization of $N_2$ and the deoxidization of $NO_x$ at this speed, so temperature is the only factor influencing $NO_x$ emissions of each fuel. When the speed increases to 1855 rpm, the difference at 25% load is small and increases to the largest between 50% and 75% load, and then becomes tiny at 100%. It is probably because the catalysis of $CeO_2$ nanopowder is not strong at 25% load due to relatively lower combustion temperature, and is improved to its maximum at mid load, after which the catalysis stays at the same level but the formation of $NO_x$ is enhanced. The phenomenon at 2220 rpm is similar to that at 1855 rpm but the overall difference becomes smaller due to short residence time.

### *5.3.7. HC emissions*

HC is the mixture of unburnt fuel compositions and the light products of the thermal degradation of large fuel molecules. It is usually promoted by poor atomisation, inadequate combustion and reduced by uniform combustion, oxidants and high temperature. Figure 5.23

to Figure 5.25 demonstrate that the HC concentration of all test fuels decreases with increasing load at all speeds. It is because HC is easy to be oxidized by oxidants and to form particulate matters (soot) via dehydrogenation and carbonization at high temperature. It is also demonstrated that the specific emission of HC is increasing when the engine speed rises, which is mainly caused by the inadequate combustion due to shorter residence time.

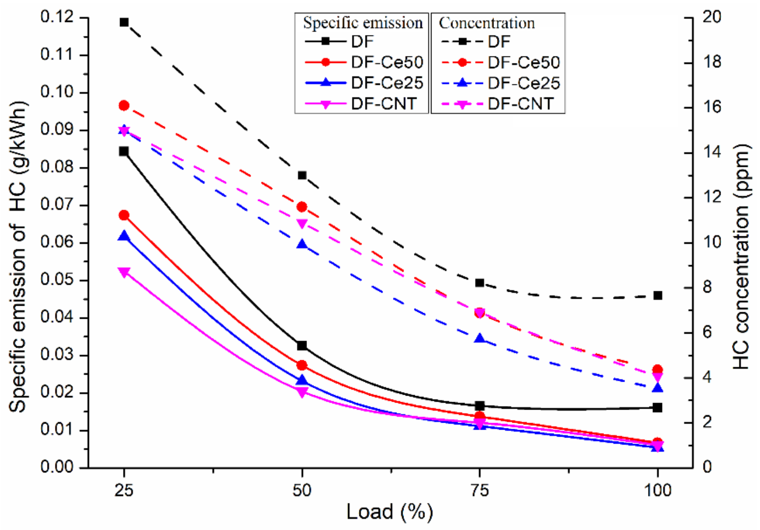

Figure 5.23. HC emissions of nano additives modified DF at 1490 rpm engine speed

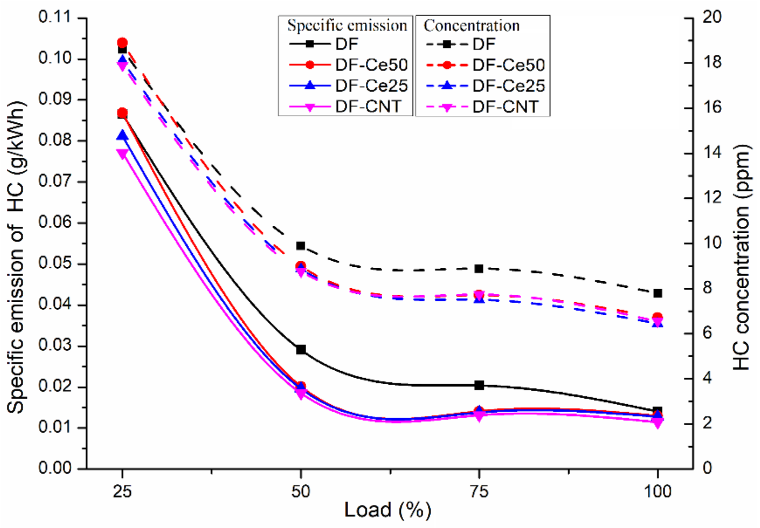

Figure 5.24. HC emissions of nano additives modified DF at 1855 rpm engine speed

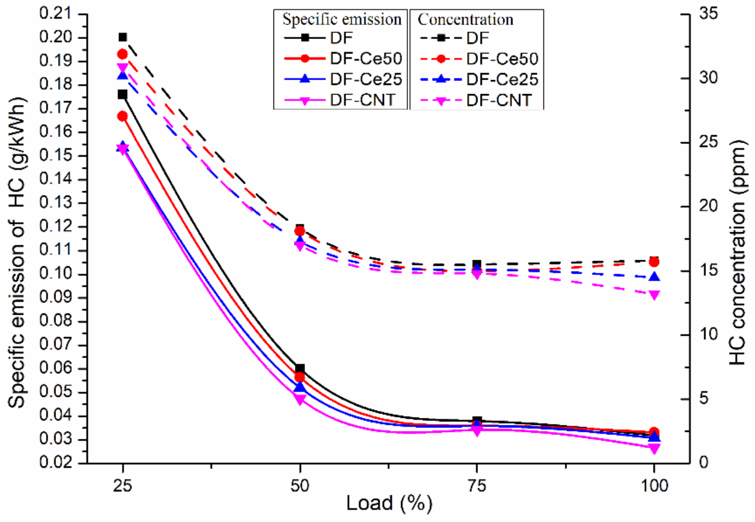

Figure 5.25. HC emissions of nano additives modified DF at 2220 rpm engine speed

The specific emission of HC is obtained by Equation (5.7) [55].

$$HC_S = \frac{0.000479 \cdot c_{HC} \cdot m_g}{Power} \qquad (5.7)$$

The units of the terms here are the same as Equation (5.3) ~ (5.4). As shown in Figure 5.23 to Figure 5.25, fuels with nano additives have lower specific emission of HC than standard diesel fuel. However, the difference between them is large at 1490 rpm and 1855 rpm engine speed but reduces at 2220 rpm, which is because the shorter residence time limits the reaction of additives. Among the fuels with nano additives, DF-CNT has the lowest specific emission of HC at most conditions. As described in aforementioned paragraph, DF-CNT generates more uniform spray field due to its lower viscosity and thermal diffusivity, and thus experiences relatively more homogenous combustion than others. As a result, despite lower in-cylinder pressure, few fuel-rich zones exist during DF-CNT combustion and thus less unburnt fuel is emitted. DF-Ce50 and DF-Ce25 produce lower HC emissions than DF mainly due to the catalytic reaction of $CeO_2$ as shown in the equation below.

$$(2x+y)CeO_2 + C_xH_y \rightarrow \left[\frac{2x+y}{2}\right] Ce_2O_3 + \frac{x}{2}CO_2 + \frac{y}{2}H_2O \qquad (5.8)$$

Where $CeO_2$ act as the oxidant for HC, and the products $Ce_2O_3$ participate in the deoxidization of $NO_x$. DF-Ce25 produces slightly lower HC due to its smaller size and larger specific surface area of nanopowder, which provide more opportunities for $CeO_2$ to react with HC.

### *5.3.8. PN emissions*

Particulate matters (PM) are usually formed by the dehydrogenation and carbonization of unburnt fuels at high temperature and low oxygen conditions. Therefore, high load and the existence of nuclei will promote the formation of PM, whilst more oxygen content and longer residence time will consume the amount of PM. In this study, the concentration of PM number (PN) is measured and then converted to specific emission (#/kWh) via Equation (5.9) [55].

$$PN_S = \frac{c_{PN} \cdot m_g \cdot 10^6}{Power \cdot \rho_g} \tag{5.9}$$

Where $c$ is the concentration of PN (#/cm$^3$), $\rho_g$ is the density of exhaust gas which is always considered as 1.293 kg/m$^3$. Figure 5.26 to Figure 5.28 illustrate the specific emission of PN of each test fuel at various conditions, which indicate that the PN concentration of all test fuels increases with the rise of load at each engine speed. Because high load enables fuel compositions more likely to experience incomplete combustion and thus form more PMs due to the relatively fuel-rich condition. Furthermore, high load also promotes the formation of smaller PMs, as the larger ones are easily to be burnt at high temperature. Meanwhile, as the shorter residence time reduces the chance of complete combustion of PMs, the overall level of PN concentration grows as the engine speed increase from 1490 rpm to 2220 rpm.

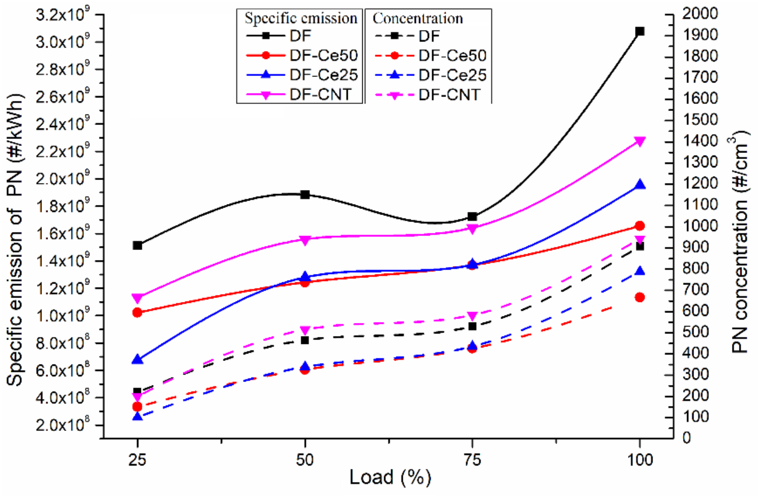

Figure 5.26. PN emissions of nano additives modified DF at 1490 rpm engine speed

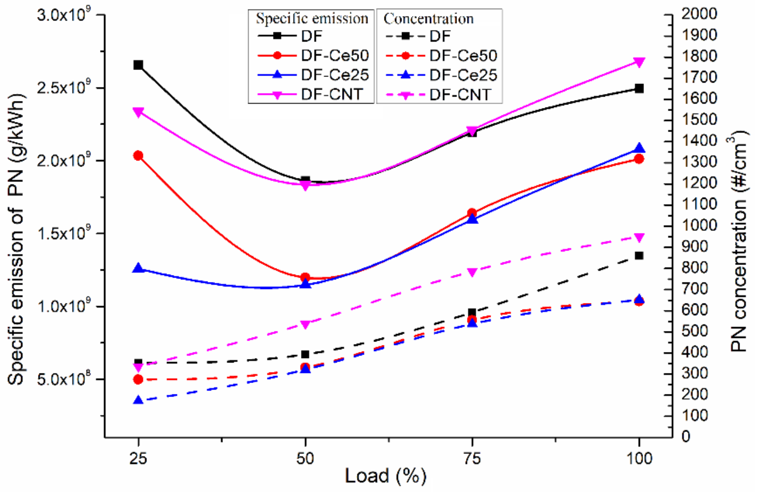

Figure 5.27. PN emissions of nano additives modified DF at 1855 rpm engine speed

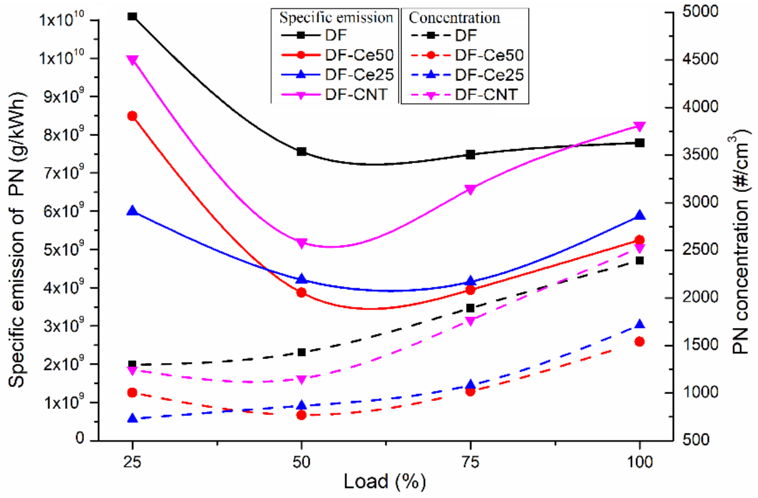

Figure 5.28. PN emissions of nano additives modified DF at 2220 rpm engine speed

DF-CNT has lower specific emission of PN at all loads when the engine speed is 1490 rpm. However, when the engine speed increases to 1855 rpm and 2220 rpm, the specific emission of PN of DF-CNT exceeds that of DF at high load (between 75% and 100%). On one hand, DF-

CNT experiences improved spray and lower combustion temperature as described in aforementioned context, which is helpful in reducing PN emissions. One the other hand, CNT can act as the nucleus for the formation of particulate matters. Accordingly, the PN emissions of CNT is the comprehensive results of the two contradictory effects. At low speed, PMs have more time to be burnt, especially in a more uniform air-fuel mixture and lower temperature brought by DF-CNT, so the specific emission of PN of DF-CNT stays at lower level than that of DF. At high speed, the residence time is not enough to burn most particulate matters, and thus CNT has the chance to participate in the formation of particulate matters as the nucleus at high load, which enables more PN emissions.

In terms of DF-Ce25 and DF-Ce50, their specific emission of PN are both significantly lower than DF at all conditions, regardless of varying load and speed. The reasons are twofold: First, $CeO_2$ can oxidize particulate matters via Equation (13), which consumes a large amount of PMs.

$$4CeO_2 + C_{PM} \rightarrow 2Ce_2O_3 + CO_2 \tag{5.10}$$

Second, $CeO_2$ consumes some HCs via Equation (12) before they convert to PMs through dehydrogenation and carbonization. However, $CeO_2$ nanoparticle is also a type of nucleus, which can contribute to the formation of PM under some conditions. It can explain the reason that DF-Ce25 has lower specific emission of PN than DF-Ce50 at low load but it becomes higher at high load, because the $CeO_2$ of smaller size is more easily to aggregate unburnt fuel molecules to form smaller PMs which is usually of larger amount than the bigger PMs.

### *5.3.9. Average specific emissions*

In order to evaluate the overall level of emissions, the average specific emissions of all pollutants are calculated via Equation (5.11) to (5.14) [55].

$$\overline{CO} = \frac{0.000966 \cdot \sum(c_{CO,i} \cdot m_{g,i} \cdot WF_i)}{\sum(Power_i \cdot WF_i)} \tag{5.11}$$

$$\overline{NO_x} = \frac{0.001587 \cdot \sum(c_{NO_x,i} \cdot m_{g,i} \cdot WF_i)}{\sum(Power_i \cdot WF_i)} \tag{5.12}$$

$$\overline{HC} = \frac{0.000479 \cdot \sum(c_{HC,i} \cdot m_{g,i} \cdot WF_i)}{\sum(Power_i \cdot WF_i)} \tag{5.13}$$

$$\overline{PN} = \frac{10^6 \cdot \sum(c_{PN,i} \cdot m_{g,i} \cdot WF_i)}{\rho_g \cdot \sum(Power_i \cdot WF_i)} \tag{5.14}$$

As demonstrated in Figure 5.29, all fuels with nano additives have lower average specific emissions of CO, $NO_x$, HC and PN than standard diesel fuel due to their modified physical-chemical properties.

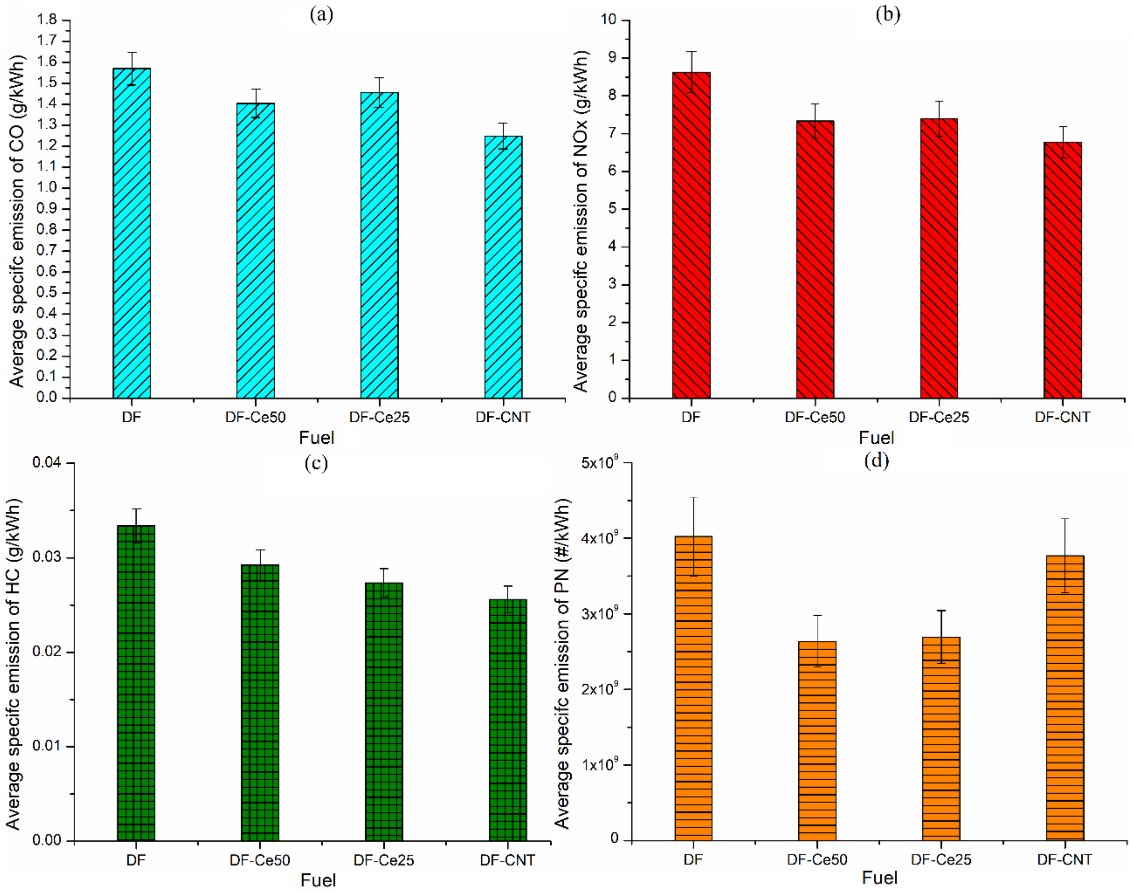

Figure 5.29. Average specific emission of CO (a), $NO_x$ (b), HC (c) and PN (d) of nano additives modified DF

Among all the fuels with nano additives, DF-CNT has the lowest average specific emissions of CO, $NO_x$ and HC (20%, 21% and 22.6% lower than DF respectively), because it generates lower combustion temperature caused by its unique two-step evaporation and more uniform combustion due to its thick wall, lower viscosity and higher thermal diffusivity. However, its average specific emission of PN is the highest among the three modified fuels, which is only 5.5% lower than DF, because CNT is highly likely to act as the nucleus for the formation of particulate matters at high load and high speed conditions despite its improved spray quality. Both DF-Ce25 and DF-Ce50 have lower level of emissions of all pollutants than DF, but DF-Ce25 is slightly higher on CO and slightly lower on HC than DF-Ce50. $CeO_2$ converts to $Ce_2O_3$ via reversible reactions, so a faster rate of the reaction from $CeO_2$ to $Ce_2O_3$ will suppress the reaction from $Ce_2O_3$ to $CeO_2$, vice versa. As HC and PM can be oxidized by $CeO_2$ and $NO_x$ is deoxidized by $Ce_2O_3$, $CeO_2$ powder of 25 nm experiences higher reaction rate from $CeO_2$ to $Ce_2O_3$ due to its larger surface area and in return slightly lowers down the rate for $Ce_2O_3$ reacting with $NO_x$, as illustrated in Figure 5.30. Despite the oxidization of PMs by $CeO_2$, the $CeO_2$ nanopowder of smaller size is a better type of nucleus forming smaller PM (larger amount), and thus enables DF-Ce25 to emit slightly higher PN than DF-Ce50.

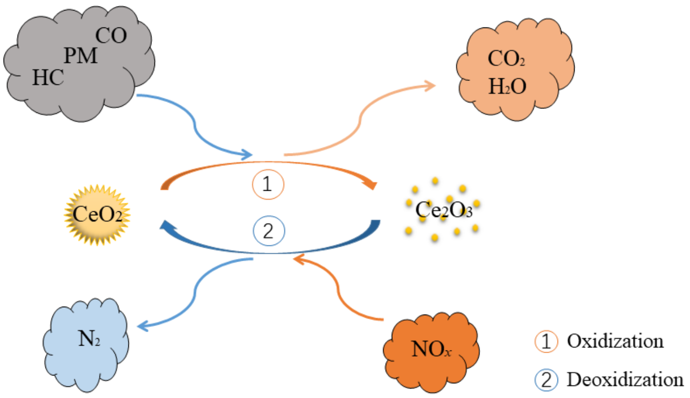

*Smaller $CeO_2$ nanopowder has higher reaction rate of ① and thus hinders reaction ②, vice versa.

Figure 5.30. Illustration of catalytic reaction of $CeO_2$ nanopowder

### *5.3.10. Summary*

As two types of nano additives, the $CeO_2$ nanopowder and CNT are capable of improving the engine performance at most conditions when blending with standard diesel fuel. The CNT modified DF produces lower gaseous emissions than $CeO_2$ nanopowder modified DF except PN. Moreover, $CeO_2$ nanopowder of smaller size promotes the conversion of HC and PM but lower down the reaction rate of $NO_x$. The advantages of $CeO_2$ nanopowder and CNT provide opportunities of application for not only standard diesel fuel but also various renewable fuels.

## 5.4. Renewable fuels

### *5.4.1. Test fuels and experimental conditions*

The renewable fuels here are the gas to liquid synthetic fuel (GTL) and the hydrotreated vegetable oil (HVO), which are employed in the spray experiments in Chapter 3. The DF is used as a reference. All the test fuels are in the drums in the fuel store of Stephenson Building.

| Fuel | HVO | GTL | DF |
|---|---|---|---|
| Density (kg/m$^3$) at 15 °C | 780.1 | 780 | 840.4 |
| Viscosity (mPa·s) at 40 °C | 3.02 | 2.74 | 2.82 |
| Aromatics content (mass%) | 0 | 2.9 | 27.5 |
| Cetane number | 78 | 76 | 51 |
| LHV (kJ/kg) | 43902 | 43600 | 42853 |

Table 5.6. Main properties of renewable fuels

These test fuels are pumped to the fuel tank of the engine before ignition. A warming up process is conducted for about 20 minutes until all the parameters of the engine test rig are in their ranges. Then, the In-cylinder data acquisition program is triggered, and the engine transits to steady state at 1500 rpm speed and 190 Nm torque for 120 seconds. Meanwhile, the Horiba 1000SPCS particle counter and Horiba MEXA 1600D gas analyser begin to measure emissions. The engine condition (1500 rpm speed and 190 Nm torque) is repeated three time, and an interval of idle state for 30 ~ 120 seconds is set between each time. The in-cylinder pressure and pollutant emissions of the renewable fuels are thus obtained.

### *5.4.2. Fuel consumption*

As shown in Figure 5.31, the BSFC of GTL is significantly smaller than that of DF, whilst that of HVO is just slightly smaller. It is mainly because the GTL and HVO have higher LHV and lower density compared with DF, and thus consume less fuel at the same speed and load condition. Moreover, the viscosity of GTL is smaller than that of HVO and thus improve the spray before combustion (shown in Chapter 3), which finally benefits combustion process and reduces the amount of consumed fuels.

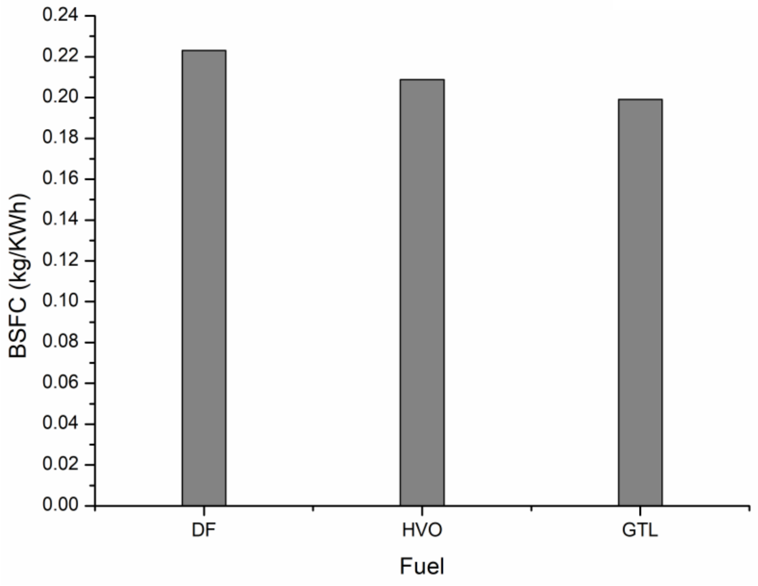

Figure 5.31. BSFC of renewable fuels

### ***5.4.3. In-cylinder behaviour***

Similar to the research on nano additives modified diesel fuels, the in-cylinder pressure and corresponding HRR are obtained and illustrated in Figure 5.32 and Figure 5.33 respectively.

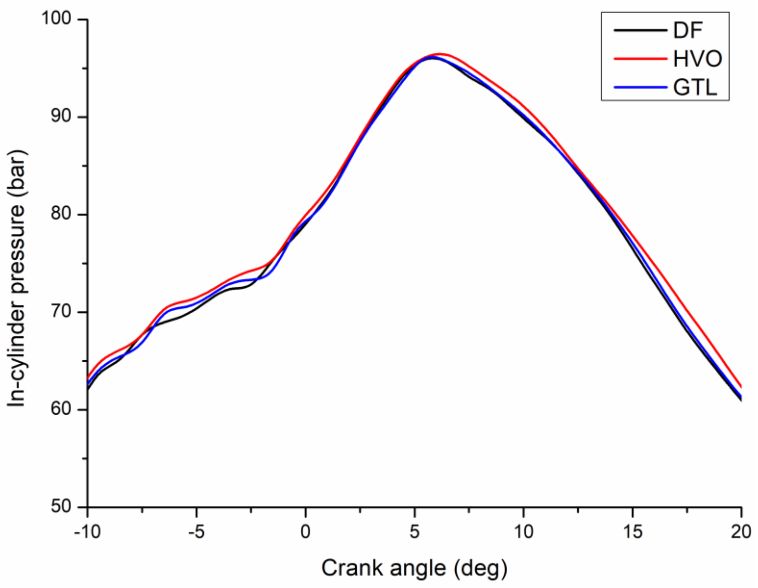

Figure 5.32. In-cylinder pressure of renewable fuels

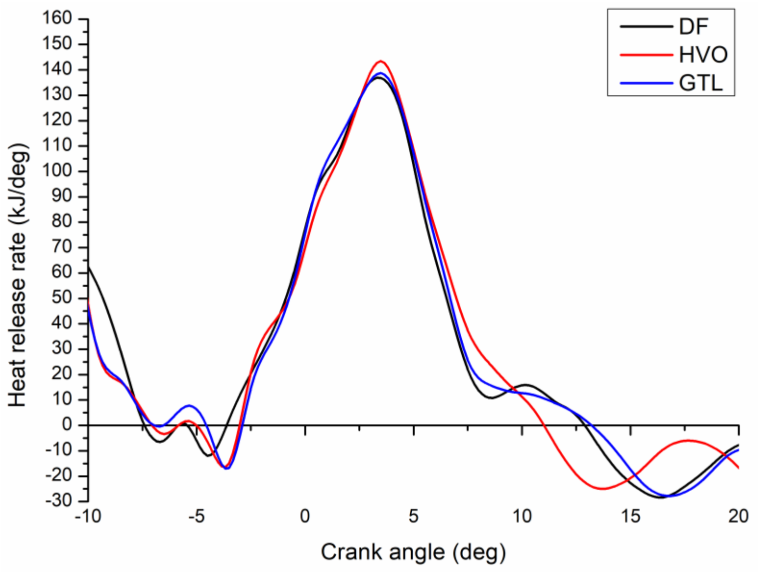

Figure 5.33. HRR of renewable fuels

As shown in Figure 5.32, the in-cylinder pressure of HVO is slightly higher than that of GTL and DF, but the difference among them are overall not comparable. Theoretically, HVO and GTL have higher LHV and cetane number (CN) than DF, which should enable faster combustion and more heat during combustion. However, the engine was running at a relatively low load condition, where the fuel flow rate of HVO and GTL is lower than DF, as shown in Figure 5.31, and thus results in closed in-cylinder pressure and heat release rate. The difference between the renewable fuels and DF would be significant only when the engine runs at full load.

### ***5.4.4. Pollutant emissions***

As illustrated in Figure 5.34, HVO shows outstanding advantages in reducing CO emissions by nearly 28.6%. In contrast, the difference of CO emissions between DF and GTL is not comparable. CO is usually formed at lower temperature and incomplete combustion. Therefore, the reduced CO emissions of HVO is mainly due to the higher combustion temperature, which is also demonstrated in Figure 5.32.

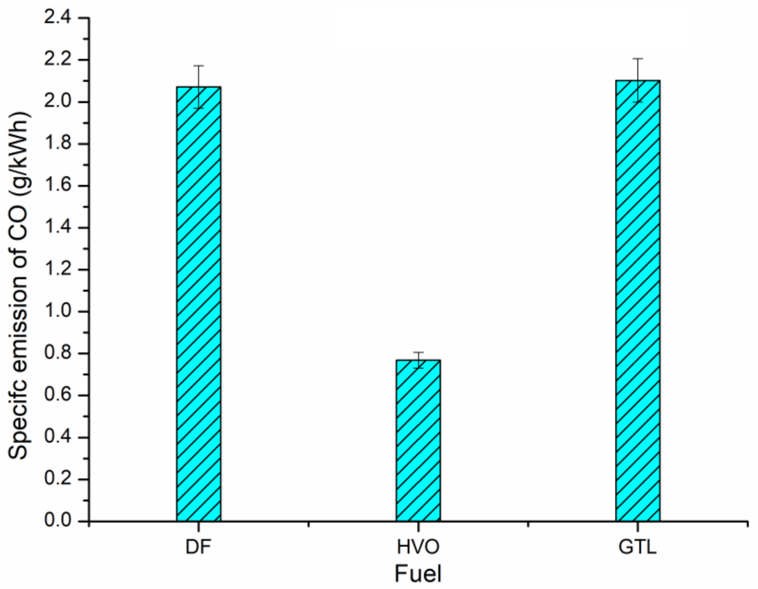

Figure 5.34. Specific emission of CO of renewable fuels

However, the performance of HVO and GTL on $NO_x$ emissions is quite different. GTL can significantly reduce the specific emission of $NO_x$ by 20.9% at the speed and load, but HVO only reduce $NO_x$ slightly. In the aforementioned context, $NO_x$ is mainly generated via the thermal mechanism and prompt mechanism. In the thermal mechanism, temperature dominate when the temperature is high, whilst the prompt mechanism becomes significant at fuel-rich zones at relatively lower temperature. Given the fact that the engine load is only 25% in this experiment, the overall temperature during combustion is still not high enough to activate the thermal path, when the prompt path enables GTL generate less $NO_x$ due to its better spray quality than HVO.

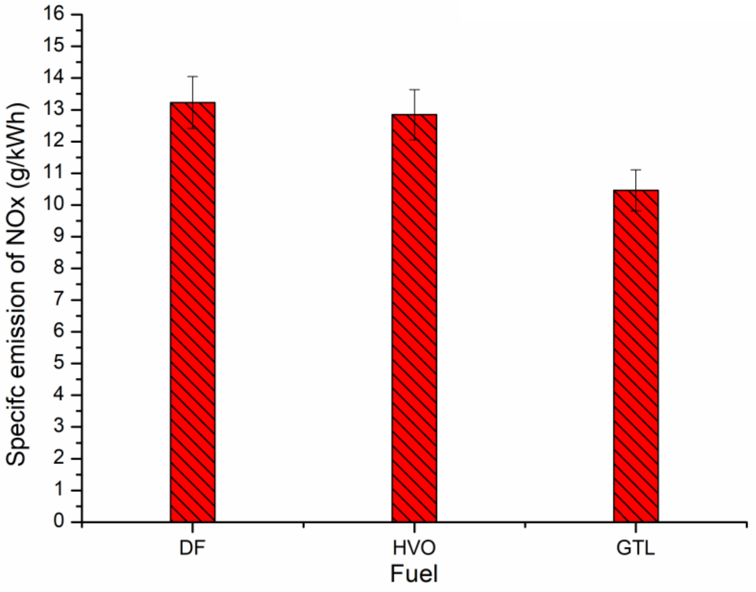

Figure 5.35. Specific emission of $NO_x$ of renewable fuels

In terms of HC emissions, the influence of both HVO and GTL is significant. HVO and GTL can reduce HC by as much as 60.5% and 15.4% respectively. As HC is usually formed at fuel rich zones at low temperature and will be consumed when temperature rises, the phenomenon can be attributed to the higher combustion temperature of HVO and GTL, compared to that of DF.

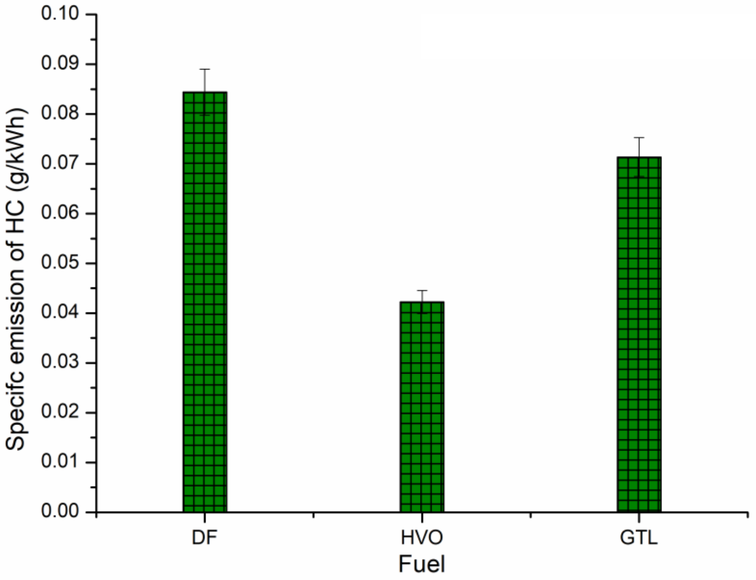

Figure 5.36. Specific emission of HC of renewable fuels

The formation of particulate matters (PM) are mainly impacted by three factors: spray quality, combustion temperature, fuel composition. In the fuel rich zones, the unburnt fuel compositions, mainly aromatics, dehydrogenate and carbonize at high temperature to PM precursors and then aggregate to PMs. Therefore, HVO produces the least PN as it contains no aromatics as shown in Figure 5.37, whilst PN produced by HVO is between GTL and DF. In addition, we can see that the effect of temperature and spray in fact are not significant at this engine condition.

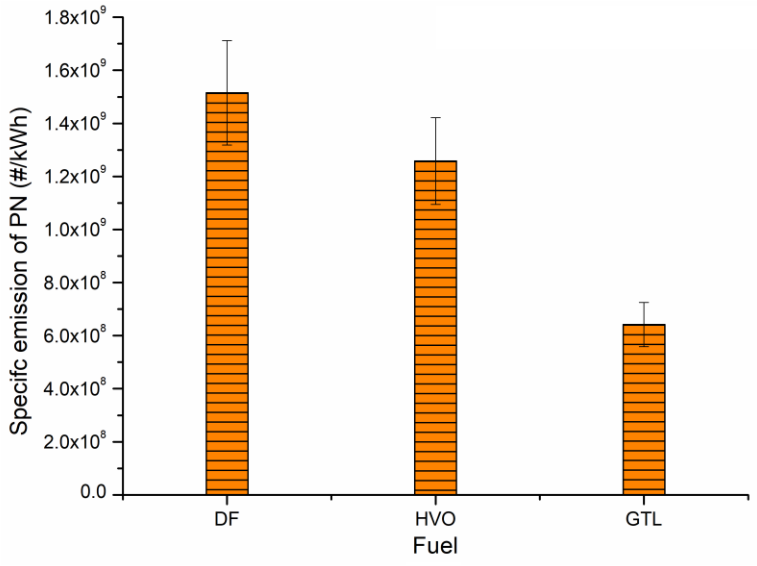

Figure 5.37. Specific emission of PN of renewable fuels

### *5.4.5. Summary*

As two promising renewable fuels, HVO and GTL show better performance in fuel consumption, in-cylinder behaviour and pollutant emissions at 1500 rpm engine speed and 190 Nm torque. However, both of them cannot reduce all the pollutant emissions at the same time, which provides possibilities of employing nano additives together with them.

## 5.5. Combination of nano additives and renewable fuels

### *5.5.1. Fuel formulation and experimental conditions*

In aforementioned context, both nano additives and renewable fuels are demonstrated effective in improving engine performance, which inspires the idea of combining them for further improvement. Therefore, we blend GTL with CeO2 nanopowder and CNT respectively, and study their behaviour of combustion and emissions at the same condition as renewable fuels (1500 rpm and 190 Nm). The standard diesel fuel is used as a reference.

| Fuel | Density (kg/m$^3$) at 15 °C | Viscosity (mPa·s) at 40 °C | LHV (kJ/kg) |
|---|---|---|---|
| GTL | 780 | 2.74 | 43600 |
| GTL-Ce50 | 780 | 2.74 | 43600 |
| GTL-Ce25 | 780 | 2.72 | 43600 |
| GTL-CNT | 780 | 2.68 | 43600 |

Table 5.7. Properties of nano additive modified GTL

### *5.5.2. Fuel consumption*

Figure 5.38 illustrates the BSFC of all test fuels at 1500 rpm and 190 Nm torque. Obviously, GTL and the nano additive modified GTL fuels all have reduced BFSC (by about 10.8%) than standard diesel fuel caused by higher LHV of GTL. In contrast, the modification to GTL seems to have no impact on BSFC, as the difference among GTL with nano additives and pure GTL is neglectable. It indicates that the addition of $CeO_2$ nanopowder and CNT cannot change the power output of the engine because the LHV of GTL stays constant.

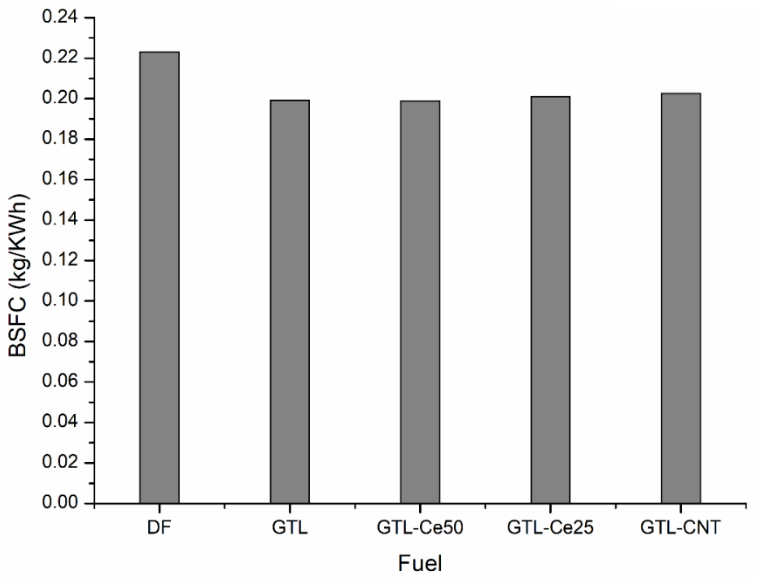

Figure 5.38. BSFC of nano additive modified GTL

### *5.5.3. In-cylinder behaviour*

As shown in Figure 5.39, the in-cylinder pressure of GTL-Ce25 and GTL-Ce50 are always higher than that of GTL and DF, especially at the peak. And similar phenomenon is also found for HRR at the peak in Figure 5.40. The function of $CeO_2$ nanopowder for GTL is in fact the same as it for DF, as demonstrated in the Chapter 0, where two reasons are claimed. First, $CeO_2$ nanopowder increases thermal diffusivity of GTL and thus improves spray. Second, $CeO_2$ nanopowder is an effective catalyst accelerate the combustion reactions via Equation (5.2), where $CeO_2$ converts to $Ce_2O_3$ through reverse reactions. However, unlike the phenomenon of DF, $CeO_2$ nanopowder has no difference in the in-cylinder pressure and HRR during the main combustion. It indicates that the impact of the size of $CeO_2$ nanopowder is not significant on the in-cylinder behaviour of GTL at the selected engine condition.

In contrast, GTL-CNT produces lower in-cylinder pressure than GTL during the main combustion period, which is likely determined by the unique heat absorption and evaporation process due to the hollow structure of the CNT, as described in Chapter 3. The liquid fuel outside the CNT firstly absorbs heat from the compressed air and evaporates, and then the liquid fuel inside the CNT absorbs heat from the heated CNT wall and evaporates. Due to the thick multi-wall structure, the temperature of CNT wall increases slower than the fuel outside. As a result, more heat is absorbed by the fuel-CNT mixture and the overall duration of the evaporation process is enlarged, which results in lower in-cylinder pressure and HRR.

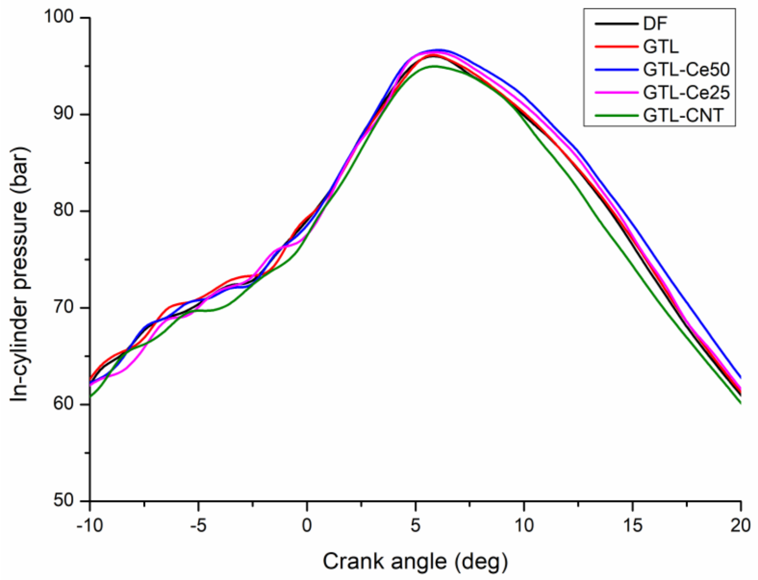

Figure 5.39. In-cylinder pressure of nano additive modified GTL

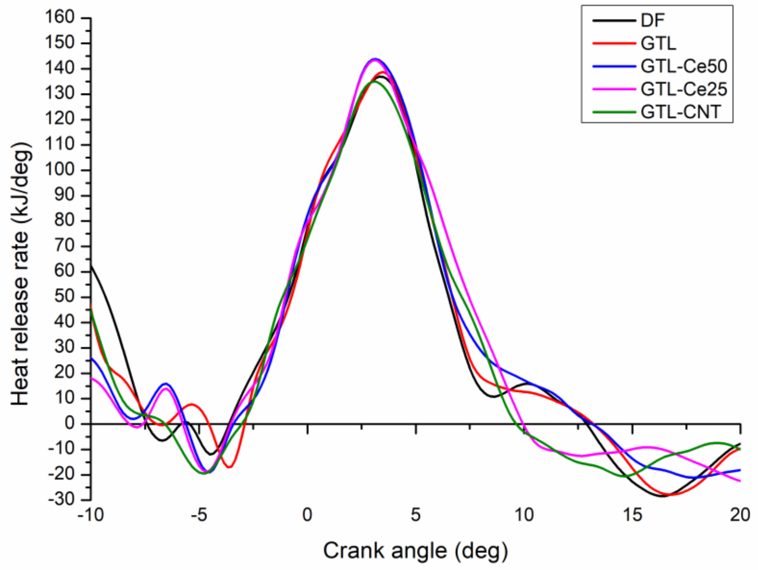

Figure 5.40. HRR of nano additive modified GTL

### *5.5.4. Pollutant emissions*

Similar to the CO emissions of DF, those of GTL is also significantly reduced by nano additives as shown in Figure 5.41. Among these nano additives, $CeO_2$ nanopowder of 50 nm and 25 nm size can reduce CO emissions of GTL by 16.7% and 18.1% respectively, whilst CNT can only reduce it by 11%. As CO is usually formed at lower temperature and incomplete combustion, $CeO_2$ nanopowder generates higher combustion temperature, and it of smaller size has higher combustion rate and thus reduces more CO. In contrast, the reduction of CO by CNT is mainly due to its improved spray despite its lower combustion temperature.

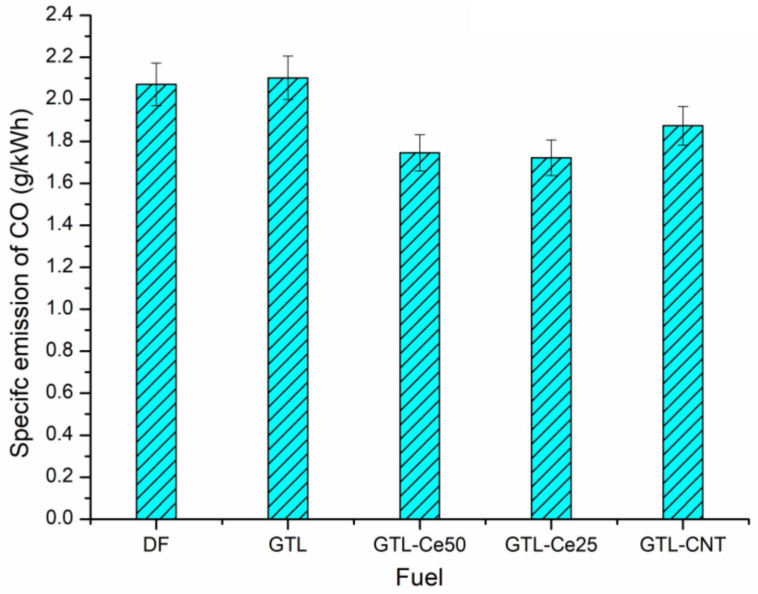

Figure 5.41. Specific emission of CO of nano additives modified GTL

As shown in Figure 5.42, all nano additives are capable of reducing $NO_x$ emissions. Similar to CO emissions, the difference between GTL-CNT and GTL is still the smallest in terms of $NO_x$ emissions, because the reduction of $NO_x$ by GTL-CNT is only determined by its lower combustion temperature due to more heat absorption during evaporation. In terms of $CeO_2$ nanopowder modified GTL, GTL-Ce50 produces the slightly fewer $NO_x$ emissions (5.1% lower than GTL) than GTL-Ce25 (4.8% lower than GTL). The difference of $NO_x$ emissions is not obvious between $CeO_2$ nanopowder of 25 nm size and that of 50 nm at this condition, because the engine is at low load where the temperature is not high enough to influence the reaction rate of different nanopowder sizes.

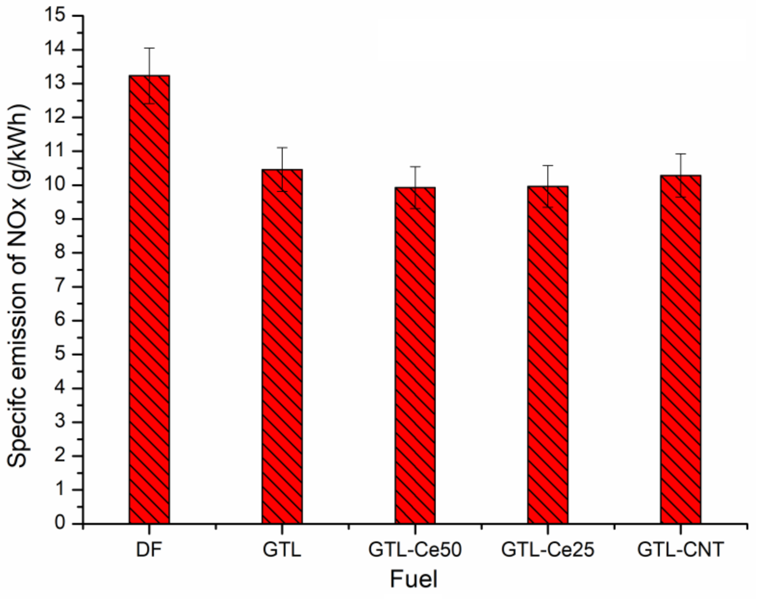

Figure 5.42. Specific emission of $NO_x$ of nano additives modified GTL

Compared with effect of CNT on standard diesel fuel, that on GTL is opposite in HC emissions, as Figure 5.43 shows that GTL-CNT produces more HC than GTL. According to Chapter 0, CNT has two contradictory effects. On one hand, CNT reduce viscosity and increase thermal diffusivity of fuel, which results in better spray and thus more complete combustion. On the other hand, CNT contributes to lower combustion temperature which is easier for the formation of HC. In this case, it is believed that the reduction of combustion temperature is more significant in HC emissions, as the difference of in-cylinder pressure between GTL and GTL-CNT is larger than that between DF and DF-CNT.

In terms of $CeO_2$ nanopowder, both modified GTL fuels can reduce HC emissions, and GTL-Ce25 brings in a larger reduction of HC emissions by 15.5%. According to Chapter 0, $CeO_2$ acts as the oxidant for HC as shown in Equation (5.8), and the product $Ce_2O_3$ participates in the deoxidization of $NO_x$. Therefore, the smaller size of $CeO_2$ nanopowder provides larger specific surface area and then enables higher reaction rate for $CeO_2$ to react with HC.

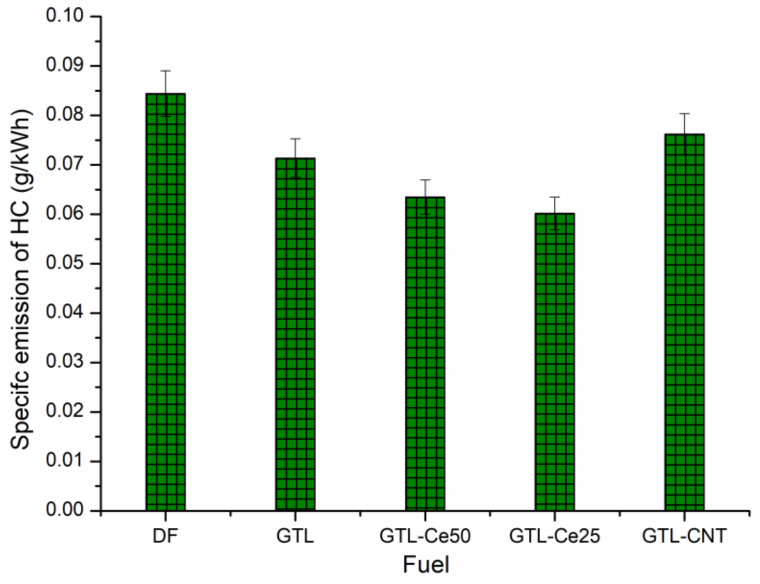

Figure 5.43. Specific emission of HC of nano additives modified GTL

As illustrated in Figure 5.44, all nano additives modified GTL fuels emit less PN than pure GTL. Among these fuels, GTL-CNT has the smallest level of reduction. First, GTL-CNT experiences improved spray and lower combustion temperature, which prohibits the formation of PM, as it is more easily to be formed in the fuel-rich zones at high temperature. Second, CNT can act as the nucleus for the formation of particulate matters at some conditions. Accordingly, the PN emissions of GTL-CNT is the comprehensive results of the two contradictory effects.

Compared with GTL-CNT, the $CeO_2$ nanopowder modified GTL fuels produce less PN emissions, especially GTL-Ce25, whose PN emissions are 34% lower than that of GTL. As mentioned in Chapter 0, $CeO_2$ nanopowder can reduce PN via two pathways. First, $CeO_2$ oxidizes PMs through Equation (5.10) after they are formed at high temperature. Second, $CeO_2$ consumes some HCs before they convert to PMs through dehydrogenation and carbonization. Moreover, $CeO_2$ nanopowder of 25 nm size has higher reaction rate due to its larger specific surface area.

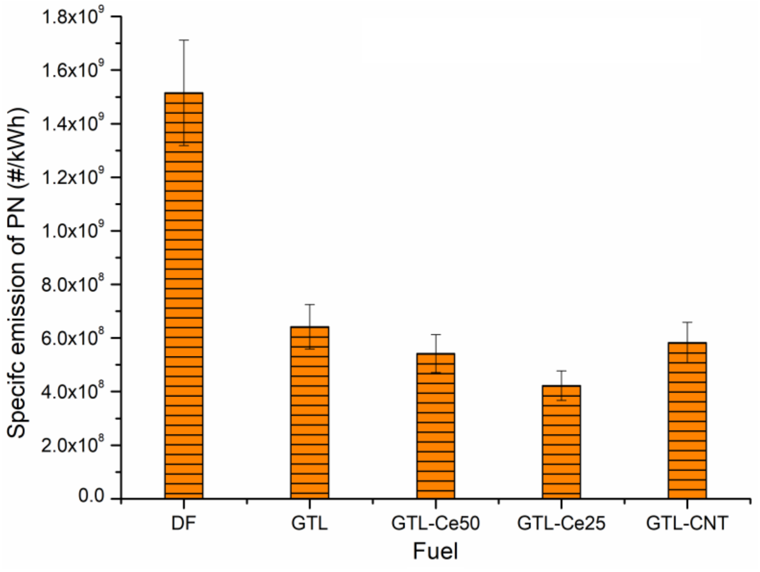

Figure 5.44. Specific emission of PN of nano additives modified GTL

### *5.5.5. Summary*

A combination of one type of renewable fuel (GTL) and two types of nano additives ($CeO_2$ nanopowder of different sizes and CNT) is analysed at constant engine speed and load. $CeO_2$ nanopowder modified GTL fuels generate higher in-cylinder pressure and produce fewer pollutant emissions including CO, $NO_x$, HC and PN than pure GTL due to its catalysis during combustion. Moreover, $CeO_2$ nanopowder of smaller size promotes the conversion of HC and PM but lower down the reaction rate of $NO_x$, because its larger specific surface area accelerates the reactions with combustion products. In contrast, the CNT modified GTL reduces both in-cylinder pressure and most pollutant emissions except HC, because the evaporation of GTL-CNT absorbs more heat and takes longer time, which influences the spray quality and combustion temperature.

## 5.6. Summary of Chapter 5

In this chapter, the engine performance including in-cylinder pressure, fuel consumption and pollutant emissions of nano additives modified standard diesel fuels (DF with $CeO_2$ nanopowder and CNT), renewable fuels (HVO and GTL) and nano additives modified renewable fuels (GTL with $CeO_2$ nanopowder and CNT) is investigated in a Cummins ISB 4.5 diesel engine. The main results are summarised below:

- The CNT modified diesel fuel experiences lower in-cylinder pressure and emits less CO, $NO_x$, HC and PN than standard diesel fuel, whilst their fuel consumptions have no comparable difference.
- The $CeO_2$ nanopowder modified diesel fuels have slightly higher in-cylinder pressure and almost the same fuel consumption compared with standard diesel fuel. Meanwhile, they

produce significantly lower level of $NO_x$, HC and PN emissions, whilst the reduction of CO can only happen within a certain maximum and minimum limits of engine condition (load and speed).

- CNT works in the engine mainly due to its unique two-step evaporation that absorbs more heat and takes longer time, whilst $CeO_2$ nanopowder act as a catalytic and coverts between $CeO_2$ and $Ce_2O_3$ via reversible reactions, where CO, HC and PM are oxidised and $NO_x$ is deoxidised.
- Diesel fuel with $CeO_2$ nanopowder of 25 nm size emits less HC and slightly more $NO_x$ than that with $CeO_2$ nanopowder of 50 nm size, because $CeO_2$ nanopowder of 25 nm has higher reaction rate of $CeO_2$ oxidizing HC and PM due to its larger surface area and in return reduces the reaction rate of the $Ce_2O_3$ deoxidizing $NO_x$.
- The renewable fuels HVO and GTL have lower fuel consumption and higher in-cylinder behaviour due to their higher LHV. $NO_x$, HC and PN can be reduced by the two renewable fuels, but CO is increased by GTL slightly.
- The influences of CNT and $CeO_2$ nanopowder of the two sizes on the renewable fuel (GTL) are similar to that on standard diesel fuel except that GTL-CNT produces higher HC emissions than pure GTL, probably because the evaporation of GTL-CNT absorbs more heat and thus reduces the spray quality and combustion temperature significantly.

In general, renewable fuels HVO and GTL show better performance in fuel consumption and in-cylinder behaviour than standard diesel fuel. However, both of them cannot reduce all the pollutant emissions simultaneously. In contrast, nano additives can reduce all pollutant emissions at most engine conditions for both standard diesel fuel and renewable fuels. Considering the spray characteristics in Chapter 3 and 4, it can be concluded that the benefits of $CeO_2$ nanopowder in CI engines is mainly attributed to its chemical properties, whilst renewable fuels and CNT improve the engine performance by the comprehensive effects of their physical and chemical properties.

# Chapter 6 . CFD model of supercritical fuel combustion

As illustrated in Chapter 5, the employment of renewable fuels and the modification of fuels by nano additives are two fuel pre-treatments of changing physical or chemical properties of the fuel before combustion to improve the performance of compression ignition engines. Nevertheless, both methods have shortcomings of high price of renewable fuels and nano additives, and limits of blending ratio with standard diesel fuel. Chapter 4 investigates the influence of high fuel temperature on spray, and thus inspires the idea of study the performance of fuel over its critical temperature. Consequently, the supercritical (SC) fuel combustion is analysed here to explore its potential for CI engines, as it is another fuel pre-treatment to change fuel properties before injected to the cylinder. In this chapter, a CFD model of a cylinder in the diesel engine is built, and then the standard diesel fuel at SC state is injected into the cylinder to burn. The reason of selecting standard diesel fuel is that the database of ANSYS Fluent contains sufficient properties of standard diesel fuel, especially properties at SC state, instead of those of HVO and GTL. The combustion behaviours and main products are compared with conventional spray combustion to estimate the benefits of SC fuel combustion to the engine performance.

## 6.1. 3D model and meshing work

### *6.1.1. Geometric model of the cylinder*

According to the full load curve in the Appendix B of the Cummins ISB 4.5 diesel engine, the output power stays around its maximum in the speed range of 1800 rpm to 2400 rpm, whilst the torque keeps highest level between 1400 rpm and 1800 rpm. Accordingly, 1800 rpm is the speed that both the power and torque can stay at around their maximum. The in-cylinder condition at 1800 rpm speed and 100% load is thus selected for the CFD model.

According to the in-cylinder pressure of the engine at the condition (Appendix C), the start of injection (SOI) and the peak in-cylinder pressure are found to occur at -5.47° crank angle and 10.2° crank angle, which means the duration of this period is 1.45 ms. The in-cylinder pressure in this period is shown in Figure 6.1.

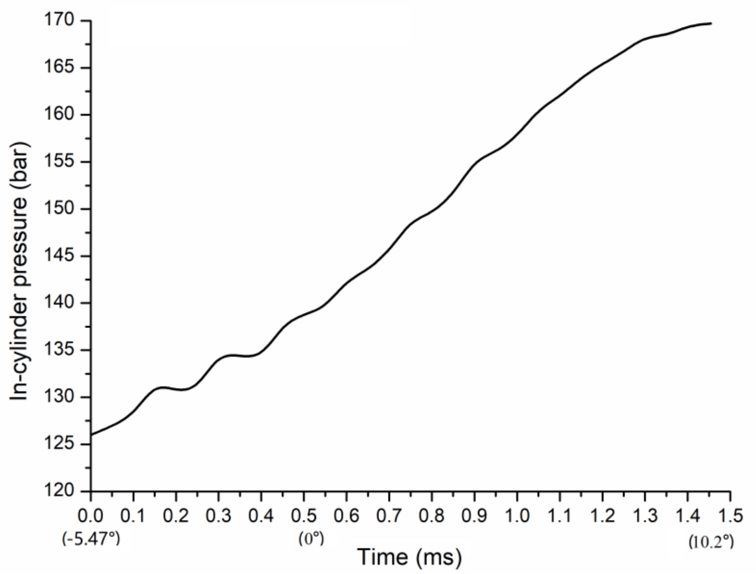

Figure 6.1. In-cylinder pressure of the diesel engine at 1800 rpm and full load from the SOI to the peak

According to engine speed and the geometric features of the engine in Table 6.1, we can calculate that the movement of the piston from the SOI to the top dead centre (TDC) is 0.405 mm and that from the TDC to the peak pressure is 1.29 mm. Therefore, the volume change during the 1.45ms is neglectable compared with the displacement of the piston in the whole stroke. Consequently, the combustion during this period can be treated as constant volume combustion. The positions of the piston head from the SOI to the peak pressure are illustrated in Figure 6.2.

| Parameter | Value |
|---|---|
| Displacement (L) | 4.5 |
| Stroke length (mm) | 124 |
| Bore size (mm) | 107 |
| Minimum volume (L) | 0.0918 |
| Length of connecting rod (mm) | 192 |
| Number of holes on each injector | 8 |
| Orifice of injection hole (mm) | 0.167 |

Table 6.1. Geometric data of the cylinder

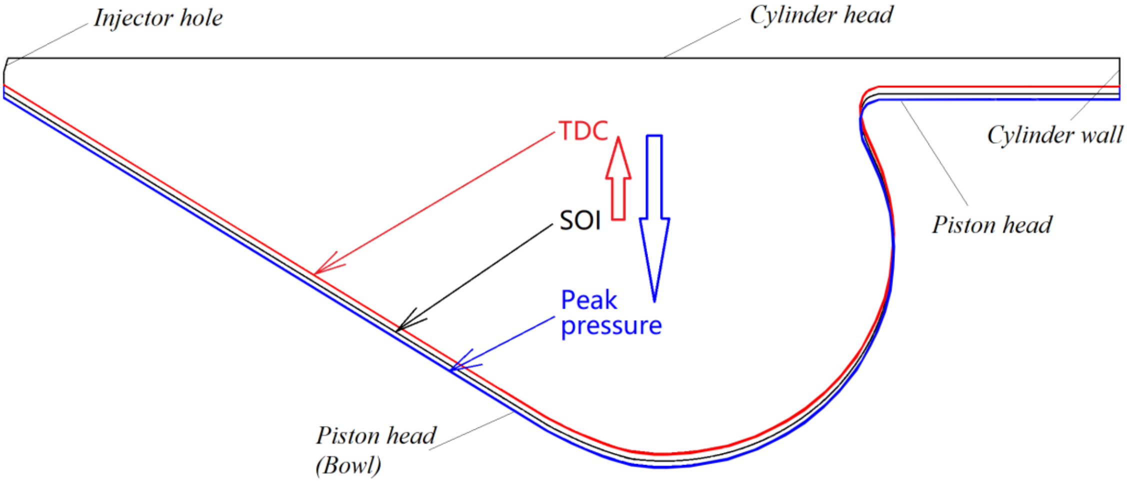

Figure 6.2. Positions of the piston head at each time

Figure 6.3 (a) is the P-V diagram of the cylinder during a whole cycle. It can be simplified and shown in Figure 6.3 (b), where 1-2 is the isentropic compression, 2-3 is the constant volume combustion, 3-4 is the constant pressure combustion, 4-5 is the isentropic expansion, and 4-1 is the constant volume cooling. Accordingly, the period from the SOI to the peak pressure is approximate viewed as the process of 2-3, and the pressure at the point 3 should be the peak in-cylinder pressure. As the area inside the cycle is the power, the peak in-cylinder pressure can significantly influence the output power of the engine. The cylinder model is thus built to simulate the conditions of the cylinder in the process of 2-3, the constant volume combustion in the cylinder.

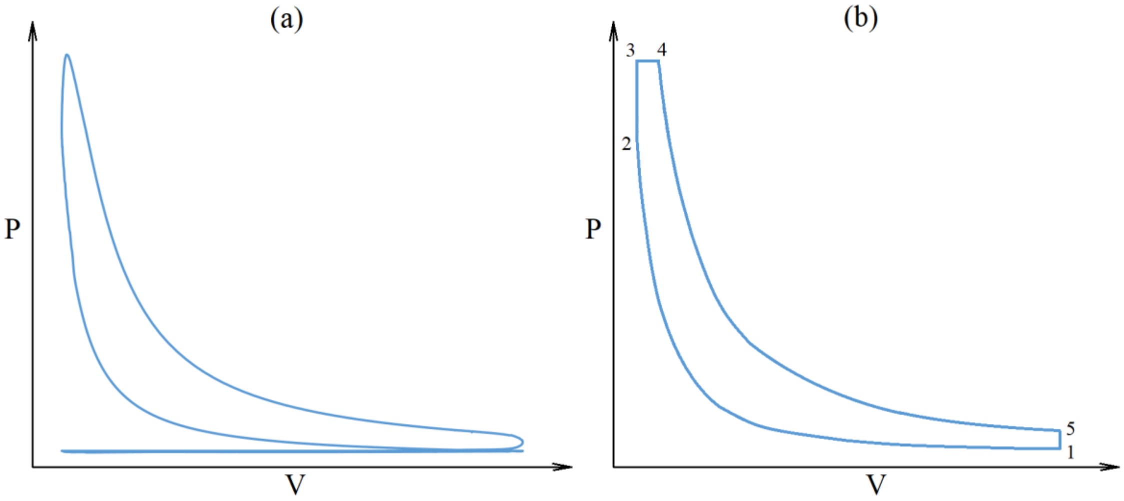

Figure 6.3. P-V diagram (a) and its simplified diagram (b) at selected engine condition

The total injected fuel of each injector per injection is 134.81 mg, which is calculated by the fuel flow rate in Table 6.2. Cummins Ltd provides the relationship between injected fuel mass per injection and the injection duration of the injector when working in the experimental engine (shown in Appendix D), and the injection duration is thus confirmed to be 2.06 ms, which is longer than the duration from the SOI to the peak pressure.

| | |
|---|---:|
| Speed (rpm) | 1800 |
| Load (%) | 100 |
| Power (kW) | 142.42 |
| Fuel flow rate (kg/h) | 29.12 |
| Fuel Temperature (°C) | 39.7 |
| Fuel density (kg/m$^3$) | 835 |
| SOI (°) | -5.47 |
| In-cylinder temperature at BDC (°C) | 43.43 |
| In-cylinder pressure at BDC (bar) | 2.73 |

Table 6.2. Fuel and in-cylinder conditions at selected speed and load

As the injector has 8 injection holes at the tip, a geometric model of 1/8 cylinder with constant volume is built to reduce the cost of computation. The volume of the model is set to 0.0119L, which is the 1/8 volume of the cylinder at the time of SOI. The 3D geometric model of the cylinder is finally built by ANSYS ICEM 18.1 as illustrated in Figure 6.4.

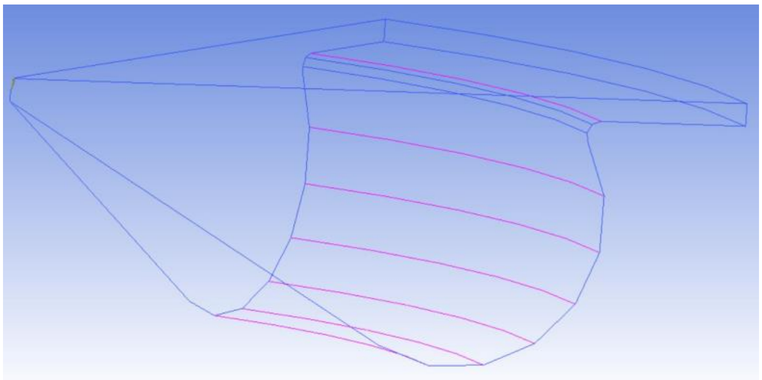

Figure 6.4. 3D geometric model of the cylinder

### *6.1.2. Meshes of the cylinder model*

Considering the complex geometric structure of the cylinder, the tetra/mixed unstructural mesh type is employed to generate meshes automatically with high quality of internal meshes. However, the tetra/mixed unstructural mesh are likely to have a poor quality at surface zones. Therefore, it is essential to refine the mesh around important surfaces to obtain higher precision. Finally, three cylinder models, Mesh-1, Mesh-2 and Mesh-3, are generated with the amount of meshes 139,426, 194,178 and 315,167, based on different maximum sizes of the global meshes and levels of refinement around the injector. The key information of the three models are listed in Table 6.3.

| Name | Mesh amount | Refinement size (mm) | Layers of refinement | Maximum global size (mm) | Mesh quality |
|---|---|---|---|---|---|
| Mesh-1 | 139,426 | 0.02 ~ 0.4 | ~ 80 | 2 | > 0.4 (99.69%) |
| Mesh-2 | 194,178 | 0.02 ~ 0.4 | ~ 80 | 1.5 | > 0.4 (99.71%) |
| Mesh-3 | 315,167 | 0.02 ~ 0.4 | > 200 | 1 | > 0.4 (99.99%) |

Table 6.3. Specification of the meshing work

The minimum size of the refined mesh is 0.02 mm, considering the orifice of the injection hole is 0.167 mm. The layers of refinement are determined by the sizes of the refined meshes and the thickness of the refined zone. The refinement is conducted by the Mesh density function in the ANSYS ICEM 18.1. The mesh quality is a value from 0 (poor) to 1 (good), and the percentage means how many meshes are over the quality. Usually the quality less than 0.3 is likely to result in difficulties in the convergence of the computation. In this case, over 99% meshes have the quality higher than 0.4, and the majority of them (about 60%) are between 0.9 and 1. One of the meshed and refined cylinder models is illustrated in Figure 6.5.

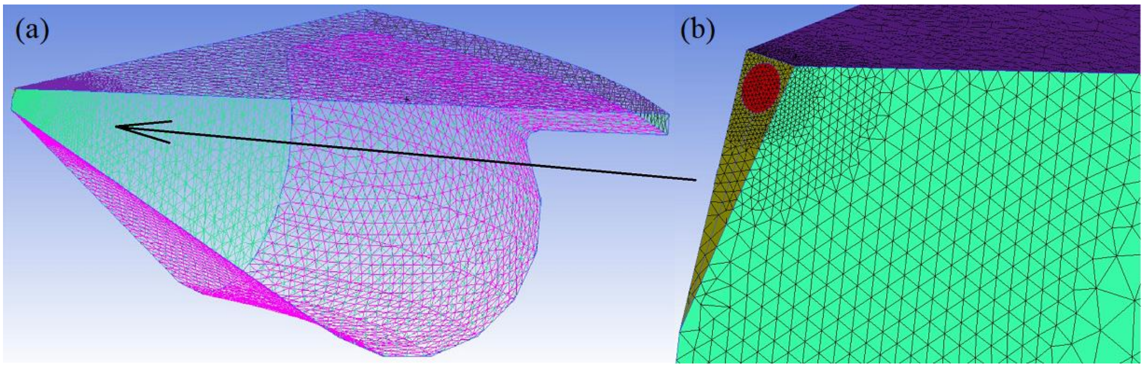

Figure 6.5. Meshes of the cylinder model (a) and its refinement (b) (194,178 meshes)

## 6.2. Theoretical principles

### *6.2.1. Breakup model of spray combustion*

The Wave breakup model is an important sub-model employed for the conventional spray combustion, which is the same as that in the spray CFD model. The detailed description can be found in Chapter 4.

### *6.2.2. Turbulence model*

The RNG k-ε model is a commonly used turbulence model for viscous fluids, which is the same as that in the spray model in Chapter 4.

### 6.2.3. Combustion model

In the cylinder, the fuel is injected to hot air and burn, and thus can be treated as diffusion combustion, which is strongly dependent on droplets breakup, evaporation and fuel-air mixing as well as chemical reactions. The non-premixed combustion model with the Probability Density Function (PDF) approach is selected to model both conventional spray combustion and SC fuel combustion, because it is specifically developed for turbulent diffusion flames with fast reactions.

The non-premixed combustion model assumes that the reaction chemistry is sufficiently rapid for equilibrium, which enables it to predict the formation of intermediate species (radicals), dissociation effects and rigorous turbulence-chemistry coupling via chemical equilibrium approach [169]. Meanwhile, the instantaneous thermochemical state of the fluid is assumed related to a conserved scalar quantity, the mixture fraction $f$. The mixture fraction can be written in terms of the atomic mass fraction as [197]:

$$f = \frac{Z_i - Z_{i,ox}}{Z_{i,fuel} - Z_{i,ox}} \tag{6.1}$$

where $Z_i$ is the elemental mass fraction for element $i$. The subscript $ox$ oxdenotes the value at the oxidizer stream inlet and the subscript $fuel$ denotes the value at the fuel stream inlet. If the diffusion coefficients for all species are equal, Equation (6.1) is identical for all elements, and the mixture fraction definition is unique. The mixture fraction is therefore the elemental mass fraction that originated from the fuel stream [41].

As the non-premixed combustion model is turbulent reacting flow, the PDF $p(f)$ is employed to describe the temporal fluctuations of $f$ and calculate averaged values of variables dependent on $f$. It is described by the equation below:

$$p(f)\Delta f = \lim_{T \to \infty} \frac{1}{T} \sum_i \tau_i \tag{6.2}$$

Where T is the time scale and $\tau_i$ is the amount of time that $f$ spends in the $\Delta f$ band. The shape of the PDF depends on the nature of the turbulent fluctuations in $f$, and is usually assumed as the β-function PDF for the single or two-mixture-fraction cases, as shown in Equation (6.3).

$$p(f) = \frac{f^{\alpha-1}(1-f)^{\beta-1}}{\int f^{\alpha-1}(1-f)^{\beta-1} df} \tag{6.3}$$

$$\alpha = \bar{f}[\frac{\bar{f}(1-\bar{f})}{\overline{f'^2}} - 1] \qquad (6.4)$$

$$\beta = (1-\bar{f})[\frac{\bar{f}(1-\bar{f})}{\overline{f'^2}} - 1] \qquad (6.5)$$

Where the $\bar{f}$ and $\overline{f'^2}$ are the mean fraction and its variance. Thus, the assumed PDF shape can be computed and used as the weighting function to determine the mean values of species mass fractions, density, and temperature via Equation (6.6) in adiabatic systems.

$$\overline{\emptyset}_i = \int_0^1 p(f)\emptyset_i(f)df \qquad (6.6)$$

Where $\emptyset_i$ is the equivalence ratio of the composition *i*, and $\overline{\emptyset}_i$ is its averaged value. Considering most combustion systems are not adiabatic, Equation (6.6) is then extended to the non-adiabatic systems, where turbulent fluctuations is included by means of a joint PDF $p(f, H)$, and $H$ is the instantaneous enthalpy. As $p(f, H)$ cannot be calculated for most engineering applications, it is simplified by the assumption that heat loss does not influence the turbulent enthalpy fluctuations significantly. As a result, $p(f, H)$ can be converted to Equation (6.7), and $\overline{\emptyset}_i$ is thus presented by Equation (6.8).

$$p(f, H) = p(f)\delta(H - \overline{H}) \qquad (6.7)$$

$$\overline{\emptyset}_i = \int_0^1 \emptyset_i(f, \overline{H})p(f)df \qquad (6.8)$$

Where $\overline{H}$ is the mean enthalpy, and it can be solved by the transport equation:

$$\frac{\partial(\rho\overline{H})}{\partial t} + \nabla \cdot (\rho\vec{v}\overline{H}) = \nabla \cdot \left(\frac{k_t}{c_p}\nabla\overline{H}\right) + S_h \qquad (6.9)$$

Where Sh is the source terms due to radiation, heat transfer to wall boundaries, and heat exchange with the dispersed phase.

#### *6.2.4. NO$_x$ emission models*

NO$_x$ and soot are the two types of emissions considered in this cylinder model.

NO$_x$ consists of mostly nitric oxide (NO), and a lesser degree of nitrogen dioxide (NO$_2$) and nitrous oxide (N$_2$O). The main pathways of NO$_x$ formation in the diesel engine are the thermal and prompt NO$_x$ mechanisms [169], which are mentioned in Chapter 5.

The thermal $NO_x$ formation is determined by a set of highly temperature-dependent chemical reactions known as the Zeldovich mechanism. The principal reactions governing the thermal $NO_x$ formation are shown in Equation (6.10) and (6.11) [41]:

$$O + N_2 \rightleftharpoons N + NO \tag{6.10}$$

$$N + O_2 \rightleftharpoons O + NO \tag{6.11}$$

In the near-stoichiometric or fuel-rich zones, another reaction is added to extend the thermal $NO_x$ formation:

$$N + OH \rightleftharpoons H + NO \tag{6.12}$$

In terms of the reaction rate of the thermal $NO_x$ formation, several reaction rate coefficients have been measured in studies [198-200] and critically evaluated in literature [201, 202]. The expression of the rate coefficients for Equation (6.10), (6.11) and (6.12) are given in Equation (6.13) to (6.18):

$$k_{f,1} = 1.8 \times 10^8 e^{-38370/T} \tag{6.13}$$

$$k_{f,2} = 1.8 \times 10^4 e^{-4680/T} \tag{6.14}$$

$$k_{f,3} = 7.1 \times 10^7 e^{-450/T} \tag{6.15}$$

$$k_{r,1} = 3.8 \times 10^7 e^{-425/T} \tag{6.16}$$

$$k_{r,2} = 3.81 \times 10^3 e^{-20820/T} \tag{6.17}$$

$$k_{r,3} = 1.7 \times 10^8 e^{-24560/T} \tag{6.18}$$

Where $k_{f,1}$, $k_{f,2}$ and $k_{f,3}$ are the reaction rate coefficients for Equation (6.10), (6.11) and (6.12) respectively, whilst $k_{r,1}$, $k_{r,2}$ and $k_{r,3}$ are the corresponding reverse reaction rate coefficients. The unit of these coefficients is $m^3/(mol \cdot s)$. The net rate of NO formation ($mol/m^3 \cdot s$) is thus given by:

$$\frac{d[NO]}{dt} = k_{f,1}[O][N_2] + k_{f,2}[O][N_2] + k_{f,3}[N][OH] - k_{r,1}[NO][N] - k_{r,2}[NO][O] - k_{r,3}[NO][H] \tag{6.19}$$

Where [O], [H] and [OH] are the concentration (mol/m$^3$) of them to calculate the rates of NO and N.

The rate of formation of NO$_x$ is significant only at high temperatures (over 1800 K), because it needs dissociation energy of 941 kJ/mol to break the strong triple bond of nitrogen. This effect is represented by the high activation energy of reaction Equation (6.10), which makes it the rate-limiting step of the extended Zeldovich mechanism. However, the activation energy for oxidation of N atoms is small. In a fuel-lean flame where oxygen is sufficient, the rate of consumption of free nitrogen atoms becomes equal to the rate of its formation, and thus a quasi-steady state can be established. This assumption is valid for most combustion cases, except in extremely fuel-rich combustion conditions. Therefore, the formation rate becomes:

$$\frac{d[NO]}{dt} = 2k_{f,1}[O][N_2]\frac{(1-\frac{k_{r,1}k_{r,2}[NO]^2}{k_{f,1}[N_2]k_{f,2}[O_2]})}{(1+\frac{k_{r,1}[NO]}{k_{f,2}[O_2]+k_{f,3}[OH]})} \qquad (6.20)$$

Equation (6.20) indicates that rate of NO formation will increase with increasing oxygen concentration. Meanwhile, thermal NO formation should be highly dependent on temperature but independent of fuel type. The concentrations (mol/m$^3$) of O-atom and OH radical are required for Equation (6.20). The partial equilibrium approach is employed to calculate the concentrations due to higher precision as shown in Equation (6.21) [203] and (6.22) [204, 205] respectively.

$$[O] = 36.64T^{1/2}[O_2]^{1/2}e^{-27123/T} \qquad (6.21)$$

$$[OH] = 2.129 \times 10^2 T^{-0.57}[O]^{1/2}[H_2O]^{1/2}e^{-4595/T} \qquad (6.22)$$

Therefore, the source term of NO due to thermal NO$_x$ mechanism is obtained in Equation (6.23).

$$S_{thermal,NO} = M_{w,NO}\frac{d[NO]}{dt} \qquad (6.23)$$

Where $M_{w,NO}$ is the molecular weight of NO (kg/mol).

The prompt NO$_x$ mechanism is a second mechanism for small amount of NO$_x$ formation which is most prevalent in low-temperature, fuel-rich and short residence time conditions [45]. Its reactions are now simplified as below:

$$CH + N_2 \rightleftharpoons \mathrm{HC}N + N \qquad (6.24)$$

$$N + O_2 \rightleftharpoons NO + O \tag{6.25}$$

$$HCN + \mathrm{OH} \rightleftharpoons H_2O + CN \tag{6.26}$$

$$CH + O_2 \rightleftharpoons NO + CO \tag{6.27}$$

A number of species from fuel fragmentation are the source of prompt $NO_x$ formation in hydrocarbon flames, and among them the $CH$ and $CH_2$ make the major contribution via Equation (6.24) and (6.28).

$$CH_2 + N_2 \rightleftharpoons HCN + NH \tag{6.28}$$

These HCN and NH can then form NO via reactions similar to those in the thermal $NO_x$ formation.

For hydrocarbon fuels, the rate of the prompt $NO_x$ formation can be shown as [41]:

$$\frac{d[NO]}{dt} = f k_{pr} [O_2]^a [N_2][FUEL] e^{-E_a/RT} \tag{6.29}$$

Where $f$ is a correction factor obtained by Equation (6.30), $k_{pr}$ is the reaction rate coefficient obtained by Equation (6.31), $a$ is the oxygen reaction order, $R$ is the universal gas constant, $T$ is the temperature, $E_a$ is 303474.125 J/mol. All the parameters are in SI units.

$$f = 4.75 + 0.0819n - 23.2\emptyset + 32\emptyset^2 - 12.2\emptyset^3 \tag{6.30}$$

$$k_{pr} = 6.4 \times 10^6 (RT/p)^{a+1} \tag{6.31}$$

Where $n$ is the number of carbon atoms in each fuel molecule, $\emptyset$ is the overall equivalence ratio for the flame, and $p$ is the pressure (Pa). And the source term of NO by prompt NOx mechanism can be obtained by:

$$S_{prompt,NO} = M_{w,NO} \frac{d[NO]}{dt} \tag{6.32}$$

In addition to the chemical mechanisms of $NO_x$ formation, ANSYS Fluent employs a transport equation for the NO concentration derived from the fundamental principle of mass conservation. In the equation, the convection and diffusion of NO and related species are taken into account. The transport equations of NO concentration are solved based on a given flow field and combustion solution, which makes the $NO_x$ emission to be post-processed from a combustion simulation. For thermal and prompt NOx mechanisms, only the NO species transport equation is in need as below:

$$\frac{\partial}{\partial t}(\rho Y_{NO}) + \nabla \cdot (\rho \vec{v} Y_{NO}) = \nabla \cdot (\rho \mathcal{D} \nabla Y_{NO}) + S_{NO} \qquad (6.33)$$

Where $\rho$ is the density, $Y_{NO}$ is the mass fraction of NO and $S_{NO}$ is the source term of NO.

### *6.2.5. Soot emission models*

Due to limited studies on the mechanism of soot formation, the one-step Khan and Greeves model is employed in this chapter, which is only based on a simple empirical rate. A single transport equation is solved in the model for the soot mass fraction as shown in Equation (6.26).

$$\frac{\partial}{\partial \mathrm{t}}(\rho Y_{soot}) + \nabla \cdot (\rho \vec{v} Y_{soot}) = \nabla \left(\frac{\mu_t}{\sigma_{soot}}\right) \nabla Y_{soot} + \mathcal{R}_{soot} \quad (6.34)$$

Where $\mu_t$ is the turbulent viscosity, $Y_{soot}$ is the soot mass fraction and $\sigma_{soot}$ is the turbulent Prandtl number for soot transport. $\mathcal{R}_{soot}$ is the net rate of soot generation (kg/(m$^3$·s)), which is the difference between soot formation $\mathcal{R}_{soot,form}$ and soot combustion $\mathcal{R}_{soot,comb}$. The soot formation and soot combustion are given by empirical equations below:

$$\mathcal{R}_{soot,form} = C_s p_{fuel} \emptyset^r e^{-E/RT} \qquad (6.35)$$

$$\mathcal{R}_{soot,comb} = \min[\mathcal{R}_1, \mathcal{R}_2] \qquad (6.36)$$

Where $C_s$ is the soot formation constant (kg/(N·m·s)), $p_{fuel}$ is the fuel partial pressure (Pa), $\emptyset$ is the equivalence ratio, *r* is the equivalence ratio exponent, and $E/R$ is the activation temperature (K). $\mathcal{R}_1$ and $\mathcal{R}_2$ are two rates which can be computed by Equation (6.37) and (6.38).

$$\mathcal{R}_1 = A\rho Y_{soot} \frac{\varepsilon}{k} \qquad (6.37)$$

$$\mathcal{R}_2 = A\rho\left(\frac{Y_{ox}}{v_{soot}}\right)\left(\frac{Y_{soot} v_{soot}}{Y_{soot} v_{soot} + Y_{fuel} v_{fuel}}\right)\frac{\varepsilon}{k} \qquad (6.38)$$

Where A is a constant, $Y_{ox}$ and $Y_{fuel}$ are the mass fractions of oxidizer and fuel, and $v_{soot}$ and $v_{fuel}$ are the mass stoichiometries for soot and fuel combustion.

### *6.2.6. Equation of state for the supercritical fuel*

As aforementioned, the fuel at supercritical (SC) state has similar compressibility, viscosity and diffusivity to gas, but its order of magnitude of density stays at the level of liquid. In the non-premixed combustion model, all materials participating in combustion are regarded as gas, which enables the viscosity and diffusivity of the fuel validated for its SC state. Nevertheless, the equations of state (EOS) for either liquid or ideal gas are not validated for the SC fuel in terms of its compressibility and density. As summarised in Chapter 2, the Peng-Robinson (P-R) EOS and the Soave-Redlich-Kwong (S-R-K) EOS are the two equations describing fluids near and above their critical points.

The P-R EOS is written as below [206]:

$$p = \frac{RT}{V-b} - \frac{a}{V^2+2bV-b^2} \tag{6.39}$$

Where $p$ is absolute pressure (Pa), $T$ is temperature (K), $V$ is specific molar volume ($m^3$/kmol), and $R$ is the universal gas constant (J·/(K·mol)). The parameters $a$ and $b$ are determined by Equation (6.40) and (6.41).

$$a = a_0[1 + n(1 - (T/T_c)^{0.5})]^2 \tag{6.40}$$

$$b = \frac{0.0778RT_c}{p_c} \tag{6.41}$$

Where $T_c$ and $p_c$ are the critical temperature and critical pressure respectively. $a_0$ and $n$ are calculated by the following equations:

$$a_0 = \frac{0.457247R^2T_c^2}{p_c} \tag{6.42}$$

$$n = 0.37464 + 1.5422\omega - 0.26992\omega^2 \tag{6.43}$$

Where $\omega$ is the acentric factor.

For the S-R-K EOS, it is written as Equation (6.44) [207].

$$p = \frac{RT}{V-b} - \frac{a}{V^2+bV} \tag{6.44}$$

Where $a$ is also obtained by Equation (6.40), whilst $a_0$ and $b$ are calculated by the following equations:

$$a_0 = \frac{0.42747R^2T_c^2}{p_c} \tag{6.45}$$

$$b = \frac{0.08664RT_c}{p_c} \tag{6.46}$$

And *n* here is determined by Equation (6.47).

$$n = 0.48 + 1.574\omega - 0.176\omega^2 \tag{6.47}$$

## 6.3. Model configuration for conventional spray combustion

### *6.3.1. Sub-model setup*

The Wave breakup model is configured the same as that in Chapter 4, where the breakup constants $B_0$ and $B_1$ are set to 0.61 and 20 according to the recommendation in literature [169], as it demonstrated a precise prediction on the in-cylinder combustion of diesel fuel. The dynamic-drag is employed as the drag law. The RNG k-ε model and the Standard Wall Functions are selected for the turbulence model and the near-wall treatment.

In terms of the non-premixed combustion model, the initial species are the diesel fuel, $O_2$ and $N_2$. The inlet diffusion and compressibility effects are also taken into account. As the non-premixed combustion assumes the combustion is in chemical equilibrium, the rich flammability limit (RFL) is brought in, because it is an important parameter controlling the suspension of the equilibrium chemistry calculation. It is set to 0.1 according to literature [169].

The thermal and prompt $NO_x$ models are activated and the partial equilibrium approach is selected for [O] and [OH] models. In the one-step Khan and Greeves (K-G) model for soot generation, the diesel fuel is selected as the fuel and $O_2$ is the oxidant.

The configuration of these models can be summarised in Table 6.4.

| Model | Approach | Parameter | Value |
|---|---|---|---|
| Droplet breakup | Wave breakup model | $B_0$ | 0.61 |
| | | $B_1$ | 20 |
| | | Drag law | Dynamic drag |
| | | Injection type | Surface injection |
| Combustion | Non-premixed model | Initial species | DF, $O_2$, $N_2$ |
| | | RFL | 0.1 |
| $NO_x$ emission | Thermal mechanism | [O] | Partial equilibrium |
| | Prompt mechanism | [OH] | Partial equilibrium |
| Soot emission | One-step K-G model | Oxidant | $O_2$ |

Table 6.4. Summary of models

### *6.3.2. Boundary conditions*

According to Table 6.2, the fuel temperature at the injector hole is 312.85 K, and the fuel mass flow rate and velocity are 0.00819 kg/s and 447.79 m/s respectively. The in-cylinder pressure is 126 bar at the SOI according to Figure 6.1, so the corresponding in-cylinder temperature can be calculated as 1175.68 K.

Besides, Cummins Ltd provides some empirical equations to calculate the average temperature of the cylinder head, cylinder wall and piston head, as shown below:

$$T_{w1} = 100 + 70p_e \tag{6.48}$$

$$T_{w2} = 100 + 40p_e \tag{6.49}$$

$$T_{w3} = 100 + 120p_e \tag{6.50}$$

Where $T_{w1}$, $T_{w2}$ and $T_{w3}$ are the temperature of cylinder head, cylinder wall and piston head (°C). And $p_e$ refers to the effective pressure (MPa), which can be obtained by Equation (6.47).

$$p_e = \frac{0.12 \cdot Power}{n \cdot V_d \cdot i} \tag{6.51}$$

Where *Power* is the engine output power (kW), *n* is engine speed (rpm), $V_d$ is the displacement volume of the cylinder ($m^3$), and *i* is the number of the cylinder. According to the equations above, the temperature of the cylinder head, cylinder wall and piston head can be calculated as 522.15 K, 458.29 K and 628.58 K. All the initial boundary conditions can thus be summarised in Table 6.5.

| Zone | Parameter | Value |
|---|---|---|
| Injector hole | Fuel (DF) molar fraction | 1 |
| | $N_2$ molar fraction | 0 |
| | $O_2$ molar fraction | 0 |
| | Fuel temperature (K) | 312.85 |
| | Fuel pressure (bar) | 1600 |
| | Fuel mass flow (kg/s) | 0.00819 |
| | Fuel velocity (m/s) | 447.79 |
| | Fuel droplet size (mm) | 0.167 |
| In-cylinder zone | Fuel (DF) molar fraction | 0 |
| | $N_2$ molar fraction | 0.21 |
| | $O_2$ molar fraction | 0.79 |
| | Temperature (K) | 1175.68 |
| | Pressure (bar) | 126 |
| Cylinder head | Constant temperature (K) | 522.15 |
| Cylinder wall | Constant temperature (K) | 458.29 |
| Piston head | Constant temperature (K) | 628.58 |

| Side face | Adiabatic wall | |
|---|---|---|

Table 6.5. Initial boundary conditions of conventional spray combustion

## 6.4. Model validation for conventional spray combustion

The CFD model is run by ANSYS Fluent 18.1 with three amounts of meshes. The in-cylinder pressure from the SOI to the peak pressure is obtained to validate the model, as it is the most important measurable parameter indicating the performance of the engine.

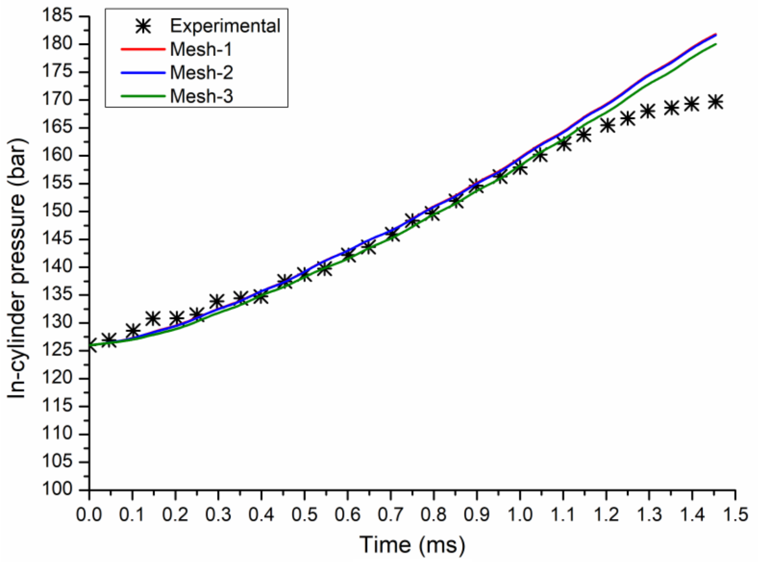

Figure 6.6. Predicted in-cylinder pressure by three CDF models versus the experimental data

As shown in Figure 6.6, the predicted in-cylinder pressure agrees with the experimental data with the bias no more than 1.4% at most time (0 ~ 1.1 ms), which indicates high precision of the CFD model. The bias stays relatively stable before 1.1 ms but then increases to 7.1% at 1.45 ms, because the volume of cylinder expands to larger than the SOI after about 1.1 ms, which reduces the in-cylinder pressure, although the combustion behaviour is still accurately predicted. Moreover, the CFD models Mesh-1, Mesh-2 and Mesh-3 obtain very closed in-cylinder pressure, and the error among them is within 1%. It demonstrates that the performance of the model is not sensitive to the amount of meshes. In other words, even the smallest amount of mesh, 139,426, is large enough to predict the in-cylinder pressure. Therefore, the CFD model is capable of predicting the in-cylinder combustion of the diesel engine from the SOI to the peak pressure.

## 6.5. Model configuration for SC fuel combustion

### *6.5.1. Sub-model setup*

At SC state, the surface tension is too low to main the phase boundary [117], and thus the droplet breakup model is no long validated. As the fuel is now SC fluid, the P-R EOS and S-R-K EOS are enabled for the injected fuel respectively to describe its physical behaviour in the cylinder. In contrast, the turbulence model, non-premixed combustion model, $NO_x$ and soot emission models are configured the same as those for the conventional spray combustion.

### *6.5.2. Boundary conditions*

As diesel fuel is in fact a mixture of many compounds, its critical pressure and critical temperature varies with different types. According to the data of fuel properties in literature [208, 209], the critical point of diesel fuel are set to 30 bar and 708 K respectively in this case. Considering the rail pressure is 1600 bar and the in-cylinder pressure and temperature are 126 bar and 1175.68 K, which are all over the critical point of diesel fuel, the fuel temperature at the injector hole is set to 730 K to ensure the fuel is at SC state. Other boundary conditions remain the same as the spray combustion. All the initial boundary conditions are summarised in Table 6.6.

| Zone | Parameter | Value |
|---|---|---|
| Injector hole | Fuel (DF) molar fraction | 1 |
| | $N_2$ molar fraction | 0 |
| | $O_2$ molar fraction | 0 |
| | Fuel temperature (K) | 730 |
| | Fuel pressure (bar) | 1600 |
| | Fuel mass flow (kg/s) | 0.00819 |
| | Fuel velocity (m/s) | 447.79 |
| | Fuel droplet size (mm) | 0.167 |
| In-cylinder zone | Fuel (DF) molar fraction | 0 |
| | $N_2$ molar fraction | 0.21 |
| | $O_2$ molar fraction | 0.79 |
| | Temperature (K) | 1175.68 |
| | Pressure (bar) | 126 |
| Cylinder head | Constant temperature (K) | 522.15 |
| Cylinder wall | Constant temperature (K) | 458.29 |
| Piston head | Constant temperature (K) | 628.58 |
| Side face | Adiabatic wall | |

Table 6.6. Initial boundary conditions of SC fuel combustion

## 6.6. Performance of the SC fuel combustion

Similar to the running of spray combustion model, the SC fuel combustion is also run by the three models of different amount of meshes to exclude the influence of meshes on results. The in-cylinder pressure of SC fuel combustion from the SOI to the peak pressure is thus obtained and shown in Figure 6.7, where the dash curves refer to the SC fuel combustion, and the solid curves are the conventional spray combustion.

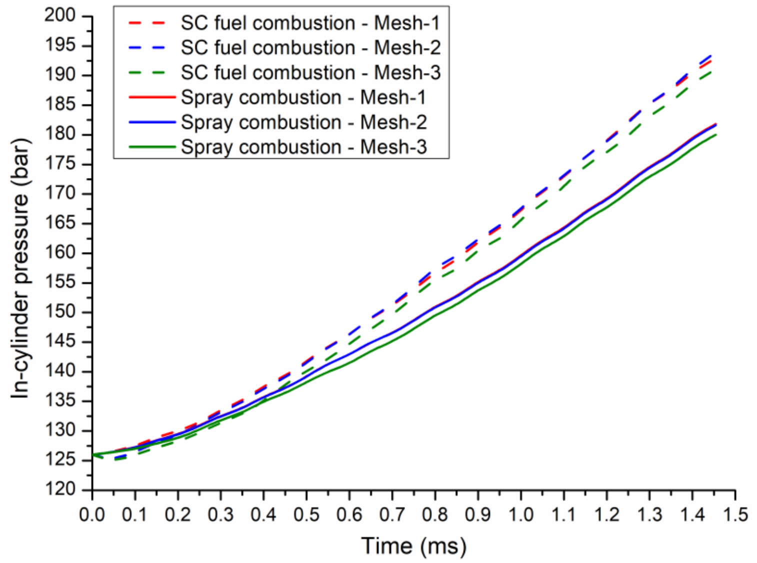

Figure 6.7. Comparison of in-cylinder pressure between SC fuel combustion and spray combustion obtained by three amounts of meshes

In Figure 6.7, the SC fuel combustion are all done using the P-R EOS. It illustrates that the in-cylinder pressure of SC fuel combustion is higher than that of spray combustion at most time after the SOI. Moreover, the difference between them increases with time and finally reaches 12.3 bar at the peak pressure. It indicates that the fuel at SC state experiences significantly more uniform fuel-air mixing process due to its gas-like properties, and thus results in more sufficient combustion and more heat release. Phenomenon is also likely to be caused by the heat loss during the conventional spray combustion, where liquid fuel droplets absorb heat from hot in-cylinder gas to evaporate, which does not exist in the SC fuel combustion. Meanwhile, the error of pressure among the three amounts of meshes at SC fuel combustion is within 1.5%, which means the performance of the SC fuel combustion model is stable to different amount of meshes. According to the in-cylinder pressure in Figure 6.7, a P-V diagram is obtained to indicate the performance of SC fuel combustion on the diesel engine as shown in Figure 6.8.

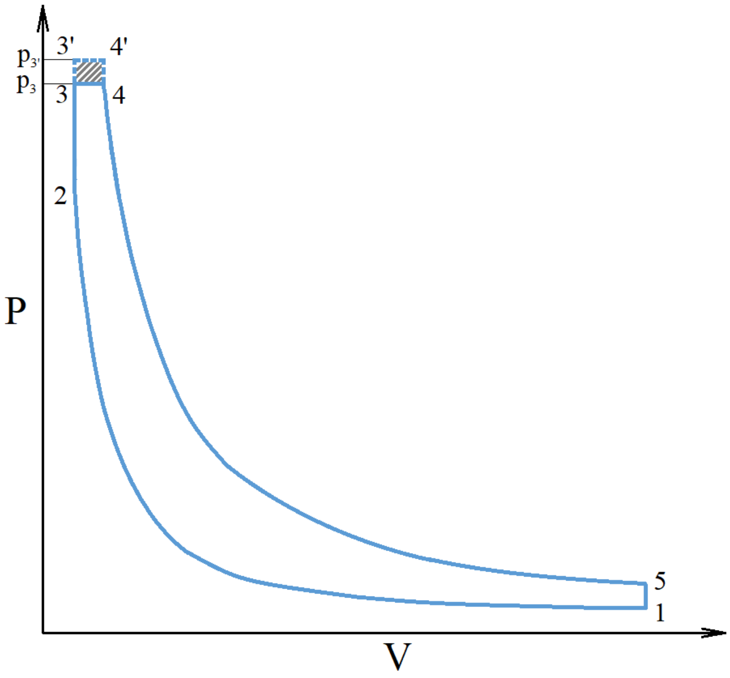

Figure 6.8. P-V diagram between the SC fuel combustion and spray combustion

In the P-V diagram, $p_3$ is the peak in-cylinder pressure of conventional spray combustion, and $p_{3'}$ is that of the SC fuel combustion. Assuming that 3’-4’ are constant pressure combustion as 3-4, and other processes in the cycle remain the same (the actual curve 4’-5 should be higher than that in Figure 6.8), the output power of the cylinder per cycle is improved by the improved peak pressure, and the growth of power is equal to the area of 3-3’-4’-4. After integrating the P-V diagram, the power of the engine can be obtained, which is at least improved from 142.42 kW to 145.92 kW by the SC fuel combustion. In other words, the efficiency of the engine can be increased by 2.5% by employing the method of the SC fuel combustion.

Moreover, the P-R EOS and S-R-K EOS are also compared on their performance by running the SC combustion model on Mesh-2. The results are shown in Figure 6.9, which indicates the difference between the results obtained using the P-R EOS and the S-R-K EOS is neglectable because it is less than 1%. In other words, the SC combustion model employing the P-R EOS and the S-R-K EOS have the same precision in predicting the in-cylinder pressure. However, the model using the S-R-K EOS is more difficult and slower to converge during the computation, compared with that using the P-R EOS of the same amount of meshes. Therefore, the following results are all obtained by the SC combustion model Mesh-2 employing the P-R EOS.

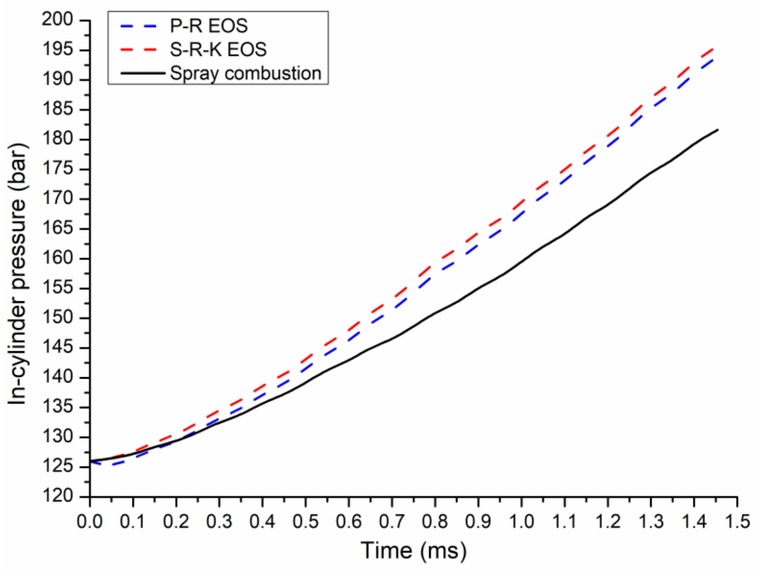

Figure 6.9. Comparison of SC combustion between P-R EOS and S-R-K EOS

In aforementioned context, I put forth the idea that the higher in-cylinder pressure of the SC fuel combustion is the result of more sufficient fuel-air mixing process. In order to further understand the details during combustion, the fuel distribution and temperature field in the cylinder should be analysed. Therefore, the contours of DF fuel mass fraction of conventional spray combustion (a) and SC fuel combustion (b) are illustrated in Figure 6.10, where the number 1, 2, 3, 4, 5 and 6 in the brackets refer to the order of time, 0.1 ms, 0.3 ms, 0.6 ms, 0.9 ms, 1.2 ms and 1.45 ms.

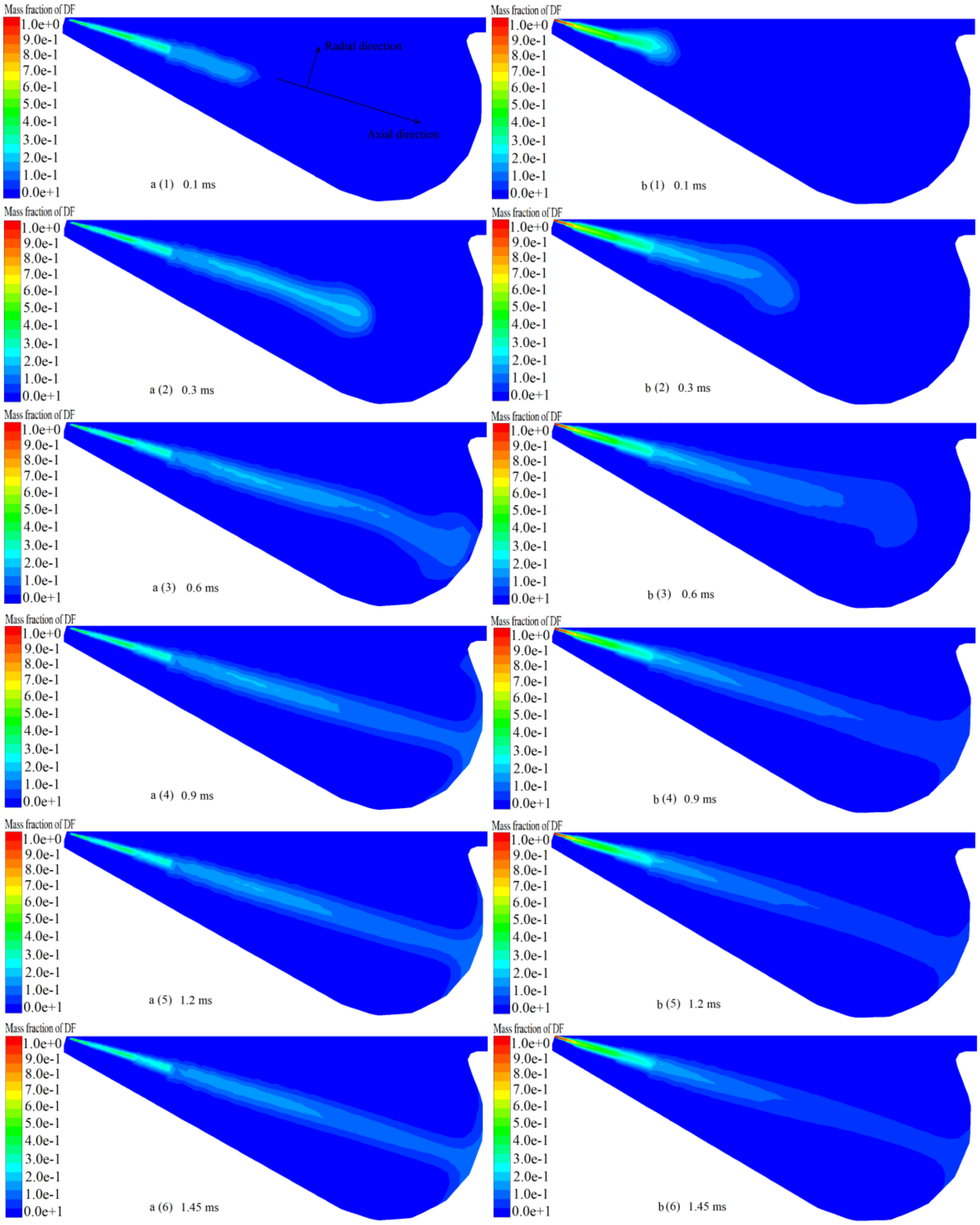

Figure 6.10. Contours of DF fuel mass fraction of conventional spray combustion (a) and SC fuel combustion (b) at the time 0.1, 0.3, 0.6, 0.9, 1.2 and 1.45 ms

As shown in Figure 6.10, before about 0.6 ms, the time that the unburnt fuel reaches the piston bowl, the penetration of unburnt fuel of the SC fuel combustion is always significantly shorter compared with that of the conventional spray combustion. The main reasons are twofold: First, the fuel at SC state burns immediately when injected to the high pressure and high temperature in-cylinder air, which results in higher consumption rate of fuel. In contrast, during the spray combustion, the cold fuel requires more time to breakup and evaporate before burning, which means more time is in need to consume the same amount of fuel during combustion. Second, in the spray combustion, the injected fuel is initially in the form of cold liquid droplets with high viscosity, surface tension and low diffusivity, which enables larger momentum to penetrate longer before being burnt. In the case of the SC fuel combustion, the SC fuel has no phase boundary and lower viscosity but higher diffusivity, which means it can fully and quickly mix with air to burn in short time, and thus results in smaller fuel-rich zone along the direction of injection axis.

After 0.6 ms, the difference in fuel penetration between the two combustion types is gone, but the mass fraction of fuel at the axial and radial directions are still significantly different between them. From the contours of 0.9 ms to 1.45 ms, the fuel mass fraction in the SC combustion decays dramatically along the injection axis to a very low level at the end, whilst that in the spray combustion keeps at very high level along the axial direction and is only slightly reduced at the bowl. In other words, the SC combustion has larger axial gradient of fuel mass fraction, but the axial gradient in spray combustion is much smaller. The difference in axial gradient of fuel mass fraction is mainly due to more sufficient fuel-air mixing and higher consumption rate of fuel, which on one hand reduces the global fuel concentration, and on the other hand consumes more local fuel compositions respectively. The relatively lower fuel concentration around the zone that piston bowl facing the injected fuel bring in advantages in prohibiting coking and carbon deposition, which is helpful to maintain the engine output performance and reduce pollutant emissions.

In the radial direction, the fuel at SC state spread to a larger area at the early stage of injection (before 0.6 ms) but the fuel mass fraction is overall at relative lower level, which means the radial gradient of fuel mass fraction and the overall fuel concentration in SC combustion are smaller than that in spray combustion. The phenomenon is mainly caused by the faster diffusion of fuel at the SC state. However, at the late stage of injection (after 0.6 ms), the overall fuel concentration of the SC fuel combustion in the radial direction is still lower than that of the spray combustion, but its radial gradient of fuel mass fraction becomes larger. It is mainly because most fuel at SC state has been burnt and thus less unburnt fuel left in the radial direction.

As a result of different fuel distribution in the cylinder, the temperature field of the two types of combustion are also distinct, which are shown in Figure 6.11.

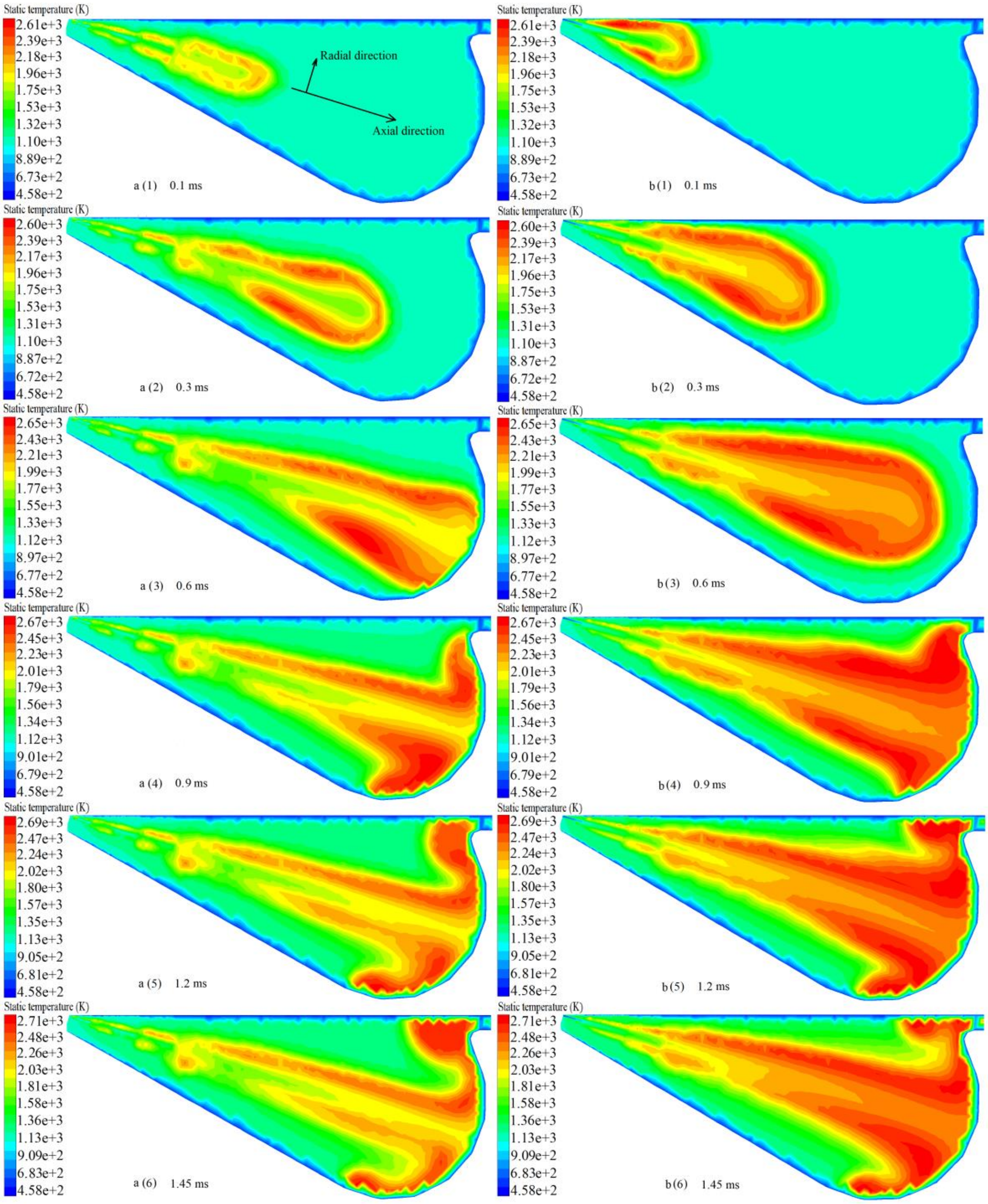

Figure 6.11. Contour of static temperature of conventional spray combustion (a) and SC fuel combustion (b) at the time 0.1, 0.3, 0.6, 0.9, 1.2 and 1.45 ms

In Figure 6.11, it can be observed that a low temperature zone exists along the axis in both types of combustion at the beginning (0.1 ms), which is mainly due to the lower temperature of fuel compared with the air temperature. However, with the combustion proceeding (after 0.1 ms), the temperature of the SC combustion along the axis grows dramatically to much higher than that in the unburnt zones, and finally becomes closed to the maximum temperature. In contrast, the zone along the axis in the spray combustion is always the low temperature zone, where the temperature is significantly lower than surroundings. The long-existing low temperature zone along the axis in the spray combustion is mainly because the unburnt fuel has low temperature and the cold fuel absorbs heat during evaporation, which does not occur to the SC fuel combustion.

Figure 6.11 also indicates that the flame of SC fuel combustion is located at obviously higher position than that of the spray combustion, especially at the early stage of injection (before 0.6 ms). It is mainly because the fuel in the spray combustion are in the form of liquid droplets before evaporating and burning, and thus tends to deposit to lower position until burning, whilst the SC fuel is quickly mixed with air and burnt, which avoids the problem of deposition.

The most important difference can be observed from Figure 6.11 is in the distribution of temperature field between the spray combustion and the SC fuel combustion. Along the axis, the temperature in the spray combustion is overall closed to the surrounding air temperature and thus the temperature gradient is very small, whilst that in the SC combustion experiences significant increase and enhance has larger gradient. This phenomenon illustrates faster fuel-air mixing and combustion in the SC fuel combustion, which results in more sufficient combustion is the axial direction of fuel injection, compared with the spray combustion. In the radial direction, the high temperature zones in the SC fuel combustion is larger and more homogeneous than that in the spray combustion. Furthermore, its radial temperature gradient is relatively smaller than that in the spray combustion. Compared with the SC combustion, the high temperature zones in the spray combustion are more concentrated. The difference in radial temperature distribution is also the consequence of higher fuel-air mixing and combustion rates.

Apart from the difference in the temperature field, the overall average value of the in-cylinder temperature are also different between the SC fuel combustion and the spray combustion, as shown in Figure 6.12.

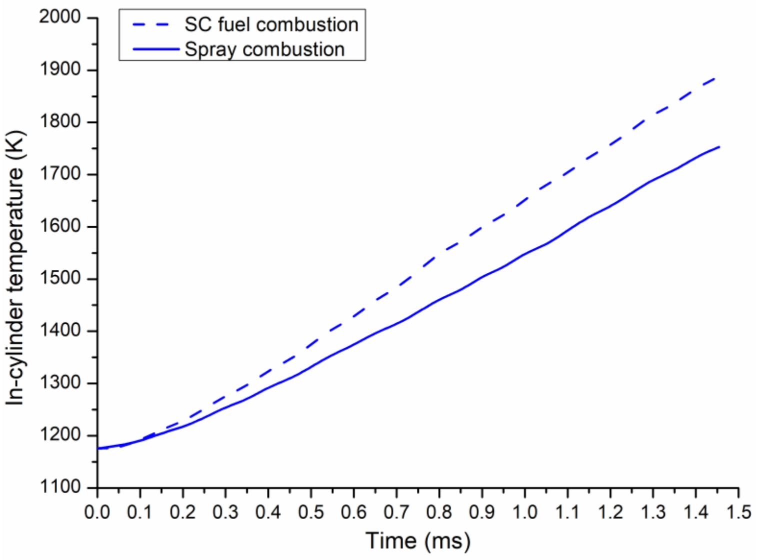

Figure 6.12. The area-averaged in-cylinder temperature of the SC fuel combustion and the spray combustion

In Figure 6.12, the SC fuel combustion demonstrates higher area-averaged in-cylinder temperature at most time after the SOI than the spray combustion, which the reason of higher in-cylinder pressure during SC fuel combustion. In addition to the more uniform temperature field in the SC fuel combustion, the SC fuel combustion is capable of not only improving the engine output power, but also prohibiting the formation of pollutant emissions. It is easier to notice that the formation of $NO_x$ and soot would be especially influenced, when viewing the contours of fuel and temperature together as shown in Figure 6.13. In order to observe the fuel distribution more clearly, the fuel mass fraction in Figure 6.13 is set to smaller scale.

In Figure 6.13, zone A is the fuel-lean zone during both spray combustion and SC fuel combustion. However, during the spray combustion, the temperature of zone A is higher and the area of high temperature zone is larger than those during SC combustion. This phenomenon will promote $NO_x$ formation in spray combustion according to the Thermal $NO_x$ mechanism. In the zone B, both the spray combustion and the SC fuel combustion are fuel-rich, but the temperature of zone B in the spray combustion is lower than that in the SC combustion, which promotes the Prompt $NO_x$ formation. As a result, the total $NO_x$ emission in the spray combustion is highly likely higher than that in the SC fuel combustion.

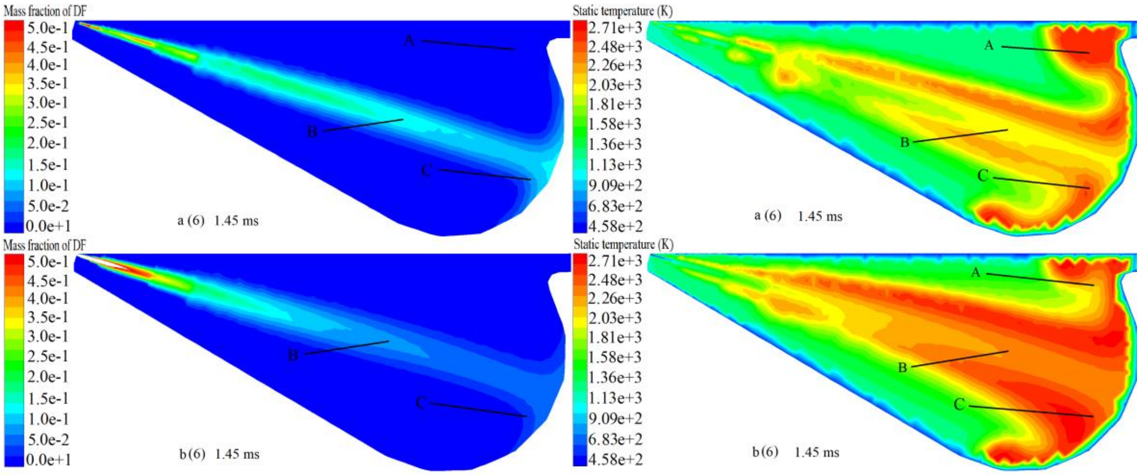

Figure 6.13. Illustration of temperature field associated with fuel distribution at 1.45 ms during spray combustion (a) and SC fuel combustion (b)

Compared with $NO_x$, the soot formation is more related to geometric location, because it is very easy to generate soot in fuel-rich zones of high temperature, especially in the near-wall areas, where coking or carbon deposition tend to occur. In zone C, the temperature of the SC fuel combustion is closed to that of the spray combustion, but the fuel mass fraction there is much lower than that of the spray combustion. Consequently, more soot is likely to be generated by the spray combustion in zone C. Moreover, the high temperature area in zone C during the spray combustion is more closed to the wall (piston bowl) compared to that during the SC fuel combustion, which is the seedbed for soot formation. Consequently, the situation in the spray combustion is beneficial to soot generation.

According to the fuel distribution and temperature field, the $NO_x$ and soot generation are obtained by the end of the process (the time of the peak pressure). As shown in Figure 6.14, the masses of $NO_x$ and soot in the SC fuel combustion are both significantly lower than those in the spray combustion at the end of constant volume combustion, respectively. The reduction of $NO_x$ during SC fuel combustion at this time seems to conflict with the results in Figure 6.12, where the area-averaged in-cylinder temperature of SC fuel combustion is higher than spray combustion. However, according to the thermal $NO_x$ formation mechanism, $NO_x$ formation can be promoted in fuel-lean zones at high temperature. In this case, the fuel-lean zone in SC fuel combustion has lower temperature than that in spray combustion, as shown in Figure 6.13. As a result, the $NO_x$ formation would be reduced in SC fuel combustion even though its area-averaged temperature is higher. Similar result was also found in an experimental study in a vessel [165], where $NO_x$ was not found in SC fuel combustion. The phenomenon indicates the SC fuel combustion is capable of significantly reducing $NO_x$ and soot emissions simultaneously during the constant volume combustion period, due to its more sufficient fuel-air mixing process and more evenly distributed temperature fields.

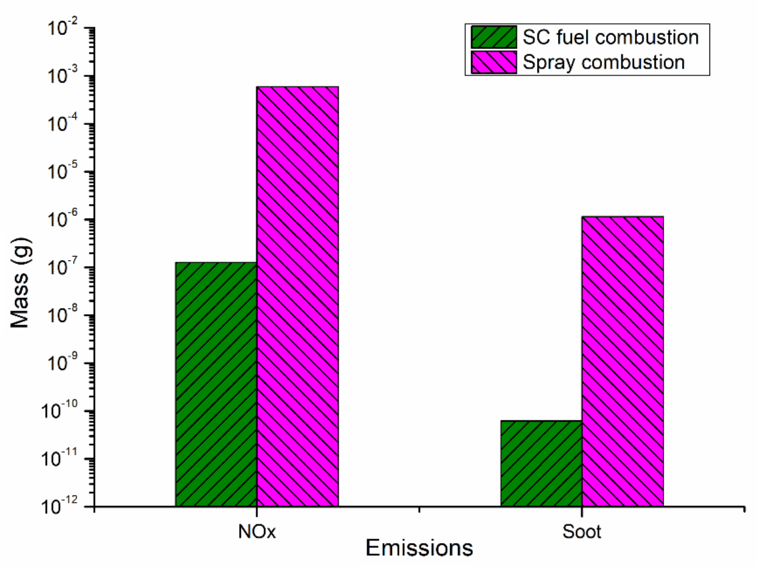

Figure 6.14. Mass of $NO_x$ and soot at the time of peak pressure

## 6.7. Summary of Chapter 6

In this chapter, a CFD model of the diesel engine cylinder is built, and both the conventional spray combustion and SC fuel combustion are investigated by it in the period from the SOI to the peak pressure. The SC fuel combustion is demonstrated superior to other fuel pre-treatments due to its benefits to engine output power and emissions. The main results are summarised as follows:

- The CFD model can predict the spray combustion well in this period, as the bias between the predicted in-cylinder pressure and the experimental data is within 1.4% at most time.
- The in-cylinder peak pressure of SC fuel combustion is 12.3 bar higher than that of spray combustion due to its more complete combustion, which can improve the engine output power by at least 2.5%.
- The injected fuel in the SC fuel combustion is less concentrated compared with that in the spray combustion, caused by faster fuel-air mixing and fuel consumption rate.
- The temperature field in the SC fuel combustion is relatively more homogeneous than that in the spray combustion, due to more uniform fuel-air mixture and faster combustion.
- The $NO_x$ and soot generated in the SC fuel combustion are significantly reduced simultaneously during the constant volume combustion period, compared with those in the conventional spray combustion.

# Chapter 7 . Conclusions and future work

## 7.1. Conclusions

This project aims to estimate the potential of three fuel pre-treatments prior to combustion for combustion improvement on a compression ignition engine by changing fuel properties, which are the employment of renewable fuels (HVO and GTL), nano additive modified fuels (multi-wall carbon nanotube and $CeO_2$ nanopowder of 25 nm and 50 nm) and supercritical (SC) fuel combustion respectively. The study is conducted from the perspective of macroscopic spray characteristics and engine performance via both experimental and numerical (CFD) methods. Therefore, the average cone angle, spray tip penetration, engine in-cylinder pressure and pollutant emissions of renewable fuels and nano additive modified fuels are comparatively investigated. And SC fuel combustion is researched by the CFD approach on its in-cylinder pressure, fuel distribution, temperature field and pollutant emissions. Meanwhile, the influence of fuel conditions (fuel temperature and rail pressure) and ambient conditions (ambient pressure and temperature) is analysed on spray characteristics. Moreover, the impact of engine speed and load is also investigated on engine pollutant emissions of the test fuels. The conclusions can be drawn as follows:

- GTL has the best macroscopic spray characteristics, because it shows the smallest spray tip penetration during both the injection and post-injection periods, whilst DF has the largest penetration, and the penetration of HVO is between that of GTL and DF. Meanwhile, the average cone angles of them are almost the same. It indicates GTL will perform best in the diesel engine in terms of reducing carbon deposition on the piston or cylinder wall.
- Nano additive such as $CeO_2$ nanopowder has no significant impact on the macroscopic spray characteristics, because its ultra-low concentration cannot change the fuel physical properties significantly. It means the $CeO_2$ nanopowder will influence diesel engines via chemical reactions instead of improving any physical properties. CNT can increase spray tip penetration slightly in the post-injection period, because a large amount of fuel is inside the CNT, and the fuel can only evaporate via the two ends of CNT instead of all directions due to its thick wall and hollow structure. As a result, the duration of evaporation of the liquid fuel is enlarged. It indicates the CNT mainly works by changing the evaporation process of fuels in the engine.
- In the CFD spray model, the Wave breakup model has higher precision than the KHRT breakup model on predicting the spray tip penetration and the average cone angle.

- The rail pressure is capable of increasing the spray tip penetration significantly but has no impact on the average cone angle, which can only be enlarged significantly by increasing ambient pressure but reduced slightly by increasing ambient temperature.
- During injection, the spray tip penetration can be significantly reduced by growing ambient pressure but increased by increasing ambient temperature slightly. However, in the post-injection period, high ambient temperature reduces the spray tip penetration due to faster evaporation.
- The increasing fuel temperature can only slightly reduce the spray tip penetration at high ambient temperature during the injection, and its influence becomes more significant in the post-injection period. However, the average cone angle is not sensitive to the fuel temperature.
- The renewable fuels HVO and GTL have lower fuel consumption and higher in-cylinder pressure than the standard diesel fuel at the fixed engine condition. Moreover, GTL and HVO can reduce $NO_x$, HC and PN. Considering HVO and GTL have higher CN and LHV, some modifications such as retarding fuel injection and reducing fuel flow rate might be required when employing these renewable fuels for CI engines.
- The $CeO_2$ nanopowder can slightly increase the in-cylinder pressure, and significantly reduce $NO_x$, HC and PN emissions at most engine conditions, whilst CO can only be reduced when the engine load and speed are within certain maximum and minimum limits. It is because $CeO_2$ nanopowder is a catalytic and coverts between $CeO_2$ and $Ce_2O_3$ via reversible reactions, and thus oxidises CO, HC and PM and deoxidises $NO_x$.
- CNT slightly reduces the in-cylinder pressure and significantly lowers down the emissions of CO, $NO_x$, HC and PN when blending with all test fuels except GTL, mainly because its evaporation absorbs more heat and costs longer time before the combustion.
- The SC fuel combustion shows advantages in compression ignition engines, because the in-cylinder peak pressure of SC fuel combustion is significantly higher than that of conventional spray combustion, which can improve the engine output power and efficiency by at least 2.5%.
- The fuel concentration and temperature field in the cylinder during the SC combustion are more evenly distributed compared with those during the spray combustion, and thus enable more sufficient combustion and can significantly reduce the formation of $NO_x$ and soot simultaneously during the constant combustion period.

## 7.2. Future work

Although the three fuel pre-treatments for a compression ignition engine are investigated in this project from the perspective of macroscopic spray characteristics and engine performance, some other work is still worth doing to further explore their performance. The recommended future work is mainly about the retrofitting of the CVV system and the more experiments on the compression ignition engine:

- Replace with heaters of larger and adjustable power to further increase the ambient temperature in the CVV. By this means, the CVV will be capable of conducting the combustion experiment to observe the detailed combustion process of fuels, e.g., ignition delay, flame shape, flame velocity etc.
- Investigate the SC fuel combustion in the CVV to obtain more detailed information about its temperature, pressure and products etc.
- Conduct the engine experiments of renewable fuels and nano additive modified fuels at more various conditions to analyse the influence of conditions on their engine performance.
- More detailed analysis of exhaust gas and PM emissions should be done. For instance, using the scanning electron microscope or chromatograph to observe the composition of PM and identify the existence of $CeO_2$ nanopowder in the exhausted PM and track its evolution after combustion.
- Retrofit a compression ignition engine to conduct the experiment on SC fuel combustion and evaluate its actual on-road performance in terms of power output and pollutant emissions.
- SC fuel combustion requires the injector to withstand high temperature for long time, which is a challenge to current compression ignition engines. Therefore, new injectors would be fabricated for SC fuel combustion in the future.
- Explore the potential of the combination of the three fuel pre-treatments, e.g., using some nano additives to modify a type of renewable fuel, and thus obtain nano additive modified renewable fuels which are easier to be converted to the SC state.

# References

[1] B. Dudley, "BP Energy Outlook - 2018 edition," 2018.

[2] A. Ajanovic and R. Haas, "Economic challenges for the future relevance of biofuels in transport in EU countries," *Energy,* vol. 35, no. 8, pp. 3340-3348, 2010.

[3] P.-q. Tan, Z.-y. Hu, D.-m. Lou, and Z.-j. Li, "Exhaust emissions from a light-duty diesel engine with Jatropha biodiesel fuel," *Energy,* vol. 39, no. 1, pp. 356-362, 2012.

[4] H. Yun and R. D. Reitz, "Combustion optimization in the low-temperature diesel combustion regime," *International Journal of Engine Research,* vol. 6, no. 5, pp. 513-524, 2005.

[5] *COMMISSION REGULATION (EU) 2016/1718,* C. R. (EU) 2016/1718, 2016.

[6] V. Praveena and M. L. J. Martin, "A review on various after treatment techniques to reduce NOx emissions in a CI engine," *Journal of the Energy Institute,* vol. 91, no. 5, pp. 704-720, 2018/10/01/ 2018.

[7] G. Gilpin, O. J. Hanssen, and J. Czerwinski, "Biodiesel's and advanced exhaust aftertreatment's combined effect on global warming and air pollution in EU road-freight transport," *Journal of Cleaner Production,* vol. 78, pp. 84-93, 2014/09/01/ 2014.

[8] G. Knothe, "Some aspects of biodiesel oxidative stability," *Fuel Processing Technology,* vol. 88, no. 7, pp. 669-677, 2007.

[9] D. Leung, B. Koo, and Y. Guo, "Degradation of biodiesel under different storage conditions," *Bioresource technology,* vol. 97, no. 2, pp. 250-256, 2006.

[10] A. Bouaid, M. Martinez, and J. Aracil, "Long storage stability of biodiesel from vegetable and used frying oils," *Fuel,* vol. 86, no. 16, pp. 2596-2602, 2007.

[11] F. Millo, B. K. Debnath, T. Vlachos, C. Ciaravino, L. Postrioti, and G. Buitoni, "Effects of different biofuels blends on performance and emissions of an automotive diesel engine," *Fuel,* vol. 159, pp. 614-627, 2015.

[12] T. Bohl, A. Smallbone, G. Tian, and A. P. Roskilly, "Particulate number and NOx trade-off comparisons between HVO and mineral diesel in HD applications," *Fuel,* vol. 215, pp. 90-101, 2018.

[13] A. C. Vosloo, "Fischer–Tropsch: a futuristic view," *Fuel processing technology,* vol. 71, no. 1-3, pp. 149-155, 2001.

[14] H. C. Heng and S. Idrus, "The future of gas to liquids as a gas monetisation option," *Journal of Natural Gas Chemistry,* vol. 13, no. 2, pp. 63-70, 2004.

[15] A. Fayyazbakhsh and V. Pirouzfar, "Comprehensive overview on diesel additives to reduce emissions, enhance fuel properties and improve engine performance," *Renewable and Sustainable Energy Reviews,* vol. 74, pp. 891-901, 2017.

[16] B.-J. Rho, S.-J. Kang, J.-H. Oh, and S.-G. Lee, "Swirl effect on the spray characteristics of a twin-fluid jet," *KSME International Journal,* vol. 12, no. 5, pp. 899-906, 1998.

[17] S. H. Park, I. M. Youn, Y. Lim, and C. S. Lee, "Influence of the mixture of gasoline and diesel fuels on droplet atomization, combustion, and exhaust emission characteristics in a compression ignition engine," *Fuel Processing Technology,* vol. 106, pp. 392-401, 2013.

[18] J. B. Heywood, "Internal combustion engine fundamentals," 1988.

[19] A. H. Lefebvre, *Gas turbine combustion*. CRC Press, 2010.

[20] A. Lefebvre, *Atomization and sprays*. CRC press, 1988.

[21] H. Liu, *Science and Engineering of Droplets:: Fundamentals and Applications*. William Andrew, 1999.

[22] W. A. Sirignano and C. Mehring, "Review of theory of distortion and disintegration of liquid streams," *Progress in energy and combustion science,* vol. 26, no. 4, pp. 609-655, 2000.

[23] W. A. Sirignano, *Fluid dynamics and transport of droplets and sprays*. Cambridge University Press, 1999.

[24] R. D. Reitz and F. V. Bracco, "Mechanism of atomization of a liquid jet," *Physics of Fluids (1958-1988)*, vol. 25, no. 10, pp. 1730-1742, 1982.

[25] S. P. Lin and R. D. Reitz, "Drop and spray formation from a liquid jet," *Annual Review of Fluid Mechanics*, vol. 30, no. 1, pp. 85-105, 1998.

[26] M. Arai, M. Tabata, H. Hiroyasu, and M. Shimizu, "Disintegrating process and spray characterization of fuel jet injected by a diesel nozzle," SAE Technical Paper1984.

[27] S. K. Das and O. T. Lim, "Spray Simulation of n-heptane in a Constant Volume Combustion Chamber Over a Wide Range of Ambient Gas Density and Fuel Temperature," *Energy Procedia*, vol. 105, pp. 1813-1820, 2017.

[28] Z. Zhang, Y. Lu, A. P. Roskilly, X. Yu, Y. Wang, and A. Smallbone, "Investigation of the macroscopic characteristics of Hydrotreated Vegetable Oil (HVO) spray using CFD method," *Fuel*, vol. 237, pp. 28-39, 2019.

[29] T. Hulkkonen, H. Hillamo, T. Sarjovaara, and M. Larmi, "Experimental study of spray characteristics between hydrotreated vegetable oil (HVO) and crude oil based EN 590 diesel fuel," SAE Technical Paper0148-7191, 2011.

[30] J. Ryu, H. Kim, and K. Lee, "A study on the spray structure and evaporation characteristic of common rail type high pressure injector in homogeneous charge compression ignition engine," *Fuel*, vol. 84, no. 18, pp. 2341-2350, 2005.

[31] J. Legg, A. Narvaez, and V. McDonell, "Performance of algae-derived renewable diesel in a twin-fluid airblast atomizer," in *Proceedings of the 12th triennial international conference on liquid atomization and spray systems, Heidelberg, Germany Google Scholar*, 2012, pp. 56-65.

[32] Y. Ma, R. Huang, P. Deng, and S. Huang, "The development and application of an automatic boundary segmentation methodology to evaluate the vaporizing characteristics of diesel spray under engine-like conditions," *Measurement Science and Technology*, vol. 26, no. 4, p. 045004, 2015.

[33] J. Gao, D. Jiang, and Z. Huang, "Spray properties of alternative fuels: A comparative analysis of ethanol–gasoline blends and gasoline," *Fuel*, vol. 86, no. 10-11, pp. 1645-1650, 2007.

[34] P.-C. Chen, W.-C. Wang, W. L. Roberts, and T. Fang, "Spray and atomization of diesel fuel and its alternatives from a single-hole injector using a common rail fuel injection system," *Fuel*, vol. 103, pp. 850-861, 2013.

[35] Ö. O. Taşkiran and M. Ergeneman, "Experimental study on diesel spray characteristics and autoignition process," *Journal of Combustion*, vol. 2011, 2011.

[36] J. B. Heywood, *Internal combustion engine fundamentals*. Mcgraw-hill New York, 1988.

[37] M. I. Ltd. (2014). *Handbook*. Available: www.malvern.com

[38] L. Zheng, X. Ma, Z. Wang, and J. Wang, "An optical study on liquid-phase penetration, flame lift-off location and soot volume fraction distribution of gasoline–diesel blends in a constant volume vessel," *Fuel*, vol. 139, pp. 365-373, 2015.

[39] R. Stone, "Introduction to Internal Combustion Engines. 2012," ed: SAE International and Macmillan Press.

[40] L. M. Pickett, D. L. Siebers, and C. A. Idicheria, "Relationship between ignition processes and the lift-off length of diesel fuel jets," SAE technical paper0148-7191, 2005.

[41] I. ANSYS, ANSYS Fluent Theory Guide, USA: ANSYS, Inc., 2016. [Online]. Available.

[42] S. R. Turns, *An introduction to combustion*. McGraw-hill New York, 1996.

[43] G. A. Lavoie, J. B. Heywood, and J. C. Keck, "Experimental and theoretical study of nitric oxide formation in internal combustion engines," *Combustion science and technology,* vol. 1, no. 4, pp. 313-326, 1970.

[44] C. T. Bowman, "Kinetics of pollutant formation and destruction in combustion," *Progress in energy and combustion science,* vol. 1, no. 1, pp. 33-45, 1975.

[45] F. Barnes, J. Bromly, T. Edwards, and R. Mandyczewsky, "NO (x) emissions from radiant gas burners," *Journal of the Institute of Energy,* vol. 61, no. 449, pp. 184-188, 1988.

[46] C. Fenimore, "Formation of nitric oxide in premixed hydrocarbon flames," in *Symposium (International) on Combustion*, 1971, vol. 13, no. 1, pp. 373-380: Elsevier.

[47] P. Malte and D. Pratt, "Measurement of atomic oxygen and nitrogen oxides in jet-stirred combustion," in *Symposium (international) on combustion*, 1975, vol. 15, no. 1, pp. 1061-1070: Elsevier.

[48] R. Barlow, G. Fiechtner, C. Carter, and J.-Y. Chen, "Experiments on the scalar structure of turbulent CO/H2/N2 jet flames," *Combustion and Flame,* vol. 120, no. 4, pp. 549-569, 2000.

[49] E. Corporan, O. Monroig, M. Wagner, and M. J. DeWitt, "Influence of fuel chemical composition on particulate matter emissions of a turbine engine," in *ASME Turbo Expo 2004: Power for Land, Sea, and Air,* 2004, pp. 837-848: American Society of Mechanical Engineers.

[50] D. B. Kittelson, "Engines and nanoparticles: a review," *Journal of aerosol science,* vol. 29, no. 5-6, pp. 575-588, 1998.

[51] P. Eastwood, *Particulate emissions from vehicles*. John Wiley & Sons, 2008.

[52] H. Wang and M. Frenklach, "A detailed kinetic modeling study of aromatics formation in laminar premixed acetylene and ethylene flames," *Combustion and flame,* vol. 110, no. 1-2, pp. 173-221, 1997.

[53] L. Chen *et al.*, "Experimental study of the gaseous and particulate matter emissions from a gas turbine combustor burning butyl butyrate and ethanol blends," *Applied energy,* vol. 195, pp. 693-701, 2017.

[54] G. Greeves, I. Khan, C. Wang, and I. Fenne, "Origins of hydrocarbon emissions from diesel engines," *SAE Transactions,* pp. 1235-1251, 1977.

[55] T. Bohl, "Investigation of biofuelled combustion and their performance optimisation strategies for internal combustion engines," PhD, Newcastle University, 2016.

[56] M. Canakci and H. Sanli, "Biodiesel production from various feedstocks and their effects on the fuel properties," *Journal of industrial microbiology & biotechnology,* vol. 35, no. 5, pp. 431-441, 2008.

[57] A. E. Atabani, A. S. Silitonga, I. A. Badruddin, T. Mahlia, H. Masjuki, and S. Mekhilef, "A comprehensive review on biodiesel as an alternative energy resource and its characteristics," *Renewable and sustainable energy reviews,* vol. 16, no. 4, pp. 2070-2093, 2012.

[58] L. Lin, Z. Cunshan, S. Vittayapadung, S. Xiangqian, and D. Mingdong, "Opportunities and challenges for biodiesel fuel," *Applied energy,* vol. 88, no. 4, pp. 1020-1031, 2011.

[59] Y. Chisti, "Biodiesel from microalgae," *Biotechnology advances,* vol. 25, no. 3, pp. 294-306, 2007.

[60] B. R. Moser, "Biodiesel production, properties, and feedstocks," *In Vitro Cellular & Developmental Biology-Plant,* vol. 45, no. 3, pp. 229-266, 2009.

[61] A. Demirbas, "Relationships derived from physical properties of vegetable oil and biodiesel fuels," *Fuel,* vol. 87, no. 8-9, pp. 1743-1748, 2008.

[62] I. Atadashi, M. Aroua, and A. A. Aziz, "High quality biodiesel and its diesel engine application: a review," *Renewable and sustainable energy reviews,* vol. 14, no. 7, pp. 1999-2008, 2010.

[63] W. Gis, A. Żółtowski, and A. Bocheńska, "Properties of the rapeseed oil methyl esters and comparing them with the diesel oil properties," *Journal of KONES*, vol. 18, pp. 121-127, 2011.

[64] L. Meher, D. V. Sagar, and S. Naik, "Technical aspects of biodiesel production by transesterification—a review," *Renewable and sustainable energy reviews,* vol. 10, no. 3, pp. 248-268, 2006.

[65] A. Murugesan, C. Umarani, T. Chinnusamy, M. Krishnan, R. Subramanian, and N. Neduzchezhain, "Production and analysis of bio-diesel from non-edible oils—a review," *Renewable and Sustainable Energy Reviews,* vol. 13, no. 4, pp. 825-834, 2009.

[66] M. J. Ramos, C. M. Fernández, A. Casas, L. Rodríguez, and Á. Pérez, "Influence of fatty acid composition of raw materials on biodiesel properties," *Bioresource technology,* vol. 100, no. 1, pp. 261-268, 2009.

[67] C. Song, C. Hsu, and I. Mochida, "Introduction to chemistry of diesel fuels," *Chemistry of diesel fuels,* pp. 1-60, 2000.

[68] A. Ramadhas, C. Muraleedharan, and S. Jayaraj, "Performance and emission evaluation of a diesel engine fueled with methyl esters of rubber seed oil," *Renewable energy,* vol. 30, no. 12, pp. 1789-1800, 2005.

[69] M. Balat, "Potential alternatives to edible oils for biodiesel production–A review of current work," *Energy conversion and management,* vol. 52, no. 2, pp. 1479-1492, 2011.

[70] H. Sanli, M. Canakci, and E. Alptekin, "Predicting the higher heating values of waste frying oils as potential biodiesel feedstock," *Fuel,* vol. 115, pp. 850-854, 2014.

[71] G. Labeckas, S. Slavinskas, and I. Kanapkienė, "The individual effects of cetane number, oxygen content or fuel properties on performance efficiency, exhaust smoke and emissions of a turbocharged CRDI diesel engine–Part 2," *Energy Conversion and Management,* vol. 149, pp. 442-466, 2017.

[72] H. Aatola, M. Larmi, T. Sarjovaara, and S. Mikkonen, "Hydrotreated vegetable oil (HVO) as a renewable diesel fuel: trade-off between NOx, particulate emission, and fuel consumption of a heavy duty engine," *SAE International Journal of Engines,* vol. 1, no. 2008-01-2500, pp. 1251-1262, 2008.

[73] I. O. Stanley, "Gas-to-Liquid technology: Prospect for natural gas utilization in Nigeria," *Journal of natural gas science and engineering,* vol. 1, no. 6, pp. 190-194, 2009.

[74] D. A. Wood, C. Nwaoha, and B. F. Towler, "Gas-to-liquids (GTL): A review of an industry offering several routes for monetizing natural gas," *Journal of Natural Gas Science and Engineering,* vol. 9, pp. 196-208, 2012.

[75] T. Wu, Z. Huang, W.-g. Zhang, J.-h. Fang, and Q. Yin, "Physical and chemical properties of GTL− diesel fuel blends and their effects on performance and emissions of a multicylinder DI compression ignition engine," *Energy & Fuels,* vol. 21, no. 4, pp. 1908-1914, 2007.

[76] P. Soltic, D. Edenhauser, T. Thurnheer, D. Schreiber, and A. Sankowski, "Experimental investigation of mineral diesel fuel, GTL fuel, RME and neat soybean and rapeseed oil combustion in a heavy duty on-road engine with exhaust gas aftertreatment," *Fuel,* vol. 88, no. 1, pp. 1-8, 2009.

[77] H. Aatola, M. Larmi, T. Sarjovaara, and S. Mikkonen, "Hydrotreated Vegetable Oil (HVO) as a Renewable Diesel Fuel: Trade-off between $NO_x$, Particulate Emission, and Fuel Consumption of a Heavy Duty Engine," *SAE International journal of engines,* vol. 1, no. 1, pp. 1251-1262, 2009.

[78] B. Mohan, W. Yang, K. L. Tay, and W. Yu, "Experimental study of spray characteristics of biodiesel derived from waste cooking oil," *Energy Conversion and Management,* vol. 88, pp. 622-632, 2014.

[79] Y. Gao, M. Wei, F. Yan, L. Chen, G. Li, and L. Feng, "Effects of cavitation flow and stagnant bubbles on the initial temporal evolution of diesel spray," *Experimental Thermal & Fluid Science*, vol. 87, 2017.

[80] Y. Ma, R. Huang, S. Huang, Y. Zhang, S. Xu, and Z. Wang, "Experimental investigation on the effect of n-pentanol blending on spray, ignition and combustion characteristics of waste cooking oil biodiesel," *Energy Conversion and Management,* vol. 148, pp. 440-455, 2017.

[81] Y. Ma, S. Huang, R. Huang, Y. Zhang, and S. Xu, "Spray and evaporation characteristics of n-pentanol–diesel blends in a constant volume chamber," *Energy Conversion and Management,* vol. 130, pp. 240-251, 2016.

[82] Y. Liu, J. Li, and C. Jin, "Fuel spray and combustion characteristics of butanol blends in a constant volume combustion chamber," *Energy Conversion and Management,* vol. 105, pp. 1059-1069, 2015.

[83] K. Sugiyama, I. Goto, K. Kitano, K. Mogi, and M. Honkanen, "Effects of hydrotreated vegetable oil (HVO) as renewable diesel fuel on combustion and exhaust emissions in diesel engine," *SAE International Journal of Fuels and Lubricants,* vol. 5, no. 1, pp. 205-217, 2012.

[84] T. Bohl, G. Tian, A. Smallbone, and A. P. Roskilly, "Macroscopic spray characteristics of next-generation bio-derived diesel fuels in comparison to mineral diesel," *Applied Energy,* vol. 186, pp. 562-573, 2017.

[85] K. Kannaiyan and R. Sadr, "Experimental investigation of spray characteristics of alternative aviation fuels," *Energy Conversion and Management,* vol. 88, pp. 1060-1069, 2014.

[86] J. Jeon and S. Park, "Effects of pilot injection strategies on the flame temperature and soot distributions in an optical CI engine fueled with biodiesel and conventional diesel," *Applied Energy,* vol. 160, pp. 581-591, 2015.

[87] O. Özener, L. Yüksek, A. T. Ergenç, and M. Özkan, "Effects of soybean biodiesel on a DI diesel engine performance, emission and combustion characteristics," *Fuel,* vol. 115, pp. 875-883, 2014.

[88] X. Shen *et al.*, "Real-world exhaust emissions and fuel consumption for diesel vehicles fueled by waste cooking oil biodiesel blends," *Atmospheric Environment,* vol. 191, pp. 249-257, 2018.

[89] M. N. Nabi, A. Zare, F. M. Hossain, Z. D. Ristovski, and R. J. Brown, "Reductions in diesel emissions including PM and PN emissions with diesel-biodiesel blends," *Journal of Cleaner Production,* vol. 166, pp. 860-868, 2017.

[90] M. Lapuerta, O. Armas, and J. Rodriguez-Fernandez, "Effect of biodiesel fuels on diesel engine emissions," *Progress in energy and combustion science,* vol. 34, no. 2, pp. 198-223, 2008.

[91] N. Kumar and S. R. Chauhan, "Performance and emission characteristics of biodiesel from different origins: a review," *Renewable and Sustainable Energy Reviews,* vol. 21, pp. 633-658, 2013.

[92] K. Lehto, A. Elonheimo, K. Hakkinen, T. Sarjovaara, and M. Larmi, "Emission reduction using hydrotreated vegetable oil (HVO) with Miller timing and EGR in diesel combustion," *SAE International Journal of Fuels and Lubricants,* vol. 5, no. 2011-01-1955, pp. 218-224, 2011.

[93] D. Singh, K. Subramanian, and S. Singal, "Emissions and fuel consumption characteristics of a heavy duty diesel engine fueled with hydroprocessed renewable diesel and biodiesel," *Applied Energy,* vol. 155, pp. 440-446, 2015.

[94] S.-Y. No, "Application of hydrotreated vegetable oil from triglyceride based biomass to CI engines–A review," *Fuel,* vol. 115, pp. 88-96, 2014.

[95] A. Abu-Jrai *et al.*, "Performance, combustion and emissions of a diesel engine operated with reformed EGR. Comparison of diesel and GTL fuelling," *Fuel,* vol. 88, no. 6, pp. 1031-1041, 2009.

[96] A. Hassaneen, A. Munack, Y. Ruschel, O. Schroeder, and J. Krahl, "Fuel economy and emission characteristics of Gas-to-Liquid (GTL) and Rapeseed Methyl Ester (RME) as alternative fuels for diesel engines," *Fuel,* vol. 97, pp. 125-130, 2012.

[97] S. Ushakov, N. G. Halvorsen, H. Valland, D. H. Williksen, and V. Æsøy, "Emission characteristics of GTL fuel as an alternative to conventional marine gas oil," *Transportation Research Part D: Transport and Environment,* vol. 18, pp. 31-38, 2013.

[98] H. Hao, H. Wang, L. Song, X. Li, and M. Ouyang, "Energy consumption and GHG emissions of GTL fuel by LCA: Results from eight demonstration transit buses in Beijing," *Applied Energy,* vol. 87, no. 10, pp. 3212-3217, 2010.

[99] S. U. Choi and J. A. Eastman, "Enhancing thermal conductivity of fluids with nanoparticles," Argonne National Lab., IL (United States)1995.

[100] S. Gumus, H. Ozcan, M. Ozbey, and B. Topaloglu, "Aluminum oxide and copper oxide nanodiesel fuel properties and usage in a compression ignition engine," *Fuel,* vol. 163, pp. 80-87, 2016.

[101] V. Saxena, N. Kumar, and V. K. Saxena, "A comprehensive review on combustion and stability aspects of metal nanoparticles and its additive effect on diesel and biodiesel fuelled CI engine," *Renewable and Sustainable Energy Reviews,* vol. 70, pp. 563-588, 2017.

[102] J. L. Sabourin, R. A. Yetter, and V. S. Parimi, "Exploring the effects of nanostructured particles on liquid nitromethane combustion," *Journal of Propulsion and Power,* vol. 26, no. 5, pp. 1006-1015, 2010.

[103] Y. Gan and L. Qiao, "Combustion characteristics of fuel droplets with addition of nano and micron-sized aluminum particles," *Combustion and Flame,* vol. 158, no. 2, pp. 354-368, 2011.

[104] R. N. Mehta, M. Chakraborty, and P. A. Parikh, "Nanofuels: Combustion, engine performance and emissions," *Fuel,* vol. 120, pp. 91-97, 2014/03/15/ 2014.

[105] S. Balamurugan and V. Sajith, "Stabilization Studies of Zirconium-Cerium Oxide Nanoparticle-Diesel Suspension," *Advanced Materials Research,* vol. 685, pp. 128-133, 2013.

[106] A. Fayyazbakhsh and V. Pirouzfar, "Investigating the influence of additives-fuel on diesel engine performance and emissions: Analytical modeling and experimental validation," *Fuel,* vol. 171, pp. 167-177, 2016.

[107] G. Vairamuthu, S. Sundarapandian, C. Kailasanathan, and B. Thangagiri, "Experimental investigation on the effects of cerium oxide nanoparticle on calophyllum inophyllum (Punnai) biodiesel blended with diesel fuel in DI diesel engine modified by nozzle geometry," *Journal of the Energy Institute,* vol. 89, no. 4, pp. 668-682, 2016.

[108] H. S. Saraee, H. Taghavifar, and S. Jafarmadar, "Experimental and numerical consideration of the effect of CeO2 nanoparticles on diesel engine performance and exhaust emission with the aid of artificial neural network," *Applied Thermal Engineering,* vol. 113, pp. 663-672, 2017.

[109] M. Mirzajanzadeh *et al.*, "A novel soluble nano-catalysts in diesel–biodiesel fuel blends to improve diesel engines performance and reduce exhaust emissions," *Fuel,* vol. 139, pp. 374-382, 2015.

[110] M. Aghbashlo *et al.*, "A novel emulsion fuel containing aqueous nano cerium oxide additive in diesel–biodiesel blends to improve diesel engines performance and reduce exhaust emissions: Part II–Exergetic analysis," *Fuel,* vol. 205, pp. 262-271, 2017.

[111] E. Khalife *et al.*, "A novel emulsion fuel containing aqueous nano cerium oxide additive in diesel–biodiesel blends to improve diesel engines performance and reduce exhaust emissions: Part I–Experimental analysis," *Fuel,* vol. 207, pp. 741-750, 2017.

[112] M. S. Gross, B. S. Sánchez, and C. A. Querini, "Diesel particulate matter combustion with CeO2 as catalyst. Part II: Kinetic and reaction mechanism," *Chemical engineering journal,* vol. 168, no. 1, pp. 413-419, 2011.

[113] G. Najafi, "Diesel engine combustion characteristics using nano-particles in biodiesel-diesel blends," *Fuel,* vol. 212, pp. 668-678, 2018.

[114] K. Heydari-Maleney, A. Taghizadeh-Alisaraei, B. Ghobadian, and A. Abbaszadeh-Mayvan, "Analyzing and evaluation of carbon nanotubes additives to diesohol-B2 fuels on performance and emission of diesel engines," *Fuel,* vol. 196, pp. 110-123, 2017.

[115] M. Ghanbari, G. Najafi, B. Ghobadian, T. Yusaf, A. Carlucci, and M. K. D. Kiani, "Performance and emission characteristics of a CI engine using nano particles additives in biodiesel-diesel blends and modeling with GP approach," *Fuel,* vol. 202, pp. 699-716, 2017.

[116] G. Anitescu, *Supercritical fluid technology applied to the production and combustion of diesel and biodiesel fuels*. ProQuest, 2008.

[117] M. Wensing, T. Vogel, and G. Götz, "Transition of diesel spray to a supercritical state under engine conditions," *International Journal of Engine Research,* vol. 17, no. 1, pp. 108-119, 2016.

[118] G. Anitescu, L. L. Tavlarides, and D. Geana, "Phase transitions and thermal behavior of fuel− diluent mixtures," *Energy & Fuels,* vol. 23, no. 6, pp. 3068-3077, 2009.

[119] D. Kusdiana and S. Saka, "Kinetics Of Transesterification In Rapeseed Oil To Biodiesel Fuel As Treated In Supercritical Methanol," *Fuel,* vol. 80, no. 5, pp. 693–698, 2001.

[120] W. Iijima, Y. Kobayashi, K. Takekura, and K. Taniwaki, "The non-glycerol process of biodiesel fuel treated in supercritical methanol," presented at the ASAE/CSAE Annual International Meeting, Ottawa, Ontario, Canada, August 1-4, 2004, Paper no. 046073.

[121] W. Cao, H. Han, and J. Zhang, "Preparation of biodiesel from soybean oil using supercritical methanol and co-solvent," *Fuel,* vol. 84, no. 4, pp. 347–351, 2005.

[122] S. Saka and D. Kusdiana, "Biodiesel fuel from rapeseed oil as prepared in supercritical methanol," *Fuel,* vol. 80, pp. 225–231, 2001.

[123] M. A. Dasari, M. J. Goff, and G. J. Suppes, "Noncatalytic alcoholysis kinetics of soybean oil," *Journal of the American Oil Chemists Society,* vol. 80, no. 2, pp. 189-192, 2003.

[124] K. Bunyakiat, S. Makmee, R. Sawangkeaw, and S. Ngamprasertsith, "Continuous Production of Biodiesel via Transesterification from Vegetable Oils in Supercritical Methanol," *Energy Fuels,* vol. 20, no. 2, pp. 812-817, 2006.

[125] M. Busto *et al.*, "Influence of the Axial Dispersion on the Performance of Tubular Reactors during the Noncatalytic Supercritical Transesterification of Triglycerides," *Energy Fuels,* vol. 20, no. 6, pp. 2642-2647, 2006.

[126] Y. Warabi, D. Kusdiana, and S. Saka, "Reactivity of triglycerides and fatty acids of rapeseed oil in supercritical alcohols," *Bioresour Technol,* vol. 91, no. 3, pp. 283–287, 2004.

[127] A. Demirbas, "Biodiesel production from vegetable oils via catalytic and non-catalytic supercritical methanol transesterification methods," *Progress in Energy & Combustion Science,* vol. 31, no. 5-6, pp. 466–487, 2005.

[128] H. He, T. Wang, and S. Zhu, "Continuous production of biodiesel fuel from vegetable oil using supercritical methanol process," *Fuel,* vol. 86, no. 3, pp. 442–447, 2007.

[129] M. Diasakou, A. Louloudi, and N. Papayannakos, "Kinetics of the non-catalytic transesterification of soybean oil," *Fuel,* vol. 77, no. 12, pp. 1297-1302, 10// 1998.

[130] G. Madras, C. Kolluru, and R. Kumar, "Synthesis of biodiesel in supercritical fluids," *Fuel,* vol. 83, no. 14-15, pp. 2029–2033, 2004.

[131] M. N. Varma and G. Madras, "Synthesis of Biodiesel from Castor Oil and Linseed Oil in Supercritical Fluids," *Industrial & Engineering Chemistry Research,* vol. 46, no. 1, pp. 1-6, 2007.

[132] A. Demirbas, "Biodiesel fuels from vegetable oils via catalytic and non-catalytic supercritical alcohol transesterifications and other methods: a survey. Energy Conservat Manage," *Energy Conversion and Management 2003 Vol. 44 No. 13 pp. 2093-2109,* vol. 44, no. 2, pp. 2093–2109, 2003.

[133] B. Chehroudi, "Recent experimental efforts on high-pressure supercritical injection for liquid rockets and their implications," *International Journal of Aerospace Engineering,* vol. 2012, 2012.

[134] C. W. Haldeman, B. S. Ahern, and K. H. Johnson, "Supercritical water fuel composition and combustion system," ed: Google Patents, 2000.

[135] B. Ahern *et al.*, "Dramatic emissions reductions with a direct injection diesel engine burning supercritical fuel/water mixtures," SAE Technical PaperNo. 2001-01-3526, 2001.

[136] X. J. Cheng CHEN, Yi SUI, "Prediction of transport properties of fuels in supercritical conditions by molecular dynamic simulation," in *10th International Conference on Applied Energy (ICAE2018),* Hong Kong, 2018: Elsevier.

[137] C. H. Twu, J. E. Coon, M. G. Kusch, and A. H. Harvey, "Selection of Equations of State Models for Process Simulator," in *Simulation Science Inc. Workbook Meeting,* 1994, vol. 24.

[138] G. Zhu and S. Aggarwal, "Transient supercritical droplet evaporation with emphasis on the effects of equation of state," *International Journal of Heat and Mass Transfer,* vol. 43, no. 7, pp. 1157-1171, 2000.

[139] P. C. Ma, M. Ihme, and L. Bravo, "Modeling and simulation of diesel injection at transcritical conditions," *arXiv preprint arXiv:1705.07232,* 2017.

[140] C. Schaschke, I. Fletcher, and N. Glen, "Density and viscosity measurement of diesel fuels at combined high pressure and elevated temperature," *Processes,* vol. 1, no. 2, pp. 30-48, 2013.

[141] R. Lin and L. L. Tavlarides, "Thermophysical properties needed for the development of the supercritical diesel combustion technology: Evaluation of diesel fuel surrogate models," *The Journal of Supercritical Fluids,* vol. 71, pp. 136-146, 2012.

[142] E. D. Nikitin, P. A. Pavlov, and P. V. Skripov, "Measurement of the critical properties of thermally unstable substances and mixtures by the pulse-heating method," *The Journal of Chemical Thermodynamics,* vol. 25, no. 7, pp. 869-880, 1993.

[143] A. L. Scheidgen and G. M. Schneider, "Complex phase equilibrium phenomena in fluid ternary mixtures up to 100 MPa: cosolvency, holes, windows, and islands—review and new results," *Fluid phase equilibria,* vol. 194, pp. 1009-1028, 2002.

[144] T. Charoensombut-Amon, R. J. Martin, and R. Kobayashi, "Application of a generalized multiproperty apparatus to measure phase equilibrium and vapor phase densities of supercritical carbon dioxide in n-hexadecane systems up to 26 MPa," *Fluid Phase Equilibria,* vol. 31, no. 1, pp. 89-104, 1986.

[145] H. Tanaka, Y. Yamaki, and M. Kato, "Solubility of carbon dioxide in pentadecane, hexadecane, and pentadecane+ hexadecane," *Journal of Chemical and Engineering Data,* vol. 38, no. 3, pp. 386-388, 1993.

[146] A. Fenghour, J. P. M. Trusler, and W. A. Wakeham, "Densities and bubble points of binary mixtures of carbon dioxide and n-heptane and ternary mixtures of n-butane, n-heptane and n-hexadecane," *Fluid phase equilibria,* vol. 185, no. 1, pp. 349-358, 2001.

[147] C. K. Westbrook, W. J. Pitz, O. Herbinet, H. J. Curran, and E. J. Silke, "A comprehensive detailed chemical kinetic reaction mechanism for combustion of n-alkane hydrocarbons from n-octane to n-hexadecane," *Combustion and Flame,* vol. 156, no. 1, pp. 181-199, 2009.

[148] S. D. Givler and J. Abraham, "Supercritical droplet vaporization and combustion studies," *Progress in Energy and combustion Science,* vol. 22, no. 1, pp. 1-28, 1996.

[149] D. J. Rosenthal and A. S. Teja, "The critical properties of n-alkanes using a low-residence time flow apparatus," *AIChE journal*, vol. 35, no. 11, pp. 1829-1834, 1989.

[150] S. S. Abhinav Kumar, Ramesh Chand, Vishnu Saini, Raja Sekhar Dondapati, "TEMPERATURE DEPENDENT THERMODYNAMIC PROPERTIES OF DIESEL FUEL SURROGATE AT CRITICAL PRESSURE FOR COMBUSTION MODELING IN COMPRESSION IGNITION ENGINES " *International Journal of Mechanical Engineering andTechnology (IJMET)* vol. 8, no. 7, pp. 1492 - 1499, 2017.

[151] S. Rahmani, W. C. McCaffrey, H. D. Dettman, and M. R. Gray, "Coking kinetics of asphaltenes as a function of chemical structure," *Energy & fuels*, vol. 17, no. 4, pp. 1048-1056, 2003.

[152] K. Miwa, A. Mohammadi, and Y. Kidoguchi, "A study on thermal decomposition of fuels and NOx formation in diesel combustion using a total gas sampling technique," *International Journal of Engine Research*, vol. 2, no. 3, pp. 189-198, 2001.

[153] D. H. Scharnweber and L. O. Hoppie, "Hypergolic combustion in an internal combustion engine," SAE Technical Paper1985.

[154] G. Anitescu, T. J. Bruno, and L. L. Tavlarides, "Dieseline for supercritical injection and combustion in compression-ignition engines: volatility, phase transitions, spray/jet structure, and thermal stability," *Energy & Fuels*, vol. 26, no. 10, pp. 6247-6258, 2012.

[155] G. Karakas, T. Dogu, and T. G. Somer, "Reactivity of CO2 during thermal cracking of heavy paraffins under supercritical conditions," *Industrial & engineering chemistry research*, vol. 36, no. 11, pp. 4445-4451, 1997.

[156] D. Graham-Rowe. (2009) Supercritical Fuel Injection. *MIT technology review*.

[157] M. J. Anselme, M. Gude, and A. S. Teja, "The critical temperatures and densities of the n-alkanes from pentane to octadecane," *Fluid Phase Equilibria*, vol. 57, no. 3, pp. 317-326, 1990.

[158] T. J. Bruno, A. Wolk, A. Naydich, and M. L. Huber, "Composition-explicit distillation curves for mixtures of diesel fuel with dimethyl carbonate and diethyl carbonate," *Energy & Fuels*, vol. 23, no. 8, pp. 3989-3997, 2009.

[159] T. J. Bruno, T. M. Lovestead, M. L. Huber, and J. R. Riggs, "Comparison of diesel fuel oxygenate additives to the composition-explicit distillation curve method. Part 2: Cyclic compounds with one to two oxygens," *Energy & Fuels*, vol. 25, no. 6, pp. 2508-2517, 2011.

[160] T. J. Bruno, T. M. Lovestead, J. R. Riggs, E. L. Jorgenson, and M. L. Huber, "Comparison of diesel fuel oxygenate additives to the composition-explicit distillation curve method. Part 1: Linear compounds with one to three oxygens," *Energy & Fuels*, vol. 25, no. 6, pp. 2493-2507, 2011.

[161] T. M. Lovestead and T. J. Bruno, "Comparison of diesel fuel oxygenate additives to the composition-explicit distillation curve method. Part 3: t-Butyl glycerols," *Energy & Fuels*, vol. 25, no. 6, pp. 2518-2525, 2011.

[162] B. L. Smith, L. S. Ott, and T. J. Bruno, "Composition-explicit distillation curves of diesel fuel with glycol ether and glycol ester oxygenates: Fuel analysis metrology to enable decreased particulate emissions," *Environmental science & technology*, vol. 42, no. 20, pp. 7682-7689, 2008.

[163] J. L. Burger, E. Baibourine, and T. J. Bruno, "Comparison of diesel fuel oxygenate additives to the composition-explicit distillation curve method. Part 4: alcohols, aldehydes, hydroxy ethers, and esters of butanoic acid," *Energy & Fuels*, vol. 26, no. 2, pp. 1114-1123, 2011.

[164] G. Anitescu, R. Lin, and L. L. Tavlarides, "Preparation, injection and combustion of supercritical fluids," in *Directions in Engine-Efficiency and Emissions Research (DEER) Conference, Dearborn, MI*, 2009.

[165] G. Anitescu, "Supercritical fluid technology applied to the production and combustion of diesel and biodiesel fuels," ProQuest, 2008.

[166] Wikipedia. (2014). *Computational fluid dynamics*. Available: https://en.wikipedia.org/wiki/Computational_fluid_dynamics

[167] B. Andersson, R. Andersson, L. Håkansson, M. Mortensen, R. Sudiyo, and B. Van Wachem, *Computational fluid dynamics for engineers*. Cambridge University Press, 2011.

[168] I. ANSYS, ANSYS 18.1 Fluent Users Guide, USA, 2017. [Online]. Available.

[169] H. M. Ismail, H. K. Ng, and S. Gan, "Evaluation of non-premixed combustion and fuel spray models for in-cylinder diesel engine simulation," *Applied Energy,* vol. 90, no. 1, pp. 271-279, 2012.

[170] V. G. Levich, *Physicochemical hydrodynamics*. Prentice hall, 1962.

[171] M. Battistoni and C. N. Grimaldi, "Numerical analysis of injector flow and spray characteristics from diesel injectors using fossil and biodiesel fuels," *Applied Energy,* vol. 97, pp. 656-666, 2012.

[172] T. Kim and S. Park, "Modeling flash boiling breakup phenomena of fuel spray from multi-hole type direct-injection spark-ignition injector for various fuel components," *Energy Conversion and Management,* vol. 160, pp. 165-175, 2018.

[173] M. H. Azami and M. Savill, "Modelling of spray evaporation and penetration for alternative fuels," *Fuel,* vol. 180, pp. 514-520, 2016.

[174] B. Vajda *et al.*, "The numerical simulation of biofuels spray," *Fuel,* vol. 144, pp. 71-79, 2015.

[175] L. Postrioti, F. Mariani, and M. Battistoni, "Experimental and numerical momentum flux evaluation of high pressure Diesel spray," *Fuel,* vol. 98, pp. 149-163, 2012.

[176] Y. Gong, O. Kaario, A. Tilli, M. Larmi, and F. Tanner, "A computational investigation of hydrotreated vegetable oil sprays using RANS and a modified version of the RNG k-ε model in OpenFOAM," SAE Technical Paper0148-7191, 2010.

[177] A. Maghbouli, W. Yang, H. An, J. Li, S. K. Chou, and K. J. Chua, "An advanced combustion model coupled with detailed chemical reaction mechanism for DI diesel engine simulation," *Applied energy,* vol. 111, pp. 758-770, 2013.

[178] L. Zhou, K. H. Luo, W. Qin, M. Jia, and S. J. Shuai, "Large eddy simulation of spray and combustion characteristics with realistic chemistry and high-order numerical scheme under diesel engine-like conditions," *Energy Conversion and Management,* vol. 93, pp. 377-387, 2015.

[179] D. B. Hibbert, "Experimental design in chromatography: a tutorial review," *Journal of chromatography B,* vol. 910, pp. 2-13, 2012.

[180] L. Ilzarbe, M. J. Álvarez, E. Viles, and M. Tanco, "Practical applications of design of experiments in the field of engineering: a bibliographical review," *Quality and Reliability Engineering International,* vol. 24, no. 4, pp. 417-428, 2008.

[181] A. Faes, J.-M. Fuerbringer, D. Mohamedi, A. Hessler-Wyser, and G. Caboche, "Design of experiment approach applied to reducing and oxidizing tolerance of anode supported solid oxide fuel cell. Part I: Microstructure optimization," *Journal of Power Sources,* vol. 196, no. 17, pp. 7058-7069, 2011.

[182] B. Wahdame, D. Candusso, X. François, F. Harel, J.-M. Kauffmann, and G. Coquery, "Design of experiment techniques for fuel cell characterisation and development," *International Journal of Hydrogen Energy,* vol. 34, no. 2, pp. 967-980, 2009.

[183] G. Vicente, A. Coteron, M. Martinez, and J. Aracil, "Application of the factorial design of experiments and response surface methodology to optimize biodiesel production," *Industrial crops and products,* vol. 8, no. 1, pp. 29-35, 1998.

[184] S. Madani, R. Gheshlaghi, M. A. Mahdavi, M. Sobhani, and A. Elkamel, "Optimization of the performance of a double-chamber microbial fuel cell through factorial design of experiments and response surface methodology," *Fuel,* vol. 150, pp. 434-440, 2015.

[185] L. Chen, Z. Zhang, W. Gong, and Z. Liang, "Quantifying the effects of fuel compositions on GDI-derived particle emissions using the optimal mixture design of experiments," *Fuel,* vol. 154, pp. 252-260, 2015.

[186] L. Chen, Z. Liu, P. Sun, and W. Huo, "Formulation of a fuel spray SMD model at atmospheric pressure using Design of Experiments (DoE)," *Fuel,* vol. 153, pp. 355-360, 2015.

[187] J. Brulatout, F. Garnier, C. Mounaïm-Rousselle, and P. Seers, "Calibration strategy of diesel-fuel spray atomization models using a design of experiment method," *International Journal of Engine Research,* p. 1468087415611030, 2015.

[188] A. B. Liu, D. Mather, and R. D. Reitz, "Modeling the effects of drop drag and breakup on fuel sprays," DTIC Document1993.

[189] R. REITZ, "Modeling atomization processes in high-pressure vaporizing sprays," *Atomisation and Spray Technology,* vol. 3, no. 4, pp. 309-337, 1987.

[190] W. Waidmann, A. Boemer, and M. Braun, "Adjustment and verification of model parameters for diesel injection CFD simulation," SAE Technical Paper0148-7191, 2006.

[191] H. Hiroyasu, T. Kadota, and M. Arai, "Supplementary comments: fuel spray characterization in diesel engines," *Combustion modeling in reciprocating engines,* vol. 369, 1980.

[192] C. T. S. Turk, U. C. Oz, T. M. Serim, and C. Hascicek, "Formulation and optimization of nonionic surfactants emulsified nimesulide-loaded PLGA-based nanoparticles by design of experiments," *AAPS PharmSciTech,* vol. 15, no. 1, pp. 161-176, 2014.

[193] Horiba, "MEXA-2000SPCS Brochure," ed: HORIBA Ltd.

[194] M. Hajjari, M. Ardjmand, and M. Tabatabaei, "Experimental investigation of the effect of cerium oxide nanoparticles as a combustion-improving additive on biodiesel oxidative stability: mechanism," *RSC Advances,* 10.1039/C3RA47033D vol. 4, no. 28, pp. 14352-14356, 2014.

[195] D. Ganesh and G. Gowrishankar, "Effect of nano-fuel additive on emission reduction in a biodiesel fuelled CI engine," in *Electrical and Control Engineering (ICECE), 2011 International Conference on*, 2011, pp. 3453-3459: IEEE.

[196] R. Manikandan and N. Sethuraman, "Experimental investigation of nano additive ceric oxide (CeO2)-ethanol blend on single cylinder four stroke diesel engine," *IJRDET,* vol. 3, no. 2, pp. 24-8, 2014.

[197] Y. Sivathanu and G. M. Faeth, "Generalized state relationships for scalar properties in nonpremixed hydrocarbon/air flames," *Combustion and Flame,* vol. 82, no. 2, pp. 211-230, 1990.

[198] J. Blauvens, B. Smets, and J. Peters, "In 16th Symp.(Int'l.) on Combustion," *The Combustion Institute,* p. 1055, 1977.

[199] W. Flower, R. Hanson, and C. Kruger, "In 15th Symp.(Int'l.) on Combustion," *The Combustion Institute,* vol. 823, p. 160, 1975.

[200] J. Monat, R. Hanson, and C. Kruger, "In 17th Symp.(Int'l.) on Combustion," *The Combustion Institute,* vol. 543, 1979.

[201] K. Homann, "DL Baulch, DD Drysdale, DG Horne und AC Lloyd: Evaluated Kinetic Data for High Temperature Reactions, Volume 1: Homogeneous Gas Phase Reactions of the H2-O2-System. Butter-worths & Co., London 1972, 433 S., Preis:£ 10.—," *Berichte der Bunsengesellschaft für physikalische Chemie,* vol. 77, no. 2, pp. 136-136, 1973.

[202] R. K. Hanson and S. Salimian, "Survey of rate constants in the N/H/O system," in *Combustion chemistry*: Springer, 1984, pp. 361-421.

[203] J. Warnatz, "NOx formation in high temperature processes," *University of Stuttgart, Germany,* 1991.

[204] C. K. Westbrook and F. L. Dryer, "Chemical kinetic modeling of hydrocarbon combustion," *Progress in Energy and Combustion Science,* vol. 10, no. 1, pp. 1-57, 1984.

[205] D. Baulch *et al.*, "Evaluated kinetic data for combustion modelling," *Journal of Physical and Chemical Reference Data,* vol. 21, no. 3, pp. 411-734, 1992.

[206] D.-Y. Peng and D. B. Robinson, "A new two-constant equation of state," *Industrial & Engineering Chemistry Fundamentals,* vol. 15, no. 1, pp. 59-64, 1976.

[207] G. Soave, "Equilibrium constants from a modified Redlich-Kwong equation of state," *Chemical engineering science,* vol. 27, no. 6, pp. 1197-1203, 1972.

[208] E. M. Chapman *et al.*, "Annual Technical Progress Report for Project Entitled "Impact of DME-diesel Fuel Blend Properties on Diesel Fuel Injection Systems,"" *The Pennsylvania State University, The Pennsylvania State University The Energy Institute University Park, PA,* vol. 168022003, 2003.

[209] B. S. Rahardjo, "PERFORMANCE OF DIESEL ENGINE USING DIESEL OIL, DME AND THEIR MIXTURES," *International Journal of Engineering,* vol. 3, no. 2, p. 8269, 2013.

# Appendix A

## Code of Matlab program for HRR calculation

```
close all;
clear; clc;
% Read data of in-cylinder pressure and cylinder volume
CAD0 = xlsread('X: \1.1.xlsx','pressure','A2:A1442');
P0 = xlsread(' X: \1.1.xlsx','pressure','C2:C1442');
V0 = xlsread(' X: \1.1.xlsx','pressure','B2:B1442');

% Select in-cylinder pressure data from 1442 to 720
Phi = -360:360;
for e = 2:2:1441
    c = e/2;
    CAD(c) = CAD0(e);
    V(c) = V0(e);
    P(c) = P0(e);
end

% Smooth
N = numel(P);
Y(1) = (39*P(1)+8*P(2)-4*(P(3)+P(4)-P(6))+P(5)-2*P(7))/42;
Y(2) = (8*P(1)+19*P(2)+16*P(3)+6*P(4)-4*P(5)-7*P(6)+4*P(7))/42;
Y(3) = (-4*(P(1)+P(6))+16*P(2)+19*P(3)+12*P(4)+2*P(5)+7*P(7))/42;
if N < 7
   return;
end
for k = 4:(N-3)
    Y(k) = (-2*(P(k-3)+P(k+3))+3*(P(k-2)+P(k+2))+6*(P(k-1)+P(k+1))+7*P(k))/21;
end
Y(N-2) = (P(N-6)-4*(P(N-5)+P(N))+P(N-4)+12*P(N-3)+19*P(N-2)+16*P(N-1))/42;
Y(N-1) = (4*P(N-6)-7*P(N-5)+4*P(N-4)+6*P(N-3)+16*P(N-2)+19*P(N-1)+8*P(N))/42;
Y(N) = (-2*P(N-6)+4*(P(N-5)-P(N-3)-P(N-2))+P(N-4)+8*P(N-1)+39*P(N))/42;

% Preparation for HRR calculation
% Engine conditions
n = 1490;
Te = 726;
BSFC = 0.2272; % kg/kWh
% Fuel properties
Hu = 42853; % Fuel heating value kJ/kg
C = 0.870; % Content of C
H = 0.130; % Content of H
O = 0; % Content of O

% Other constants
p = 0.1*Y; % Pressure Mpa
power = Te*n/9550; % Power kw
D = 0.107; % Bore diameter
S = 0.124; % Stroke
```

```
L = 0.192; % Connecting rod
e = 17.3; % Compression ratio
i = 4; % Cylinder number
z = 4; % Stroke
lb = S/(2*L); % Crank radius - connecting rod length ratio
Hc = 0.0011; % Clearance height m
r = 0.02; % Residual exhaust gas coefficient
CAC = 0; % Crank angle for calculating the end of combustion
CAB = 0; % Crank angle for calculating the start of combustion
Vs = pi*D^2*S/4; % Cylinder working volume m^3
Vc = 9.182*10^(-5); % Cylinder clearance volume m^3

% Geometric features
t = S/2*(1-cosd(phi)+1./lb*(1-sqrt(1-lb^2*sind(phi).^2))); % Piston displacement
V = Vc+pi*D^2*t/4; % Instantaneous volume m^3

% Engine thermal features
pe = power*0.12/(n*Vs*i); % Effective pressure Mpa
Tw1 = 100+70*pe+273.15; % Cylinder head temperature
Tw2 = 100+120*pe+273.15; % Piston temperature
Tw3 = 100+40*pe+273.15; % Cylinder liner wall temperature

% Variables for HRR calculation
R = 8.3145; % Molar gas constant J/(mol.K)
Rg = 287; % Air constant J/(kg*K)
L0 = 1/0.21*(C/12+H/4-O/32); % Calculated air consumption for fuel kmol/kg
B0 = 1+(H/4+O/32)/L0; % Molecular variation coefficient ??
Cm = n*S/30; % Speed of piston
A3 = pi*D*(Hc+t); % Wet surface area of cylinder liner wall m^2
f = power*BSFC/(30*n*i); % Fuel consumption in each cycle kg

% Combustion products coefficient
ar = 4.7513;
br = 1.199*10^(-3);
cr = -1.4232*10^(-7);
% Air coefficient
a0 = 4.678;
b0 = 6.8723*10^(-4);
c0 = -6.0683*10^(-8);

NUM1 =-135+361; % Start point of calculation
NUM2 = 135+361; % End point of calculation
Dp=zeros(size(phi));

for j = NUM1:NUM2
   Dp(j) = p(j)-p(j-1);
end

pa = p(NUM1); % The In-cylinder pressure at the start point of calculation
Va =V(NUM1); % The cylinder volume at the start point of calculation
Ta = 298; % The In-cylinder temperature at the start point of calculation
Ma = pa*Va/( Ta*R)*1e3;
```

```
a = Ma/(1+r)/f/L0; % Excess air ratio
Ua = 4.1868*(a0+b0*Ta+c0*Ta^2)*Ma*1000*Ta; % Internal energy of working medium
at the start point of calculation
T = zeros(size(phi));
M = zeros(size(phi));
W = zeros(size(phi));
U = zeros(size(phi));
F = zeros(size(phi));
dW = zeros(size(phi));
dQw = zeros(size(phi));
dQ = zeros(size(phi));
Q = zeros(size(phi));
dU = zeros(size(phi));
X = zeros(size(phi));
for j = NUM1:NUM2
   X(j) = Q(j-1)/(f*Hu*1e3);
   dW(j) = ((p(j-1)+p(j))*(V(j)-V(j-1))/2)*1e6; % Work of working medium
   W(j) = sum(dW);
   while 1
      % Increase of internal energy of working medium
      M(j) = Ma*(1+(B0-1)*X(j)/((1+r)*a));% Amount of substance kmol
      T(j) =1e3*p(j)*V(j)/(M(j)*R); % In-cylinder temperature K
      k = ((a-1+B0)*B0*X(j)+B0*a*r)/((a-1+B0)* ((1+r)*a+ X(j)*(B0-1)));
                                                % Percentage of air in gas mixture
      cva(j) = 4.1868*(a0+b0*T(j)+c0*T(j)^2);
      cve(j) = 4.1868*(ar+br*T(j)+cr*T(j)^2);
      cv(j) = k*cva(j) + (1-k)*cve(j);
      U(j) = cv (j)*M(j)*T(j)*1000-Ua; % Internal energy of working medium
      dU(j) = U (j) - U(j-1);
      dQ(j) = dU(j) + dW(j); % Heat release rate
      dF(j) = dQ(j)/( Hu*1000); % Instantaneous fuel consumption

      if j == NUM1
         F(j) = 0;
      else
         if j < 350 && dF (j) < 0
            dF(j) = 0;
         end
         if j > 380 && dF(j ) < 0
            dF(j) = 0;
         end
         F(j+1) = F(j) + dF(j);
      end
      Xnew = F(j)/f;
      if abs(Xnew - X(j)) < 1e-3 % Convergence condition
         if j < 350 && X(j) <= 0
            CAB = CAB + 1;
         end
         if j > 380 && dQ(j) < 0
            CAC = CAC + 1;
         end
         break;
```

```
        else
            X(j) = Xnew;
        end;
    end;
    Q(j) = sum(dQ);
end;
CAB = NUM1 - 360 + CAB;
CAC = NUM2 - 360 - CAC;

N = numel(dQ);
ddQ(1) = (39*dQ(1) + 8*dQ(2)-4*(dQ(3)+dQ(4)-dQ(6))+dQ(5)-2*dQ(7))/42;
ddQ(2) = (8*dQ(1)+19*dQ(2)+16*dQ(3)+6*dQ(4)-4*dQ(5)-7*dQ(6)+4*dQ(7))/42;
ddQ(3) = (4*(dQ(1)+dQ(6))+16*dQ(2)+19*dQ(3)+12*dQ(4)+2*dQ(5)+7*dQ(7))/42;
if N < 7
    return;
end

% Smooth
for k = 4:(N-3)
    ddQ(k) = (-2*(dQ(k-3)+dQ(k+3))+3*(dQ(k-2)+dQ(k+2))+6*(dQ(k-
1)+dQ(k+1))+7*dQ(k))/21;
end

ddQ(N-2) = (dQ(N-6)-4*(dQ(N-5)+dQ(N))+dQ(N-4)+12*dQ(N-3)+19*dQ(N-
2)+16*dQ(N-1))/42;
ddQ(N-1) = (4*dQ(N-6)-7*dQ(N-5)+4*dQ(N-4)+6*dQ(N-3)+16*dQ(N-2)+19*dQ(N-
1)+8*dQ(N))/42;
ddQ(N) = (-2*dQ(N-6)+4*(dQ(N-5)-dQ(N-3)-dQ(N-2))+dQ(N-4)+8*dQ(N-
1)+39*dQ(N))/42;
% Smooth
figure(1)
plot((CAD(NUM1):CAD(NUM2)),T(NUM1:NUM2),'red');
xlabel('Crank angle (deg)');ylabel('In-cylinder temperature (K)');
grid on
figure(2)
plot(CAD,Y);
xlabel('Crank angle (deg)'),ylabel('In-cylinder pressure (bar)')
grid
figure(3)
plot((CAD(NUM1):CAD(NUM2)),ddQ(NUM1:NUM2));
xlabel('Crank angle (deg)'),ylabel('HRR (kJ/deg)')
grid on;
title={'Crank angle (deg)','In-cylinder pressure (bar)','Heat release rate (kJ/deg)','In-cylinder
temperature (K)'};
xlswrite(' X: \HRR\1.xlsx',title,'Sheet1','A1:D1')
xlswrite(' X: \HRR\1.xlsx',CAD(NUM1:NUM2)','Sheet1','A2:A272')
xlswrite(X: \HRR\1.xlsx',Y(NUM1:NUM2)','Sheet1','B2:B272')
xlswrite(' X: \HRR\1.xlsx',ddQ(NUM1:NUM2)','Sheet1','C2:C272')
xlswrite(' X: \HRR\1.xlsx',T(NUM1:NUM2)','Sheet1','D2:D272')
```

# Appendix B

## Full load curve of the experimental diesel engine

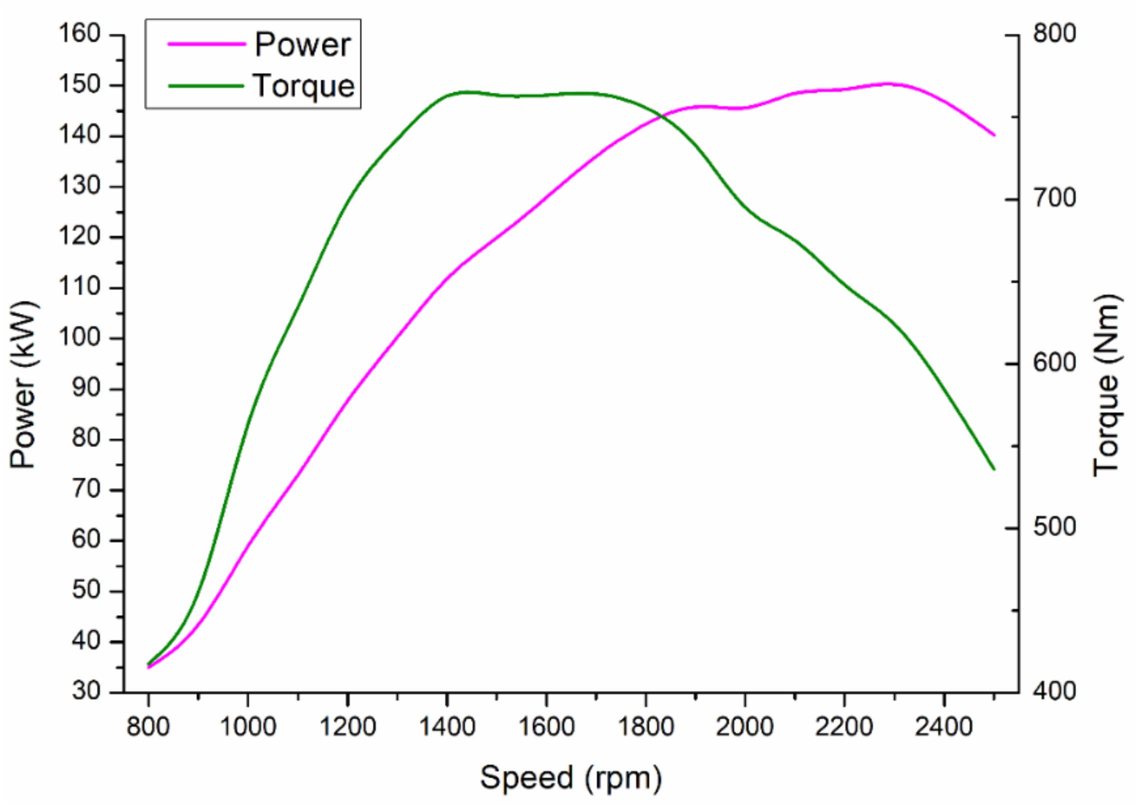

# Appendix C

## In-cylinder pressure of the experimental engine at 1800 rpm and full load

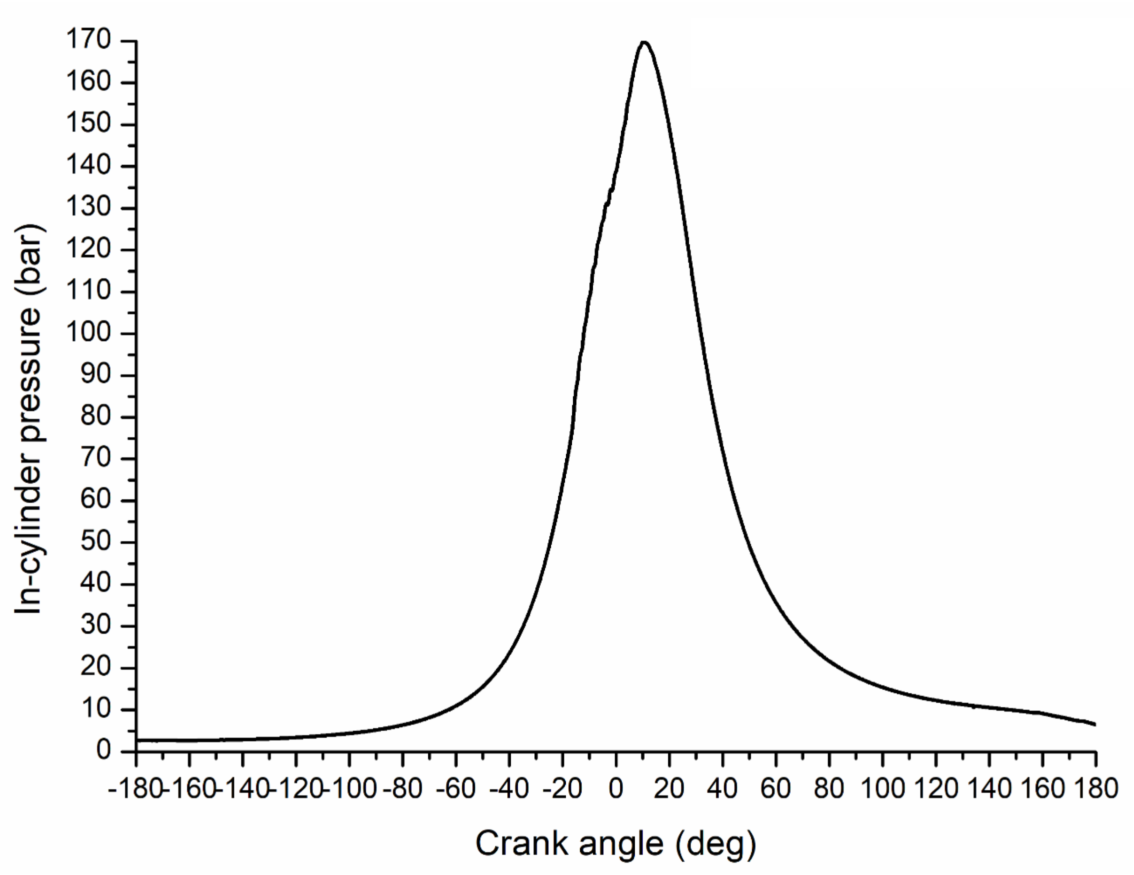

# Appendix D

## Relationship between injection duration and injected fuel mass of the injector